Applications of Atmospheric Pressure Plasma in Surface Engineering

Thesis

Applications of Atmospheric Pressure Plasma in Surface Engineering

THESIS SUBMITTED FOR THE AWARD OF THE DEGREE OF DOCTOR OF PHILOSOPHY

by

Avishek Dey

THE OPEN UNIVERSITY
SCHOOL OF ENGINEERING AND INNOVATION
MILTON KEYNES, UNITED KINGDOM.
July 2017

Supervised by:
Dr. Satheesh Krishnamurthy
Professor Nicholas St. John Braithwaite
Dr. Tony Nixon
Dr. Alex Chroneos

Amended on 2 April 2020

Abstract

Plasma processing of materials has grown to be a key technology for various industrial applications. Low pressure plasmas have found wide applications; they require expensive vacuum systems and need orderly maintenance. Atmospheric pressure plasma jets (APPJs) on the other hand are less technically demanding. APPJs can generate a high flux of active species and are a promising alternative to low pressure plasmas for surface treatment. For an APPJ the plasma is not confined within the dimensions of the electrodes and can be directed towards the desired region. This dissertation is aimed at three novel applications of atmospheric pressure plasmas: printing nanomaterials, functionalization of nanomaterials and deactivation of airborne microbes. For all the contributions presented in this thesis emphasis have be given on studying the effects of plasma on surfaces.

A novel APPJ based printing technique is proposed and developed to address issues of material degradation in conventional printing techniques. The process involves printing using nano-colloidal ink. The novelty of this printing technique is that it can tune the electronic properties of the nanomaterials *in-situ* while printing. Near edge X-ray fine structure (NEXAFS) spectroscopy of the deposited copper nanoparticles confirmed that the oxidation state of copper can be reduced equally at the surface and in the bulk. Also, by varying the gas mixture in the plasma the morphology of the films can be varied from uniform to porous. The film formed from copper nanoparticles tend to be insulating but can be transformed to conductive films through use of APPJ processes.

Graphene oxide (GO) has found applications in multi-junction devices as charge transport layers or transparent electrodes. This is because, the work function of GO can be tuned to the device specifications. A lower power APPJ has been used to dope GO films with nitrogen. High resolution X-ray photoelectron (XPS) and NEXAFS spectroscopy revealed that the plasma induces finite changes in the surface chemistry and also influences the electronic properties of GO. Kelvin probe microscopy on the functionalized films has shown that the work function of GO can be tuned by 120 mV. This variation has been linked to the specific nitrogen configuration in the graphitic lattice.

An APPJ device has also been used for depositing graphene oxide (GO) films. Hummer's method is widely used for the oxidative exfoliation of graphite. Due to the use of strong acids, the resultant GO suspension is highly acidic and need extensive dilution to neutralize pH. It has been demonstrated for the first time that an APPJ can *in-situ* reduce highly acidic graphene oxide while deposition. XPS and NEXAFS spectroscopy revealed marked differences in the oxygen containing functional groups after deposition. Both NEXAFS and Raman spectroscopy revealed the healing of sp^2 graphitic structure. Subsequent increase in conductivity was also observed from the electrostatic force microscopy measurements.

The decontamination of airborne microbes using an atmospheric pressure dielectric barrier discharge has been demonstrated. Here, air has been used as the process gas and is found to be highly efficient in the inactivation of microbes. After interaction with the plasma, the physical structure of the microbes was found to be severely distorted and changes in surface chemical composition were also observed from NEXAFS studies. These physiochemical changes lead to the annihilation of microbes.

Acknowledgements

I would like to take this opportunity to thank all, without whom this thesis would not have been possible. Firstly, I owe my heartfelt thanks to Dr. Satheesh Krishnamurthy, my lead supervisor for his patience, guidance and enormous support throughout the years of my PhD. No words are enough for the opportunities he has provided me to grow as a researcher. Collaborations with leading scientists and research visit at NASA has enhanced my scientific skills enormously, all courtesy to him. I also want thank my co-supervisors Professor Nicholas Braithwaite, Dr. Tony Nixon and Professor Alex Chroneos for their invaluable guidance and constant encouragement during my studies

I am grateful to Dr. Ramprasad Gandhiraman and Dr. Meyya Meyyappan for hosting me at NASA Ames research center. The research, I carried out at NASA contributed enormously to this thesis. I am also thankful to Dennis Nordlund, staff scientist beamline 10-1 at SSRL for helping me out with X-ray spectroscopy studies. I would also like to thank Professor Bodh Raj Mehta and Dr. Aadesh P. Singh from IIT Delhi, Dr. Amit Kumar Chakraborty form NIT Durgapur, Dr. Mike Coto form Cambridge University for their valuable collaborations.

I am indebted to the support given by staff in our department: Gordon Imlach for training me for scanning electron microscopy, Heather Davies (retired) for training me for transmission electron microscopy and Angie Jones for helping me out during the NASA visit.

I wish to thank the group members and fellow colleagues of Materials engineering for their insights during the group meetings. I would also like to thank my friends Safaa Lebjioui, Rahul Pandey, Rahul Unnikrishnan, Yadunandan Das. Special thanks goes to Dr. Shanmukha Moturu, Paheli Ghosh and Nilanjan chakrabarty for helping me out during tough times. My best wishes to all members of The Open University cricket club with whom I thoroughly enjoyed playing cricket.

Finally, my cordial thanks to the most important persons of my life for their constant support and unconditional love. My beloved parents Mr Bisweswar Dey, Mrs Lipika Dey and my lovely wife Mrs. Arpita Banerjee without them I wouldn't have made through this journey. I dedicate this thesis entirely to them.

"Do not lower your goals to the level of your abilities. Instead, raise your abilities to the height of your goals."

Swami Vivekananda

Table of Contents

List of Figures

Attributions

Data Source: Dr. Ramprasad Gandhiraman group data archive.

Figure	Attribution
3.2 (b, c & d)	Data provided by Dr. Gandhiraman drawing on work conducted under his supervision by Ms Arlene Lopez.
3.5	Data provided by Dr. Gandhiraman drawing on work conducted under his supervision by Mr Aditya Jayan.
3.6 (a, b & c)	Data provided by Dr Gandhiraman drawing on work conducted under his supervision by Mr Aditya Jayan.
3.8	Data provided by Dr Gandhiraman for analysis drawing on samples prepared and measured by Ms Arlene Lopez, Mr Luis Figueroa Toro and Dr Dennis Nordlund from experiments conducted at the SLAC laboratory.
3.9	Data provided by Dr Gandhiraman for analysis drawing on samples prepared and measured by Ms Arlene Lopez, Mr Luis Figueroa Toro and Dr Dennis Nordlund from experiments conducted at the SLAC laboratory.
3.10	Data provided by Dr Gandhiraman for analysis drawing on samples prepared and measured by Ms Arlene Lopez, Mr Luis Figueroa Toro and Dr Dennis Nordlund from experiments conducted at the SLAC laboratory.
3.15	Experiments were carried out jointly by Mr Avishek Dey and Ms Arlene Lopez under the supervision of Dr Gandhiraman.
3.16	Experiments were carried out jointly by Mr Avishek Dey and Ms Arlene Lopez under the supervision of Dr Gandhiraman.
3.17	Experiments were carried out jointly by Mr Avishek Dey and Ms Arlene Lopez under the supervision of Dr Gandhiraman.
6.2 (b)	Data provided by Dr. Gandhiraman drawing on work conducted under his supervision by Ms Diana Diaz-Cartagena.
6.3	Data provided by Dr. Gandhiraman drawing on work conducted under his supervision by Ms Diana Diaz-Cartagena and Ms Nadja Solis-Marcano.
6.4	Data provided by Dr. Gandhiraman drawing on work conducted under his supervision by Ms Diana Diaz-Cartagena.
6.5 (a)	Data provided by Dr. Gandhiraman drawing on work conducted under his supervision by Diana Diaz-Cartagena and others.

6.5 (d)	Data provided by Dr. Gandhiraman drawing on work conducted under his supervision by Ms Marjorie Lopez-Nieves, Ms Diana Diez-Cartagena, Ms Nadja Solis Marcano and others.
6.6	Data provided by Dr. Gandhiraman drawing on experiments carried out by Ms Marjorie Lopez-Nieves, Ms Vilynette Santiago-Garcia, Ms Jaione Romero Mangado. SEM imaging done jointly by Mr Avishek Dey, Ms Arlene Lopez and Ms Jaione Romero Mangado.
6.7	Data provided by Dr. Gandhiraman for analysis drawing on samples prepared and measured by Ms Jaione Romero Mangado and Dr Dennis Nordlund from experiments conducted at the SLAC laboratory.
6.8	Data provided by Dr. Gandhiraman for analysis drawing on samples prepared and measured by Ms Jaione Romero Mangado and Dr Dennis Nordlund from experiments conducted at the SLAC laboratory.
6.9	Data provided by Dr. Gandhiraman for analysis drawing on samples prepared and measured by Ms Jaione Romero Mangado and Dr Dennis Nordlund from experiments conducted at the SLAC laboratory.
6.10	Data provided by Dr. Gandhiraman for analysis drawing on samples prepared and measured by Ms Jaione Romero Mangado and Dr Dennis Nordlund from experiments conducted at the SLAC laboratory.
6.11	Data provided by Dr. Gandhiraman for analysis drawing on samples prepared and measured by Ms Jaione Romero Mangado and Dr Dennis Nordlund from experiments conducted at the SLAC laboratory.
6.12	Data provided by Dr. Gandhiraman for analysis drawing on samples prepared and measured by Ms Jaione Romero Mangado and Dr Dennis Nordlund from experiments conducted at the SLAC laboratory.

List of Tables

List of Acronyms

CVD	Chemical vapor deposition
DC	Direct current
DSSC	Dye sensitized solar cell
FET	Field effect transistor
ORR	Oxygen reduction reaction
PECVD	Plasma enhanced chemical vapor deposition
RF	Radio frequency
SCCM	Standard cubic centimeter per minute
SLM	Standard litre per minute
SERS	Surface-enhanced Raman scattering

Chapter 1. Introduction and Motivation

This chapter introduces various plasma based techniques in the field of materials processing and mentions their advantages over the conventional techniques. Recent advances in plasma processing of nanomaterials particularly targeted towards deposition and functionalisation has been discussed and corresponding research gaps are identified. To address these gaps, new methods for surface engineering of nanomaterials such as copper and graphene oxide using atmospheric pressure plasmas has been proposed. Atmospheric pressure plasma can offer a wide spectrum of applications along with the benefits of low cost and in-line capabilities. The efficacy of atmospheric pressure plasma for air sterilizations has also been explored which adds another dimension related to biomedicine to this technique. In terms of analysis, soft X-ray spectroscopy is introduced for revealing the changes in electronic and chemical properties induced by plasma functionalization of surfaces.

1.1 Plasma in material processing

Over the years, plasma processing has grown to be a key unit of various manufacturing industries. Plasma technologies are of vital importance to industries such as aerospace, automotive, steel, biomedical and toxic waste management. Moreover, plasmas have become indispensable for large scale integrated and micro electronic manufacturing.[1] Plasmas have attracted the attention of industries primarily due to two reasons. First is the high power and energy density of thermal plasmas. The second advantage of plasma is that, they consist of large number of active species having sufficient energies to initiate chemical reactions on their own. In the case of high power plasma such as electrical arcs and plasma torches have varying power density in the range of 100 W/cm^2 to several kW/cm^2. The operating temperature during the process rises to hundreds and thousands of degrees higher than ambient temperature. Hence, this plasma is implemented for high temperature material processing such as melting, cutting, welding or coating. There are many applications where high temperatures associated with thermal plasmas is undesired and in some cases strictly

avoided. It needs to be mentioned that, it is also possible to sustain a discharge at much lower temperatures, even at room temperature. Secondly, the active species is enabled to perform complex modifications at the materials surfaces, which are rather unfeasible in many ways via other conventional techniques. [2] One of the most important factors of using plasma is that these processes are dry which doesn't generate chemical waste and are environmental friendly as well.

The work presented in this thesis focusses on non-thermal atmospheric pressure plasmas. One of the key advantages of this plasma is that they can be operated at low temperatures and are superior to other non-destructive techniques. Non-thermal plasmas have found applications in the field of materials processing for much of the last century. One of the major advantages of non-thermal plasma, as already mentioned is the abundance of chemically active species for reaction with different surfaces. Thus, non-thermal plasma processing will provide unique opportunities for low temperature material processing. Current industrial applications of non-thermal plasmas are presented in **Figure 1.1.** According to the survey by marketsandmarkets.com, the market value of non-thermal plasma processes in various sectors is estimated to grow at a compound annual growth rate (CAGR) of 16.2% from 2016 to 2021 to reach an estimated value of 2.91 Billion by 2021.

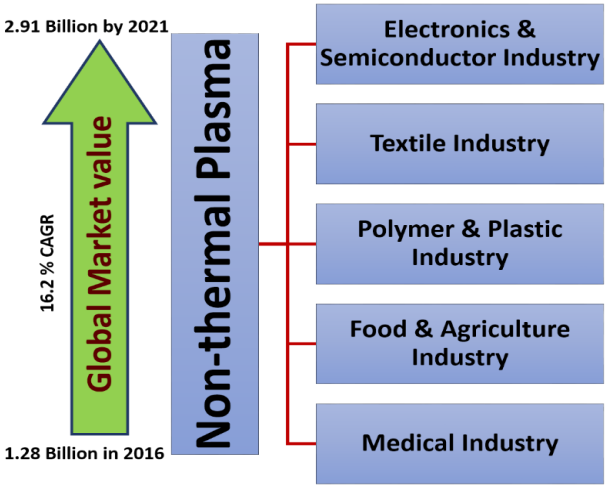

Figure 1.1 Current applications of Non-thermal plasma processes. The global market value of these processes is estimated to reach a value of 2.91 billion USD by 2021.

In industries, plasmas are operated at various pressure regimes ranging from vacuum to several atmospheres. Recently, there has been an increasing interest for atmospheric pressure plasmas in materials processing, as it does not require the sophisticated vacuum equipment with respect to the conventional vacuum based plasma systems. Thus, atmospheric plasma designs can easily be incorporated into production lines. The need for capital-intensive vacuum chambers for creating low pressure activations is effectively eliminated, hence, reducing the material processing cost.

Atmospheric pressure plasma jets (APPJs) have evolved as a tool of significant practical importance. This is because the plasma jets are not restricted within the dimensions of the electrodes. APPJs consist of charged particles, neutral metastable species, radicals, and radiations in the UV and visible regions.[3] The capabilities of APPJs have been realized extensively for biomedical applications. For example, Laroussi *et al.*[4] demonstrated the

potential of APPJ by killing various types of bacteria. The low cross section of the jet resulted in a localized effect. This illustrates the advantage of selectivity involved with this process. This low temperature process can be used to sterilize medical equipment, which is sensitive to heat. It also finds applications in the field of food safety because of its ability to deactivate bacterial growth. The active species present in APPJ can change the wettability of surfaces.[5] APPJ with extremely low concentration of oxygen mixed with an inert gas can be used for surface cleaning purposes. A recent review by Penkov *et al.* [6] provides a detailed overview on the various applications of APPJs. Clearly, APPJs possess an advantage over other conventional techniques including vacuum based plasma technologies. Its key features are simplicity of use, low cost, ease to design, and minimal power consumption. [7] It can prove to be a powerful tool in the field of surface engineering, functionalization and synthesis of nanomaterials, and this thesis is intended to justify this claim. The aim of this thesis is to use atmospheric pressure plasma in different configurations for three different applications such as selective doping, printing and sterilization and to understand the surface electronic/chemical properties using soft X-ray spectroscopy.

In the next sections, a brief overview of various plasma based processes in relation to metal deposition, carbon nanotechnology and sterilizations are presented. This is then followed by a brief introduction to plasmas and types of plasma used in the thesis.

1.2 Motivation

1.2.1 Plasma in material deposition

Plasma-assisted deposition, implantation, and surface modification are important materials processes for producing films on surfaces and modifying their properties.[8] **Figure 1.2** presents an overview of various plasma based deposition techniques. These techniques have been branched under the thermal characteristics of plasma. Most thermal plasma based

deposition techniques use arc discharges.[9] Arc discharges provide a high temperature region between the electrodes in presence of high gas flow. Due to the high gas flow the plasma can extend beyond the electrodes in the form of a plasma jet. Thermal plasma based deposition techniques provide high deposition rates for a wide variety of materials. As high temperatures are involved, this process leads to thermal distortion and poor metallurgical properties. High temperature plasmas are mostly used in coating, arc welding and arc cutting purposes. Low temperature plasmas are especially suited for operations that are sensitive to high temperatures such as modern integrated circuit manufacturing. Non-thermal plasmas have been a revolution as films that require high temperature for synthesis can be deposited at much lower temperatures. Additionally, the film properties like chemical composition, crystal morphologies can be improved and controlled in a way that is unattainable under equilibrium deposition conditions at any temperature. For example, films of diamond that are unique can be grown and deposited using plasms enhanced processes. Well known techniques like sputtering, physical vapour deposition (PVD) and chemical vapour deposition (CVD) have been enhanced by introducing plasma into the process. Best example is the deposition of SiN insulating layers. A normal CVD requires temperatures near to 900 ºC for SiN film growth. However, with plasma-enhanced chemical vapour deposition (PECVD) the same process can be carried out at 250 ºC.[10] Both in PEPVD and PECVD the plasma is generated by ionization caused by electric discharge near the deposition materials. [11] It is noteworthy to mention that low pressure non-thermal plasma processes have achieved great progress and impressive technological advancements. The evolution of nanotechnology and development of advanced functional materials for next generation applications have presented atmospheric pressure plasma opportunities to succeed.[12] Additionally, the increasing drive by industries for low cost deposition techniques have brought atmospheric pressure plasmas to the forefront of research.

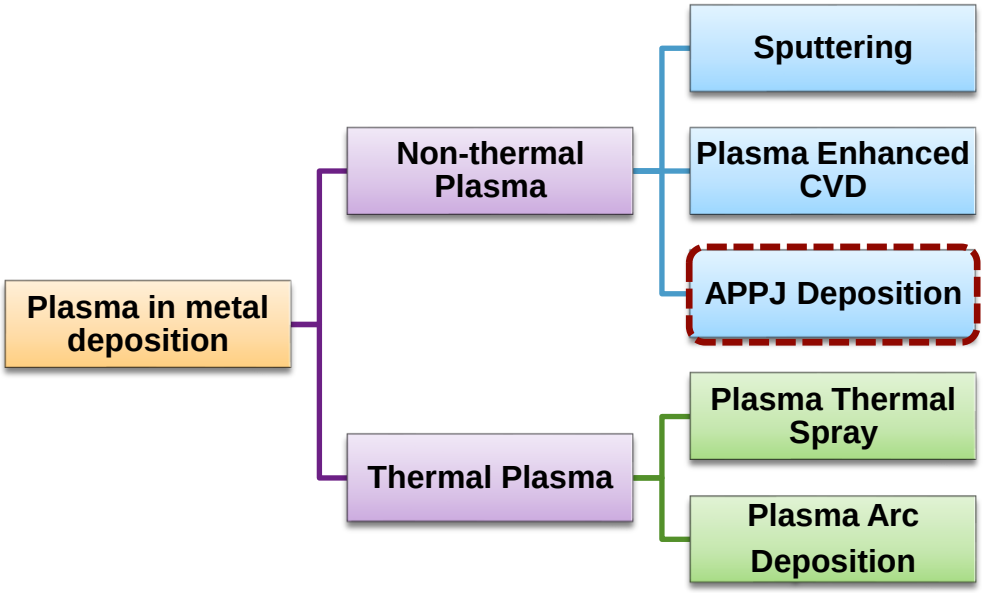

Figure 1.2 Types of plasmas deposition processes branched under the thermal characteristics. Along with the established techniques of sputtering and PECVD, APPJ based deposition (dashed box) is proposed as a new tool in the field of non-thermal plasma techniques.

Modern technological areas of electronics, biomedicine, and semiconductor are in continuous search for low cost solutions to functionalize, coat and selectively modify surfaces. Patterned growth/deposition of metals onto varied substrates is key to the applications demands of these technologies. The creation of patterned coating or surface modifications onto two- and three-dimensional substrates is in effect "printing". Conventional techniques that carry out this task include photolithography, wet chemical etching, laser ablation, ink jet printing, microcontact printing (mCP), gravure printing, screen printing and flexographic printing. [13] Ink jet printing is the most widely used technology for printing conductive patterns. The advantages of ink-jet printing are accurate and fast deposition, mask-less and non-contact printing and it is compatible with a broad range of functional materials.[14] However, this techniques have several disadvantages; [15,16]

1) Strong dependence on rheology of the ink.
2) Pre-treatment of the substrate to match surface energy.
3) Post treatment steps, (to remove solvents, to sinter the nanoparticles).

Plasmas are often used in pre-treatment or in post-treatment process steps. Substrates are pre-treated with plasma to alter their wettability [15] while printed patterns are post-treated with plasma to replace high temperature sintering.[17] Atmospheric pressure plasma based printing technology could be an ideal solution to address the above issues. Penache *et al*. [18] were the first to report atmospheric pressure based micropatterning technique and referred it to as "plasma printing". Michael Thomas from the same research group published a review article on Plasma Printing.[19] Here he presented a number of atmospheric-pressure plasma printing setups that they developed in their lab. Their plasma printing technique was based on plasma stamps. Plasma stamps for this purpose were produced by photolithographic techniques or by electromechanical or laser-based engraving. Which in my knowledge is the major drawback to this technique. As a need to replace stamp is inevitable for multiple patterns.

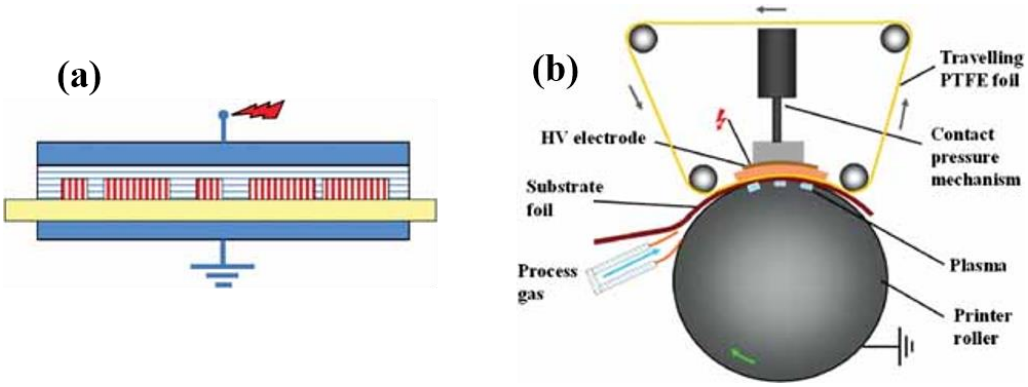

Figure 1.3 (a) Principle of plasma printing with closed cavities defined in a dielectric material (''mask'', horizontal hatching) with mDBDs (vertical hatches) used to treat an insulating or conductive substrate. The arrangement of dielectric and substrate is sandwiched by the electrodes. (b) set-up used for the development of reel-to reel plasma printing.[19]

Objective 1: Atmospheric pressure plasma jet printing technology

Silver nanoparticle inks have most commonly been used for printing conductive patterns using ink jet printing. However, the large-scale implementation of Ag inks is restricted due to the high material cost. Inks of Cu nanoparticles have the potential to replace nano silver inks commonly used in conductive printing. Copper has electrical conductivity, which is only 6% lower than that of silver, and the current cost of copper is about 100-times lower than that of silver. [17] However, Cu nanoparticles have an inherent tendency to oxidize in ambient conditions. Several approaches have been adopted to overcome this issue. [13] Such as polymer coating, Carbon/graphene encapsulation, metallic core-shell structure and silica coating. [20] None of them could provide long term solutions. In this thesis, a novel atmospheric pressure plasma jet based printing technique is developed. Here the printing is carried out using nano-colloidal ink of copper. The APPJ printing technology proposed in chapter 3 has the ability to reduce the nanoparticles *in-situ* during the printing process. This negates the need for fresh inks every time. It is found that the printing could be carried out on varied substrates including polymer, silicon wafer and even paper. NEXAFS studies revealed that the electronic property of the deposited film can be enhanced by using reducing gases in the plasma. Another advantage of this technique is that by increasing the hydrogen content in plasma the porous structure could be achieved. Current voltage measurements show that with plasma printing better conductance could be achieved compared to 5-hour annealing. Third chapter of this thesis is dedicated to this work.

1.2.2 Plasma engineering of Graphene Oxide

Carbon based nanomaterials have empowered the world of nanotechnology with their fascinating properties. A prodigious amount of research and commercialisation of technology has occurred over the past decade or so on new forms of carbon. New exciting properties have continued to emerge from amorphous carbon, DLC (diamond like carbon) to graphene. Carbon nanotubes (CNT) have been a major focus of attraction to the scientific world of carbon until the discovery of graphene whereas hard carbon coatings continue to be in spotlight for engineering community. There are numerous research articles and review articles on carbon nanotubes. [21–24] Graphene the 2-D allotrope of carbon has gained significant attention, since it was isolated in 2004 by Geim and Novoselov**.**[25] Graphene is one atom thick honeycomb lattice of sp^2 bonded carbon atoms and is the elementary unit of all the graphite allotropes. When wrapped it forms 0D dimensional fullerenes, after rolling it becomes 1D dimensional nanotubes and when stacked takes the 3D dimensional graphite. Graphene is renowned for its remarkable electronic and optical properties. The most interesting properties are its high thermal conductivity (5000 W/mK) [26], extremely high room temperature mobility of charge carriers (250,000 $cm^2/V/s$) [27] which exceeds its theoretical predicted value of 200,000 $cm^2/V/s$,[28] high surface area (2630 m^2/g) [29], optical absorption of $\pi\alpha \approx 2.3\%$ [30] and ability to withstand extremely high current densities. [31] Graphene oxide (GO) is considered to be a promising alternative to graphene and is in essence the monolayer of graphitic oxide. It can be produced in large scale from low cost graphite powder.[32,33] The history of graphite powder extends back to year 1859 when British chemist B.C Brodie investigated the chemistry of graphite oxide.[34] Brodie determined the chemical composition of graphite oxide and found it be dispersible in basic water. His synthesis involved “chlorate of potash” (potassium chlorate, $KClO_3$), graphite and concentrated nitric acid. The most attractive property of GO is that it can form stable dispersion in variety of solvents compared to graphene, which is highly hydrophobic.[35]

Enabling it to be appealing for cheap, solution processed flexible electronic devices.[33]

The oxygen containing functional groups in GO have a profound influence on its optical, electronic, mechanical and electrochemical properties. There have been extensive studies carried out to understand the structure of GO. Numerous models have been suggested to depict the structure of GO.[36] According to these models the basal plane of GO is decorated with hydroxyl and epoxy functional groups. While small amounts of carboxyl, carbonyl, phenol groups occupy the sheet edges. The polar oxygen groups render it highly hydrophilic. This enables GO to interact with a varied range of organic, inorganic materials via covalent and ionic bonds. Moreover, GO is an electronically hybrid material. The sites with sp^2 carbon (π states) are conductive while the C-O sp^3 sites (σ states) have a large band gap. Thus by adjusting the ratio between sp^2 and sp^3 domains, GO can be transformed from insulator to a semiconductor and even to graphene like semi-metal.[37] The defects created due to these oxygen functional groups reduce the conductivity of GO sheets and in turn makes it more electro-active. Reduction of GO (forming rGO) is usually carried out through chemical and thermal processes to achieve properties like of graphene. Thus finding applications in bio sensing and electrochemical systems. [38] All these properties makes rGO/GO, a suitable alternative to graphene for various applications.[39]

Low temperature non-thermal plasmas have been successfully implemented for processing (synthesis and functionalization) of nanomaterials. They are also very significant for the silicon-integrated chip (IC) manufacturing.[40] The techniques of reactive ion etching (RIE) and plasma enhanced chemical vapour deposition (PECVD) are of utmost importance for semiconductor processing. With its accomplishments in the silicon industry, applications of plasma have been broadened to carbon nanomaterials (CNT and Graphene).[41] PECVD has emerged as the alternative to high temperature CVD processes for the synthesis of CNT and graphene. Recent studies by Meyyappan [42] and Neyts [43] present a comprehensive review

on PECVD growth of CNT along with the advantages of this technique. PECVD has also been successfully implemented to dope CNT and graphene. [44,45] Plasma based techniques have been predominantly applied to the initial synthesis of carbon-based materials rather than post processing. Plasma also has considerable potential for post synthesis functionalization of carbon based materials. Plasma discharges can allow the fixation of different chemical species of the same element to the graphene structure. Selectivity associated with plasma can open new dimensions in functionalising graphene in terms of creating definite structural defects and precision in doping. **Table 1.1** presents a summary of articles that report functionalization of Graphene/GO using plasma. The table mentions the plasma parameters used for functionalization along with the enhanced properties achieved. However, most of the plasma processes involve low-pressure vacuum based systems. APPJ can be a promising alternative to low pressure plasmas for functionalization of GO.

		Plasma						
S. No.	**Graphene Type**	**Species/ Element**	**Generation**	**Time**	**Parameters**	**Characteristic changes**	**Application**	**Ref**
1	Mechanically exfoliated	NH_3	Grid- assisted diffusion plasma reactor	10 min	13.56 MHz, 0.1 Torr, 20 Watt , 750 mm distance between the electrodes.	Controlled edge functionalization.	Electronics	46
2	CVD	Ar and NH_3 (5% by flow)	Electron beam generated plasma	60 secs	2keV electron beam, 2 ms pulse width, 20 ms period	Higher signal to noise ratio in BioFET device.	DNA attachment	47
3	CVD	N_2 (50 SCCSM)	Rf Plasma	5 min	70 W , base pressure of 2.7×10^{-4} Pa ,working pressure 0.7 Pa	work function from 4.91 eV to 4.37 eV	Electronics	48
4	Chemical exfoliation	N_2	Rf Magnetron sputtering system	30 min	13.56 Mhz, 130 W ,0.1 mBar chamber pressure	Increased electrical conductivity between carbon and catalyst	ORR	49
5	Chemical exfoliation	N_2	Rf Magnetron sputtering system	30 min	13.56 Mhz, 130 W ,0.1 mBar chamber pressure	Enhanced interaction between graphene and metal *d* orbitals	H_2 Storage	50
6	Chemical exfoliation	N_2	Harrick model PDC-32G plasma cleaning unit	20,40,60,100 min	750 mTorr. Plasma power 100 W	Enhanced electron transfer efficiency	Glucose biosensing	51

S. No.	Graphene Type	Species/ Element	Generation	Time	Parameters	Characteristic changes	Application	Ref
7	Chemical exfoliation	N_2 (91 sccm)	PECVD	1-3 min	14 Torr, 500 W	~280 F/g	Ultracapacitor	52
8	CVD	N_2	DC plasma chamber	20,40 secs	300 ~ 350 V negative bias, 460 Pa	Increase in number of active sites after plasma treatmnet	Bifacial DSSC	53
9	CVD	N_2 (25 slm)	APPJ	1 to 30 secs	15 kv , 25 kHz	Hydrophobic to hydrophilic, N doping with minimum structural damage	Electronics	54
10	Micromechanical exfoliation	O_2	Parallel plate rf plasma System	3 sec	13.57 MHz, 15 W(50 mW/cm^2 power density), 20 mTorr	Band gap opening	Optoelectronics	55
11	Chemical exfoliation	O_2	Cesar 133 RF power generator	10 sec	13.56 MHz, 200 W , 100 Pa pressure	Increased response towards electrochemical activity	Graphene film Actuator	56
12	CVD	O_2	Microwave radical generator	2 min	1000 W DC power ,1 Torr, 100 sccm O_2 flow	Cleaning polymer residue after transfer.	Electronics	57
13	CVD	O_2/Ar (1:10)	Harrick model PDC-32G plasma cleaning unit	10,15,20 sec	6.8 W input power	Increased thermo power	Thermo electric effect	58
14	Chemical exfoliation	O_2	Capacitively coupled plasma	1 - 5 min	120 mTorr chamber pressure, 25− 200W , 13.56 MHz	Patterning	Flexible transparent electrodes	59

S. No.	Graphene Type	Species/ Element	Generation	Time	Parameters	Characteristic changes	Application	Ref
15	CVD	O_2	Parallel plate rf plasma System	5 sec – 2 min	13.57 Mhz, , 2-5 W,0.15 mBar chamber pressure	O_2 induced lattice dipole, downshift of E_F	SERS, Molecular sensing	60
16	CVD	Ar/H_2 (85/15) 200 sccm	Reactive ion etching system		13.56 Mhz, 3 W(power density is 4 mW/cm^2),0.05 mBar chamber pressure	Reversible Hydrogenation	Electronics	61
17	Peel-off	H_2	Tube furnace with rf plasma source	60 min	300 °C, 300mTorr H_2 pressure, 20 W plasma power	Selective etching at the edges	FET with high on/off ratio	62
18	CVD	H_2	Rf plasma (Fischione 1070)	10,20,40 sec	13.56 Mhz, 10^{-6} mBar chamber pressure	Uniform protein distribution	Cryo em grids	63
19	PECVD	Ar (10 sccm)	Rf plasma	1,3,5 min	800 °C, 150Pa and 150W	Decreases the turn-on electric field and increase in the maximum emission current density	Graphene field emission devices	64
20	Peel -off	Ar (60 sccm)	Atmospheric pressure plasma reactor	1 min	1 Torr, 130 V	Tunable photoresponse	Photodetector	65

Table 1.1 Overview of the recent progresses in plasma engineering of graphene and graphene oxide.[66]

In the fourth and fifth chapter APPJ is presented as an alternative to engineer properties of GO. APPJ functionalization is advantageous in terms of controllability and selectivity associated with it. The ionic species present in plasma can tune electronic and optical properties of graphene and can even control the surface hydrophobicity (refer to **Figure 1.4**). Wet chemical functionalization involving precursors and by-products fails in achieving localized effects in GO. With APPJ, we can precisely tailor graphene properties by inducing localized changes. Advantages of this technique include time and cost effectiveness. This process, being clean and reliable, opens future pathways for large-scale industrial implementation. The two objectives of this chapter are as follows:

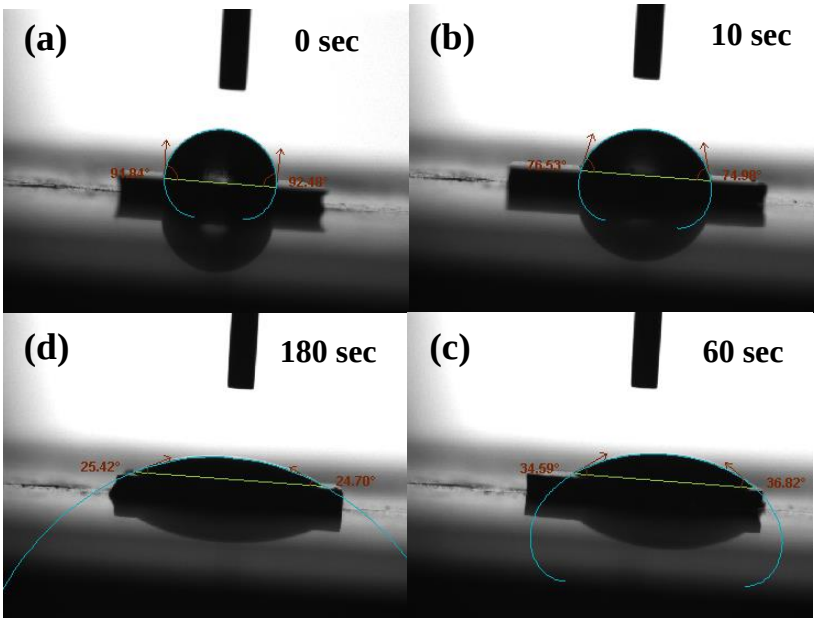

Figure 1.4 Changes in surface wettability of GO with duration of plasma treatment. For the untreated GO film the water contact angle is~92° and decreases to ~25° with 180 seconds of plasma treatment. The plasma conditions are same as in Chapter 4.

Objective 2: Tuning the work function of GO

Work function is the energy difference between Fermi level and Vacuum level. Ability to tune the work function is a key requirement in multi junction devices. In solar cells and other electroluminescent devices, the work function of the electrode is an important factor for the choice of material. GO has the potential to be the ideal candidate for transparent electrodes [67] or as charge transport layers [68]. For GO, theoretical studies have shown that the WF can be varied by up to 2.5 eV.[69] Mishra *et al*. [70] demonstrated that the WF of GO gate electrode in a complementary metal oxide semiconductor (CMOS) structure can be modulated from 4.35 eV (n-type metal) to 5.28 eV (p-type metal). Theoretical studies have revealed doping graphene with substitutional impurities can significantly alter its electronic properties. [71–74] Due to its comparable atomic radii and five valence electrons, nitrogen has been considered as the appropriate element for such doping. In comparison to carbon (2.55), nitrogen has higher electronegativity (3.04). Nitrogen can occupy different positions on the graphene lattice (refer to **Figure 4.6** in chapter 4). Depending on its bonding configuration, nitrogen can distort the π electron cloud of graphene and can also change the hybridization state from sp^2 to sp^3. [75] In the case of GO, changes in oxygen functionalities on the graphene sheet with nitrogen doping have also been reported. The charge distribution of the carbon atom in graphitic lattice will be strongly influenced by the neighbouring nitrogen atoms. Transforming the carbon atom into an active site. [76] The presence of these active sites extends the application of GO to semiconductor devices [77], sensors [78], batteries [79], ultracapacitors [80] and as catalyst in oxygen reduction reactions [81].

Using nitrogen plasma to dope GO is an eco-friendly and energy-saving alternative to the conventional chemical processes. Several strategies of plasma assisted nitrogen doping have been adopted so far. [66] Out of which APPJ can be a rapid and non-invasive technique to functionalize GO. APPJ functionalization have been reported to have enhanced the

properties of GO in Dye-Sensitized Solar Cells as well as for supercapacitor applications. [82,83] Recently there has been efforts to functionalize graphene using APPJ. Reports by Lee *et al.* [54] and Huang *et al.*[84] suggests that APPJ can be used to change the surface free energy and even to dope graphene. Lee *et al.* [54] powered the plasmas using a 15 kV source while Huang *et al.*[84] did the treatments at 10.7 kV and 14 mA. However, there are no reports on controlled nitrogen doping of graphene oxide using APPJ. In this thesis, an APPJ operating at a power as low as 4 watts has been used to dope GO films with nitrogen. The surface chemical and electronics properties were studied extensively using X-ray spectroscopy. The results reveal that a specific configuration of nitrogen in the graphitic lattice could be achieved. Kelvin probe force microscope (KPFM) studies revealed that the WF of GO could be modulated by a value of 120 mV with this functionalization technique.

Objective 3: Deposition of rGO from acidic GO solution (in-situ reduction)

Hummer's method of chemical exfoliation is the widely-used technique for bulk production of water dispersible graphene oxide (GO). Due to the involvement of strong oxidative reagents, a large portion of sp^2 carbon atoms gets converted to sp^3 configurations. This disrupted sp^2 network renders GO electrically insulating.[85] At room temperature the transport gap of GO is 0.5 eV. [86] To restore the electrical conductivity GO needs to be reduced. Use of strong reducing agents like hydrazine results in increased conductivity by about 5 orders of magnitude (~10^{-3} to 10^2 S/m) .[85] **Figure 1.5** shows the various steps in the synthesis process of rGO. As synthesized GO suspension is highly acidic and need extensive washing to neutralize the pH. Additionally, the step to reduce GO involves toxic reducing agents. Thermal annealing in Ar/H_2 or ultrahigh vacuum (UHV) environments are also an efficient way to reduce GO. [87,88] However, the required high temperatures (> 500 ºC) limits the range of substrates that can be used. Hence there is a need for sustainable alternatives to this technique, as the series of steps involved in reduction of GO including dispersion, filtration, washing and drying, will eventually increase the processing cost.

Reducing GO using plasmas have already been realized as an eco-friendly and energy-saving alternative to existing chemical processes.[89–93] In this thesis it has been demonstrated for the first time the ability to reduce highly acidic graphene oxide in situ with deposition using an APPJ. This would negate all the intermediate steps as shown in **Figure 1.5**. Here the starting material is the acidic GO suspension (pH < 2) and with a single step deposition GO could be reduced to rGO. To confirm this claim, changes in surface chemistry were studied using XPS and NEXAFS. Spectral features showed marked difference in the oxygen containing functional groups. Subsequent increase in conductivity is also evident from the electrostatic force microscopy measurements. [94]

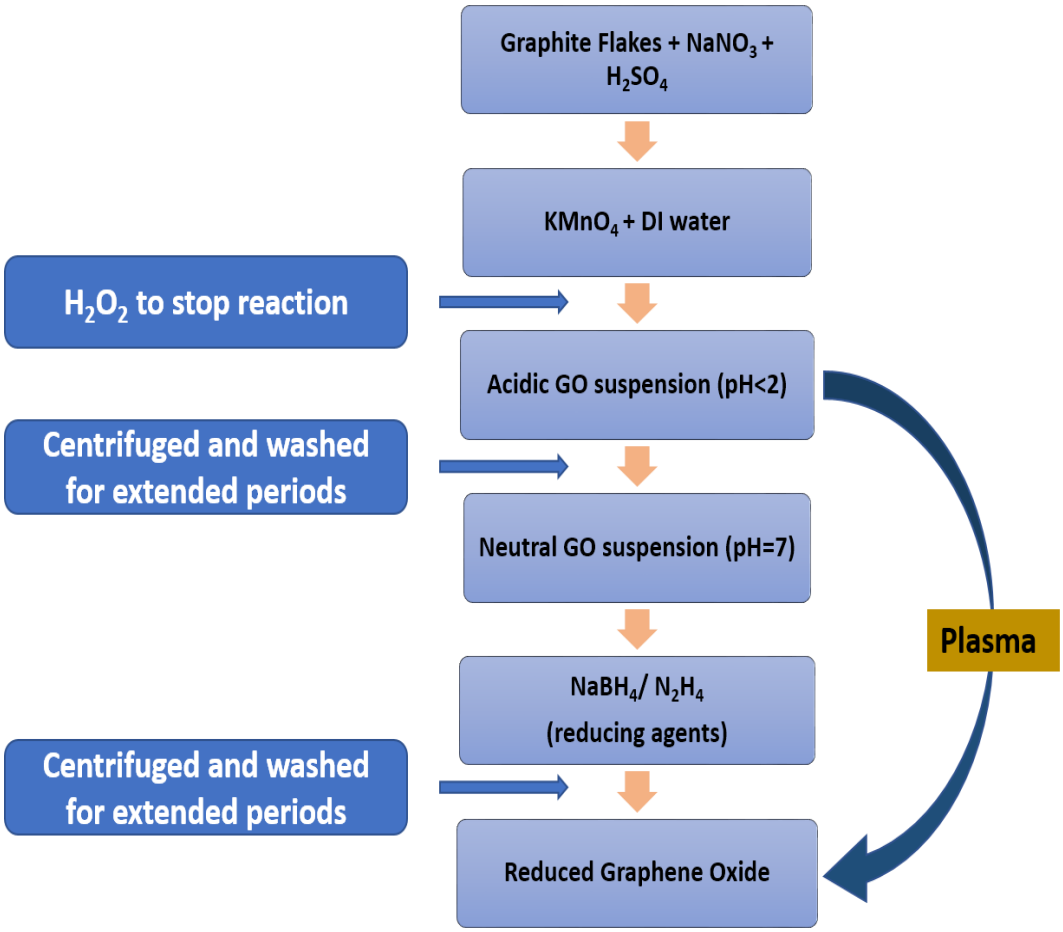

Figure 1.5 Stages of rGO synthesis. The "plasma bypass" step is the find of this thesis. It can be seen that it reduces substantially the overall process.

1.2.3 Plasma in sterilization

Sterilization is rendered as a process which results in complete elimination of microorganisms from a material or a media. Sterilization is essential for a better health of human beings. With the plethora of applications, plasma has been mostly used for sterilization of air, water and material surfaces. Conventional techniques of sterilization include heat (both dry and wet), chemical and irradiation treatments. Although being widely accepted, these established techniques carry their own disadvantages as well, such as uncontrolled antimicrobial efficacy, long processing times, expensive equipment/chambers, potential harmful byproducts and are also material specific. According to Moisan *et. al.* [95] an ideal sterilization process should be: 1) For short duration. Less than those required by steam autoclave or dry heat processes. 2) Operating at lower processing temperature (< 55 ^{o}C) 3) Versatile in operation and can deal with wide range of materials and 4) Environmentally friendly.

Plasma is an ideal alternative to the conventional techniques. As plasma sterilization provides advantages in all these criteria. There are three underlying mechanisms that promote sterilization using plasmas. First is the chemistry of the free radicals, second is the presence of UV/VUV photons and third is the physical damage of microbial cytoplasm/matter due to direct impact of heavy ions. Moisan *et al.* [96] related the biocidal property of plasma to, erosion (etching) causing structural damage of the cell and photon irradiation causing genetic damage (DNA and RNA). However, the effectiveness of the sterilization depends strongly on the properties of the plasma. Lerouge *et al.* [97] described this in the form of a flow diagram as shown **Figure 1.6**."Internal" plasma parameters such as electron density (n_e), energy distribution function *f(*E), number of active species (N), residence time (t) are influenced by gas composition, input power, frequency of excitation, gas flow rate, pressure, and geometrical factors related to the chamber. Plasma based

sterilization processes use gases that are non-germicidal on their own but, become biocidal only in their plasma state. Examples of this gas mixtures are air, helium/air or helium/O_2, and N_2/O_2. [98] Plasmas operating both at the low pressure ($\leq$ 10 Torr) and atmospheric pressure regime have been used for sterilization purposes.

At low pressure, plasmas can cover a larger area uniformly while for atmospheric pressure plasma the treatment is localized but can yield a very fast inactivation. Review articles by Lerouge *et al.*[97], Mounir Laroussi [98] and Moreau *et al.*[99] describes in detail the various applications of non-thermal plasma technologies in bio-decontamination and sterilization. Despite all the advantages, low pressure plasma sterilization has its disadvantages as well. With the presence of organic residues or packaging material the effectiveness of plasma is severely diminished. One way to overcome this issue is to introduce UV radiation of wavelength 254 nm, which is known to be most effective on microorganisms[100] in addition to using packaging materials that are transparent to this wavelength. Another solution is to generate plasma inside the package itself, which can be achieved in atmospheric pressure plasma configuration. Cullen *et al.* [101] were able to sterilize cherry tomatoes inside a 3.5 litre sealed commercial polypropylene package using Dielectric barrier discharge (DBD) plasma. In addition to being operational at atmospheric pressure, the presence of abundant active species and low temperature are the major advantages for atmospheric pressure plasma. There are several different techniques to generate plasmas at atmospheric pressure with macroscopic temperature close to ambient, [100] and their applications are multiple, including the treatment of surfaces, gases and aqueous solutions. Atmospheric pressure plasmas sustained in ambient air contains highly reactive nitrogen and oxygen species like ozone, hydrogen peroxide, hydroxyl radical and various NO_x species. These active species can directly or indirectly affect the structure and function of proteins, lipids and nucleic acids (DNA damage).[102] Thus atmospheric pressure air plasma are ideal candidate to achieve optimum inactivation and also negates the use of costly process gasses.

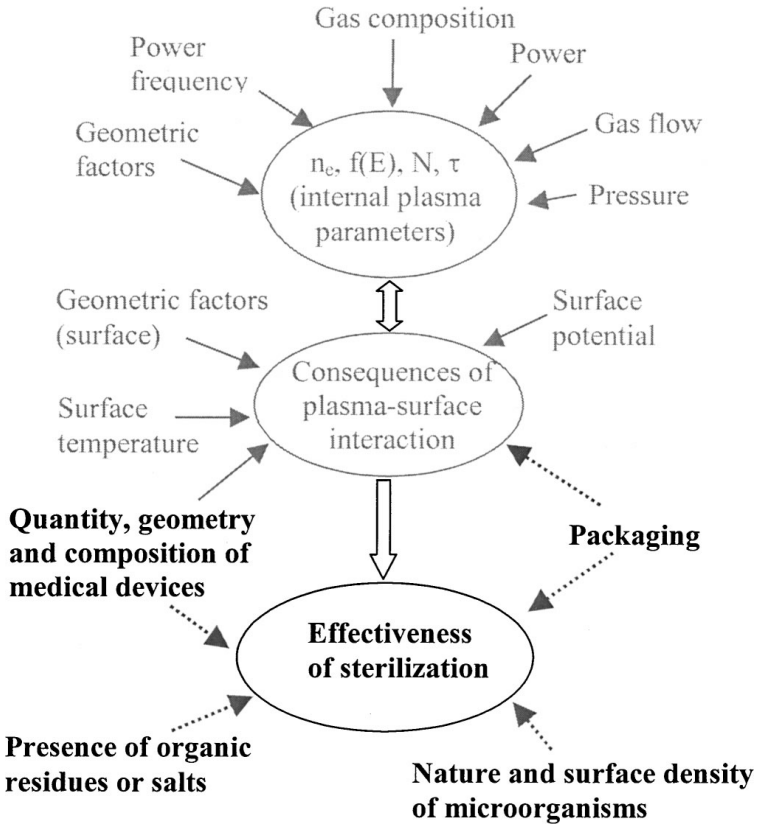

Figure 1.6 Diagram to show the influence of various parameters influencing the sterilizing efficiency of the plasma. [97]

Objective 4: Atmospheric pressure plasma in Air sterilization

Most of the plasma based sterilization have been targeted for surface bound contaminants. However, one third nosocomial infections occur due to airborne transmission. The work presented in Chapter 5 emphasizes on airborne microbial decontamination. Here a plasma is ignited using a dielectric barrier discharge configuration with air as the process gas. The efficacy of air plasma was measured using microscopy and X-ray spectroscopy studies. Microbes were found to be severely distorted and changes in surface chemical

composition was also observed leading to the microbial inactivation. The modular system developed and tested in collaboration with a company will play a critical role in providing safer and healthier air for commercial and healthcare environments.

1.3 Soft X-ray spectroscopy for surface analysis

During plasma processing, a major part of chemical reactions takes place at the very surface of matter. To gain insight into these processes a tool is required that can provide information about the interactions between the atoms and molecules at the surface. Soft X-ray spectroscopy has emerged as a powerful tool to study surface and interfaces of materials. Soft X-ray spectroscopy uses photons to probe the valence band electrons. Since the valence band of a material is strongly influenced by the neighbouring atoms this gives extremely high chemical sensitivity to this technique. In this thesis, soft X-ray spectroscopy techniques have been extensively used to analyse surfaces that are engineered using atmospheric pressure plasmas.

X-rays typically in the energy range of 0-1500 eV are referred to as Soft X-rays.[103] This energy range is sufficient for the spectroscopic studies of most of the important elements in periodic table. Soft X-ray Spectroscopy techniques involve the excitation of an element using X-ray photons and monitoring its decay process, which occurs either via radiative or non-radiative process. For a simple one electron system, X-ray photons can excite a core level electron to an unoccupied bound state or eject it into the continuum. The first process forms the basis of X-ray absorption spectroscopy (XAS) while the second is used in X-ray photoelectron spectroscopy (XPS). A schematic representation of these processes is shown in **Figure 1.7.**

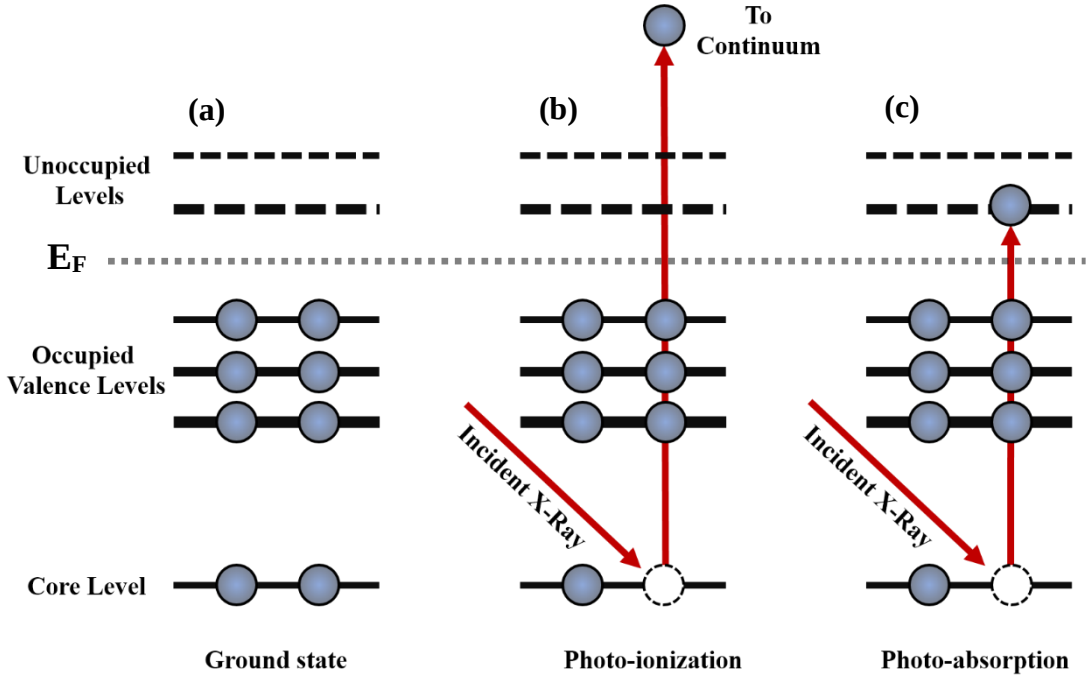

Figure 1.7 Schematic of soft X-ray induced excitation process. (a) Ground state electronic configuration, (b) the process of photoionization where the incident photon excites the core electron to continuum termed as XPS, (c) photo absorption (XAS) occurs when a core electron is excited to the unoccupied levels of the conduction. XPS probes the total density of states while XAS probes the partial density of states.

XPS relies on the photoionization of an electron to the continuum where it becomes a free particle. Here kinetic energy of the ejected photoelectron is measured from which binding energy of the electron can be determined. This emitted electron can be from a deep core level or from a shallow valence shell. To probe the core levels X-rays should have energy high enough to ionize a core electron while for valence bands low energy photons are used. In most cases Mg Kα (1253.6 eV) / Al Kα (1486.6 eV) sources are used for core level and He I (21.2 eV) /He II (40.8 eV) discharge lines are used for valence band.

Soft X-ray absorption spectroscopy provides information about the unoccupied density of states above the Fermi level. These transitions are governed by dipole selection rules. The atomic nature of the core hole implies elemental and site selectivity. XAS is divided into two regimes as shown in **Figure 1.8**. Spectra obtained for electrons excited to low energy bound states is called Near Edge X-ray absorption fine structure (NEXAFS). While for electrons excited to high energy bound states is known as Extended X-ray absorption fine structure (EXAFS).

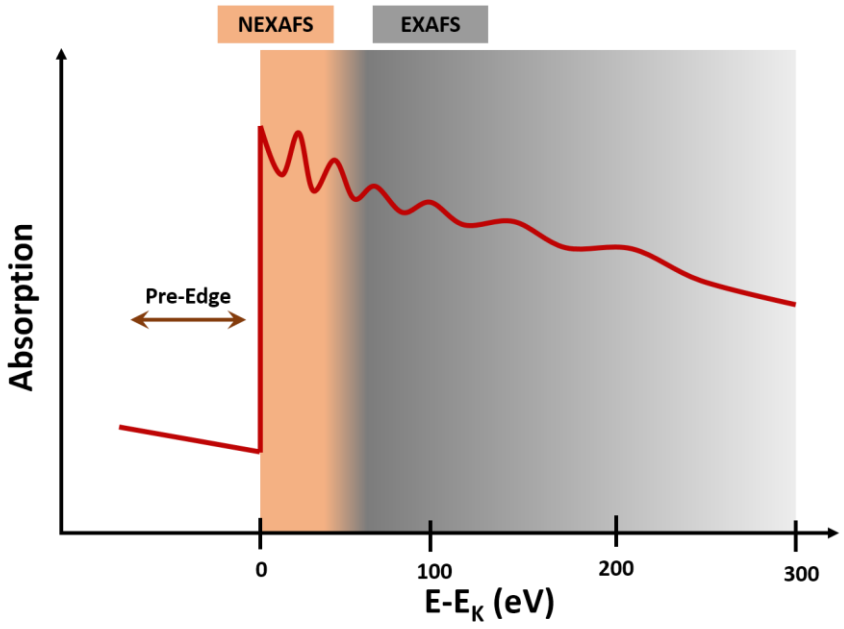

Figure 1.8 X-ray absorption spectra showing NEXAFS and EXAFS regions of the spectra. There is no strict energy value where the transition occurs. In most cases 50 eV above the edge jump is considered for reference. X-axis is the energy difference between incident photon and kinetic energy of the excited core electron. Y-axis is the number of electrons excited. At 0 eV ionization occurs followed by an exponential decay in the wavefunction.

In this thesis NEXAFS has been used to study the surface chemical and electronic properties. NEXAFS can involve both “photon in /electron out” and “photon in/photon out” processes. Due to the short mean free path (~10 nm) of electrons “photon in /electron out” also known as electron yield method is highly surface sensitive. While “photon in/photon out” process known as the florescence yield can be used to probe the bulk properties (about 100-200 nm) due to the larger attenuation lengths of photons. Both XPS and NEXAFS are inherently element specific. Due to the selection rules, chemically non-equivalent sites of the same atomic species can be separated in NEXAFS spectroscopy which is not possible in XPS. **Figure 1.9** shows the difference between XPS and NEXAFS. In C 1s XPS spectra of Highly oriented pyrolytic graphite (HOPG), graphene and graphene oxide resemble the same line shape with overlapped features. The carbon K-edge NEXAFS spectra for the same set of samples are markedly different. Features in the spectra represent the different chemical environments of carbon. These two techniques (XPS and NEXAFS) has been described in detail in Chapter 2.

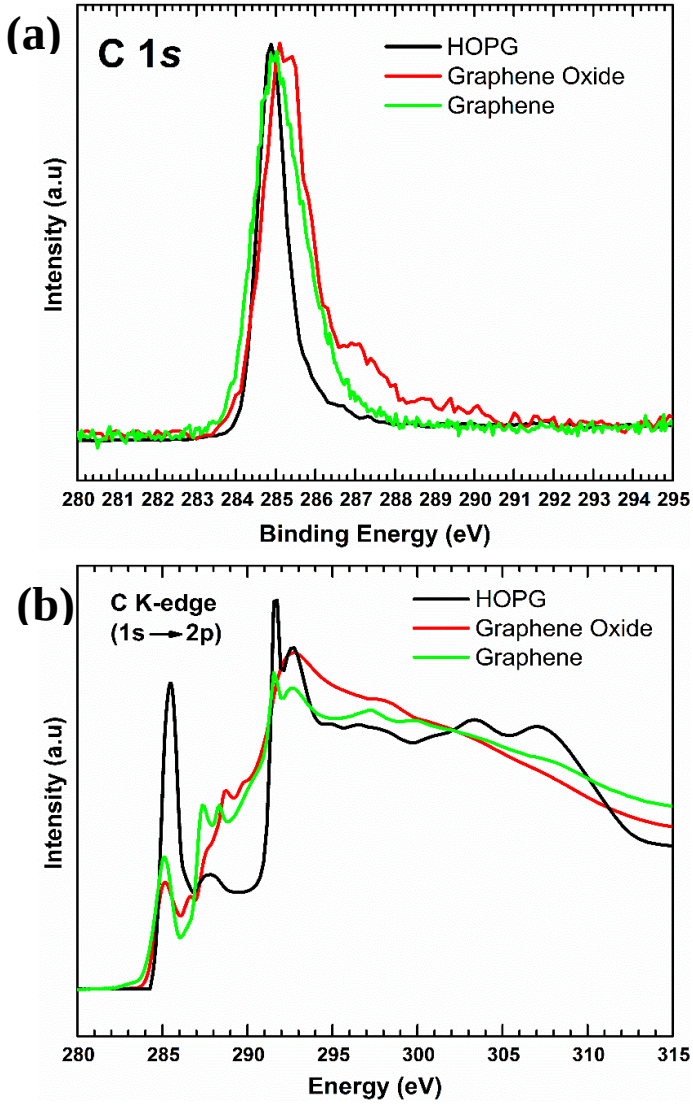

Figure 1.9 C1s (a) XPS, (b) NEXAFS spectra of HOPG, GO and Graphene.

1.4 Introduction to Plasma technology

Thermally generated plasma is often considered as the fourth state of matter. It is a gas of charged particles. Plasma can be generated by heating a gas or by applying strong electromagnetic fields. The applied energy ionizes the gas by dissociating the molecular bonds. The ionized gas contains equal densities of oppositely charged particles (electrons and ions) rendering the gas neutral. These charged particles make the plasma electrically conductive. Plasma can be classified into different categories that are listed below: [104]

- Operating pressure
    - Low pressure plasma
    - Atmospheric pressure plasma
- Temperature
    - Low temperature plasma where temperature of heavy particles is less than ~2000K
    - High temperature plasma where temperature of the plasma is more than ~2000K
- Thermodynamics
    - Thermal plasmas, which are in thermodynamic equilibrium state ($T_{electron} \approx T_{ion} \approx T_{gas}$)
    - Non-thermal plasma or non-equilibrium plasma ($T_{electron} >> T_{ion} \approx T_{gas}$)
- Generation
    - Microwave discharge (300 MHz $\leq f \leq$ 300 GHz)
    - Radio frequency discharge (e.g. 13.56 MHz)
    - DC discharge
    - Alternating current

1.5 Non-thermal plasmas

The characteristic temperature of a plasma is determined by the average kinetic energy of its components (electrons and ions). However, due to a significant difference in mass of electrons and ions their respective kinetic energies (temperature, T_e, T_i) remain different in many cases. When there is large deviation in temperature values (i.e. $T_e > T_i$) the plasma is not thermalized, and is called non-equilibrium or non-thermal plasma. In non-thermal plasmas, most part of the applied electrical energy is used to generate high energy electrons rather than heating the gas and due to low energy exchange with the light particles the ions remain relatively cold. While the electrons have enough energies to ionize molecules and atoms creating excited species and free radicals, the gas temperature remains orders of magnitude lower. These electrons with a temperature of few electron volts (eV) are capable of initiating chemical reactions which are rather forbidden under the same conditions. Thus, non-thermal plasmas can enhance the efficiency of various physical and chemical process related to material processing/manufacturing and most importantly will have appreciable lower impact on the environment than conventional techniques. Figure 1.10 shows the influence of pressure on the characteristic of plasma i.e. transition from non-thermal to thermal plasma. At low pressure electrons undergo inelastic collision with the heavy particles which are ionizing in nature and does not increase heavy particle temperature. Hence gas temperature (T_g) is much lower than the electron temperature (T_e). With an increase in pressure both inelastic collisions (influencing plasma chemistry) and elastic collisions increase the temperature of heavy particles. Hence difference between T_g and T_e decrease and plasma almost reaches thermal equilibrium. At this regime, the applied power becomes very critical. Thus, a source with low power density or a pulsed power supply is required to sustain non-thermal plasmas operating at atmospheric pressure. In the next section, different atmospheric pressure plasma sources are described in terms of design and operating conditions.

Plasmas operating at atmospheric pressure are prone to arcing (that is significant gas heating occurs). Arcing occurs when the applied current is high enough to heat up the electrodes leading to thermionic emission, which in turn increases the current to very high values even with a low applied voltage. The electron current heat the gas and the gas heats all other surrounding surface. To be feasible for practical applications arcing need to be avoided. There are four plausible solutions to this issue:

i) Adopting dielectric barrier discharge configuration.

ii) Using high frequency power sources.

iii) Pulsed DC source.

iv) Restrict the space.

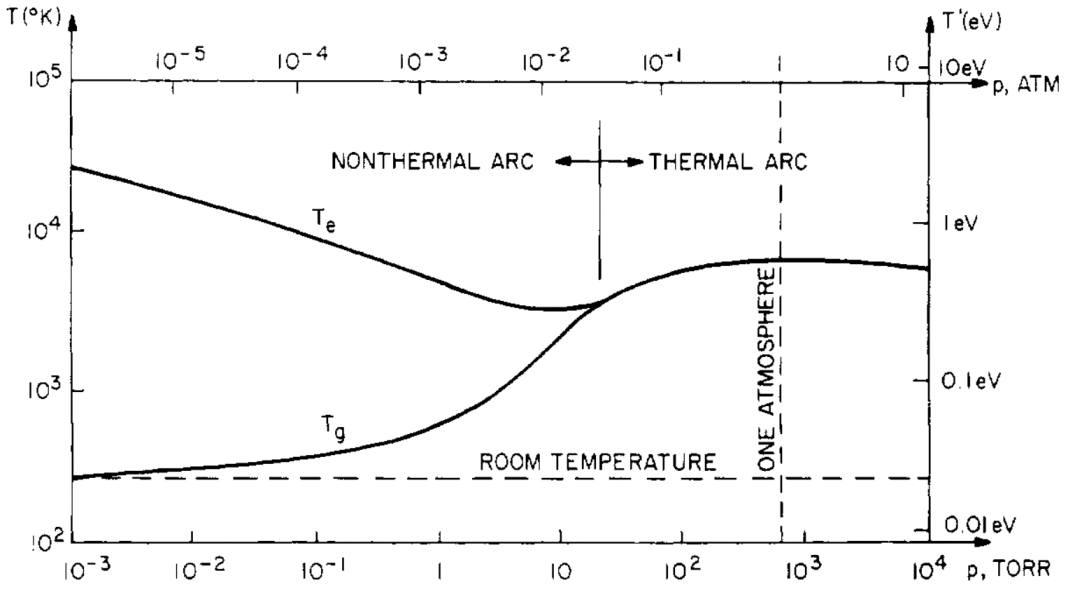

Figure 1.10 Relation between temperature and pressure for thermal (equilibrium) and non-thermal plasmas.[105]

1.6 Atmospheric pressure plasma

Atmospheric pressure plasma, as the name suggests are generated under ambient pressure. However, there exists multiple ways to generate plasmas at atmospheric pressure differentiated by the type of energy supply that sustains them and the way they are held back from reaching thermal equilibrium. Some of these are discussed below.

1.6.1 Atmospheric pressure plasma sources

The process of ionizing a gas is achieved by applying an electric field across the chosen gas. The applied field should be sufficiently strong to achieve gain/loss of electrons. With electron loss, an atom attains a positive charge while with gain of an electron atoms converts to a negatively charged ion. After being ionized the field gradient separates the ionic species further apart with respect to their original atomic or molecular structure. However other physical parameters such as gas flow rate, process pressure, gas mixture should also be carefully controlled along with power of the applied electric field to balance the ionization process and avoid a potential "ionization decay".

To generate plasmas at atmospheric pressure, different types of sources with different types of frequencies can be used. Frequency of the excitation source plays a crucial role, as it strongly influences the characteristics of electrons and ions in plasma. The sources are categorized according to their operating frequencies into three groups:

- DC (direct current) and low frequency discharges (< 100 kHz)
- Radio frequency (RF)discharge (13.56 MHz)
- Microwave(MW) discharge (2.45 GHz)

The above-mentioned frequencies have been chosen and controlled by international agreements to prevent the source frequencies from interfering with the worldwide communication bands. DC/low frequency sources are the least expensive of the lot as they are easy to build. However, plasmas ignited using a DC source are reported to be least efficient in cleaning, activation, and surface modification. [106]With DC voltage, it is easy to create a glow discharge at a low pressure. For an applied DC voltage, the process of secondary electron emission (due to ion impact) at the cathode maintains the glow discharge. But, with increasing pressure the glow discharge seemingly becomes unstable and constricted within the electrodes , making it hard to sustain a plasma. An approach to overcome this issue is to use higher gas flow rates. One important property of DC discharge at higher pressure is that the gas temperature can reach 1000K or more due to ion impact. This has been of significance, when using plasmas for direct write printing of nanoparticles as mentioned in Chapter 3.

On the other hand, RF and MW power sources are the more favoured among the plasma community. As these sources can generate more electronically charged species than low frequency plasma sources.[106] Plasma generated using RF sources are reported to be more homogenous, a characteristic more important for treating irregularly shaped or 3D objects. Plasma with MW sources are rather inhomogeneous in respect to RF sources and are suited for soft materials as they generate low energy ions. One important application is organic removal from ion sensitive materials. Other major disadvantage of MW sources is the design requirements of a microwave cavity. Geometry of the cavity and the plasma density together determine the resonance frequency, hence confines its applications to a limited range of plasma conditions.

In this work, atmospheric pressure plasma operated with DC, low frequency and RF power sources have been used for corresponding suitable applications: functionalization, printing, and sterilization.

1.6.2 Dielectric Barrier Discharge (DBD)

Siemens in 1857 proposed what we now term a DBD discharge as a means of 'ozonizing air'. DBD systems consist of two electrodes, which are separated by a gap of a few millimetres; at least one of the two electrodes are covered by a dielectric material. Preferred materials for the dielectric barrier are glass, ceramic or thin polymer layers. The electrodes can be in coaxial, cylindrical or parallel configuration. Typically, an alternating voltage ranging from tens of Hz to hundreds of MHz is applied to one of the electrodes and the other is grounded. The dielectric barrier is intended to restrict and rapidly terminate the arcs that forms in the potential field between the two electrodes. It does this by accumulating charge that suppresses the electric field in the gap until the voltage reverses, whereupon the charge enhances the field, reigniting the discharge. In DBD configuration the generated plasma is predominantly non-thermal in nature. Due to the high pressure, there are no high-energy ions (> 1 eV), so this plasma is extremely useful for surface treatment and functionalization as it doesn't cause substrate sputtering.

1.7 Thesis Structure

This thesis realizes the applications of atmospheric pressure plasma in three discrete fields. The outcome of plasma surface interactions has been extensively investigated via X-ray based surface characterization techniques. These techniques include X-ray absorption spectroscopy and X-ray photoelectron spectroscopy. While less emphasis is given on characterizing the plasma itself.

Figure 1.11 portrays the contributions to this thesis in the form of chapter 3,4 ,5 and 6. Chapter 2 is dedicated for the details of various experimental techniques and Chapter 7 is about the overall summary and where prospect lies for atmospheric pressure plasmas in the near future.

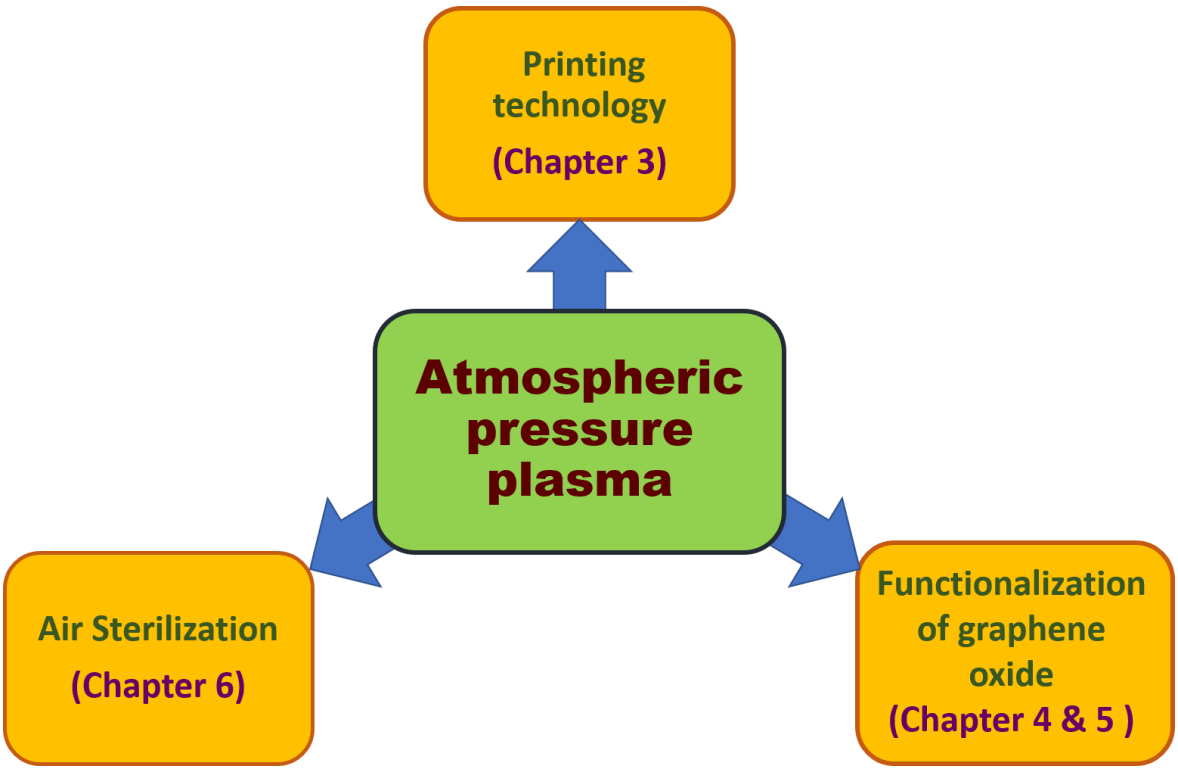

Figure 1.11 The scope of this thesis in summary.

Chapter 2. Analytical techniques

This chapter presents an overview of the various characterizations techniques used during this work. Surface sensitive techniques like X-ray photoelectron spectroscopy and X-ray absorption spectroscopy were extensively used to understand the properties of material. Additionally, the techniques associated with atomic force microscopy used to study the electronic and electrical properties are also described in this chapter.

2.1 X-ray Sources

2.1.1 Lab based X-ray sources

X-ray tubes are the primary source of radiation for in-house X-ray instruments. In X-ray tubes, electrons accelerated by an applied high voltage are focused onto a metal target. Collision with the target results in rapid deceleration of the electrons, thus a continuous spectrum of X-rays is produced known as Bremsstrahlung radiation. Incident electrons with sufficiently high energy can even ionize the atoms by knocking off electrons form the inner shell. When a free electron fills the vacant shell an X-ray photon characteristic of the target material is produced on top of the Bremsstrahlung radiation e.g. Mg K_α or Al K_α. The K_α for both these elements are the most intense and is associated with the $2p \rightarrow 1s$ transition. XPS system (Kratos Xsam 800) used for photoelectron measurements consisted of a dual anode X-ray source. Emitting characteristic Mg K_α (1254 eV) or Al K_α (1486 eV) X-ray lines. The corresponding line widths for this sources are 0.7 eV and 0.8 eV respectively. These line widths can be further reduced by using a monochromator. The line width for a monochromatized Al K_α source could be brought down to 0.2 eV but at the expense of intensity.

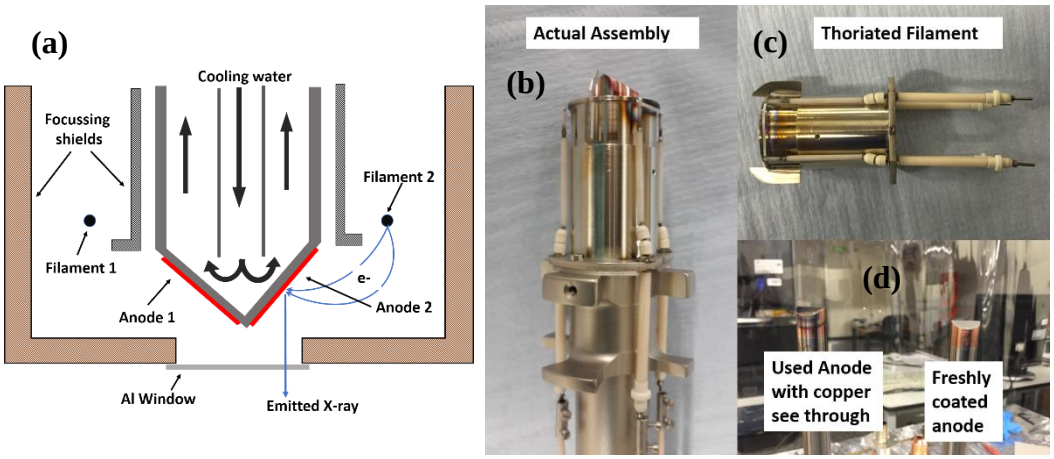

Figure 2.1 (a) Schematics of a dual anode X-ray source (b) X-ray source for Kratos Xsam 800 (c) thoriated filament as electron source (d) difference between a used and freshly coated anode.

Figure 2.1 shows the assembly of the dual anode X-ray source used in the lab based XPS system (Kratos XSAM 800). De-ionized water is used to cool the anode. A thoriated filament is used as the electron source. To get the characteristics X-rays a thin films of aluminum and magnesium is coated over the copper anode. After extensive use these films wear out resulting in copper emission lines appearing along with the characteristic Al/Mg K_α line. The presence of copper lines results in additional features in the photoelectron spectrum, which make quantification more difficult.

2.1.2 Synchrotron radiation

Laboratory based conventional X-ray sources suffer from limited photon flux of unpolarized radiation. During X-ray generation, a major part of the energy is lost in the form of heat. So, experiments that demand high intensity, tunable and polarized X-rays, turn to synchrotron radiation sources. In synchrotrons, electrons are accelerated in a circular path to produce radiation. For electrons moving with velocities close to that of light, the radiation is directed in the direction of the electron's travel and the relativistic effect confines the beam to a narrow cone (collimated beam). The angular distribution ($\Delta\phi$) of the emitted radiation is related to the Lorentz factor (γ) as:

$$\Delta\boldsymbol{\phi} \cong \boldsymbol{\gamma^{-1}} \qquad \textbf{2.1}$$

And

$$\boldsymbol{\gamma} = \frac{\mathbf{1}}{\sqrt{\mathbf{1}-\frac{v^2}{c^2}}} \qquad \textbf{2.2}$$

Where '*v*' is the speed of the electrons and '*c*' speed of light in a vacuum (c). At synchrotron sources, radiated photons have a continuum of energy spanning form infrared to X-rays. Monochromators are placed at a tangential point of the circular electron orbit, to tune to the desired monochromatic light. [107,108]

Figure 2.2 show the main components of a synchrotron radiation facility. Electrons emitted by a cathode are initially accelerated to energies of 120 MeV by the linear accelerator (Linac) and injected to booster ring in discrete bunches. The booster ring's electromagnets accelerate the electrons around the ring. Variable magnetic fields guide the electron in a circular trajectory of constant radius while RF system boosts the energy of the electron beam. Electrons rotate in the booster ring until they achieve sufficient energy (2.3 GeV) to be injected into the storage. The storage ring then ramps the energy of the particles to 3 GeV and stores for synchrotron radiation. The storage ring at Stanford Synchrotron Radiation Laboratory is named as SPEAR (Stanford Positron Electron Accumulator Ring) and was originally built for high energy physics research. Under normal conditions the SPEAR stores up to 100 mA of current in its 234-meter circumference vacuum chamber.

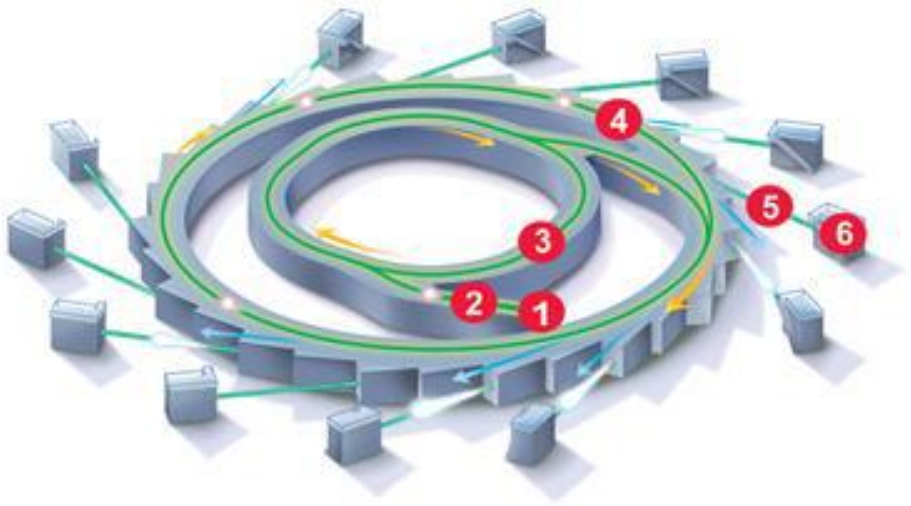

Figure 2.2 Schematics od a typical synchrotron storage ring. Labeled sections in the figure correspond to: (1) Electron gun; (2) LINAC; (3) Booster ring; (4) Storage ring; (5) Beamline; (6) End station.

2.2 X-ray photoelectron spectroscopy

The photoemission process is based on Einstein's photoelectric effect. For a typical photo-ionization process, a sample is exposed to a flux of photons and then monitoring the emitted electrons. The number of electrons emitted is then related to the concentration of emitting atoms in the sample. Considering the energy to be conserved during the photo-ionization process, the energy of the emitted electron can be presented as:

$$\boldsymbol{E_i^n + h\nu - \ E_f^{n-1} = \ E_K} \qquad \textbf{2.3}$$

Where E_i^n and E_f^{n-1} are the initial and final state energies of the system with n and n-1 electrons respectively. E_K is the kinetic energy of the emitted photo-electron from the Fermi level of the sample. In the context to of Koopmans' theorem, the binding energy of the photoelectron can be expressed in terms of these initial and final state configurations, as:

$$\boldsymbol{E_f^{n-1} - \ E_i^n = \ E_B} \qquad \textbf{2.4}$$

Thus, for well-defined photon energy (hν) , the binding energy of the emitted electron from the atom can be represented as:

$$\boldsymbol{E_B \ = h\nu - \ E_K} \qquad \textbf{2.5}$$

Figure 2.3 presents the fundamental principle of the photoemission process. As the spectrometer counts the number of electrons as a function of kinetic energy or binding energy an experimental spectrum is obtained. Electrons with binding energy E_B can be excited above the vacuum level E_{vac} by photons with energy $h\nu > E_B + \Phi_0$. Where Φ_0 is the work

function of the material under consideration. The photoelectron distribution I(E_{kin}) can be measured by the analyzer and is in essence an image of the occupied density of electronic states N(E_B) in the sample. [109] While passing through to the vacuum level the core electrons lose energy via inelastic scattering, which gives rise to the secondary electron background.

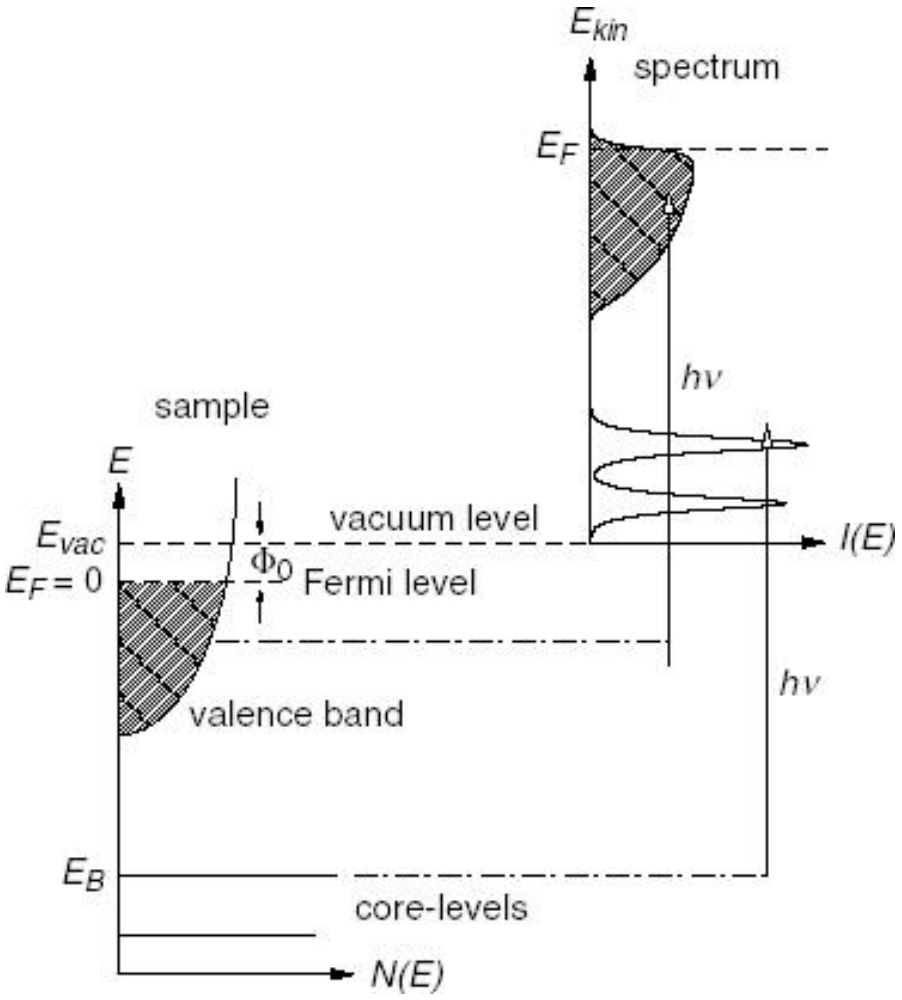

Figure 2.3 Schematic view of the photoemission process in the single-particle picture. [109]

During the photoemission process, the photocurrent can be calculated from the first order perturbation theory and Fermi's golden rule. The photocurrent, *J*, results from the

excitation of electron by the incident photons from the ground state $|\psi_i\rangle$ to a final state $|\psi_f\rangle$. Considering H_0 to be the ground state Hamiltonian of the solid, which gets perturbed by the electromagnetic field $\boldsymbol{E}$.

$$\boldsymbol{H_O} = \frac{\boldsymbol{p^2}}{\boldsymbol{2m_e}} + \boldsymbol{eV(r)} \qquad \textbf{2.6}$$

Here $\boldsymbol{p}$ is the momentum operator given by - iħ∇. This electromagnetic field transforms the momentum operator $\boldsymbol{p}$ to $\boldsymbol{p} - e/c\ \boldsymbol{E}$, thus the perturbed Hamiltonian can be written as:

$$\boldsymbol{H} = \frac{\boldsymbol{1}}{\boldsymbol{2m_e}} \left[\boldsymbol{p} - \frac{\boldsymbol{e}}{\boldsymbol{c}}\boldsymbol{E}\right]^{\boldsymbol{2}} + \boldsymbol{eV(r)} \qquad \textbf{2.7}$$

$$= \frac{\boldsymbol{p^2}}{\boldsymbol{2m_e}} + \frac{\boldsymbol{e}}{\boldsymbol{2m_e c}}(\boldsymbol{E.p} + \boldsymbol{p.E}) + \frac{\boldsymbol{e^2}}{\boldsymbol{2m_e c^2}}\boldsymbol{E^2} + \boldsymbol{eV(r)} \qquad \textbf{2.8}$$

$$= \boldsymbol{H_O} + \boldsymbol{H_{PE}} \qquad \textbf{2.9}$$

Here H_{PE} is the perturbation operator:

$$\boldsymbol{H_{PE}} = \frac{\boldsymbol{e}}{\boldsymbol{2m_e c}}(\boldsymbol{E.p} + \boldsymbol{p.E}) + \frac{\boldsymbol{e^2}}{\boldsymbol{2m_e c^2}}\boldsymbol{E^2} \qquad \textbf{2.10}$$

For low photon intensities, the quadratic term in $\boldsymbol{E}$ can be neglected and the perturbation operator can be written as:

$$\boldsymbol{H_{PE}} = \frac{\boldsymbol{e}}{\boldsymbol{m_e c}}\boldsymbol{E.p} \qquad \textbf{2.11}$$

Considering the perturbation operator, the photoelectron current density can be written as:

$$\boldsymbol{J\,(h\nu) = \frac{2\pi}{\hbar} \sum_s \left|\langle \Psi_f | H_{PE} | \Psi_i \rangle\right|^2 \delta(\epsilon_f - \epsilon_i - h\nu)} \qquad \textbf{2.12}$$

In the dipole approximation, the perturbation operator can be expressed as

$$\boldsymbol{H_{PE} = E.D} \qquad \textbf{2.13}$$

Here $\boldsymbol{D}$ is the dipole moment.

X-ray photoelectron spectroscopy is a well-established surface analysis technique used to gain insight into the electronic state, chemical state and atomic concentrations of elements at the very surface. It can provide information about the orbital and band structure of a wide range of materials by probing the occupied electronic states of a system. For a multi-electron system the electronic states are generally classified as core level states or valence states. Core level electrons have higher binding energies as they are tightly bound to the nucleus while valence electrons possess low bonding energies. Valence electrons actively take part in chemical bond formation but the core electrons are idle in this respect. Even though core electrons are not involved in chemical bonding, they are highly sensitive to the local chemical environment i.e. neighbouring atoms, molecules or surfaces.

Chemical shift (initial state effect)

In an atom, the valence electrons occupy the outer shells and core electrons are spatially contained within these valence shells. The binding energy of a core electron is the work needed to remove the inner shell electron and is affected by any changes in the potential on the valence shell.[110] The binding energy of a core electron can be presented in terms of charge potential model as:

$$\boldsymbol{E_i = E_i^0 + kq_i + V_i} \quad \text{where } \boldsymbol{V_i = \sum_{j \neq i} \frac{q_i}{r_{ij}}} \qquad \textbf{2.14}$$

Here E_i is the binding energy of a core electron, E_i^0 is the energy reference, q_i is the charge on the atom with the concerned core electron, k is a constant and V_i is the total electrostatic potential felt by this atom due to the surrounding atoms. Any changes in the valence electron cloud will redistribute the surface charge as well as the potential felt by the core electron. Hence, from equation 2.14 the shift in binding energy due to a change in valence charge can be expressed as:

$$\boldsymbol{\Delta E_i = k \Delta q_i + \Delta V_i} \qquad \textbf{2.15}$$

When a chemical bond is formed involving the valence electrons, electron density of the atom is perturbed resulting in a change in the core level binding energies (chemical shift) as mentioned in equation **2.15** . These shifts are of the order of few electron volts. When an atom is bound to another atom with higher electronegativity, the electron density of the former will shift towards the more electronegative species. Thus, the binding energy of the core electron will shift to higher values. Hence, chemical shifts can be used as a fingerprint to identify an atom in a molecule or the chemical environment of an atom in a solid. **Figure 2.4** presents an example of the mentioned chemical shift in the carbon spectra of graphene oxide. Here the binding energy of carbon has shifted to higher energy values with the presence of oxygen.

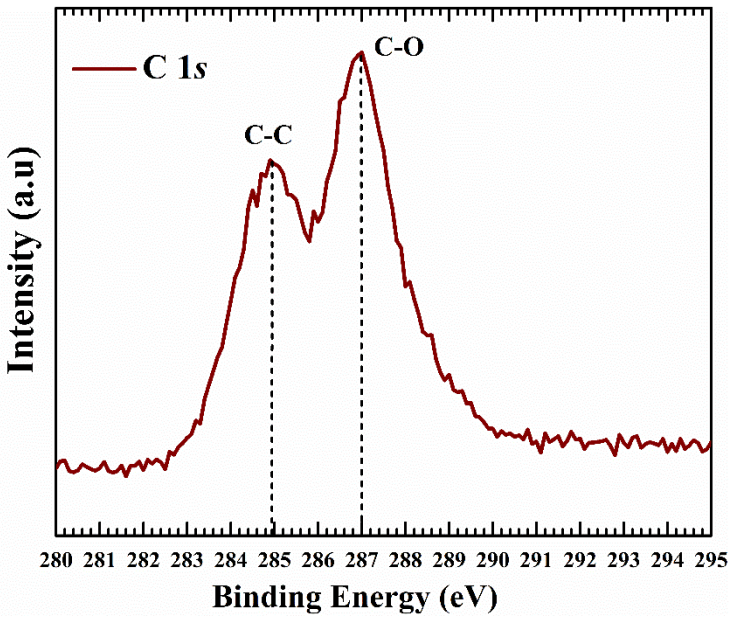

Figure 2.4 C 1s XPS spectrum of graphene oxide showing the shift in binding energy due to difference in chemical environments of carbon atoms. Here C-C denotes carbon bonded to carbon and C-O denoted carbon bonded to oxygen.

As already mentioned, the intensity of the photoemission peaks can be related to the amount each element present in the sample. For an accurate analysis, it is very important to consider two parameters; first is the photoionization cross section (σ) and second is the attenuation length (λ). The photoionization cross section is a measure of the probability that a photoelectron will be created by the incident X-ray photons, and is dependent on the energy and polarisation of the incident photons. By contrast the attenuation length can be considered as the inelastic mean free path of a photoelectron i.e. the average depth through which a photoelectron can escape without undergoing energy loss due to inelastic scattering. It is directly proportional to the kinetic energy of the photoelectrons. Sharp peaks in the XPS spectra reflect the electrons that haven't lost any energy while escaping from the surface.

However, the electrons that escape the surface after scattering and energy loss, contribute to the background signal. Thus, the photoelectric current (intensity) detected the XPS spectrometer can be expressed as:

$$\boldsymbol{I = \sigma jK \int n(x) exp\left(\frac{-x}{\lambda \cos\theta}\right) dx} \qquad \textbf{2.16}$$

where '*I*' stand for peak intensity, σ is the photoionization cross-section for a particular transition, *j* is the flux of X-ray photons, *K* is an instrument factor, *n(x)* is the concentration of the element of interest at a depth "*x*" below the sample surface while λ is the attenuation length, θ is the angle between the surface normal and the ejected electron.[111]

High surface sensitivity of XPS can be correlated to the universal curve for inelastic mean free path (**Figure 2.5**). It's clearly discernible from the figure, at very low kinetic energies, the photoelectron doesn't have enough energy for excitation and hence the mean free path is long. As well as at high energies, the electron passes quite swiftly through a given thickness of solid and is less likely to suffer energy loss. Therefore, its mean free path is again quite long. Thus, the short escape depth of the photoelectrons is the mainstay for high surface sensitivity of XPS. Even with an electron with very high kinetic energy (1- 2 keV) the escape depth is just couple of nanometres.

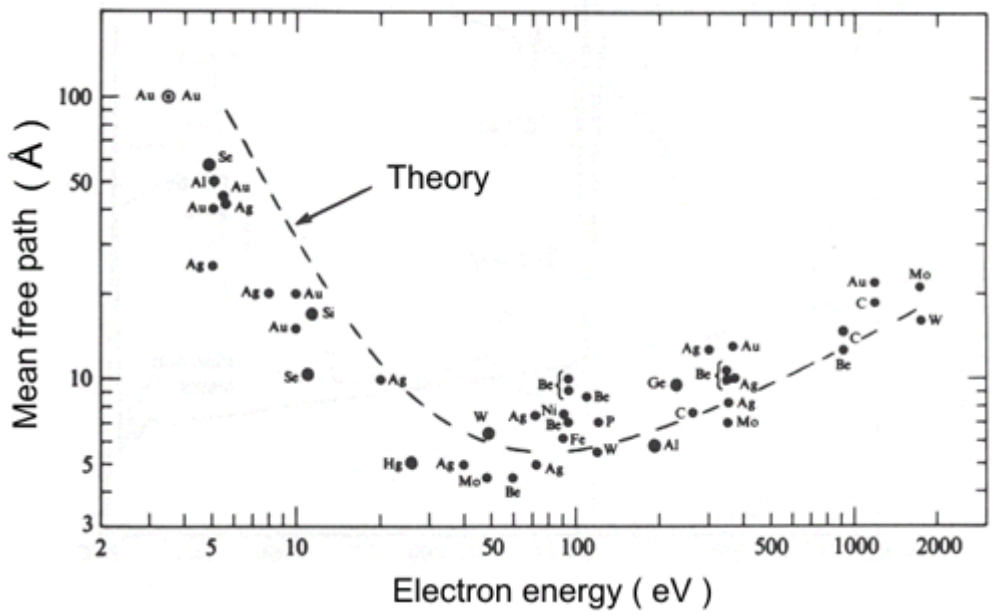

Figure 2.5 "Universal curve" for inelastic mean free path.[112]

Final State Effects

The escape of a core electron causes a significant perturbation to the electronic structure of an excited atom, which then results in a reorganization of the remaining electrons to screen the core hole. Intermolecular and intramolecular relaxation are the two dominant mechanisms to screen the created core hole, and can cause binding energy shift in the XPS spectra. Electronic polarization of the surrounding molecules gives rise to intermolecular relaxation and can cause the measured binding energy to shift by approximately 1-2 eV. During an intramolecular relaxation process, the outer shell electrons within a molecule rearrange themselves within a time frame of 10-100 femtoseconds. Intramolecular transitions can result in additional new features in the spectrum, which arise from the various excited states involved in the decay process. **Figure 2.6** depicts some excitation events that can occur during and after photoionization: shake-up, shake-off and Auger emission.[113]

When an outgoing photoelectron looses part of its kinetic energy to a valence electron and excites it to an unoccupied state, this gives rise to shake up feature in the XPS spectra for example $\pi \rightarrow \pi^*$ transition in the C1s spectra of graphite. On the other if the transferred energy is sufficient to ionize the valence electron into the continuum, it is known as shake-off. The third process namely, Auger decay, occurs when the energy released after filling the core hole excites another electron to the continuum. The features arising from these above-mentioned processes appear at higher binding energies compared to the main line.

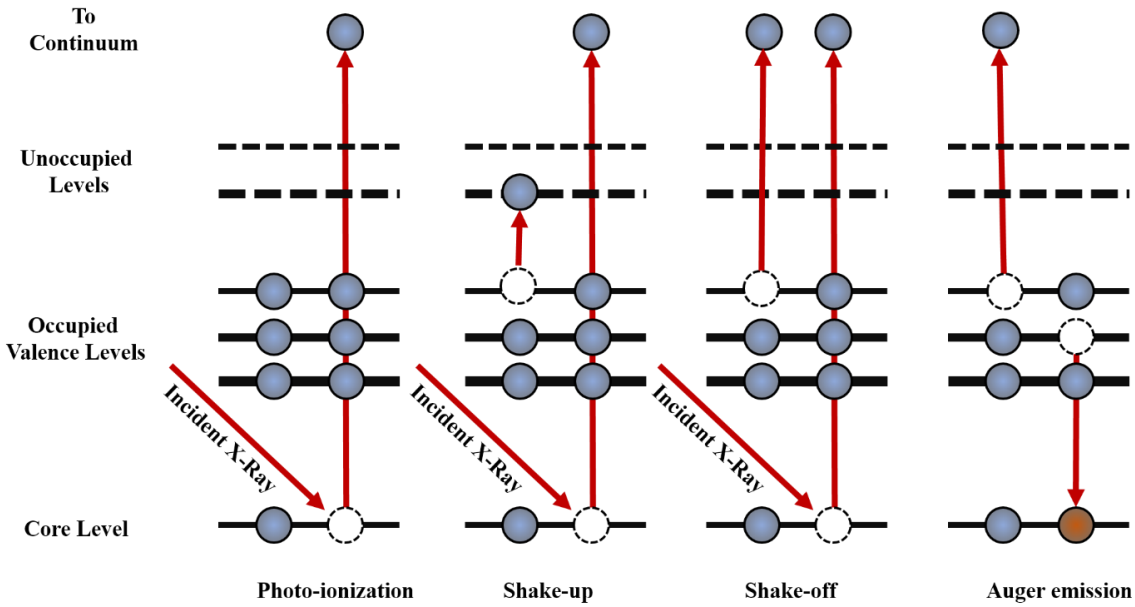

Figure 2.6 Various excitation events that can occur during or after the photoionization process.

To probe the bonding configurations in solids, understanding the valence band spectra is critical. As valence band electrons are directly involved in the bond formation. However, the valence band spectra are more difficult to interpret, because at this binding energy region, atomic orbitals overlap to form molecular orbitals and a quantum mechanical explanation is required to gain insight. A broad scan of width 1100 eV is shown in **Figure 2.7**. The core level transitions such as Cu 2*p*, Cu 3*s*, Cu 3*p*, O1*s* and C1*s* are named according to their origin. O KLL and Cu LMM are the corresponding auger transitions for oxygen and copper respectively. KLL stands for $KL_1L_{2,3}$, K represents energy state of the core hole, L_1 is initial state of the relaxing electron, and $L_{2,3}$ is the ground state energy level of the emitted auger electron from the oxygen atom. Similarly, Cu LMM corresponds to L state core hole and Auger transitions from a M level. Cu 3d orbitals form the valence state near the Fermi level.

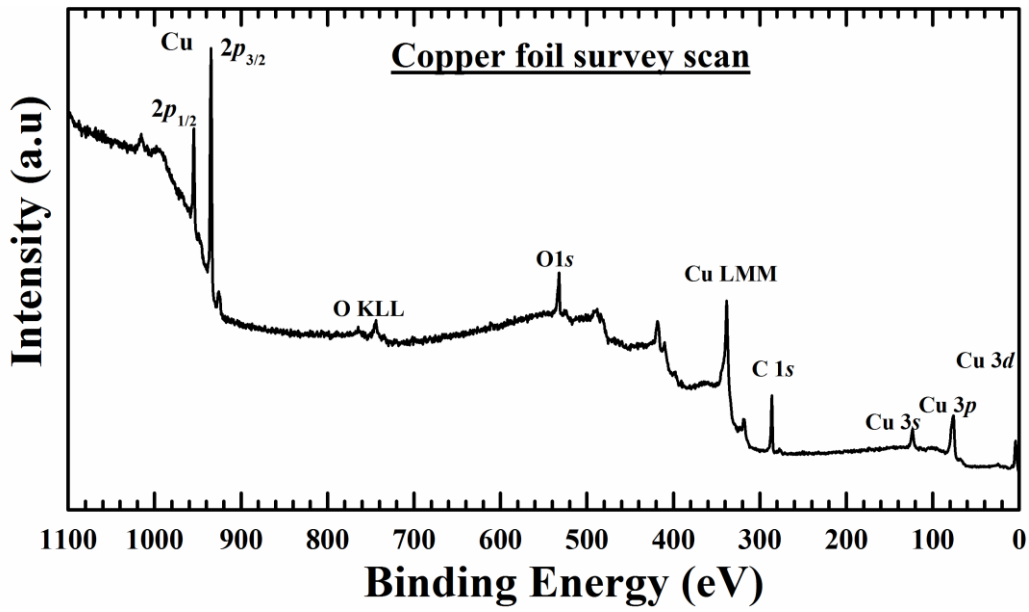

Figure 2.7 XPS survey spectrum for an oxidized copper foil with surface carbon contamination. The spectrum was obtained using Mg Kα as the radiation source.

Peak splitting

From **Figure 2.7,** it is apparent that the copper 2*p* level shows a doublet feature. This is known as spin-orbit splitting and occurs due to ***j-j*** coupling.[110] Here ***j*** = ***l*** + ***s*** , ***l*** is the angular momentum quantum number and ***s*** is the spin angular momentum quantum number and can have values +½ or -½ . For Cu 2*p* state, ***l*** is 1 hence ***j*** will have values 3/2 (upward aligned *p* orbital) and 1/2 (downward aligned *p* orbital). Additionally, this coupling is also proportional to r^{-3}, where *r* is the radius of the orbital. Hence Cu 2*p* level will spilt more than Cu 3*p* level.

Satellite for CuO

The shake-up feature is best illustrated in the Cu 2*p* spectrum of copper oxide. CuO shows an intense satellite feature at ~ 10 eV above the main Cu 2*p* peak while Cu_2O or metallic copper this feature is negligible or absent in **Figure 2.8 (a)** illustrates the difference spectral signature of oxidized copper foil before and after being etched. For divalent copper (Cu^{2+}) the ground state is in $3d^9$ configuration. For CuO the ground state exhibits contribution form of $3d^9$ and $3d^{10}$L configurations (here L corresponds to an O 2*p* ligand hole).[114] After a photoelectron is emitted from the copper 2*p* site, two final states are possible: 1) to screen the core hole , Cu 3*d* level is pulled down below the ligand level (O 2*p* for CuO) and one electron is transferred from the ligand into the Cu 3*d* level. This corresponds to the main line with a final configuration given by $c3d^{10}$L (c denotes a hole in the core level). 2) There is no charge transfer between the ligand and copper and the system stays in its $c3d^9$ configuration resulting in the satellite line. Schematics of this process is shown in **Figure 2.8 (b).**

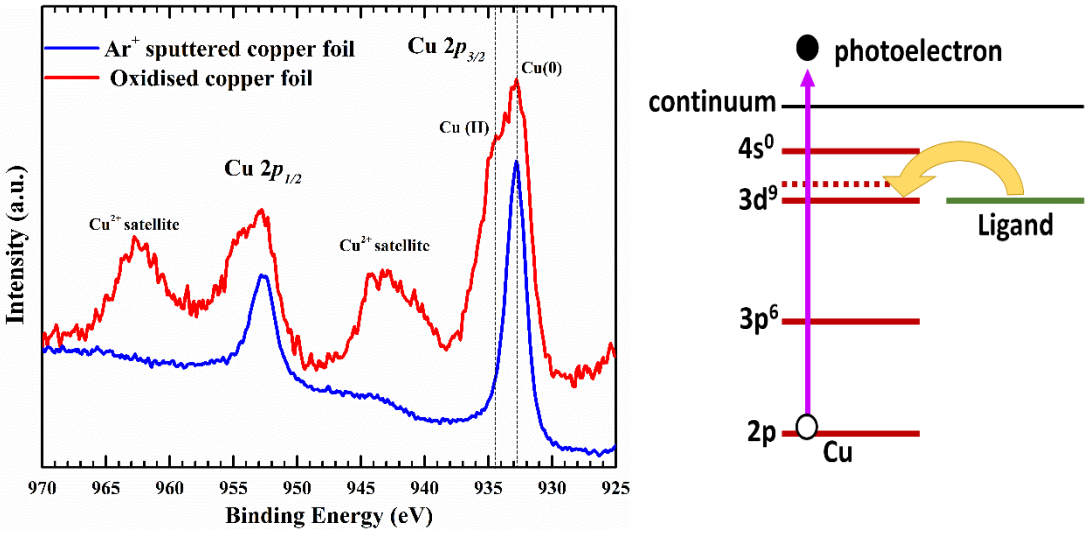

Figure 2.8 (a) Copper 2*p* spectra for oxidized Cu foil (top) and same foil after being sputter cleaned with Ar ions (bottom). Both spectra are height normalized to the Cu $2p_{3/2}$ peak. These spectra were obtained using Mg Kα radiation. (b) Schematics of the ligand-to-metal charge transfer process leading to the final states corresponding to the main line and to the satellite of Cu 2*p* core level.

2.2.1 Instrumentation

The discussion so far has been based on the kinetic energy of the emitted electrons with respect to the vacuum level of the sample. However, during the actual measurement the kinetic energy is measured with reference to the vacuum level of the spectrometer. And in practice these two levels do not have to match each other. Therefore, to define the binding energies of the photoelectrons a common reference between the sample and the spectrometer is needed. This can be done by grounding both the sample and the spectrometer. Now the Fermi level (E_F) of both the systems are at the same energy level and can be considered as the reference.

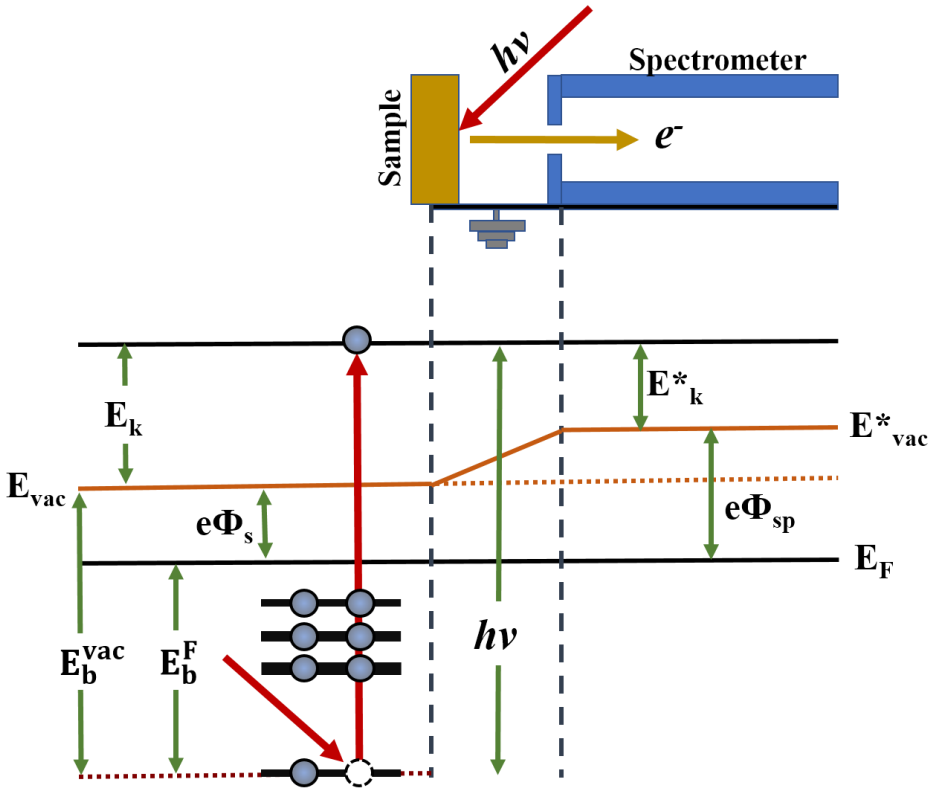

Figure 2.9 The energy level diagram showing band alignment between the sample and the spectrometer.[115]

For an actual system, the energy of the emitted electron depends on the work function difference between the sample ($e\Phi_s$) and spectrometer ($e\Phi_{sp}$). So, the kinetic energy of the photoelectron at the spectrometer (E^*_k) relates to the kinetic energy of the photoelectron at the sample (E_k) as follows:

$$E_k^* = E_k - (e\Phi_{sp} - e\Phi_s) \qquad \textbf{2.17}$$

From **Figure 2.9**, the kinetic energy of photoelectron at the sample can be related to the binding energy E_b^F (with reference to the Fermi level) and the incident photon energy by:

$$E_k = h\nu - e\Phi_s - E_b^F \qquad \textbf{2.18}$$

Replacing this in the above equation yields:

$$E_b^F = h\nu - E_k^* - e\Phi_{sp} \qquad \textbf{2.19}$$

Hence by measuring E_k^* and $e\Phi_{sp}$ values for a known incident photon energy, E_b^F can be determined. Using a sample with a well-known binding energy value, e.g. Au, Ag or Pt , the work function of the spectrometer can be calculated. In most cases a XPS system is calibrated using a clean gold surface with respect to Au $4f_{7/2}$ core line at 84 eV.

Electron Energy Analyzer

The technique of photoelectron spectroscopy relies on an electron energy analyzer to obtain the electron spectra. The analyzer used in the Kratos system is the concentric hemispherical analyzer, also called the hemispherical sector analyzer (HSA). **Figure 2.10** shows the working principle of a HSA. The HSA is comprised of two concentric hemispheres of radii R_1 (inner) and R_2 (outer) ($R_2 > R_1$). Also, the outer and inner hemispheres are applied with negative bias voltages of value V_2 and V_1 ($V_2 > V_1$) respectively. These applied biases will direct the photoelectrons between these two hemispheres in a circular path of radius R_0, so that **(**$R_2 > R_0 > R_1$). The energy of the electron entering the analyzer will be fixed to the pass energy (E_P) so that $E_P = eV_0$. The value of V_0 is such that the electrons are attracted by the inner hemisphere and repelled by the outer sphere. Therefore, any electron with kinetic energy greater than the pass energy will collide with the outer hemisphere and vice versa. The value of V_0 can be related to the applied bias and radius of the hemispheres as:[111]

$$V_2 - V_1 = V_0\left(\frac{R_2}{R_1} - \frac{R_1}{R_2}\right) \qquad \textbf{2.20}$$

To define complex chemical structure, high resolution of the analyzer is essential. High resolution will result in much narrower line width (FWHM) of the core level spectra. The instrument resolution can be defined in terms of the slit width 'w' and angular spread 'α' of the electron beam as:

$$\frac{\Delta E}{E} = \frac{w + R_0 \alpha^2}{2R_0} \qquad \textbf{2.21}$$

Thus, the resolution of the spectrometer can effectively be increased by either reducing the slit width or by increasing R_0 i.e. larger spectrometer.

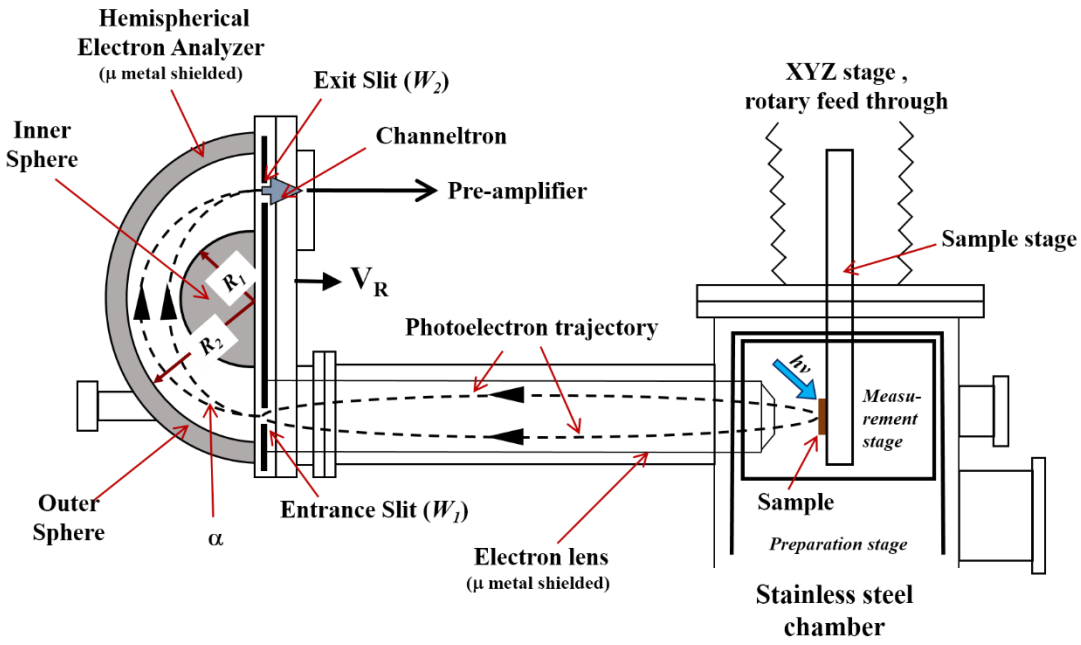

Figure 2.10 Schematics of hemispherical analyzer (HSA). [111]

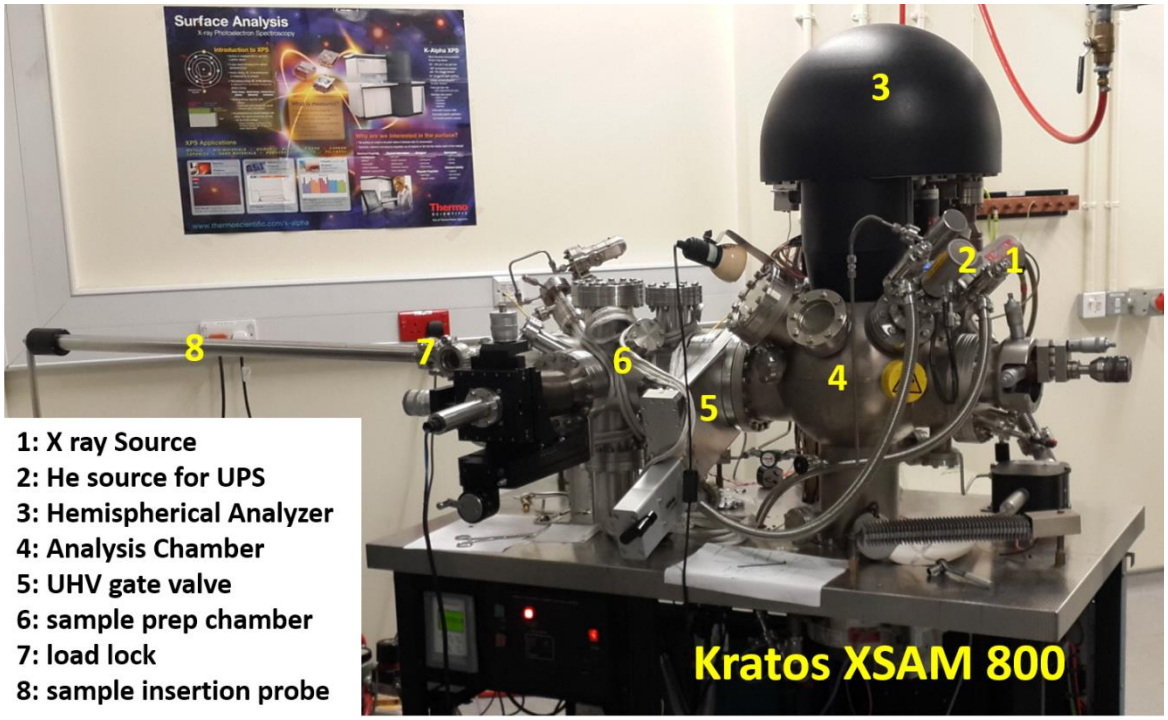

Figure 2.11 XPS instrument at The Open University.

The surface analysis equipment present at The Open University is shown in **Figure 2.11**. It is a Kratos XSAM 800 kit equipped with a dual anode X-ray source and a hemispherical analyzer (HSA). There is also a Helium discharge lamp attached to carry out ultraviolet photoelectron spectroscopy (UPS) measurements. The helium lamp produces characteristic He (I) @ 21.2 eV and He (II) @ 40.8 eV lines. These high intensity UV photons are used to probe the valence band structure (total density of states). The HSA can be operated in two modes: Fixed Analyzer Transmission (FAT) and Fix Retard Ratio (FRR). All the experiments were carried out in FAT mode with this equipment. The pass energy of the analyzer could be programmed to any of the three values: high pass (20 eV), medium pass (38 eV) and low pass (65 eV).

2.3 Near Edge X-Ray Absorption Fine Structure (NEXAFS)

XPS though being extremely surface sensitive, suffers from resolution in terms of defining complex chemical structures. NEXAFS was developed in 1980's to overcome this issue. It was initially intended to probe K-edges (deepest core shell) of '*low Z molecules'* (Z is the atomic number) such as carbon, nitrogen, oxygen and fluorine. But it has evolved over the years and has now been implemented for various other elements, molecules and materials. **Figure 2.12** presents the X-ray energy required to obtain excitation features at different absorption edges (*K, L, M* edge) . NEXAFS has been defined as a powerful structural tool that provides information on the electronic structure and orientation of molecules or molecular fragments.[103] In this thesis, NEXAFS spectroscopy has been used extensively to reveal the electronic structure and bonding environment of materials under study. Copper *L* edge showing transitions from 2*p* to unoccupied 3*d* orbitals is presented in chapter 3 while transitions from 1*s* to unoccupied 2*p* orbitals of carbon, oxygen and nitrogen have been presented in chapter 4 ,5 and 6.

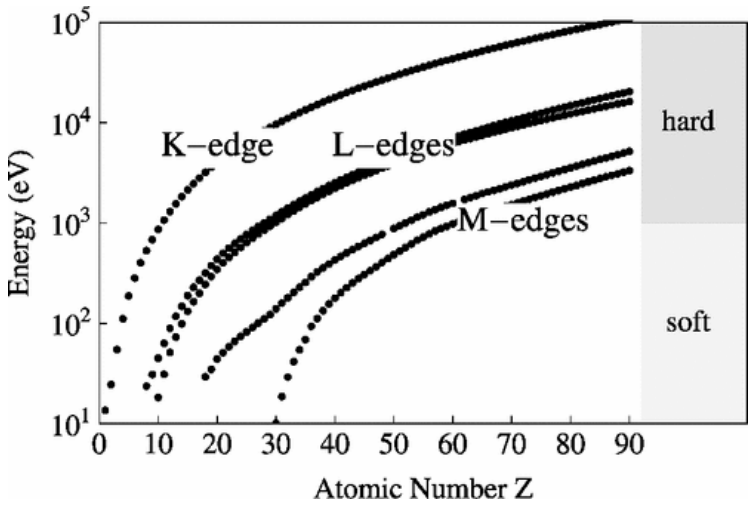

Figure 2.12 Energy of *K*, L_1, L_3, M_1, and M_5 x-ray absorption edges as a function of atomic number Z. X-ray energies below 1 keV are referred to as soft, above as hard.[116]

X-ray Absorption

X-rays that are incident on matter lose intensity in transmission due to interaction with atoms in the molecule. The incident intensity (I_0) decays exponentially with distance, as shown in **Figure 2.13**. Properties like mass density (ρ) and absorption coefficient (μ) also effect the transmitted intensity. In addition to being transmitted and absorbed some part of the incident X-ray also gets scattered elastically or in-elastically. A plot of the variation in absorption coefficient with incident photon energy is called the X-ray absorption spectrum. In a typical absorption spectrum, sharp features corresponding to the transition of a core electron to the unoccupied bound states are visible. This sharp feature also known as the absorption edge have energy value corresponding to the binding energy of the core electron.

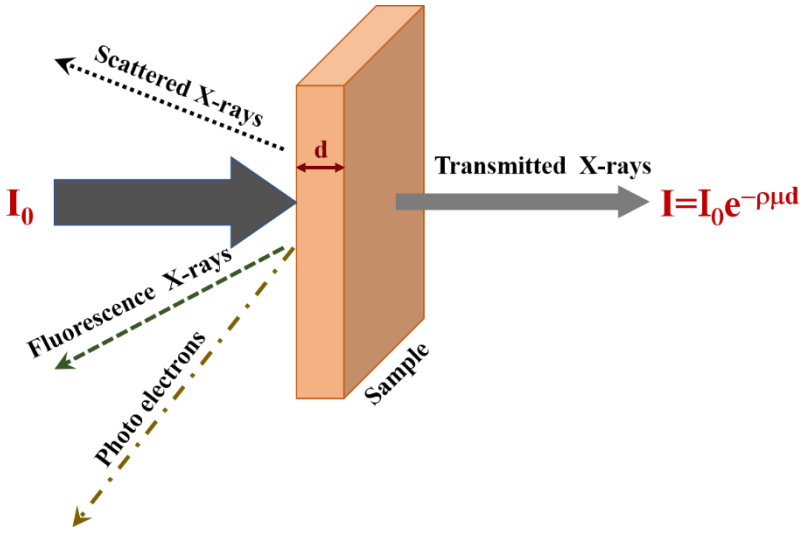

Figure 2.13 Interaction of X-ray with matter.

2.3.1 Theory of NEXAFS

The origin of NEXAFS features can be interpreted from **Figure 2.14** . It presents the potential distribution of a diatomic molecule along the X-axis with the corresponding K-shell absorption feature. π* and σ* levels are unoccupied states corresponding to the orbitals with π and σ symmetry respectively. In contrast to the energy distribution of occupied π and σ orbitals, π* orbitals have lower energies than σ* levels. For a neutral molecule, the σ* orbitals have energies above the ionization potential (IP) while the strong coulombic interaction between the excitons (electron and hole) pulls down the π* orbitals below the vacuum level. π* transitions are often of more interest as they show sharper features and are easy to resolve and identify. By contrast for the σ* orbitals life time broadening and vibrionic features makes the line shapes significantly broader. In addition to π* and σ* states , Rydberg resonances are often found just below the IP.[117]

All the absorption features described above could be seen only when an electron is excited from its ground state by the incident photon. The probability that an electron will interact with a photon is given by the absorption cross section. The X-ray absorption cross section (σ_x) is defined as the number of electrons excited per unit time divided by the number of photons incident per unit time per unit area. A detailed quantum mechanical description about the absorption cross section has been presented by Stöhr in his book *"NEXAFS Spectroscopy"*. [117]

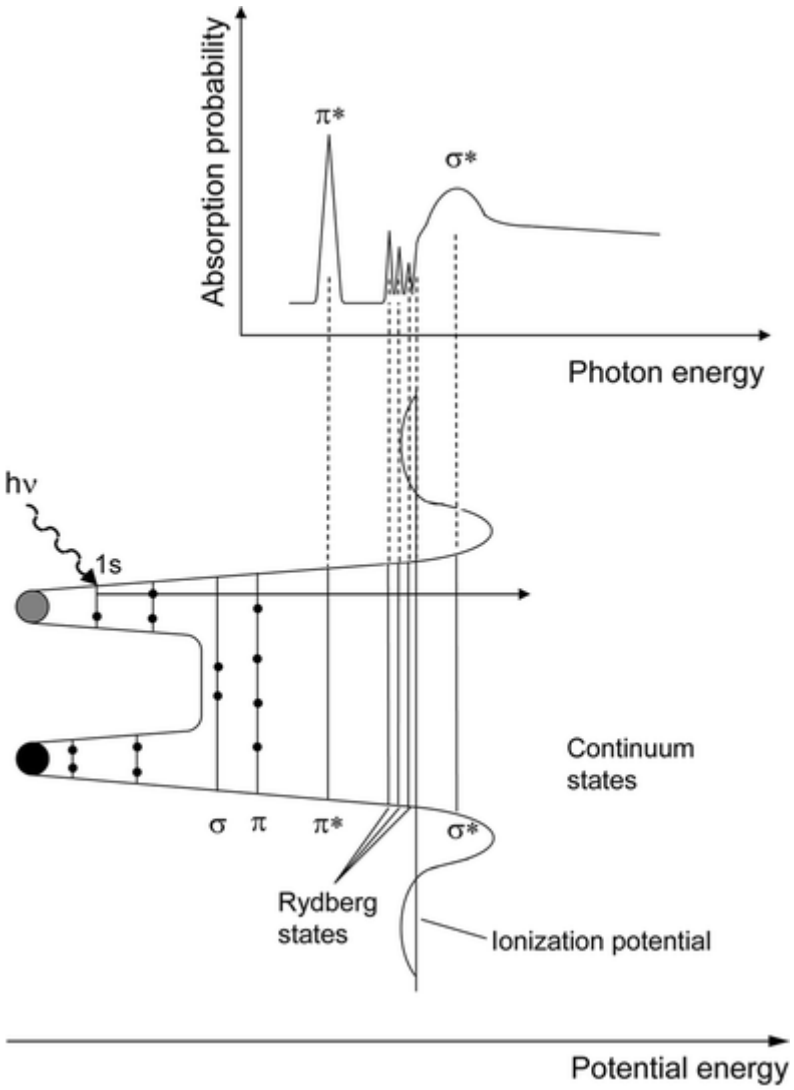

Figure 2.14 Schematic potential (bottom) and corresponding NEXAFS K-shell spectrum (top) of a diatomic molecular (sub) group. In addition to Rydberg states and a continuum of empty states similar to those expected for atoms, unfilled molecular orbitals are present, which is reflected in the absorption spectrum. [103]

The basis of this calculation originates from the Fermi's "Golden Rule" for initial and final state transitions. According to which, the probability of transition from an initial state $|i\rangle$ to a final state $|f\rangle$ driven by a harmonic time dependent perturbation $V(t) = \bar{V}e^{-i\omega t}$ is given by:

$$\boldsymbol{P_{if} = \frac{2\pi}{\hbar}|\langle f|\bar{V}|i\rangle|^2 \rho_f(E)} \qquad \textbf{2.22}$$

with the Dipole Approximation invoked, X-ray absorption cross section can be expressed as

$$\sigma_x = \frac{4\pi^2\hbar^2}{m^2}\frac{e^2}{\hbar c}\frac{1}{\hbar\omega}|\langle f|e.p|i\rangle|^2 \rho_f(E) \qquad \textbf{2.23}$$

where $\hbar\omega$ is the incident photon energy, e is the electronic charge and m is mass of electron, $\boldsymbol{\rho_f}(E)$ represents the density of final states and $\langle f|\boldsymbol{e}.\boldsymbol{p}|i\rangle$ is the dipole matrix showing the interaction between the linear momentum operator **'*p*'** with unit vector of the electric field **'*e*'** of a polarized incident light. This dipole matrix reveals the polarization dependence of the NEXAFS spectra. The transitions which involve change in angular momentum quantum number by Δl = ±1 are only allowed and this is reflected in the NEXAFS spectra. The transitions between the molecular orbitals are governed by the dipole selection rules. For linearly polarized light the dipole matrix can be written as $\boldsymbol{e}\langle f|\boldsymbol{p}|i\rangle$. The direction of this matrix element will be same as that of orientation of the orbital i.e. the vector ***O***. thus the total resonance intensity can be presented as:

$$\boldsymbol{I \propto |e\langle f|p|i\rangle|^2 \propto |eO|^2 \propto cos^2\delta} \qquad \textbf{2.24}$$

Here δ is the angle between the electric field vector, ***E***, and the direction of the final state orbital, ***O*** as shown in **Figure 2.15**. Thus, the resonant features are most intense when the electric field vector has the same direction as that of the orbital orientation. On the other hand, if the electric field vector is perpendicular to the molecular orbital then the corresponding resonance features will be absent from the spectra.

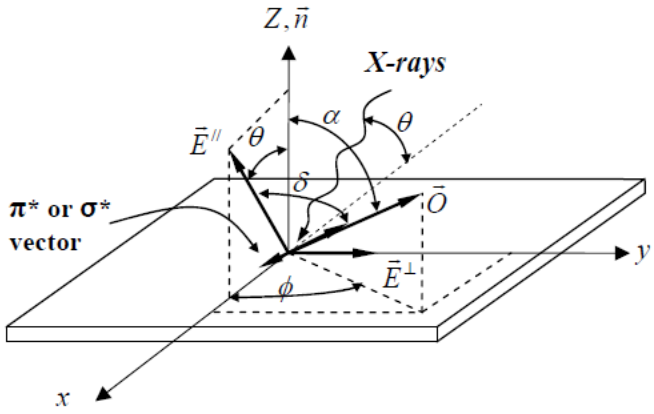

Figure 2.15 Coordinate system defining the geometry of a σ* or π* vector orbital on the surface. [117]

2.3.2 Detection schemes

In NEXAFS a tunable monochromatic X-ray source is used to excite core electrons to unoccupied bound states. Soft X-rays having energy lower than 2000 eV (soft X-ray) are used for photo-absorption. The core hole thus created is filled up either by an electron radiatively with the emission of florescence photon or non-radiatively with the emission of an Auger electron. Detection schemes for collecting NEXAFS spectra comprise of two modes. First is measuring the secondary electron known as electron yield (EY) and second is counting the florescence photons known as fluorescence yield (FY). Electron yield measurements are carried out in several different ways: Total electron yield (TEY), Partial electron yield (PEY) or Auger electron yield (AEY). In TEY mode, electrons of all energies are collected. Due to the dominance of secondary electrons the TEY signal usually has a strong intensity and low signal to noise ratio. In TEY mode, spectra are recorded by measuring the current to the sample. So, that the sample remains electrically neutral after the

photoionization process. The sampling depth for TEY mode is limited to the mean free path of the released electrons and is of the order of 10 nm into the surface. By placing a retarding voltage infront of the electron detector, only electrons with low kinetic energies are allowed through to the detector known a PEY mode. This increases the surface sensitivity. However, the electron yield methods are limited only to conducting samples. Fluorescence yield on the other hand is independent of the sample conductivity. Longer mean free path of photons renders this technique less surface sensitive. The sampling length for FY mode depends on the attenuation length of the incident X-ray and the composition of the material under study. In general, the sampling depth in FY mode is of the order of 100 nm for soft X-rays. The greatest advantage for FY mode is the ease of sample preparation as the presence of surface oxides and contaminants can effectively be tolerated.

During the actual spectrum acquisition process, spectra for TEY is acquired by measuring the sample current. Auger electrons are measured by setting the energy of the electron analyzer to specific Auger transitions. On the other hand, florescence yield detection is carried out using a photodiode placed close to the sample. Both electron yield and florescence yield are normalized by dividing by the incident photon flux measured at a gold grid placed upstream of the beam path (between the main chamber and the beamline optics).

2.4 Raman Spectroscopy

When light interacts with matter it gets scattered in a variety of ways. When the scattered wave possesses the same frequency as of the incident light the scattering is elastic, this is known as Rayleigh. On the other hand, if the scattering process is inelastic, there will be discrete shift of the frequency value- this is referred to as Raman Scattering. For Raman scattering the frequency shifts are independent of the exciting frequency, and bear characteristic footprint of the scattering molecule. Essentially these frequencies resemble the

vibrational frequencies of the molecule. Hence, Raman spectroscopy can be used to probe the vibrational energy levels of molecules. In a typical Raman spectrum, the intensity of the scattered photon is plotted as a function of the energy difference between incident and scattered photon. This frequency shift is referred to as the Raman shift and can be represented in terms of wavenumber ($\bar{\nu}$) as:

$$\Delta\bar{\nu}\ (\boldsymbol{cm^{-1}}) = \left(\frac{1}{\lambda_{incident}} - \frac{1}{\lambda_{scattered}}\right) \qquad \textbf{2.25}$$

and $$\bar{\nu}\ (\boldsymbol{wavenumber}) = \frac{\nu}{c/n} = \frac{1}{\lambda} \qquad \textbf{2.26}$$

Where, $\Delta\bar{\nu}$ is the Raman shift, $\lambda_{incident}$ is the wavelength of the excitation source and $\lambda_{scattered}$ is the corresponding scattered wavelength. c is the speed of light in vacuum (2.997925 x 10^{10} cm/sec), and (c/*n*) is the velocity of light in a medium whose refractive index is *n*, for which the wavenumber is measured.

Raman scattering is typically a very weak process, about 10^{-9} to 10^{-6} times that of Rayleigh scattering. Hence an intense monochromatic light source is essential to observe this phenomenon. Typically, lasers are used as light source to study Raman scattering process. It needs to be mentioned that, in the Raman scattering process there isn't any inherent absorption of photon by the molecule. Only the ground state of the molecule gets disturbed, resulting in vibrational and rotational transitions. These transitions are ultrafast and occur at a timescale of ~10^{-9} s.[118,119] . The elastic and inelastic scattering process can be presented schematically using the Jablonski diagram (**Figure 2.16**).

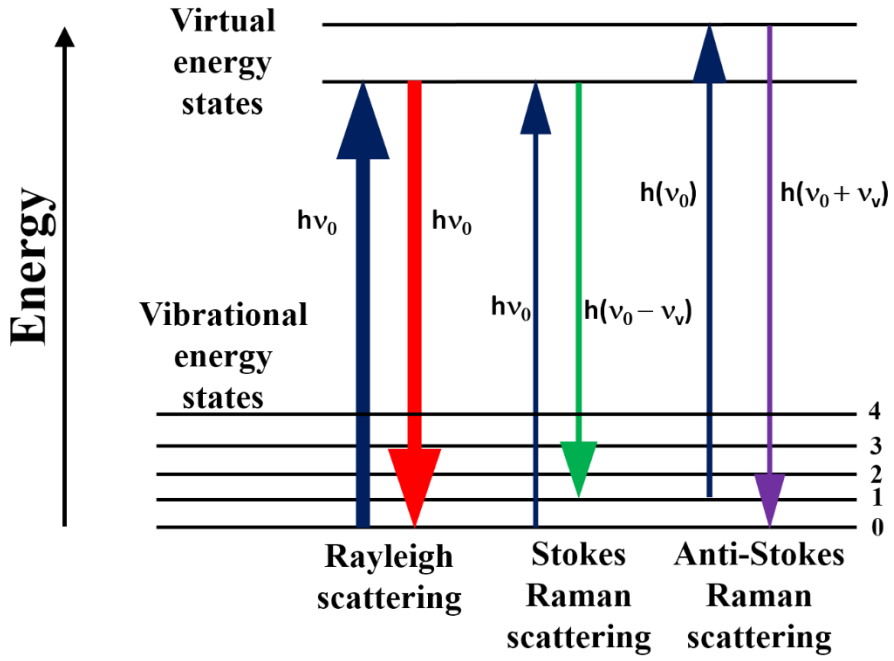

Figure 2.16 Jablonski energy diagram for Rayleigh and Raman scattering.

2.5 Atomic Force Microscopy

Atomic force microscopy is a highly versatile surface analytical tool to map surface at a resolution down to atomic or molecular level. In AFM, a sharp probe having dimensions' tens of nanometre attached to a cantilever scans the surface of interest in a raster pattern. By carefully monitoring the displacement of the probe, a 3D image of the surface can be created. The intermolecular force between the tip and the sample can be used to acquire information about the mechanical, electrical, chemical and magnetic properties of the sample at nanoscale resolution. The basic operational principle is described in the next section.[120,121]

2.5.1 Operation

The basic working principle of an AFM is shown in **Figure 2.17.** An atomically sharp Si/Si_3N_4 tip is mounted on a single beam cantilever. The tip is positioned in close proximity to the sample surface, and the deflection caused to the cantilever while scanning the surface is taken to be the measure of force between the sample and the tip. The cantilever deflection is monitored using an optical lever by reflecting a laser beam off the back of the cantilever to a position sensitive photodetector. As the laser is reflected to the detector, any deflection of the cantilever doubles the deflection of the laser beam., The larger distance between the cantilever and the detector with respect to the dimensions of cantilever sets the sensitivity. In general, an AFM operates in two modes, *static* or *dynamic*. In static mode, the cantilever is deflected statically by the force between the tip and the sample surface to a set value maintained by a feedback loop. By contrast, in dynamic mode the cantilever oscillates with a designated frequency and the amplitude of the oscillation is maintained by the feed-back loop to a set value. Thus, in static mode the tip is always in contact with the sample surface, while in dynamic mode both contact and non-contact is possible. *Intermittent contact* mode is the most popular in dynamic mode. Here the tip taps over the surface during scanning providing information about chemical and physical properties of the surface, in addition to topography.[122]

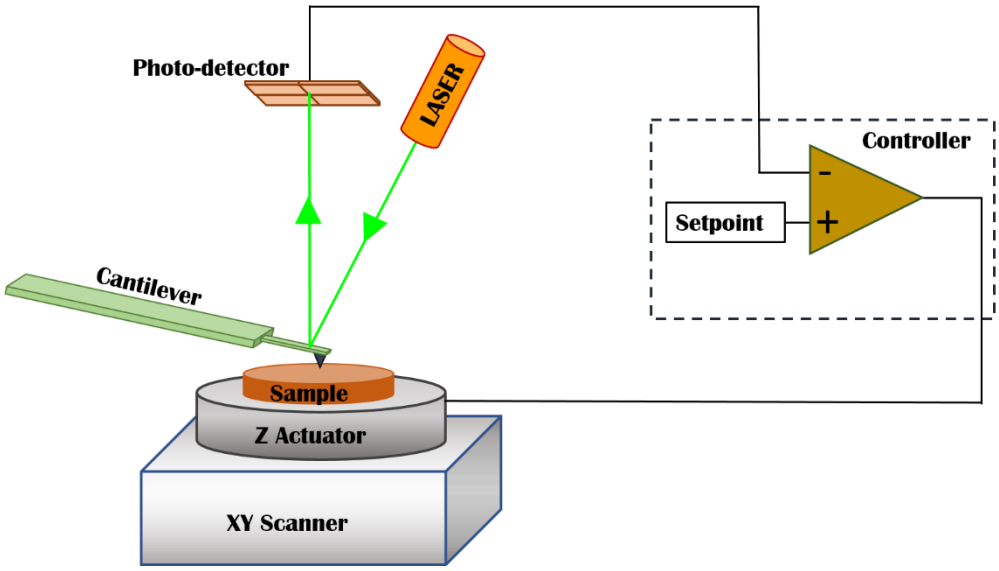

Figure 2.17 Diagram to show the basic working principle of atomic force microscope.

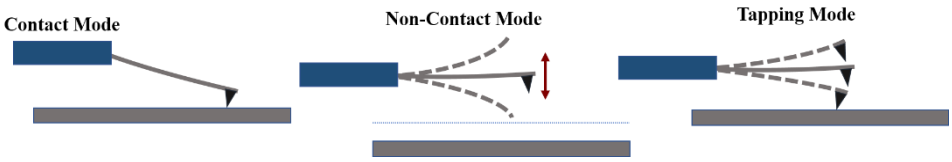

Figure 2.18 Three different modes of AFM operation.

Figure 2.18 shows the three AFM operation i.e. contact, non-contact, tapping mode. In contact mode, the tip is brought in physical contact with the sample surface. Due to which the apex of the tip experiences repulsive force and the rest of the tip is attracted towards the sample. As the tip scans over the surface the cantilever is constantly deflected due to the

surface features. Thus, a constant force proportional to the vertical deflection is applied on the cantilever, which balances the force on the tip. Because of the high sensitivity of the short-range forces high resolution topographic images can be obtained in this case. However, the resolution is strongly dependent on the contact area of the tip apex. From the Hertz model, the contact diameter (*a*) is proportional to the applied force (F) on the tip as :

$$a = 2\sqrt[3]{DRF} \qquad 2.27$$

where R is tip radius and D represents combined elastic properties of the tip and the sample.[123]

For Non-Contact mode, in-spite of being dragged over the sample surface, the tip oscillates at its resonant frequency above the sample surface. The distance between the surface and the tip is such that the magnitude of the attractive forces at the tip is more that the repulsive force. These attractive forces shift the oscillation frequency between the tip and the sample. The signals in the form of frequency shift is then used to control the tip sample distance. The major disadvantage of this technique is that it cannot be used in a liquid environment. To overcome this issue intermittent contact mode can be used. Here the cantilever oscillates in a way that the tip touches the surface first and then retracts to avoid damage to the surface. The intermittent contact to the surface reduces the free amplitude of the oscillating cantilever, which can be used to measure and identify the surface features (height difference). In this operation mode, the oscillation frequency is kept constant by the feedback loop. The system optimizes the force applied by the tip on the sample and maintains it to the lowest possible value. Tapping mode is particularly important for soft samples , e.g. polymers and biological samples, as the tip doesn't stick to the sample surface avoiding any damage.

In tapping mode any change in material properties e.g. composition, adhesion, friction and viscoelasticity would introduce a phase lag between the piezoelectric drive frequency and cantilever oscillation frequency. Thus, for a flat surface with varying composition no changes could be observed in the height image but would be reflected in phase image. Phase imaging has been used to resolve features from fine contaminants which are hard to evince otherwise. Resolution of the microscope depends significantly on the tip dimensions. A tip sharper than the surface features will lead to high quality AFM images. Additional artefacts may be visible in the images resulting from a contaminated or a damaged tip having multiple protrusions at the apex.

2.5.2 Scanning Kelvin Probe Microscopy

The principle of operation for Scanning Kevin Probe Microscopy (SKPM) is similar to that of macroscopic Kelvin probe technique. In this technique, a conductive tip is rastered over the surface in two passes ,as shown in **Figure 2.19.** In the first pass the normal topography is captured, while in second pass the tip raises to a height to negate the Van der Waals forces and just the electrical map is obtained called the nap pass. In the nap mode, the system retraces the same line as in topography so that the distance between the sample surface is always constant.[124]

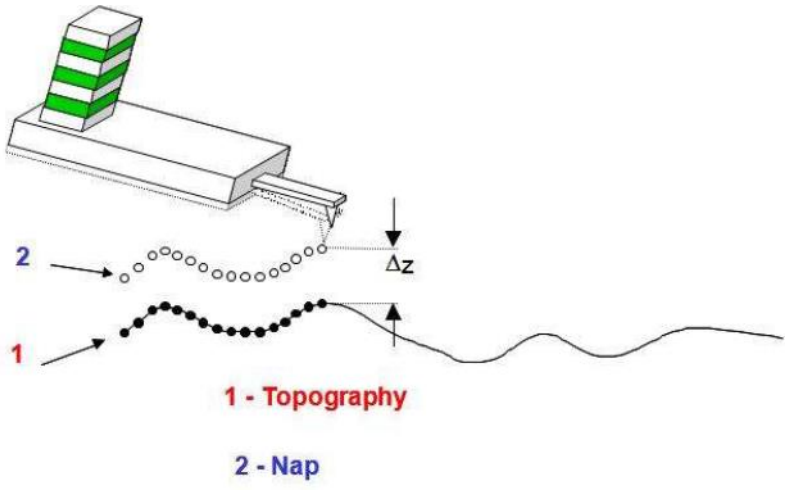

Figure 2.19 Schematics of nap mode. (From instrument brochure)

Here an external ac bias is applied on the tip, which results in an electric field on the cantilever due to the difference in potential between the tip and the sample. During the nap pass no piezo induced mechanical force is applied, only the AC bias induces the oscillations. In the nap mode, the tip and sample can be modelled as a parallel plate capacitor. The electrostatic force between the two is proportional to the square of the applied voltage:

$$\boldsymbol{F = \frac{1}{2}\frac{\partial C}{\partial z}V^2} \qquad \textbf{2.28}$$

To compensate for the contact potential difference (CPD) between the tip and sample an external DC bias (V_{DC}) is applied to the tip. CPD is the measure of work function/surface potential difference between the tip and the sample material: $e.V_{sp} = \Phi_{sample} - \Phi_{tip}$ (e is the electronic charge). Considering the applied DC bias, the total potential difference between the probe and the sample is:

$$\boldsymbol{V = (V_{DC} - V_{SP}) + V_{ac}\sin(\omega t)} \qquad \textbf{2.29}$$

After squaring equation 2.29

$$\boldsymbol{V^2 = (V_{DC} - V_{SP})^2 + 2(V_{DC} - V_{sp})V_{ac}\sin(\omega t) + \frac{1}{2}V_{ac}^2(1 - \cos(2\omega t))} \qquad \textbf{2.30}$$

After replacing equation 2.30 in 2.28 :

$$\boldsymbol{F = \frac{1}{2}\frac{\partial C}{\partial z}\left(\left[(V_{DC} - V_{SP})^2 + \frac{1}{2}V_{ac}^2\right] + 2[(V_{DC} - V_{SP})\,V_{ac}\sin(\omega t)] - \left[\frac{1}{2}V_{ac}^2\cos(2\omega t)\right]\right)}$$

2.31

The term in the middle of the equation forms the heart of SKPM. Where the applied DC bias is modulated to match the surface potential different between the tip and the sample i.e. $V_{DC} - V_{SP} = 0$, so, that the electrostatic force is at its minimum value. The feedback loop operates to adjust this DC bias on the lever. However, in actual operation there are various factors that affect the surface potential. Thus, the measured surface potential difference even when being accurate have multiple contributions which renders this technique pseudo-quantitative. **Figure 2.20**shows schematically the circuit diagram for the SKPM system used for determining the changes in work function of graphene oxide. These results have been presented in **Chapter 4.**

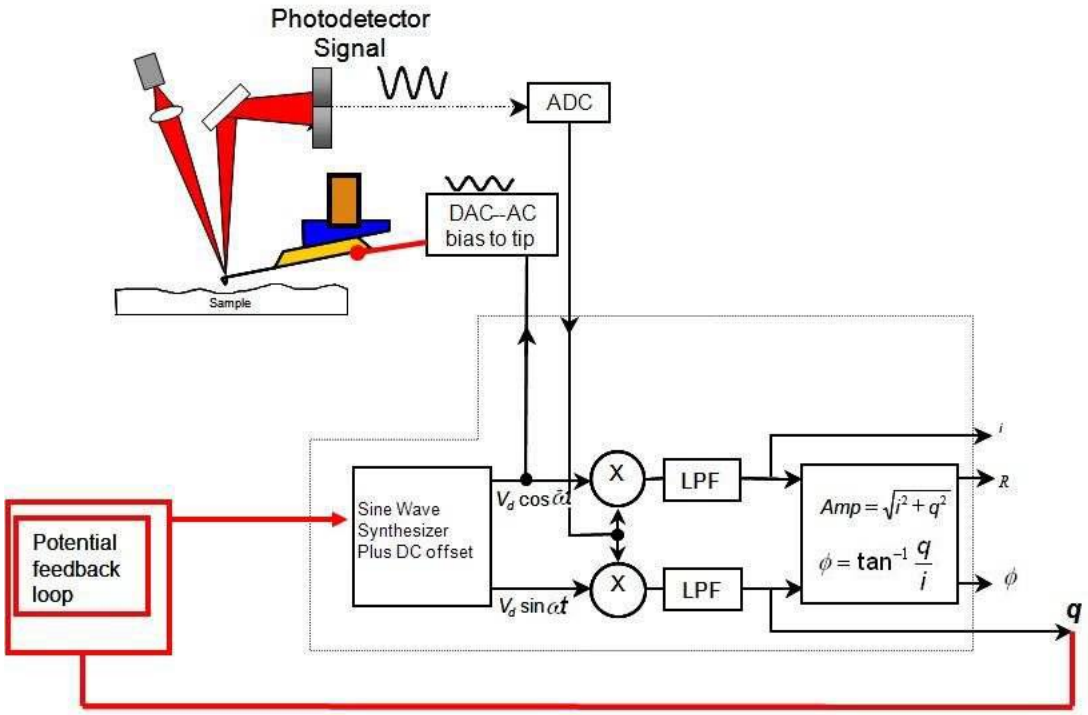

Figure 2.20 Schematic showing how SKPM is done on Asylum AFM. The probe is driven electrically with an AC bias. The potential difference between the tip and the sample causes the probe to oscillate. These oscillations are then canceled by a potential feedback loop. The voltage required to match the probe to the sample is captured as the surface potential channel in the software. (From instrument brochure)

2.5.3 Electrostatic force microscopy

The operation of electrostatic force microscopy (EFM) is similar to that of SKPM. But there is no active feedback loop in this case. A voltage is applied to an oscillating tip, which hovers over the sample without touching it. The force gradient created between the tip and sample shifts the oscillation frequency of the cantilever. This frequency shift introduces a phase lag between the drive frequency and that of the cantilever. So, by tracking the phase shift, areas on the sample with varying electrical properties can be identified. A clear contrast in the EFM images will be observed for a considerable change in conductivity within a sample.[125] **Figure 2.21** shows the working principle of EFM. With respect to SKPM the EFM circuit doesn't have a feedback loop.

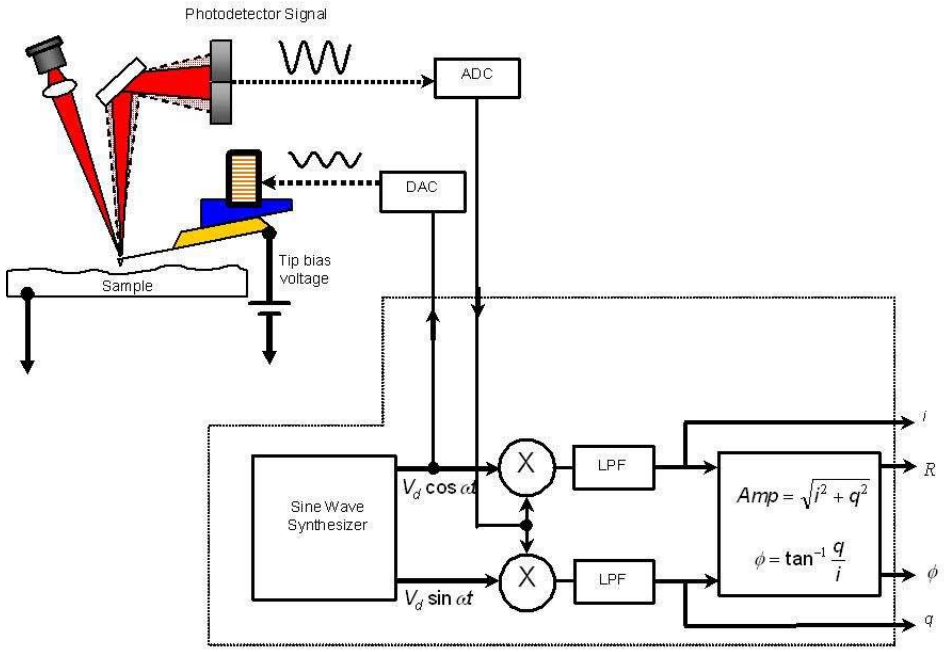

Figure 2.21 Schematic of Electric Force Microscopy (Asylym research MFP 3D). The Probe is oscillated both during the main scan and during the nap scan. During the nap scan, the probe is lifted off of the surface, and a bias applied between the tip and sample to show the location of areas that are conductive or strongly charged. (From instrument brochure)

As shown in **Figure 2.22**, if a conductor is introduced in a insulating matrix, the field lines around the conductor rearrange themselves in order to make the electric field inside the Gaussian surface zero. The electric field gradient between the tip and the sample will change with any changes in the field lines which in turn will change the resonant frequency of the cantilever and will reflect as a change in phase. However, for an insulator placed in a conductive matrix, the phase is visible only of its on the surface, and the insulating particles embedded inside the conductor will not be detected by EFM. Additionally, if the tip and sample is considered as a capacitor,then with the introduction of a conductor will essentialy make the system as two capacitors; tip to conductor and conductor to ground. Changing the capacitance value where is no conductor. The ability to differentiate between conductive and non conductive domains in a materials can also be used to reflect the the changes in conductivity. EFM studies of graphene oxide is presented in Chapter 5 to reveal the increase in conductivity after reduction with plasma.

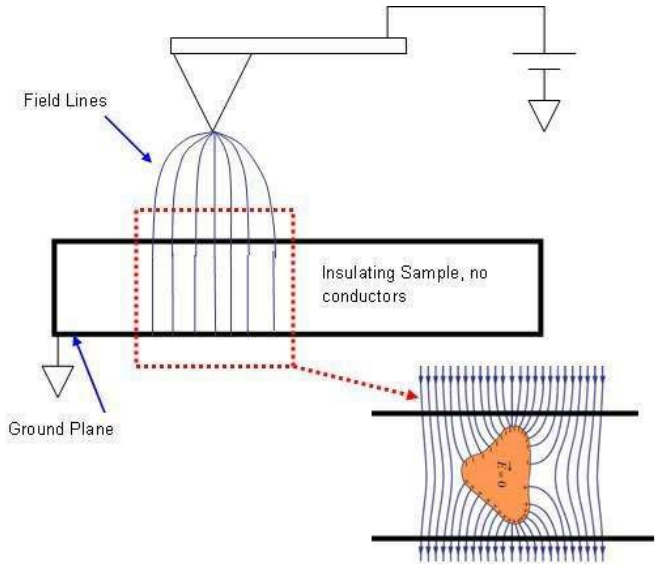

Figure 2.22 This schematic shows how the introduction of a conductor into the electric field between the tip and sample can effect the field lines. (From instrument brochure)

Chapter 3. Plasma Jet Printing of Cupric Oxide Nano-colloids

The printing of nanostructured films with tailored oxidation state and electronic properties has applications in several areas including printed electronics, optoelectronics, solar cells and catalytic conversion. Widely used inkjet/aerosol/screen printing techniques require pre-and post-processing to enhance adhesion and to tailor physical and chemical state of the printed materials. The use of nano-colloidal ink in general results in undesirable oxidation of the nanoparticles in the ink stock. Controlled deposition of functional materials with tailored physical, chemical and electronic characteristics is thus needed for advanced manufacturing of flexible electronic devices. In this chapter, a new state-of-the-art printing technology using an atmospheric pressure plasma jet will be discussed. Plasma jet printing technology's unique ability to print and tune in-situ the electronic and surface properties of copper oxide nanoparticles has been demonstrated. Direct write plasma printing of copper thin film with tailored oxidation states has been studied using X-ray and Raman spectroscopy techniques and further characterized using current and voltage measurements.

3.1 Introduction

Recently, there has been an increased interest in fabricating electronic devices on flexible substrates, which include plastics, cellulose, textiles and metal foils with enhanced emphasis on recyclable materials. Printing of electronic/optoelectronic devices using colloids faces numerous challenges.[126] The major issue being oxidation of the material to be printed, leading to decreased mobility of the charge carriers. Copper is one of the most important Earth abundant material (26th) and has been used for various applications due to its high thermal (~385.0 W m^{-1} K^{-1} at 20 ºC) and electrical conductivity (1.7241 μΩ-cm at 20°C). Nanostructured copper with varying oxidation states from pure metallic to cuprous oxide often finds applications in printed electronics, optoelectronics and catalysis.[127–129] In electronic industry, interconnects in integrated circuits (IC) plays a key role in deciding the system performance and speed. Printing of copper interconnects with controlled morphology

and oxidation state is important in 3D IC packaging, flexible printed circuit boards and vertical integration. In catalysis, nanostructured materials with high surface area and porosity have proven to have higher conversion efficiency. Oxide-derived copper with a nano-crystalline surface has shown promising conversion efficiency compared to metallic copper in electro-reduction of CO_2 and CO (57% vs 22% total Faraday efficiency for CO reduction) [126,130]. Porous metal structure for catalysis often formed from metal deposited on polymeric templates and are then post-processed to remove the polymer. This method thus proven to be difficult to use in a high through-put process because of the time required for polymer removal.[131]

Various printing techniques including inkjet printing, aerosol jet printing and screen printing are currently being explored for printed electronics.[132,133] The routine post processing required to remove solvents and contaminants, and the annealing required to reduce metal oxides, is not compatible with complex layered devices. Inkjet printing of a conductive pattern using copper nanoparticles requires post deposition annealing which limits the use of low glass transition temperature substrates and adds additional processing steps. [134,135] Different techniques need to be adopted depending on the glass transition temperature, stability in vacuum (outgassing), stability in liquid medium for electroplating etc. Screen printing is the widely used process for planar objects, however, the disadvantages include resolution, organic contaminants and the need for post print thermal treatment.[136,137] Thermal spray and laser induced sintering are also widely used industrial techniques in various other contexts.[138,139] High oxygen concentration, high porosity and difficulty in controlling the microstructure are serious disadvantages of the thermal spray process. Thermal spray and laser induced sintering do not provide the capability to tailor the oxidation state of the printed material as an *in-situ* process.[140] The state-of-the-art printing technologies lack the capability to simultaneously control the microstructure, morphology and electronic structure of the printed material.

In view of all the above there is a need for a new advanced printing technology that is compatible with a range of substrates including semiconductor wafers, textiles, paper, plastics and other flexible substrates. This technology should avoid thermal cycles and other steps that are slow or disruptive of previous treatment. The plasma jet deposition technique presented here is unique in terms of depositing metals and alloys with tailored physical and chemical characteristics. Evidence in favour of this claim has been presented in the next sections.

3.2 Experimental work

3.2.1 Synthesis of Copper Nanoparticle Ink

The inks used for the plasma jet printing process was not prepared in NASA, but were obtained from Conn Center for Renewable Energy Research, University of Louisville, United States. The steps involved in the synthesis process have already been published in their previous article and are as follows:

A total of 5 mL of Tergitol NP-9 was added to a 50 mL aqueous solution of 0.1 M $Cu(NO_3)_2$, followed by 100 mL of water. The pH of the solution was adjusted from pH 7 to 11 by the dropwise addition of NH_4OH. To this solution, 50 mL of aqueous $NaBH_4$, 0.3 M, was added, and the reaction was then stirred for 2 h. The nanoparticle ink was optimized further at pH 11, using ethylene glycol as the solvent. The Cu/Cu_2O nanoparticle inks obtained using ethylene glycol at pH 11 were used in the fabrication of the Cu films. [141,142]

3.2.2 Details of plasma jet printer

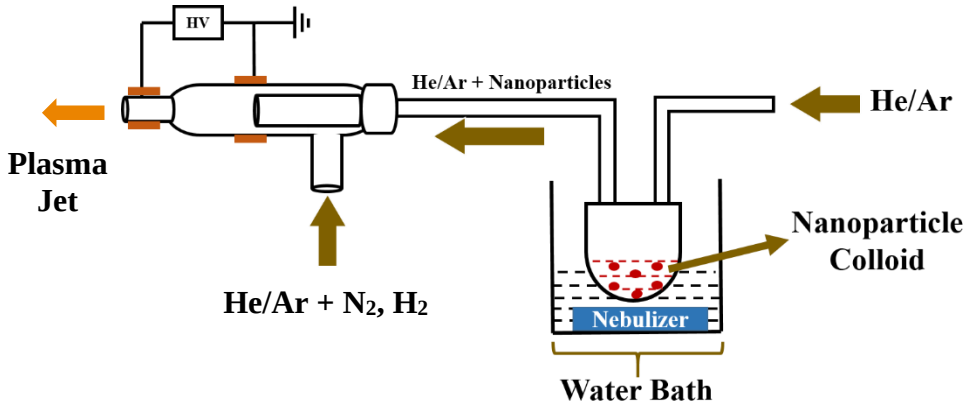

Figure 3.1 Schematics of plasma jet printer with a DBD design. The nanoparticle colloid are aerosolized using a commercial mist maker and are carried through to the plasma by He or Ar. A mixture of reducing gases is fed through the other inlet and is used to ignite the plasma.

Figure 3.1 shows the schematics of the setup used for plasma jet printing. Here the nanoparticles are aerosolized using a low-cost mist maker. A beaker containing the nanoparticle colloid is placed in a water bath with the nebulizer in it. Helium or argon is introduced into the beaker to carry the aerosolized nanoparticles through to the printing head (nozzle). A dielectric barrier discharge (DBD) configuration was used in this project (as described in section 1.3.2 of chapter 1) Here the plasma is ignited by applying a potential between two electrodes with He or Ar as the carrier gas passing through a quartz nozzle. The plasma is the most intense between the electrodes (active region) followed by the afterglow at the exit of the nozzle.[143,144] Nozzles are designed with two inlets as shown in **Figure 3.1**. The inner capillary is used to inject the nanoparticles while the other process gases were

introduced via the outer inlet. Copper tapes wrapped around the glass nozzle act as electrodes (3 cm apart) and are connected to a high-voltage (1 to 15 kV) pulsed DC power supply. The separation was optimised to avoid arcing between the electrodes both during the before the plasma is generated. Nozzles are commercially available from Meinhard. The nozzles used for this purpose are Meinhard type C Quartz nebulizer with 0.5 mm inner capillary diameter and Pyrex Sheath Gas Tube (product id: ML116063) with 5 mm diameter. With precise control and by scaling down the quartz nozzle, there lies the possibility of achieving sub 100 micron resolution.[144]

Figure 3.2 (a) shows the plasma jet and **Figure 3.2 (b), (c), (d)** shows that the plasma jet can be used for printing on various substrates such as polyethylene terephthalate(PET), paper, polyimide and silicon substrate. The size dependent melting point of the copper nano-particles has been exploited in this study for the formation of thin films structure. For a nano-particle, melting point drops drastically in comparison to the bulk material.[145,146] With the decrease in size the surface to volume ratio of the particle increases. This leads to the surface atoms to be loosely bound and diffused on the surface. Hence, the melting at the surface occurs at much lower temperatures than the bulk melting point. This phenomenon is called surface melting or pre-melting.[145] The solid copper oxide nanoparticles can be transformed to a metastable state of solid liquid phase by varying the process parameters in which the surface transforms to liquid while the bulk remains solid. This will have an impact on both the morphology and chemical structure of the material being deposited. This partial molten outer core of the nanoparticles may also aid adhesion to the substrate.

3.3 Characterization of the printed films

Microstructure and morphology of the printed samples were studied using Hitachi (Pleasanton, CA) S-4800 field-emission scanning electron microscope (SEM). Current and

voltage measurements were carried out with Hewlett-Packard 4155A Semiconductor parameter analyser with a voltage sweep from (-10 mV to 10 mV). For these measurements, a potential was applied across two points separated by 5 mm on the substrate. In order to the understand electronic properties of the samples, near edge X-ray absorption fine structure (NEXAFS) spectroscopy studies were carried out on the printed copper film. Here a tuneable monochromatic source of X-rays from synchrotron radiation with a high degree of polarization was used to excite core electrons into unoccupied bound states or continuum states. Cu L-edge (2*p* to 3*d* transitions) and O K-edge (1*s* to 2*p* transitions) NEXAFS measurements were performed in Beamline 8–2 at the Stanford Synchrotron Radiation Light source, of SLAC National Accelerator Laboratory. [147] For normalization, the incoming flux (I_0) was measured using a gold grid placed in the beam path upstream of the chamber. All samples were mounted on an aluminium stick using a conductive carbon tape and measured under ultra-high vacuum conditions ($< 1 \times 10^{-8}$ Torr). The energy of the incident beam was calibrated at the carbon dip (284.7 eV), arising from the carbon contaminations on the beamline optics. The drain current from the isolated aluminium stick was used for total electron yield and all measurements performed at the "magic angle" of ~ 55°. At this angle, the anisotropic orientations at the surface of sample can be neglected. Beamline slits and pass energy of the analyser were set to achieve a total energy resolution below 0.3 eV. All spectra were divided to the incident flux and normalized to a linear background as shown in **Figure 3.3**. Following the normalization procedure developed by Wang *et al*.[148,149], a linear background was subtracted from the electron yield data below the L_3 and above the L_2 regions. The edge jump was then normalized to unity.

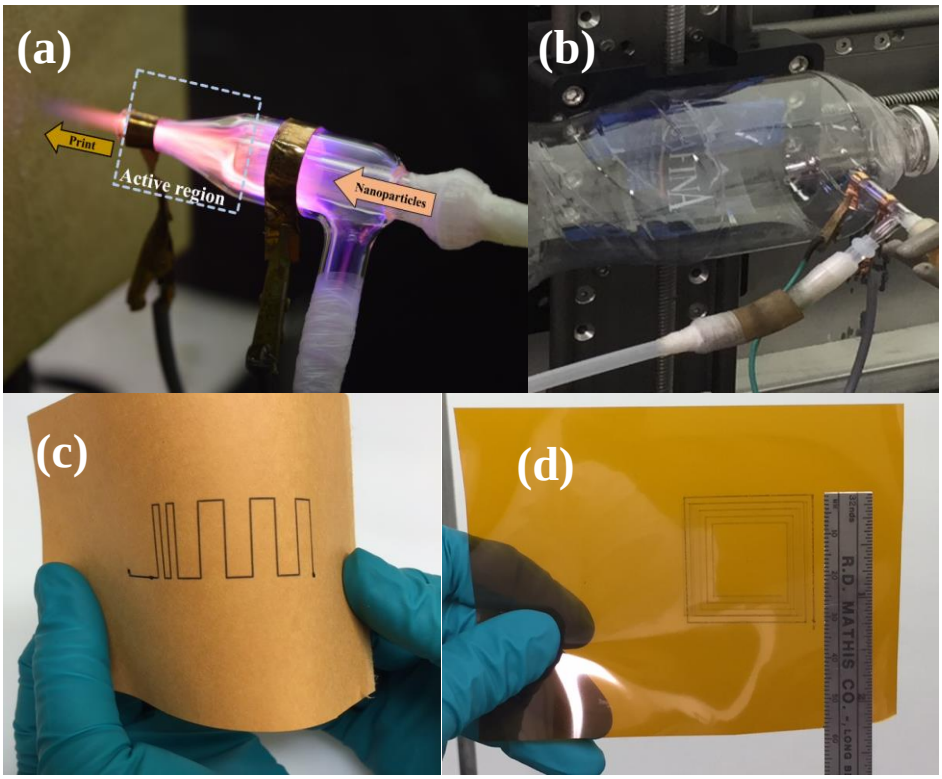

Figure 3.2 (a) plasma jet printer (b) printing on PET bottle (c) printed pattern on paper (d) printed pattern on polyimide substrate. [N.B. refer to Attributions]

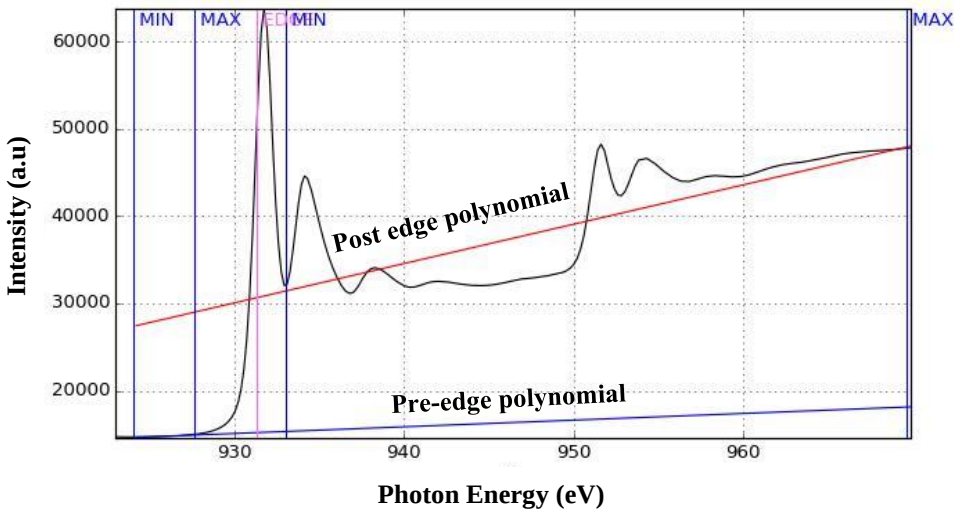

Figure 3.3 Normalization of the Cu *L* edge spectra. The pre-edge and post-edge regions were normalized with linear background subtraction algorithms.

3.4 Results and discussion

One prominent feature deciding the intensity and thermal capacity of the plasma is the nature of gas used to generate the discharge. The electron densities in argon and helium are different and that leads to the plasmas in the former appearing more intense. Argon plasma has a higher electron density than the helium plasma for the same process parameters. At atmospheric pressure, the electron density in argon is 2.5 times higher than in helium.[150] This is because of higher first ionization energy for neutral helium atoms (24.6 eV) than that for argon (15.8 eV). Thus, argon is easier to ionize at the same operating conditions and hence it will have a higher electron concentration. The thermal conductivity of the gases also varies. (1.6×10^{-3} J cm^{-1} s^{-1} K^{-1} for He and 1.8×10^{-4} J cm^{-1} s^{-1} K^{-1} for Ar at 300 K).[151] As a result, the energy of the plasma varies depending on the nature and type of gases used to generate the discharge. The higher ionization potential of the first excited state for helium and lower mass with respect to that of Argon, results in a much higher electron temperature for helium at equal operating conditions. [152] However, the gas temperature for argon is much higher with respect to helium at the same applied voltage. According to Wang *et al.*, at low flow rates the gas temperature for argon can go beyond 1000 K in comparison to helium (600 K).[151] Introduction of nitrogen and hydrogen with the carrier gas will lead to the formation of highly reactive nitrogen and hydrogen species in the plasma.[153] It is important to mention that presence of high energy metastable states He (2^3S_1), 19.82 eV; He (2^1S_0), 20.6 eV, makes it easier to excite N_2 and H_2 with He.[153] When the nanoparticle colloid enters the active region, it will be subjected to electrons, ions and radical bombardment from the plasma species. The interaction of these highly active excited species in plasma with the

nanoparticles can alter the chemical and electronic states of the nanoparticles. The momentum of the particles reaching the substrate to form the coating varies depending on various factors including the gas flow rate, nature and type of gases, applied voltage, size and shape of the nozzle and the distance between the substrate and plasma jet. One major issue with the common inkjet printing process is matching the surface energy of the substrate and surface tension of the ink leading to coffee ring effect.[154] Plasmas have often been used to increase the surface energy of substrates which can induce better adhesion of the printed material.[155] A recent study by Wang *et al*. revealed that He plasma enhances the surface energy of the materials for example, hydrophilicity on a PMMA substrate.[156] Thus, in our system the surface energy of the substrate is adjusted intrinsically resulting in better adhesion of the printed nanoparticles with the substrate.

The temperature at the substrate for different gas combinations at two different flow rates of He/Ar is listed in **Table 3.1**. Although the gas temperature of Ar is much higher than He, substrate temperature shows a different trend. It may be due to higher electron temperature and thermal conductivity of the Helium in comparison to Argon. Owing to joule heating temperature tends to be at its maximum near the cathode, almost 85 % of applied power is lost due to this process and ends up in heating the gas.[151] With introduction of nitrogen in the helium plasma the temperature at the substrate increases. This can be due to the increase in heat content with nitrogen addition in the carrier gas flow, as derived below.

From ideal gas law:

$$p_{atm} = n_g kT$$

P = pressure, n_g = number of gas atoms per unit volume , k = Boltzmann constant , T= temperature

$$n_g = \frac{p_{atm}}{kT}$$

$$n_g(He) = \frac{10^5}{1.38 \times 10^{-23} \times 300} = 2.4 \times 10^{25}\ m^{-3}$$

Now, energy density is defined as the amount of energy stored in a given system or region of space per unit volume. Energy density or energy per unit volume has the same physical units as pressure. Thus, pressure is a measure of the enthalpy per unit volume of a system. This is because, presence of a pressure gradient has the potential to perform work on the surroundings by converting enthalpy to work until equilibrium is reached.

Hence, we can compare: $p = n_g kT \equiv$ energy density or heat content (Jm^{-3})

For He, heat content at 300 K $\equiv n_g(He) \times 0.025\ (Jm^{-3})$

Since, the value of kT at room temperature is 0.025 eV

When N_2 is introduced into the carrier gas

For N_2 = 10% of He content

$$n_g(N_2) = 0.1 \times n_g(He) = 2.4 \times 10^{24}\ m^{-3}$$

If total dissociation of N_2 occurs in the plasma, energy released:

$$n_g(N) \times (eV)_{diss} = 2 \times n_g(N_2) \times 10\ eV \equiv 2 \times 2.4 \times 10^{24} \times 10\ Jm^{-3}$$

Here, 10 eV is the bond dissociation energy of N_2 molecule.

Now replacing, $2 = 80 \times 0.025$ in the above equation

$$= 80 \times 0.025 \times 2.4 \times 10^{25}\ Jm^{-3}$$

Since, $n_g(He) = 2.4 \times 10^{25}\ m^{-3}$

$$= 80 \times \{n_g(He) \times 0.025\ (Jm^{-3})\}$$

$$= 80 \times \{\text{heat content of helium at 300 K}\}$$

Hence, fully dissociated N_2 in the plasma has ≈ 80 times more heat content compared to pure He at room temperature. This might be a reason behind the observed increase in substrate temperature with addition of nitrogen. However, there are multiple factors

controlling the properties of the plasma and the temperature at the substrate. Thus, **Table 3.1** presents opportunities for further research and to study the heat transfer from the plasma in active region to the substrate

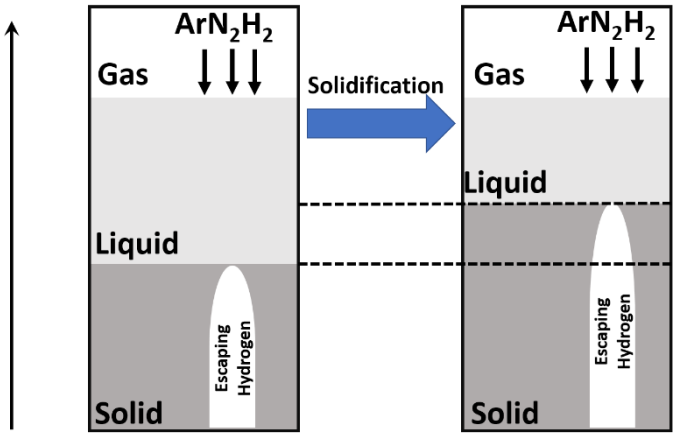

Figure 3.4 Schematic diagram of the solidification process. Solubility of hydrogen is more in the liquid phase than in the solid phase. As the molten phase solidifies: hydrogen starts escape creating pores at the interface. [157]

	Operating condition I		Operating condition II	
Gas	Temperature in °C	Flow rates in sccm	Temperature in °C	Flow rates in sccm
He	35 to 75	5000	70 to 150	1600
$He+N_2$	40 to 85	5000/100	160	1600/100
$He+H_2$	40 to 80	5000/50	200	1600/50
$He+N_2+H_2$	30 to 85	5000/100/50	120	1600/100/50
Ar	50 ± 5	5000	70	1600
$Ar+N_2$	50 ± 5	5000/100	130	1600/100
$Ar+H_2$	50 ± 5	5000/50	110	1600/50
$Ar+N_2+H_2$	50 ± 5	5000/100/50	75	1600/100/50

Table 3.1 Dependence of substrate temperature on gas flow rates and composition. The temperature range for helium plasma shows the temperature where the plasma starts and then increases with the applied voltage.

3.5 Morphology of the deposited film

Figure 3.5 shows SEM images of copper nanoparticle film printed using different plasma conditions on silicon substrates. Nanoparticles printed with a He plasma (@ 1600 sccm) retain their shape and do not undergo any significant physical deformation, as can be seen in **Figure 3.5 (a,b)** . The particles agglomerated but are mostly spherical like the as-synthesized nanoparticles. **Figure 3.5 (c,d)** shows copper nanoparticles deposited using an Ar plasma. As the ion density and gas temperature is higher in this case, the nanoparticles undergo physical deformation resulting in uniform film formation. The gas temperature of Ar plasma is sufficiently high to partially melt the nanoparticles. These fluidic Nano spheres, after reaching the substrate, tend to aggregate to reduce the surface energy forming a thin film. When nitrogen is introduced into the helium plasma, the electron density, electron temperature and the current density increase. As shown in **Figure 3.5 (e,f)**, the smaller particles undergo partial physical deformation while the larger nanoparticles retain the shape to a certain extent resulting in film formation with particles embedded on it . **Figure 3.6 (a,b)** show the copper film deposited on aluminium foil and silicon wafer respectively using the same set of nanoparticle colloids with plasma containing a combination of He, N_2 and H_2. A porous and 3D structure is formed on the Al substrate. Though the substrate temperature was 120 °C there was a visible softening of the Pyrex glass nozzle between the electrodes. Indicating that between the electrodes the temperature must have been near to the softening point of Pyrex glass (~ 800 °C) sufficient enough to melt the nanoparticles. However, the presence of highly reactive and reducing gases in the plasma creates a highly porous structure of the deposited film. A similar porous structure is also observed on silicon

substrates, but with a reduced density of pores. The formation of pores is due to the reduced solubility of hydrogen at the solid liquid interface of the copper film. This process is shown schematically in **Figure 3.4**. This variation in porosity can be linked to the thermal conductivity of the substrates. Rise in temperature at the Al substrate would be much faster with respect to Si substrate, resulting in decreased solubility of hydrogen during the growth of the film. Yamamura *et al.* related the pore formation in copper films to the high hydrogen pressure.[157] **Figure 3.6 (c)** shows a cross-sectional view of the same sample shown in **Figure 3.5 (f)**, revealing a densely packed planar copper film. Thus, it is possible to control the physical deformation of the particle by carefully controlling the gas mixtures, plasma density, operating voltage and distance between the electrode and substrate, and as a result, control the morphology, porosity and surface roughness of the film. The films then can be customised depending on the application. To the best of our knowledge, the common printing technologies fail to achieve all these properties.

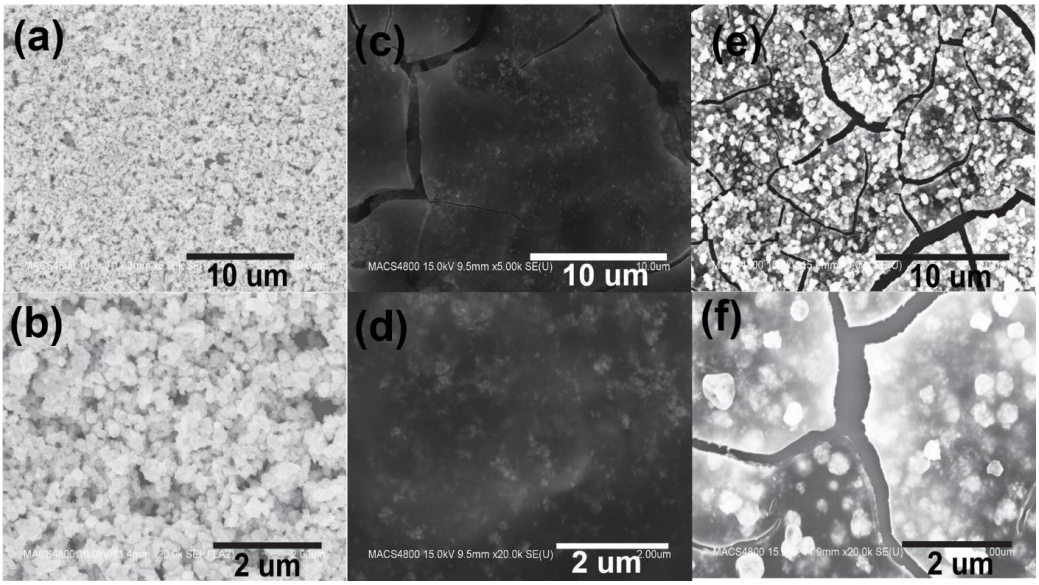

Figure 3.5 Sem images of printed copper nanoparticles on silicon substrate a,b) with He Plasma c,d) with Ar plasma e,f) Plasma with He and N_2 in 16:1 ratio. [N.B. refer to Attributions]

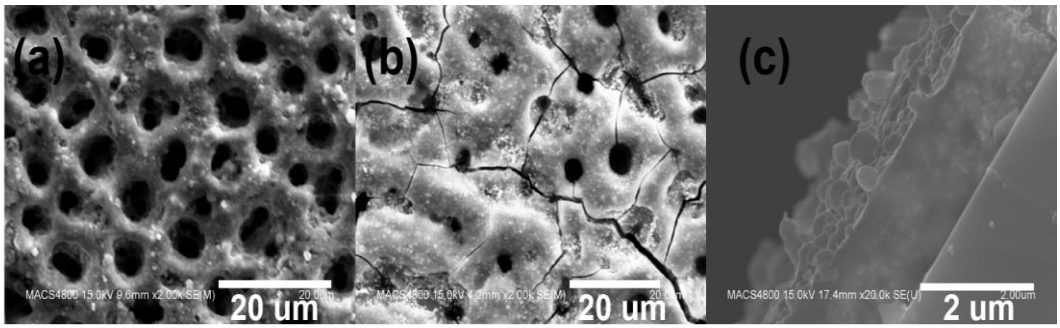

Figure 3.6 3D porous structure on a) Aluminum foil, b) Silicon wafer, c) cross section of Cu thin film deposited using He+N_2 plasma on silicon substrate. [N.B. refer to Attributions]

3.6 NEXAFS Spectroscopy of printed films

To gain an insight into the electronic state of the printed copper films NEXAFS was carried out. NEXAFS has been widely used to probe into unoccupied density of states of various materials. NEXAFS is highly sensitive towards changes in electronic state or chemical environment of an atom.[103] For metals the estimated depth of electron yield (both Auger and core electrons) is less than or equal to 5 nm, making it an extremely surface sensitive technique .[103] The florescence spectrum gives information about the bulk, which is mainly due to the longer mean free path of the emitted photons. Copper exists in valence states of Cu^{2+} or Cu^{1+} related to cupric and cuprous oxide. The electronic configurations for the states Cu^0, Cu^{1+}, Cu^{2+} are (Ar)3d $^{10}4s^1$, (Ar)$3d^{10}4s^0$, (Ar)$3d^9 4s^0$ where (Ar) denotes the first 18 electrons with configuration same as Argon ($1s^2$, $2s^2$, $2p^6$, $3s^2$, $3p^6$). In this discussion, the monovalent and divalent copper species will be referred to as d^{10} and d^9 respectively. Electronic and structural properties of Cu containing compounds have been studied using both Cu *K*-edge, Cu *L*-edge spectra using hard and soft X-rays respectively.[158,159] Cu *K*-edge has contribution from multiple final states (3*d*, 4*p* or 4*s*) at the absorption edge while Cu *L*-edge consists of single final state (3*d*) and is easier to

interpret.[160] Moreover, Cu *L*-edge features are sensitive to the valence state of copper atom and consist of sharp spectral features arising from dipole allowed $2p \rightarrow 3d$ transitions.[161] Here Cu $L_{2,3}$ NEXAFS spectra has been studied for changes in the oxidation state of copper with plasma functionalization. L_3 absorption feature is the outcome of the transition of a core electron from Cu $2p_{3/2}$ to $3d^9$ unoccupied orbital while L_2 edge is due to Cu $2p_{1/2}$ to $3d^9$ transitions. Yang *et al.* reported that the presence of a strong absorption peak at a photon energy around 931 eV is due to L_3 transitions of divalent copper species.[161] With the reduction of Cu^{2+} to Cu^{1+} another peak emerges around 934 eV resulting from Cu $2p_{3/2} \rightarrow 3d^{10}4s^0$ transitions.[162] Though the ground state is predominantly a d^{10} configuration there can be coexistence of d^9s as well in much smaller amounts.[163] The difference in spectral feature of Cu, CuO (nanoparticles) and Cu_2O (nanoparticles) can be seen in **Figure 3.7.** At the Cu $L_{2,3}$ edge signals at ~931 and ~951 eV are typical for Cu^{2+} while the features at 933.8 and 953.6 eV arise due to the presence of Cu^{1+}.[164] Similarly the difference in the electronic state is visible in the oxygen spectra as well. The peak at 530.3 eV originates due to the transition of oxygen 1s to the $3e_g$ orbital of CuO. The $3e_g$ orbital originates from the hybridization between O 2*p* and Cu 3*d* states.[165] For monoclinic CuO structure (described Section 3.6), t_{2g} (d_{xy}, d_{xz} ,d_{yz}) orbitals of copper point towards the oxygen atoms while the e_g ($d_{x^2-y^2}$ and d_{z^2}) orbitals point between the ligands. Hence for tetrahedral symmetry the e_g hybridized molecular orbitals are lowered in energy with respect to t_{2g} orbitals. For divalent copper the e_g orbitals are partially filled with 3 electrons and are termed as $3e_g$. In the oxygen spectrum of CuO, features 4-10 eV above absorption edge are due to hybridisation of oxygen *p* states (2*p* and 3*p* orbitals) with copper 4s and 4p orbitals. [165]

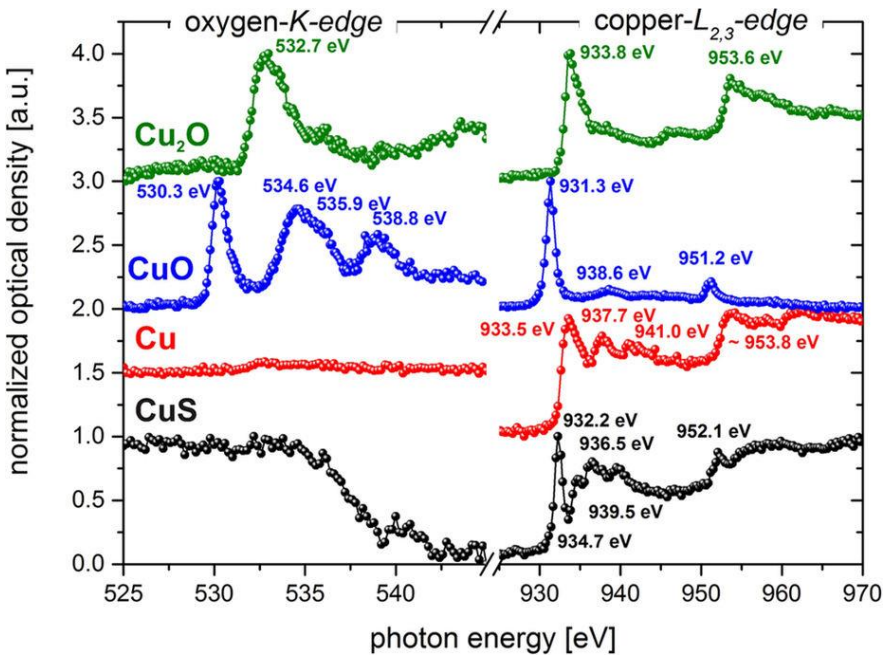

Figure 3.7 NEXAFS-spectra at the oxygen K-edge and Cu-$L_{2,3}$ edge of copper and its compounds as measured by Henzler *et al.*[164] There is an observable difference in spectral feature of Cu, CuO, Cu_2O both at the oxygen and copper spectra.

Figure 3.8 and **Figure 3.9** shows the overlaid NEXAFS spectra of copper films deposited using three different plasma conditions. The printing process was carried out using Argon and gas mixtures of argon-nitrogen, argon-hydrogen. It needs to be mentioned that all the spectra were normalized with respect to d^9 at 931.2 eV. [166] Spectra for the printed films were referenced to the spectra of copper tape, which can be considered as the best possible example for naturally occurring copper oxide thin film. Argon printed sample showed a single sharp feature of $2p \rightarrow 3d^9$ unoccupied orbital transition. Indicating a strong presence of Cu^{2+} species. With the introduction of reducing gasses i.e. nitrogen and hydrogen, the presence of reduced states is clear from the plot. The intense d^{10} feature for Ar/H_2 printed samples reflects the fact that the presence of excited hydrogen species in the plasma *in-situ* reduces the copper nanoparticles. Its noteworthy to mention that absorption

cross-section for d^{10} ($2p \rightarrow 4s$) transitions are considerably smaller (~ 25 times) than d^9 ($2p \rightarrow 3d$) features.[166] Hence, even a very small concentration of Cu^{2+} species can result in an intense absorption peak. So, it will not be a good approximation to correlate these two peaks to the surface concentration of the valence states. Also, the d^{10} peak is notably broader than d^9 due to hybridization between the final states (3*d* & 4*s* orbitals). However, the contribution of Cu^0 cannot be neglected as well.[166] Since Cu^0 also has a strong d^{10} feature, evident form the absorption feature of copper tape. The florescence yield showed the same trend as the total electron yield, to reflect no change in surface and bulk component. Referring to the fact that the thin films bear same oxidation state of copper from bulk to surface and this printing process is not just a surface functionalization technique. These NEXAFS results thereby confirms the ability to tailor the electronic properties of copper nanoparticles *in-situ* without the need for any post thermal processing. **Figure 3.10** presents the O K edge spectra both in the FY and TEY mode. The features for the copper tape are typical of CuO with a strong 1*s* to $3e_g$ transition (d^9) at 530.4 eV with respect to the spectra of copper tape the d^9 feature is absent or is masked in all the printed films. Though the peak at 532-533 eV character seems to be decreasing, it is not a signature of CuO reduction [167]because the contribution from surface carbon contaminants is dominant in this energy region. Regardless of the presence of surface contaminants, the variation in absorption of copper core levels is evident for tuning of the oxidation state of plasma printed copper film.

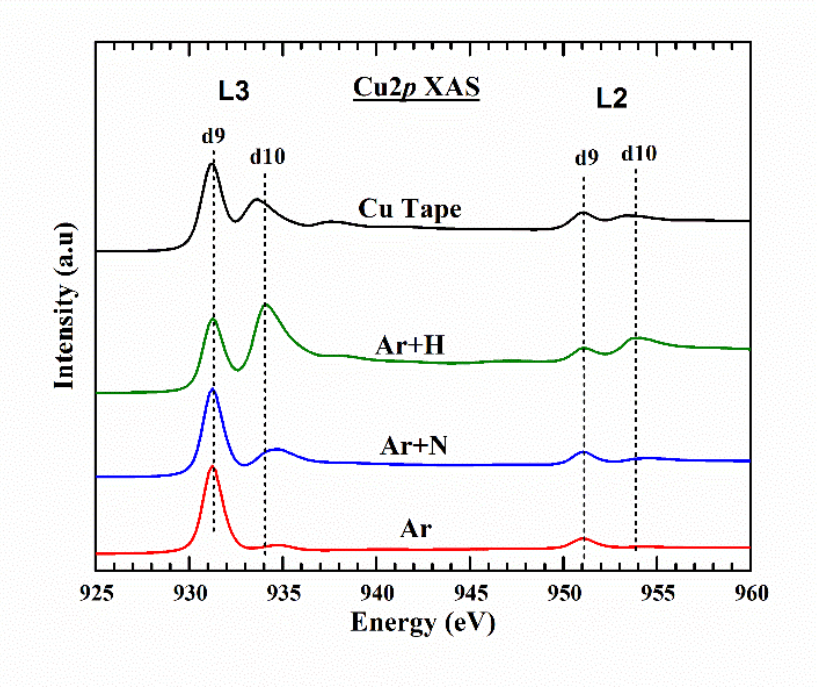

Figure 3.8 Cu $L_{2,3}$ -Edge XAS spectra of printed copper films in total electron yield (TEY) mode and a reference copper tape (no deposition). [N.B. refer to Attributions]

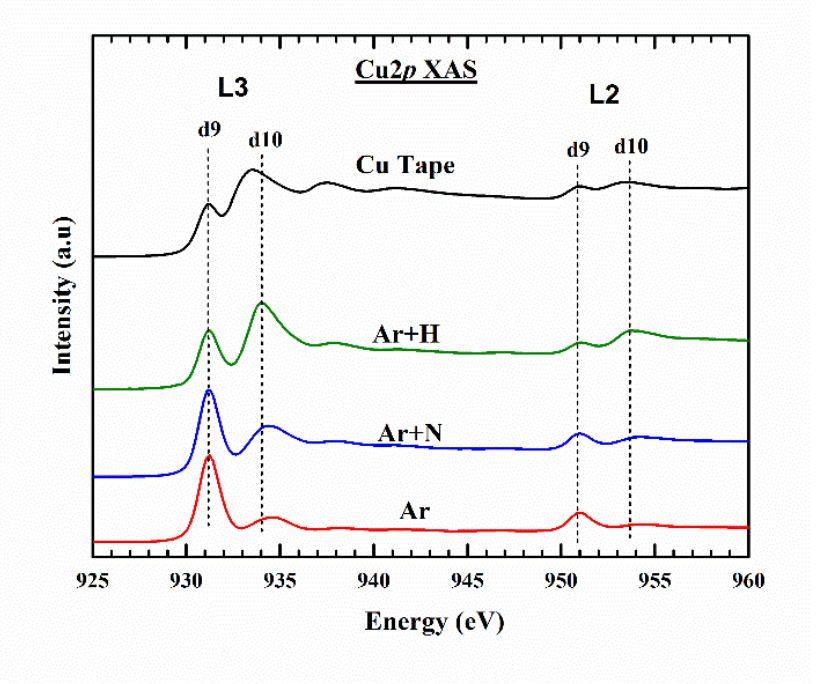

Figure 3.9 Cu $L_{2,3}$ - Edge XAS spectra of printed copper films in Florescence yield (FY) mode and a reference copper tape (no deposition). [N.B. refer to Attributions]

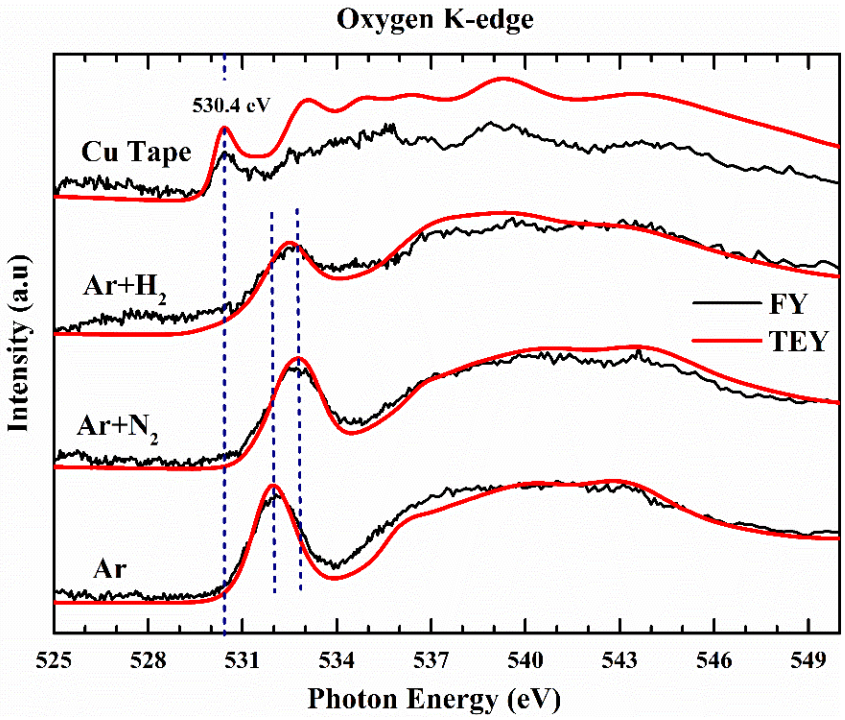

Figure 3.10 O K-Edge XAS spectra of printed copper films in Florescence yield (FY) mode and a reference copper tape (no deposition). [N.B. refer to Attributions]

3.7 Crystal structure and Raman Spectra

Raman spectroscopy is a powerful tool to depict the structural properties of nanoparticles. To understand the Raman spectra of the copper oxide films it is important to understand the crystallographic structure of this two-oxide species. As the vibrational properties of this materials are dependent on their crystal symmetry. CuO (tenorite or cupric oxide) and Cu_2O (cuprite or cuprous oxide) are the two thermodynamically stable oxides of copper.[168] The corresponding crystalline structure for CuO and Cu_2O are monoclinic and cubic respectively.[169]

The atomic arrangement for CuO belongs to the space group C_{2h}^{6} *(C2/c)* with four molecules in the crystallographic unit cell and two molecules per primitive cell. As shown in **Figure 3.11** each copper atom is coordinated to four oxygen atoms, situated at the corner

of a parallelogram. While each oxygen atom has four copper atoms as nearest neighbours in a distorted tetrahedral configuration. [170] The Bravais lattice for Cu_2O belongs to the space group (O_h^4 , $Pn\bar{3}m$). As shown in **Figure 3.12**, each Cu^+ ion is linearly coordinated with two equidistant O^{2-} ions while oxygen ion has four copper neighbours in a tetrahedral configuration.[171] For CuO, the primitive cell has 4 atoms resulting in (4×3) 12 vibrational modes. As per group theory, these 12 modes are divided into 3 acoustic modes and 9 optical modes. Of the optical modes, only three ($A_g + 2B_g$) modes are Raman active and the rest are IR-active. The cuprite structure results in 6 atoms per primitive cell and hence 18 vibrational modes. With 3 acoustic and 15 optical modes. Among the optical modes only one T_{2g} mode is Raman active. Thus, from group theory only one peak is expected in the Raman spectra of Cu_2O, corresponding to the T_{2g} mode. Debbichi *et al.* have reported a detailed theoretical and experimental study on the vibrational properties of this oxides.[172] According to them the Raman spectra of Cu_2O has several extra peaks rather than only one peak(T_{2g}). This is a contradiction to the theoretical prediction made by group theory calculations. This breakdown of selection rule has been reported by several other groups as well. The cause of this has been attributed to defects in the crystal, resonant Raman scattering and non-stochiometric configuration. [173–176]

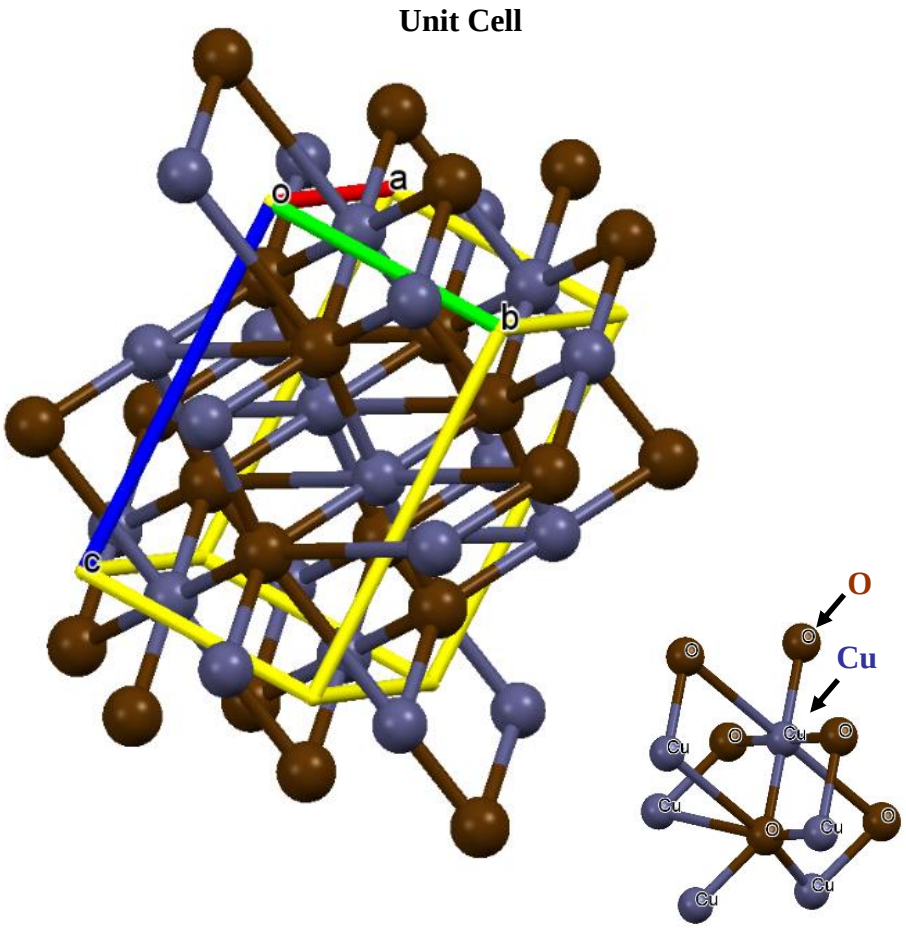

Figure 3.11 Unit cell of CuO and bond configuration of Cu-O in CuO. Drawn using the free software Mercury available from Cambridge Crystallographic Data Centre (CDCC). http://www.ccdc.cam.ac.uk/

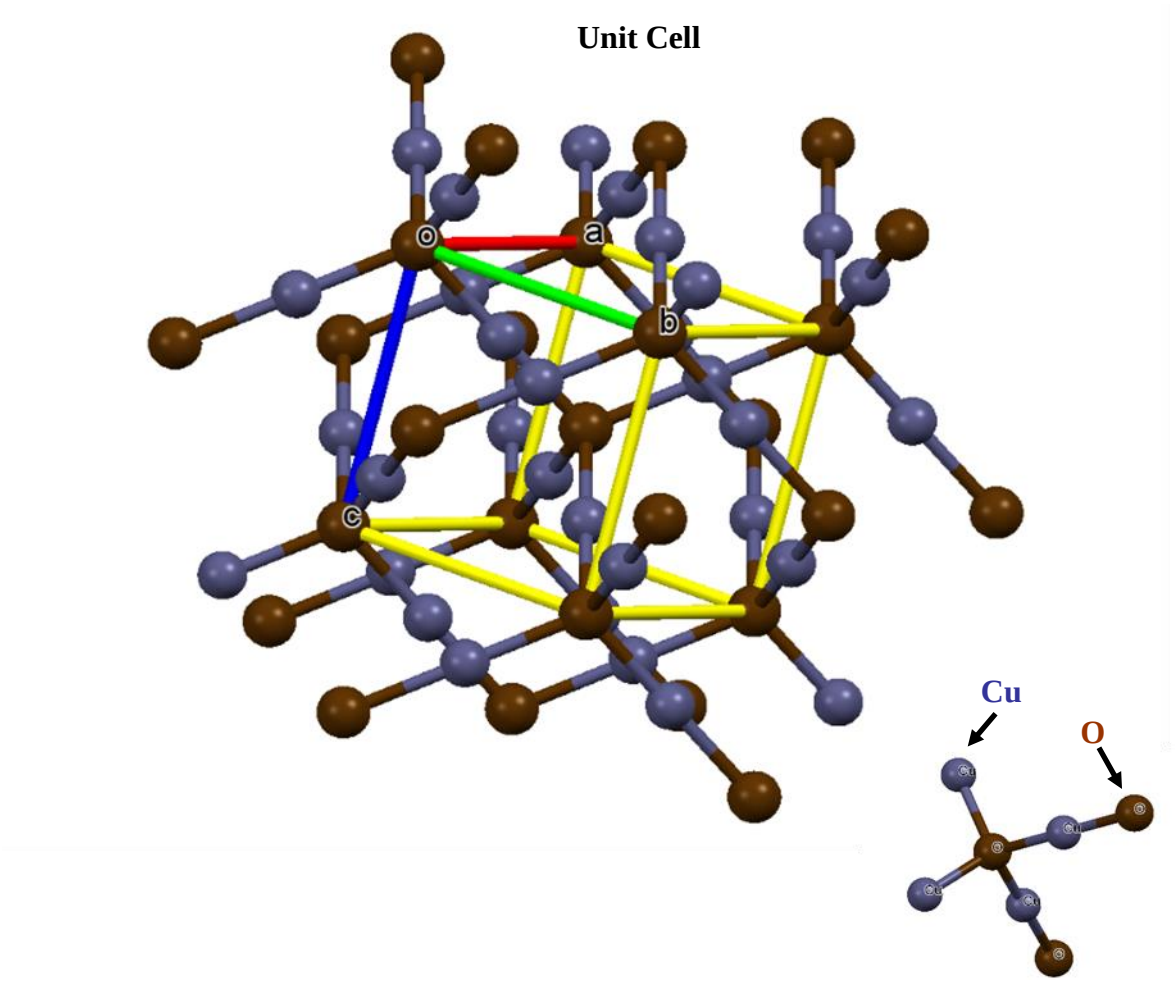

Figure 3.12 Unit cell of Cu_2O and bond configuration of Cu-O in Cu_2O. Drawn using the free software Mercury available from Cambridge Crystallographic Data Centre (CDCC). http://www.ccdc.cam.ac.uk/

	Cu_2O	**CuO**
Lattice Constant	4.2696 Å	a = 4.6837 Å b =3.4226 Å c = 5.1288 Å β = 99.54° α, γ = 90°
Space group	O_h^4 *or* $Pn\bar{3}m$	C_{2h}^6 *(C2/c)*
Cu-O bond length	1.849 Å	1.96 Å
O-O separation	3.68 Å	2.62 Å
Cu-Cu separation	3.012 Å	2.90 Å
Cell volume	$(77.833 \pm 0.055) \times 10^{-24}$ cm^3	81.08 $Å^3$
Formula weight	143.14	79.57
Density	5.749–6.140 g/cm^3	6.515 g/cm^3
Melting point	1235 °C	1201 °C

Table 3.2 Crystallographic properties of Cu_2O and CuO. [177]

Figure 3.13 shows the Raman spectra of the plasma jet printed samples already mentioned in the previous section. Spectra for all the three samples were calibrated with respect to the Si peak at 530.9 cm^{-1} (peak 3 in the figure). Raman spectra of argon printed sample shows the dominant presence of CuO phase Characterized by the peaks at 285, 335, 620 cm^{-1}. [178]. The peak at 285 cm^{-1} can be assigned to the A_g mode while the peaks at 335 and 620 cm^{-1} correspond to the B_g phonon modes of CuO crystal. But a presence of Cu_2O phase in small proportions is reflected by the weak peak around 218 cm^{-1}. This is one of the Raman forbidden modes for the Cu_2O state, which becomes active due to the breakdown of selection rules. The FY and TEY mode NEXAFS spectra also showed the strong presence of Cu^{2+} state in the Ar printed sample. In an article by Xu *et al*, upon annealing CuO nanocrystals the Raman peaks became sharper and showed blue shift. [178] They related this phenomenon to the increase in grain size of the nanoparticles. This effect is evident in **Figure 3.15**. Here after being exposed to plasma the nanoparticles fused together, resulting in increased grain size. The dependence of Raman spectra on the grain size is described briefly in the next paragraph. In comparison with the Ar printed samples the other two samples showed an increase in the intensity of the peak around 218 cm^{-1}. The peak being most intense for the Ar+H_2 printed sample. The blue shift for the A_{1g} mode of CuO may be due to the increased grain size resulting from the high temperature of the plasma. The peaks around 109, 146, 628 cm^{-1} along with the intense 218 cm^{-1} peak reflects to the existence of copper in Cu^+ oxidation state in bulk, Also proven from FY mode NEXAFS spectra [179] Optical active T_{2g} phonon mode for Cu_2O meant to be present around 517 cm^{-1} seems to be masked by the intense Si peak. This Raman spectroscopic study of the printed thin films provide a strong evidence of the stated *in-situ* reduction process and is in absolute agreement with our X-ray spectroscopic studies.

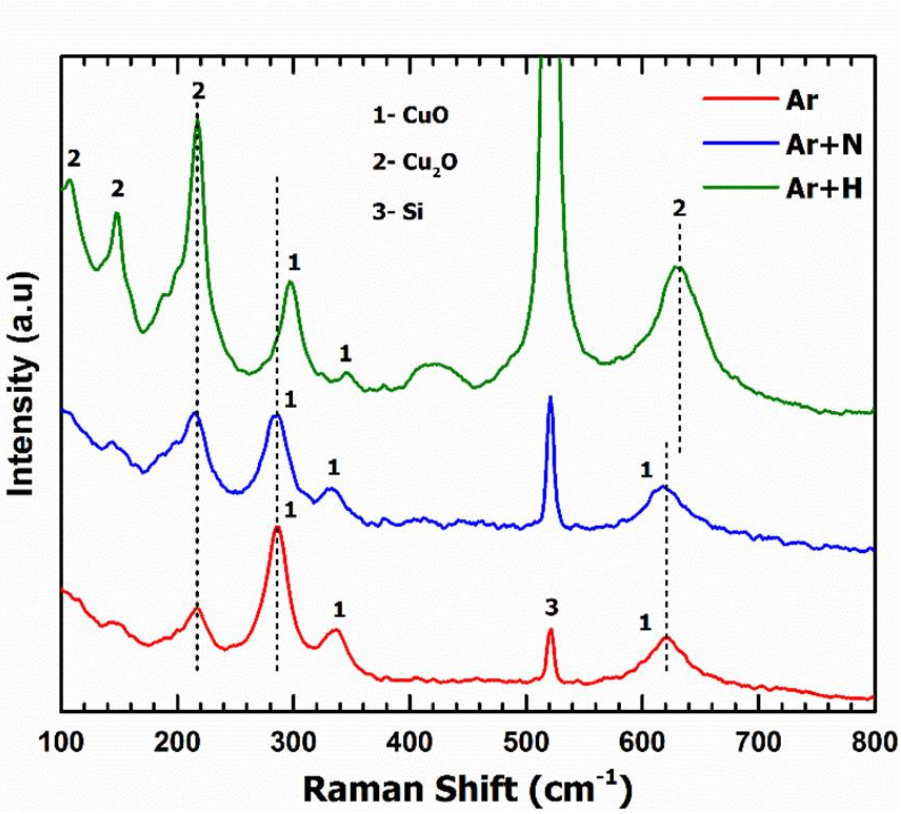

Figure 3.13 Raman spectra of plasma jet printed samples with Ar, Ar+N_2 and Ar+H_2 gas mixtures.

Dependence of Raman spectra on grain size, short description

For nanometre sized particles, phonon confinement plays a crucial role. This phenomenon leads to the apparent shift and broadening of the Raman peak. Based on Heisenberg's uncertainty principle for a spherical nanoparticle a relationship between the particle size and phonon position can be drawn as follows:

$$\Delta d \Delta k \geq \frac{\hbar^2}{4} \qquad \textbf{3.1}$$

Where d is the particle size, k is the phonon momentum and ħ is Planks constant. As the particle size decreases, the phonons get increasingly confined inside the particle dimensions resulting in a wider distribution of the phonon momenta. Meaning the fundamental selection rule of only the zone centre ($k \sim 0$) phonons being Raman active is relaxed allowing the contribution from phonons away from the Brillouin zone centre as well. From the law of conservation of momentum, the momentum distribution of the scattered phonons also gets broadened leading to the shift the Raman lines. On the other hand, the intensity of the Raman lines weighted over the entire Brillouin zone is given by:

$$\boldsymbol{I(\omega)} \int \frac{|\boldsymbol{C(0,k)}|^2}{[\,\boldsymbol{\omega - \omega(k)}]^2 + \left(\frac{\boldsymbol{\Gamma_0}}{\boldsymbol{2}}\right)^2} \boldsymbol{d^3 k} \qquad \textbf{3.2}$$

Where $\omega(k)$ is the phonon dispersion relation, Γ_0 is the FWHM of the Raman lines and $C(0,k)$ is the Fourier coefficient of the phonon confinement function and measures the $k \neq 0$ phonons participating in the scattering process.[180] The numerator in equation 3.2 bears a relation with the average size (d) of the nanocrystals as follows:

$$|C(0,k)|^2 = \exp\left(\frac{-k^2 d^2}{16\pi^2}\right) \qquad \textbf{3.3}$$

It is evident form equation 3.3 and 3.2 that with decreasing particle size the integral results in shift and broadening of the Raman peaks. However according to Reichardt *et al.* due to the strong covalent nature of the Cu-O interatomic forces there exist a considerable anisotropy in the dispersion curves for CuO lattice. [181] To remove this anisotropy a number of short range force constants are needed to be introduced into the rigid ion model. The detailed analysis of which is beyond the scope of this thesis.

3.8 I-V characteristics

Oxides of copper are known to be insulators. For large scale implementation of this plasma printing technology it needs to be proven that highly conductive films can be deposited from an insulating oxide ink. Experimental setup to carry out the measurements is shown in **Figure 3.14**. Metal clips were used as contact with the films. The resistance value at the metal and film contact was not taken into consideration, as the same setup was used for all measurements presented in this section. To start with, the copper colloidal solution was drop cast and aerosolized (without turning on the plasma) on the silicon wafer. Both these samples showed very low conductivity and their resistance values were in the order of ~ 100 MΩ. However, the same drop casted sample showed enhanced conductivity when post treated with a plasma jet for just 1 min. The conductivity of this plasma jet treated sample was rather higher than a four-hour annealed sample, where the annealing was carried out in a tube furnace at 500 °C in Ar/H reducing atmosphere. This is an indication of the advantage plasma jet processing offers over standard temperature dependent techniques.

Figure 3.15 shows the SEM images of drop casted and plasma treated samples. Plasma exposure resulted in partial melting of the nanoparticles creating electrical pathways and hence improving the conductivity. Collision of the high temperature electrons with nanoparticles may have created local hot spots. Also, the high energy free electrons and ions may have partially reduced CuO to metallic copper and the momentum they carry may have deformed the nanoparticles. Evident from these results, electron and ion temperature play a crucial role in defining the electronic properties of printed material in addition to gas temperature. The presence of energetic vacuum ultraviolet radiation at the effluent of the plasma jet cannot be negated as well. [182] Hwang *et al.* reported that Deep-UV sintering can result in dense packing of the printed nanoparticles.[183] When the same nanoparticle colloid was printed using Ar/H_2 plasma, it showed a significant rise in conductivity. Although the

resistance is of the order of 150 Ω, the rise in conductivity is indicative of the fact that *in-situ* process can be used to create conductive patterns from a rather insulating ink. When the printing process was extended with the flow of nanoparticles being cut off, the printed samples showed a drastic drop in resistance. In this case the sample was printed then treated in two cycles.

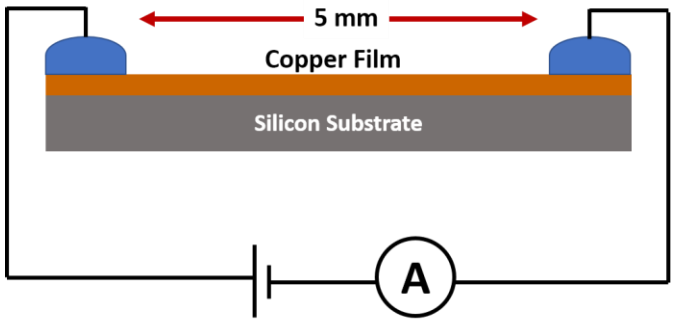

Figure 3.14 Schematic illustration of the I-V measurement setup. Metal clips were made as contacts with the film. Contact resistance between the clips and the film was not considered for these measurements.

Figure 3.18 shows that the extended plasma print technique results in a very dense network of copper nanoparticles ideal for various catalytic applications. **Figure 3.16** and **Figure 3.17** shows I-V characteristics of copper films prepared using different process parameters. The steep rise in conductance is shown in the inset of **Figure 3.17** . Thus, exposing the sample with the same plasma jet resulted in ~20 times decrease in resistance value (7 Ω). The increased concentration of metallic copper may be the principle cause of this phenomenon, which is in line with our XAS results. One may argue in favour of using other non-plasma printing processes and using the plasma jet for a post treatment of the samples for improving conductivity. But it needs to be realized that the formation of

conductive interconnects within the films (**Figure 3.15**) will be hard to achieve. It is evident that the conductance of the plasma printed and post treated samples are 80-100X than that of the drop-casted and post treated sample.

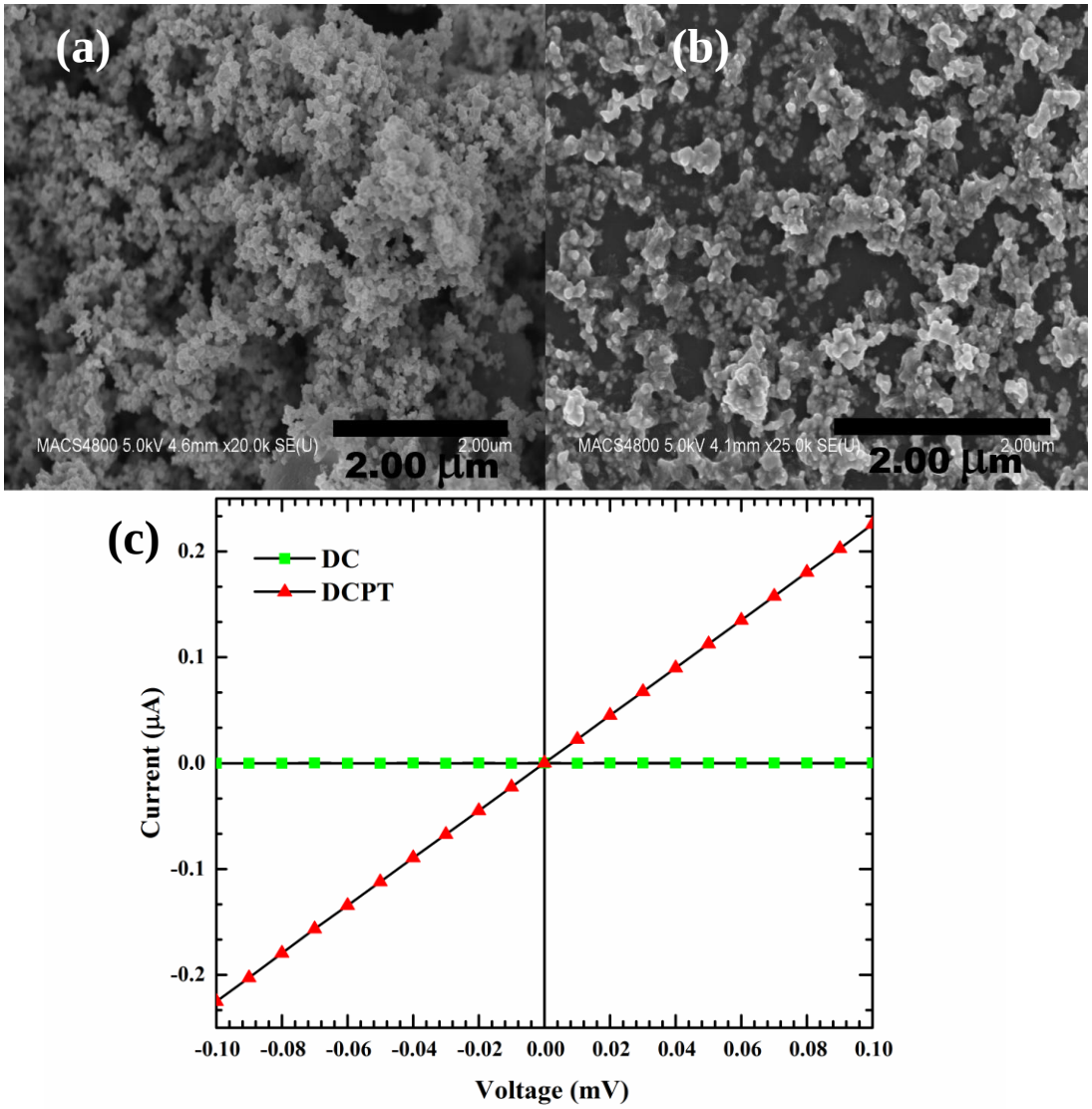

Figure 3.15 Sem image of (a) Copper ink Dropcasted on silicon, (b) treated with plasma (c) difference in I-V characteristic of this two samples. [N.B. refer to Attributions]

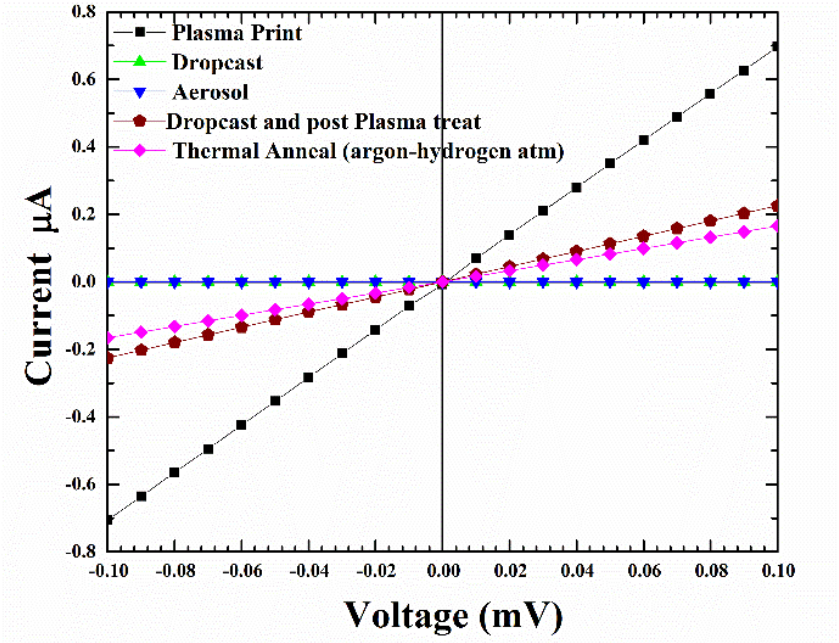

Figure 3.16 Comparison between the I-V characteristic of plasma printed thin films with thermal annealed and post plasma treated copper oxide thin films. [N.B. refer to Attributions]

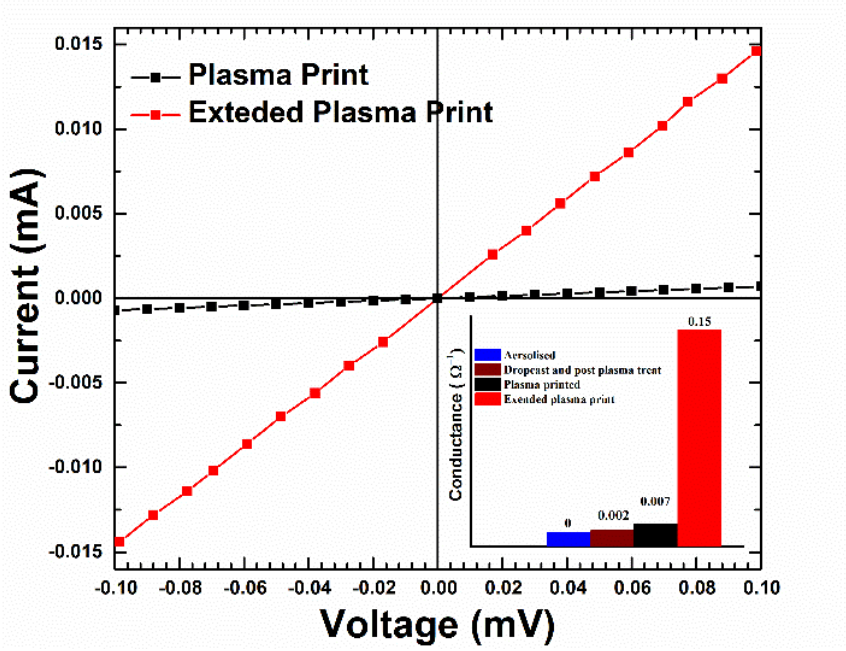

Figure 3.17 Decrease in resistance with "extended print'. Inset showing the conductance values of thin films produced via different process parameters**.** [N.B. refer to Attributions]

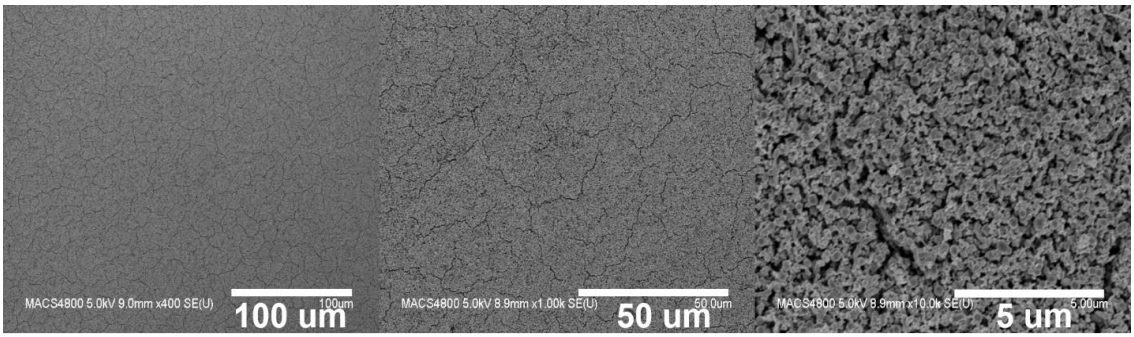

Figure 3.18 SEM images reveal the Uniform thin film after "extended plasma print".

3.9 Conclusion

With the increased need for flexible electronics, printing copper nanoparticles has attracted a lot of interest from the scientific community. One major issue in this process that needs to be addressed is the oxidation of copper in the ink stock. Most state-of-the-art printing technologies fail in this regard and must seek various post processing techniques to achieve desired results. This chapter presents a novel plasma based printing technology that can tune the electronic property of the printed material in-situ.

Here the proposed technique is deposition of copper oxide nano-particles using a DBD plasma jet operated with a gas mixture of He/Ar with N2 and H2. I-V measurements of the films confirm that a conductive pattern can be printed from a highly resistive oxide ink. With plasma treatment (printing and post treatment), the value of resistance for a deposited film could be decreased from 100 MΩ to as low as 7Ω. Raman measurements reveal that the high temperature associated with the plasma promotes grain growth. NEXAFS spectra both in TEY mode and FY mode reveal that the plasma induced reduction happens both at the bulk and at the surface. Additionally, the morphology and electronic structure of the printed films

can be controlled through the gas composition. SEM micrographs show that a highly porous film can be synthesised by increasing the concentration of hydrogen in the plasma. With further optimization of the dimensions of the printing nozzle there lies the possibility of achieving much higher resolution than reported here i.e. < 100 micron. The findings presented in this chapter confirm plasma jet printing as a promising technology for manufacturing of next-generation printed electronics.

Chapter 4. Work function tuning of graphene oxide using atmospheric pressure plasma jet

A significant amount of research has been performed on graphene during the last decade. This is driven by the realization of the immense capabilities possessed by this wonder material. Applications already recognized ranges from ultrafast and flexible electronics to optoelectronic devices, super-capacitors, water remediation, DNA attachment, photocatalysis and many more. To achieve these pathways, functionalization of graphene and its oxide plays a crucial role. In this work, functionalization of graphene oxide using atmospheric pressure plasma jet (APPJ) with He and N_2 gas mixture is proposed. It is found that APPJ functionalization can be a potential alternative to conventional techniques for tuning the electronic properties of GO. XPS and NEXAFS studies show that the excited nitrogen species in plasma induces localized changes in bonding configuration of GO. This in turn effects the work function of the graphene oxide films, evident from the Kelvin probe measurements.

4.1 Introduction

Graphene, since its discovery in 2004 has attracted enormous interest due to its physical and chemical properties, and applications.[25] Graphene oxide (GO) has emerged as an attractive alternative to graphene due to low cost, large scale production and solution process-ability. GO is prepared by oxidative exfoliation of graphite.[184] Due to the presence of polar oxygen functional groups GO is highly hydrophilic and is easily dispersible in water and many other organic solvents. These, oxygen containing functional groups play a crucial role in defining its optical and electronic properties.[36] The basal plane of GO is decorated with hydroxyl and epoxy functional groups while carboxyl, carbonyl and phenol groups are attached to the edges of graphene sheet.[36] The presence of these functional groups is critical in determining the electronic properties of graphene oxide. The work function is a fundamental electronic property of a material and can be used to interpret the relative position of the Fermi level.[185] The work function defined as the energy required to remove an electron from the highest occupied level in the Fermi distribution of a solid to vacuum.

For efficient transport of electron or hole in a heterojunction device, work function of the materials plays a crucial role. Since, work function determines how the bands will align at the contact.

Recently there has been an increased interest in applications of GO for interfacial layers [186,187] and transparent electrode materials in optoelectronic devices [33,37] e.g. liquid crystal displays (LCDs), organic light emitting diodes (OLEDs), touch screens, and Dye-Sensitized Solar Cells (DSSCs). Tuning the work function of GO is key to achieving high efficiency of these devices. The most common methods to alter the work function of GO are by reduction via thermal, chemical and electrochemical processes.[188] Molecular dynamics and density functional theory calculations by Kumar *et al.* [69] provided a detailed insight into the impact of various oxygen functional groups on the work function of reduced graphene oxide (rGO). According to them by altering the composition of oxygen-containing functional groups the work function of rGO can be tuned up to ~ 2.5 eV. Sygellou *et al.* [189] studied the variation in work function of GO via three different reduction processes. They found the work function decreases by ~1eV between GO and reduced GO. Other approaches to tailor the work function of GO include Au-ion incorporation [190], UV irradiation [191] and exposure to soft x-rays [192]. In the case of *p*-channel in organic field-effect transistors (OFETs) [193] efficient injection of holes is achieved by matching the work function of electrodes with the highest occupied molecular orbital (HOMO) level of the organic semiconductor. For LEDs efficient electron injection is achieved by matching the work function with lowest unoccupied molecular orbital (LUMO) of the active layer. The ability to tune the work function makes GO a suitable candidate for use as charge injection layers for both as electron and hole transport layers.[186]

Doping GO with nitrogen has been a widely used strategy to improve its properties as catalysts for oxygen reduction reaction, biosensors, ultracapacitors and electrodes in lithium

ion batteries.[76] Due to its comparable atomic radius and five valence electrons, nitrogen is considered as the ideal element for substituting carbon atoms in GO. Out of the various techniques used so far, functionalising with plasma is the most promising one as plasma processing doesn't involve chemical precursors and by-products. A recent review by Dey *et al.* focuses on the advantages of plasma over other functionalisation techniques. [66]Atmospheric pressure plasma jets (APPJs) deliver charged particles, neutral metastable species, radicals and radiation in the UV and visible regions conveniently in a processing plume.[194] Liu *et al.* treated graphene counter electrodes, made via screen printing process with atmospheric pressure plasma operated at 700 watts. They found that reduced graphene oxide (rGO) counter electrodes in DSSCs when treated in this way showed power conversion efficiencies of 5.19%, comparable to those of furnace calcined counter electrode while requiring a much shorter process time.[82] Note this process is not a low temperature process as the plasma is an arc discharge. Other attempts include APPJ treatment of graphene to increase hydrophilicity [54] and introduction of bandgap at an input power of 150 W.[84] In this study it will be shown that APPJ can be used as tool for controlled doping of graphene oxide. For us the APPJ is non-equilibrium in nature and is operated at 4watt power. This low power associated with the plasma source, provides an additional advantage over other plasma techniques reported so far.

4.2 Experimental details

Synthesis of GO

The graphene oxide was prepared following Hummers method. Hummer method involves oxidative exfoliation of graphite. During reaction, the strong oxidative species intercalate between the graphite layers, increasing the interlayer spacing (from 0.34 nm to ~ 1.08 nm). The loosely bound layers are then delaminated using ultrasonication to achieve

GO. The steps involved in this process are shown in **Figure 4.1** and explained in **Table 4.1**. To produce films,10 mg of GO was ultra-sonicated in 100 ml of distilled water for one hour. This solution was centrifuged at 8000 RPM for 10 minutes and the supernatant was drop casted on silicon substrate of dimension approx. 5mm × 5mm. The substrates were then heated at 80 ºC to remove excess water.

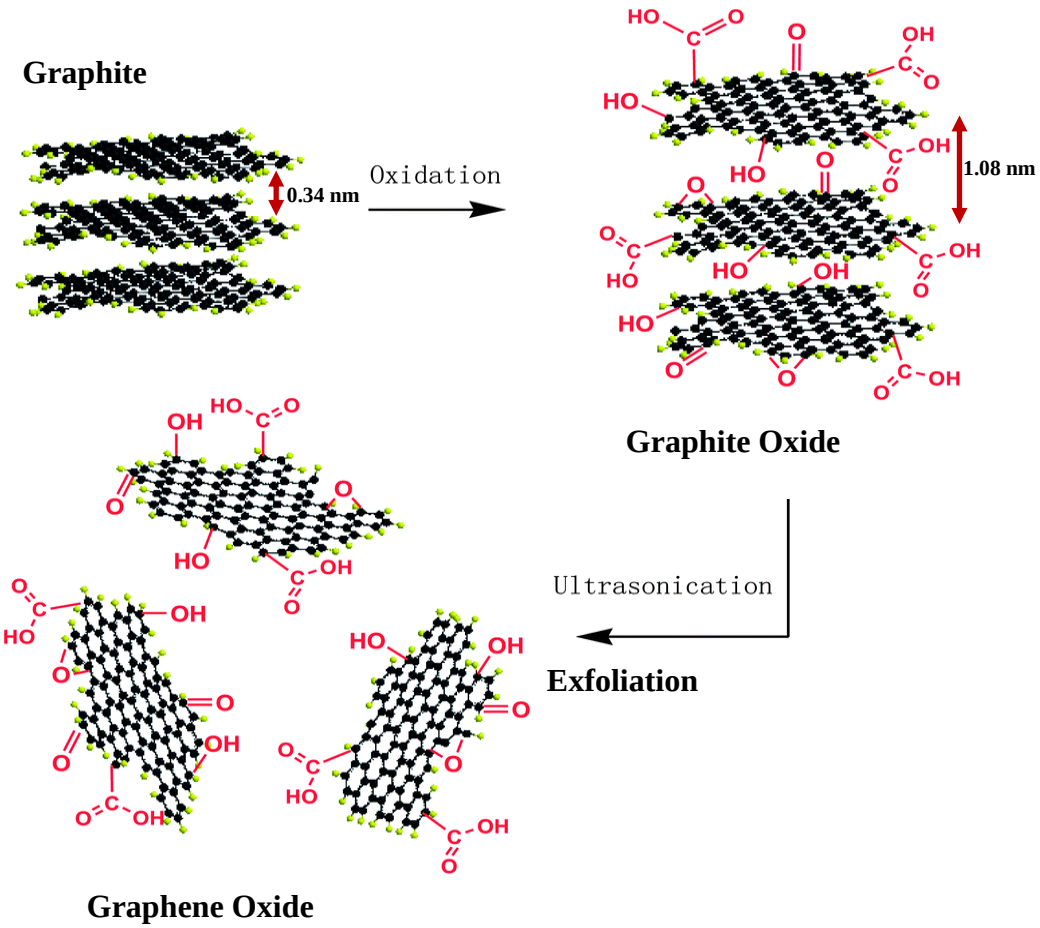

Figure 4.1 Schematics of graphene oxide synthesis involving Hummers method. Graphite flakes are oxidatively expanded to graphite oxide and then ultrasonicated to exfoliate graphene oxide. Adapted from Fu *et al.* [195]

Reactions involved [196,197]

$$KMnO_4 + 3H_2SO_4 \rightarrow K^+ + MnO_3^+ + H_3O^+ + 3HSO_4^- \quad 4.1$$

$$MnO_3^+ + MnO_4^- \rightarrow Mn_2O_7 \quad 4.2$$

$$Mn_2O_7 + 2H_2SO_4 + C(graphite) \rightarrow (C\text{-}O\text{-}C,\ C\text{-}OH,\ COOH) + Mn_2O_5 + 2H_2O + 2SO_4^{2-} \quad 4.3$$

Step	Process	Comments
1	3 g graphite flakes + 1.5 g $NaNO_3$ + 100 ml 98% H_2SO_4	Stirred at 0 °C in an ice bath
2	9 g of $KMnO_4$ added to suspension	Vigorous stirring
3	Ice bath removed	Temperature maintained at 30 ± 3 °C for 30 mins.
4	138 ml of DI water added slowly	Violent effervescence, temperature rises to 98 °C.
5	After 15 mins, 200 ml DI added	To Dilute
6	30 ml of 30% H_2O_2 added	Reduces the residual permanganate to soluble manganese sulfate.
7	Filtered and washed	Till pH reaches ~7 (Neutral)
8	Centrifuged at 8000 rpm for 10 min	To extract GO

Table 4.1 Process steps for the synthesis of graphene oxide (GO).

Functionalization of GO

Plasma treatment of the synthesised GO was the final step. Experimental setup to carry out the functionalization process is represented schematically in **Figure 4.2**. A gas mixture of helium and nitrogen was used to ignite the plasma. Design and operating principle of the plasma jet is described in the next section (**section 4.3**). GO films were kept at a minimum distance of 5 mm to avoid arcing between the sample and electrodes. Flow rates were optimised to achieve the least input power, 4 watts in this case. The GO films were then exposed to APPJ for 5 sec, 10 sec, 20 sec, 30 sec, 1 min, 2 min and 3 mins. This process yielded 8 types of specimen including the untreated material. To understand the effect of plasma, the functionalized films were analysed by: NEXAFS, XPS, AFM and KPFM measurements (refer to chapter 2 for details of these techniques). The samples prepared in April 2016 at the OU were then transported in a polymer box to Stanford for X-ray spectroscopic studies during May 2016 beamtime.

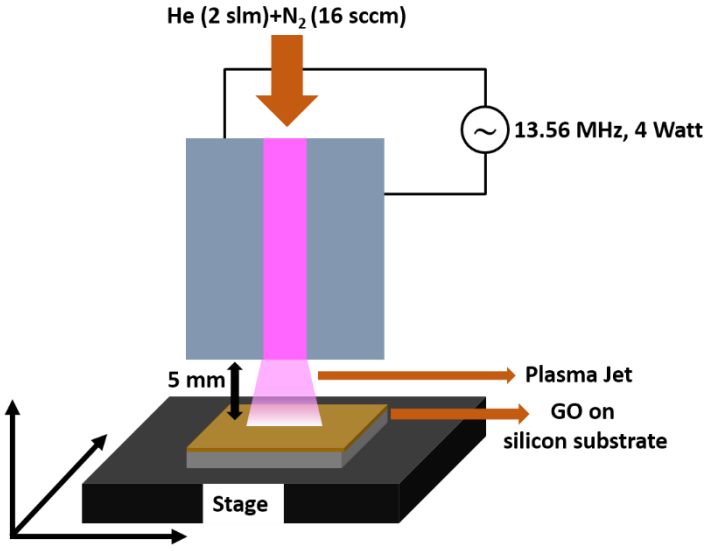

Figure 4.2 Schematics of the experimental setup for GO treatment using APPJ.

Characterization of functionalized GO

To understand the changes in electronic and chemical structure of the GO films upon plasma functionalization, X-ray spectroscopies (XPS and NEXAFS) were carried out at beamline 8-2 at the Stanford Synchrotron Radiation Lightsource (SSRL).[147] The incoming flux (I_0) was measured using a gold grid placed in the beam path upstream of the chamber and was used to normalize the spectra to avoid any artefact due to beam instability and monochromator absorption features. All samples were mounted on an aluminium stick using conductive carbon tape and transferred to the main chamber via load lock, both the chambers were under ultra-high vacuum. ($< 1 \times 10^{-8}$ Torr).

NEXAFS spectroscopy is a powerful atom-specific tool to probe the local geometric and electronic structure of carbon related materials. NEXAFS spectra correspond to transitions from core level to unoccupied or partially occupied density of states in the electronic structure and provides a unique fingerprint of local structure. For nitrogen-functionalized graphene structures where deconvolution of XPS features is ambiguous, NEXAFS becomes effective in distinguishing between different bonding configurations.[198] Carbon, oxygen and nitrogen K-edge NEXAFS spectra showing 1s–π* and 1s–σ* transitions were taken in Total electron yield (TEY) mode for GO and functionalized GO samples. To interpret the NEXAFS data, first a linear background was subtracted from the region before carbon absorption edge. Then the subtracted spectra were normalized in the post continuum region to have "one unit" in the background signal at 330 eV, following the protocols of Banerjee *et al*.[198] C K-edge spectra were calibrated to the exciton feature of HOPG at 291.65 eV and O K-edge spectra were calibrated to oxide dip from the gold mesh (531.2 eV).

XPS data analysis was performed with Casa XPS software using a Shirley background subtraction.[199] A combination of Gaussian (50%) and Lorentzian (50%) line shapes functions were used to fit the core level spectra except HOPG. Preferably to give equal

weightage to instrumental broadening (Gaussian) and intrinsic lifetime broadening of the core holes (Lorentzian).

Scanning Kelvin probe microscopy (SKPM) measurements were carried out to realize changes in work function of the GO films with plasma functionalization. The measurements were performed using Asylum research MFP-3D instrument. Surface potential measurements were performed with Pt-Ir coated silicon probes (PPP-EFM-10, Nanosensors) with force constant of 2.8 N/m. The tip was biased at +3 V with a drive amplitude of 300 mV. The image parameters were set at scan size of 10 µm by 10 µm, scan rate 1 Hz, 512 points and lines. In SKPM the instrument detects the surface potential (SP) as the work function difference between the tip and the sample surface i.e. SP = $\Phi_{Tip} - \Phi_{Sample}$. To calibrate the work function of the Pt-Ir tip, sputter cleaned polycrystalline silver was used. For silver SP was measured to be 0.29 mV. Considering for polycrystalline silver Φ_{Silver} = 4.26 eV, Φ_{Tip} can be calculated to be ~ 4.55 eV.

4.3 Radio-Frequency atmospheric pressure plasma jet

The atmospheric pressure plasma jet used for functionalization of graphene oxide films is shown in**Figure 4.3.** Plasma is ignited by applying radio frequency (RF) power between two stainless steel electrodes through a series LC circuit. The LC circuit is chosen to have a resonance frequency of 13.56 MHz. In this case the circuit consists of a tuneable capacitor (C_{ext} = 2–22 pF) and an inductor (L = 16.5µH, Micrometals T68-6 core).[200] When the applied RF frequency matches to that of the LC circuit, the voltage drop across the electrodes gets amplified (resonance) to initiate the discharge. At resonance, the voltage across the electrodes has been found to be 100 times that of the input voltage. But with an active discharge between the electrodes, this value drops by a factor of 2 due to the power dissipated in the discharge. In actual practice when the plasma is on, the discharge gap also

needs to be considered and is to be added to the series LC circuit as shown in **Figure 4.4**. To account for any shift in the resonance frequency, drive frequency of the signal generator is tuned accordingly to achieve the desired resonance.

With helium flowing between the electrodes at 2 standard litres per minute (slm), discharge could be generated for a power as low as 1 watt. However, when nitrogen or oxygen (@ 1% of He) is added to the system, the minimum power increases to 4 watts to sustain the discharge. Which is significantly less than the reported plasma jet sources for nanomaterial functionalization. [66]

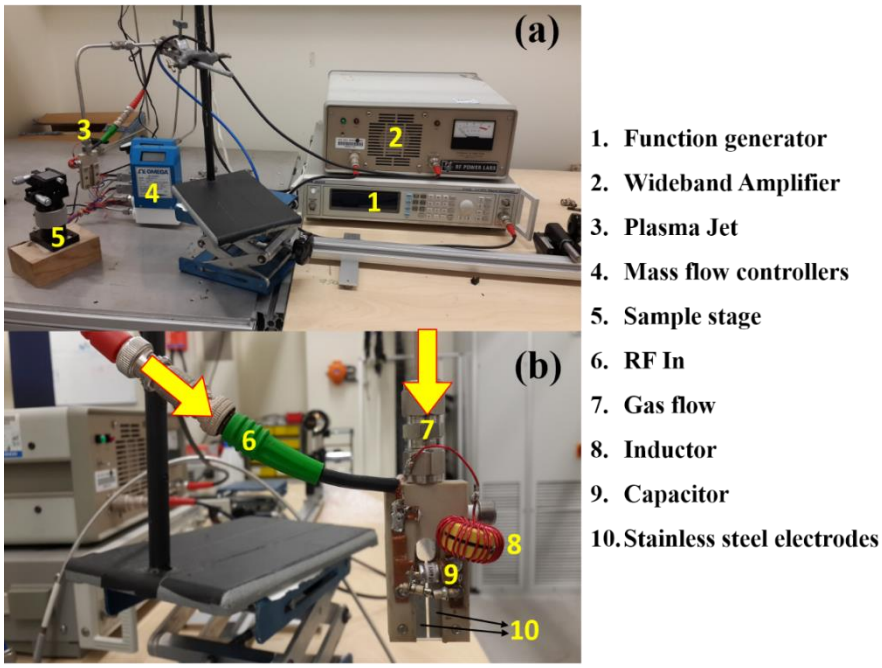

Figure 4.3 Schematics of the APPJ setup.

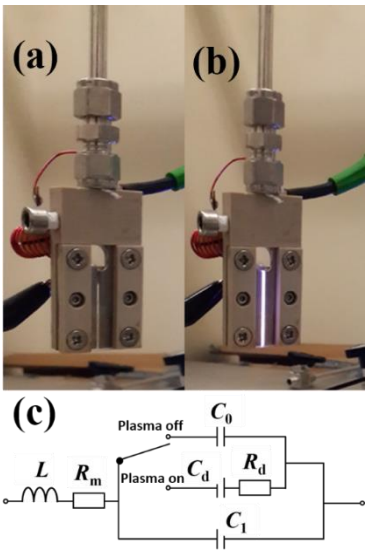

Figure 4.4 Equivalent electrical circuit (c) of the device with (a) plasma on and (b) plasma off conditions.

4.4 Optical spectroscopy of APPJ

The micro atmospheric pressure plasma jet (μAPPJ) used for functionalization has been developed by Marinov *et al.* [200] The rf plasma of He/N_2 gas mixture was generated at 13.56 MHz at an constant rf. The μAPPJ was based on a series LC resonance with the discharge gap being a part of the resonant circuit. With an applied rf power the voltage across the discharge gap is amplified at resonance, enabling the ignition of the plasma. A power of 4 watt was used to ignite the admixture of He and N_2. He and N_2 were kept at a constant flow rate of 2 standard liters per minute (slm) and 12 standard cubic centimetres per minute (sccm) respectively using mass flow controllers throughout the functionalization process. In this section, optical emission spectroscopy of the plasma is presented. The nature of the plasma depends on the gas phase composition i.e. the excited atoms, ions and molecules. **Figure 4.5** presents the Optical Emission Spectra (OES) of the plasma. The emission spectra reveal a variety of nitrogen emission peaks with in the wavelength range of 200 nm to 880

nm. In the UV region (Figure 4.5 (a)), several lines are observed between 316 nm to 406 nm corresponding to the second positive ($C^3\Pi_u \rightarrow B^3\Pi_g$) molecular series of neutral N_2 molecules. Additional peak at peaks at 391 nm and 427 nm correspond to the first-negative transitions of N_2^+ molecular ions. There also exist strong peaks in the region of 215 nm to 271 nm originating from the NO(γ) system ($A^2\Sigma^+ \rightarrow X^2\Pi$), representative of the presence of oxygen in the afterglow. Note that the plasma is not just confined within the electrode for APPJ, so oxygen incorporation is highly likely A prominent line at 308 nm corresponding to hydroxide(OH) emission is visible in the spectrum. which can be attributed to the impurities in the gas supply. The visible region is dominated by the first positive molecular series ($B^3\Pi_g \rightarrow A^3\Sigma^+$).[201,202] The helium line at 706 nm (Figure 4.5 (b)) in the nitrogen enriched He flow is strongly suppressed with respect to pure He plasma. This is mainly due to the "*quenching"* of excited helium atoms on collision with nitrogen molecules resulting in excited nitrogen species in the plasma. [203] As a result, nitrogen becomes the dominant species. The following equation presents the interaction between the helium atoms and molecules with the nitrogen molecules:

$$He^* + He^* \rightarrow He + He^+ + e^- \quad \textbf{4.4}$$

$$He^* (n = 3) + He \rightarrow He_2^+ + e^- \quad \textbf{4.5}$$

After N_2 addition:

$$He^* + N_2 \rightarrow He + N_2^+ + e^- \quad \textbf{4.6}$$

$$He_2\left(^3\Sigma_u^+\right) + N_2 \rightarrow He + He + N_2^+ + e^- \quad \textbf{4.7}$$

$$He_2^+ + N_2 \rightarrow He + He + N_2^+ \quad \textbf{4.8}$$

$$He^+ + 3N_2 \rightarrow He + 2N + 2N_2^+ + 0.3\ eV \quad \textbf{4.9}$$

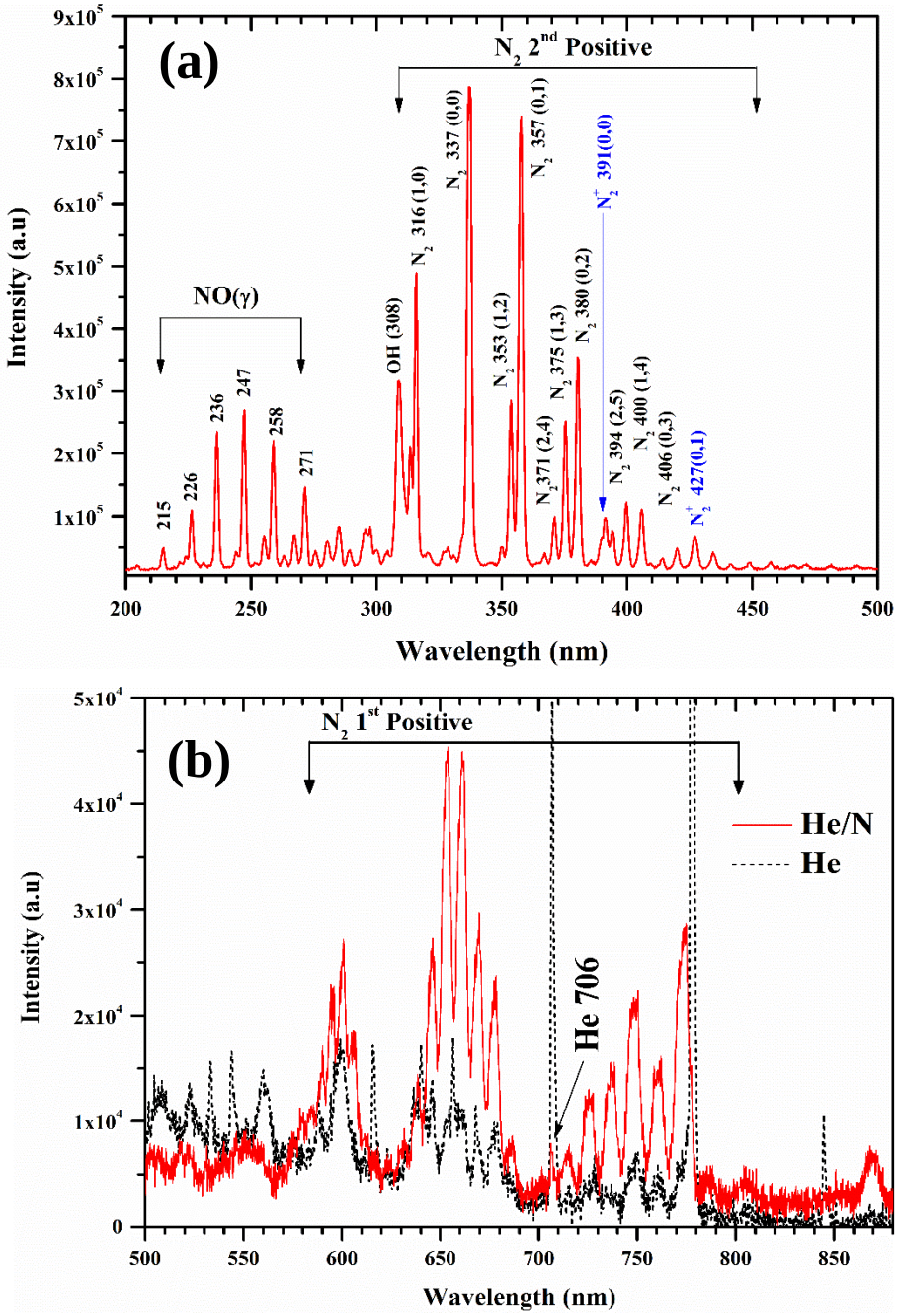

Figure 4.5 Optical emission spectra of He + N_2 Plasma, (a) in UV region (b) in visible region.

4.5 X-ray Photoelectron Spectroscopy (XPS) of functionalized graphene oxide films.

XPS is a surface analysis technique and has been used here to gain insight into the changes in atomic concentration, local chemical environment and co-ordination geometry of the GO thin films with plasma functionalization. By careful analysis of the core level spectra (C1*s*, O1*s*, N1*s*) it will be possible to understand the mechanism behind the changes in chemical environment. For nitrogen doped into graphitic lattice, there are multiple possible bonding configurations. Each of these bonding configurations effect the electronic structure of GO differently. The three most common configurations as shown in **Figure 4.6** are graphitic, pyridinic and pyrrolic nitrogen. [76] Graphitic N also referred to as Quaternary N is placed in the hexagonal lattice with three carbon neighbours. The two-fold coordinated state is called the pyridinic whereas the nitrogen bonded into the five-membered heterocyclic ring is known as pyrrolic N. Of these bonding types, graphitic and pyridinic N are sp^2 hybridized and pyrrolic N is sp^3 hybridized. In addition to these, N oxides of pyridinic N have also been reported. [204] Pyridine N donates one *p* electron to the aromatic π system while pyrrolic N contributes two electrons. Pyridinic N is highly reactive and is stable only under high vacuum conditions. Pyridinic N hasn't been of much interest as it fails in enhancing the properties of GO.[205] Graphitic N is the most effective for promoting the applications of N doped GO in oxygen reduction reaction (ORR),[204] sensor [78], water oxidation [206] and electromagnetic devices.[207] On the other hand Pyrrolic N have been found to significantly enhance the Li storage capability in lithium ion batteries.[208] As the binding energy of Li ion to pyrrole nitrogen is higher (1.3 eV) compared with quaternary nitrogen sites (0.95 eV).Though these bonding environments cannot be resolved directly in the carbon spectra, but can be extracted by deconvolving the nitrogen spectra revealing individual contributions.(within ±0.1 eV of binding energy)

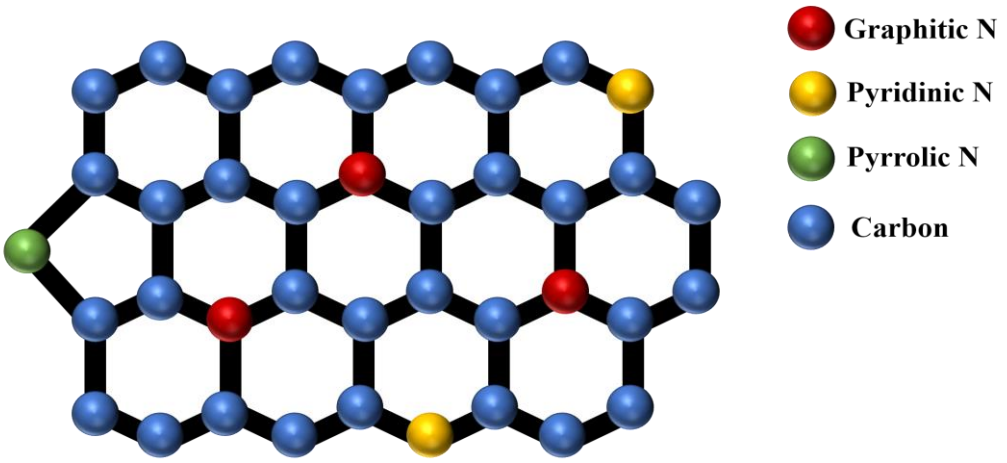

Figure 4.6 Structure of nitrogen doped Graphene. [76]

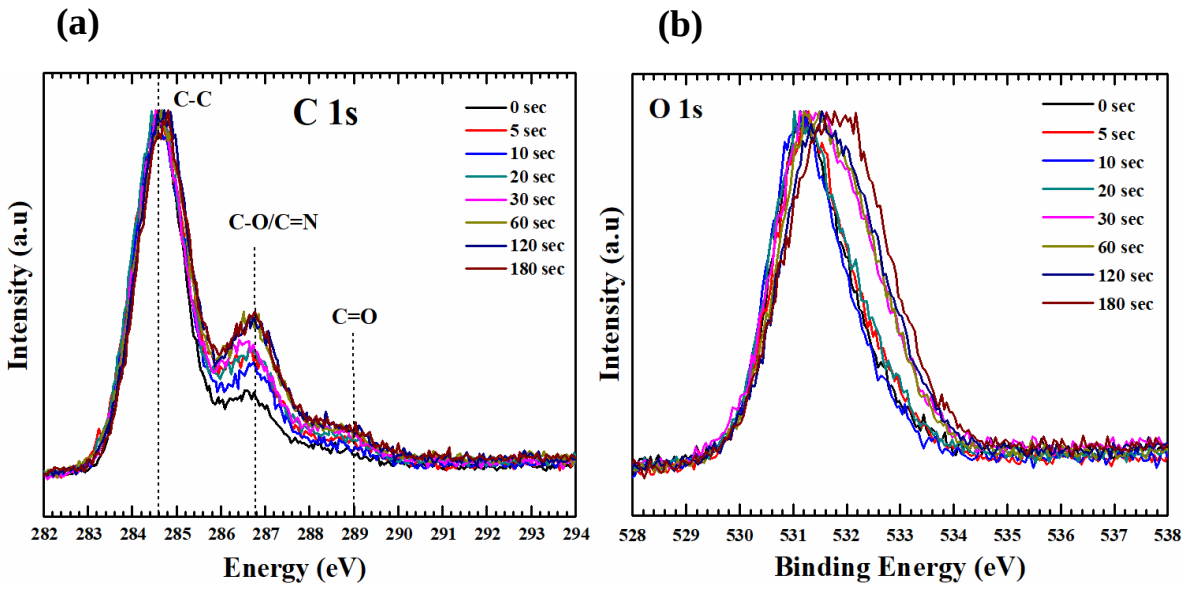

Figure 4.7 Core level photoelectron spectra for (a) carbon, (b) oxygen. Spectra from individual GO films are overlaid upon each other to recognize the effect of plasma functionalization.

Core level spectra of GO and functionalized GO

The core level photoelectron spectra for carbon and oxygen is presented in **Figure 4.7**. Spectra from individual functionalized states are overlaid to discern the effect of time varying plasma exposure on the GO films. All the spectra were energy calibrated to gold core lines at 84 eV (Au $4f_{7/2}$) and C1s of HOPG at 284.5 eV. The spectra for individual samples were aligned with respect to the Si 2*p* peak of SiO_2 at 103 eV, as expected from the SiO_2 substrate.[209] **Figure 4.7** (a) and (b) show clear variation in the line-shape of the C1*s* and O1*s* spectra as function of plasma exposure . For the C1*s* spectrum, the main peak is located around 284.6 ± 0.1 eV, which is typical for C-C in aromatic ring. The regions between 286-288 eV and 288-290 eV corresponds to the contributions from carbon singly bonded and doubly bonded to oxygen respectively.[210,211] These observations are consistent with the Lerf–Klinowski model of graphene oxide.[212] According to this model the basal planes of graphene is decorated with epoxide (C-O-C) and hydroxyl (C-OH) moieties, and the edges sites are decorated with carboxylic acid (O-C=O), quinoidal, ketone, and lactone (C=O) groups. For oxygen spectra, the peak width (FWHM) increases considerably with plasma functionalization i.e.1.5 eV for pristine GO to 2.3 eV for GO with 180 seconds exposure. This is due to the change in bonding environment of oxygen resulting from the addition of higher binding components in the spectra.

The contribution from different bonding environments of carbon in the graphitic structure is deconvolved using peak fitting, as shown in **Figure 4.8 .** Due to the semi-metallic nature of HOPG the carbon spectrum was fitted with asymmetric Doniach-Sunjic line shape. This function gives an asymptotic nature to the Doniach-Sunjic line shape function.[213] While the spectra related to GO were fitted with a combined Gaussian and Lorentzian line shape functions. **Table 4.2** presents the binding energy value along with the FWHM and percentage composition of C-C, C-O, C=O components that have been used to fit the C1*s*

spectra of GO and the functionalized GO films.

It has been reported that the disorder induced carbon appears at a binding energy of 0.5 eV above the graphitic sp^2 carbon (284.5 eV). [84] However, after considering the full width at half maxima (FWHM) of HOPG (0.72 eV) and that of the as synthesized GO (1.25 eV), it will not be a good approximation to deconvolve the C-C peak of GO into two peaks. But the absolute value of FWHM should be good measure of the increase/decrease in sp^3 carbon concentration. With increased exposure to plasma this peak broadens from 1.25 eV (0 sec) to 1.39 eV (180 sec) as shown in **Figure 4.9**. This broadening can be attributed to the increase in concentration of nitrogen. The nitrogen dopants are known to increase disorder in the sp^2 framework. [214] Increase in C=O functionalities with time (exposure to plasma) can be attributed to the increased concentration of defects. These defects originate from the impact of high energy ionic species present in the plasma. As already mentioned carbonyl / carboxyl groups found at the edge sites and dangling bonds (formed by C-C bond breaking) are more susceptible to the formation of C=O species. According to Bagri *et al.* [215] defects formed by breaking of C-C bonds in the basal plane are always decorated by the carbonyl (C=O) groups. Once the C-C bond breaks, to compensate for the electron valence C=O (double bond) is formed at that site.[215] The fitted spectra showed at consistent trail for both this functionalities. As the C-C concentration decreased from 73 to 68%, C=O increased from 4 to 9%. Despite this interplay between C-C and C=O, the concentration of single bonded species showed a small increase 22 to 24 %. However, the FWHM for this state decreased by 0.5 eV (2 eV to 1.55 eV). This apparent reduction in FWHM resembles the dominance of either of C-OH or C-O-C with extended exposure to plasma. Previous reports suggest that carbonyl groups are formed by rearrangements of epoxy groups. [216] As epoxy groups in graphene leads to a non-planar sp^3 bonding configuration and creates significant strain on the neighbouring C-C bonds while C=O bonds are sp^2 hybridized and strain free. [216] Rani *et al.* [210] found that upon oxygen plasma treatment of GO the carbonyl components

increased rather than epoxide. They inferred that the thermal energy of plasma favors clustering of the sp^2 domains and oxygen atoms attach randomly, converting sp^2 bonds to sp^3, and as the plasma exposure increased the epoxides rearranged to form carbonyls. [210] Due to low temperature associated with the plasma jet, effect of temperature can be neglected in this experiment. Nevertheless, the kinetic energy of the ions, dissociated upon impact may provide the necessary energy required for the bond rearrangements.

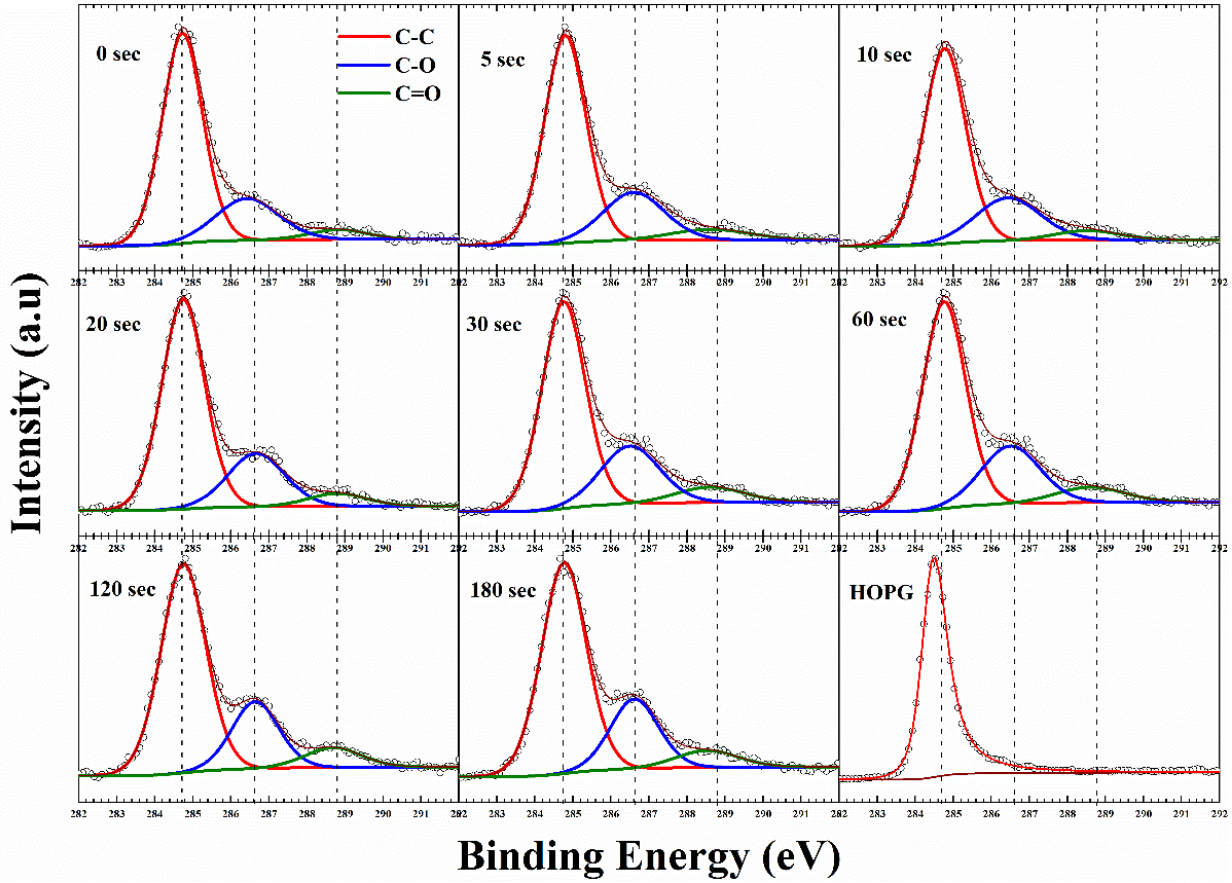

Figure 4.8 Fitted C1*s* spectra of GO, functionalized GO and HOPG. The peak intensities of all spectra have been normalized to one unit. C-C represents the carbon-carbon bonds, C-O represent carbon single bonded to oxygen and C=O represent carbon double bonded to oxygen.

GO sample	component	% concentration	FWHM
0 sec	C-C	73.0	1.25
	C-O	4.7	1.80
	C=O	22.3	1.90
5 sec	C-C	69.2	1.28
	C-O	7.0	2.50
	C=O	23.8	1.90
10 sec	C-C	70.7	1.30
	C-O	24.0	2.0
	C=O	5.3	2.0
20 sec	C-C	70.3	1.32
	C-O	23.8	1.75
	C=O	5.8	1.8
30 sec	C-C	66.9	1.34
	C-O	25.4	2.1
	C=O	7.7	1.89
60 sec	C-C	63.7	1.35
	C-O	25.8	2.2
	C=O	10.5	1.6
120 sec	C-C	68.7	1.38
	C-O	23.1	1.45
	C=O	8.2	1.74
180 sec	C-C	68.3	1.4
	C-O	24.2	1.5
	C=O	7.5	1.9

Table 4.2 The fitting parameters extracted from XPS analysis of GO and plasma functionalized GO films as shown in Figure 4.8.

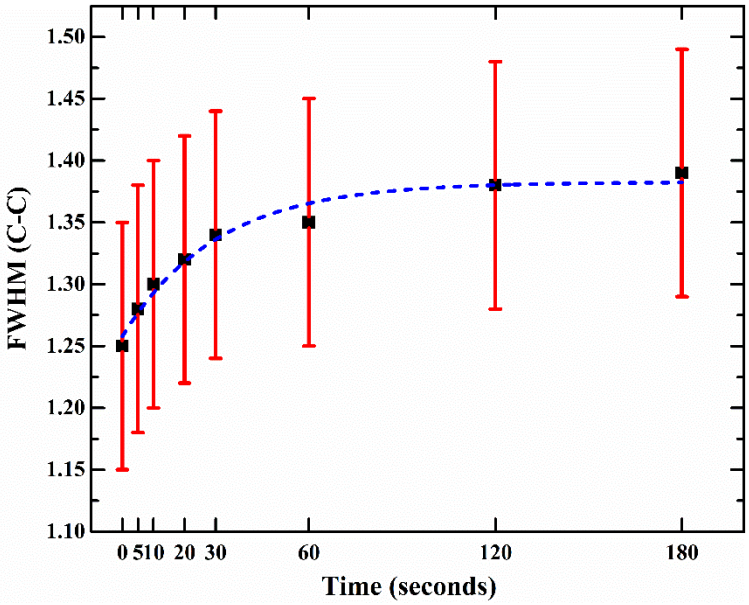

Figure 4.9 FWHM of C-C component in fitted C1s spectrum

The reorganisation of the bonding configuration between carbon and oxygen as revealed from the carbon spectra is reflected in the oxygen spectra as well. For GO the O1s peak is positioned around 531.4 eV with an asymmetric tail (534 eV). With increasing plasma exposure, there is a significant broadening of the O1s peak along with shift toward higher binding energy. The peak contains contribution from three types of oxygen (**Figure 4.10**): oxygen double bonded to carbon in aromatic structure (531.3 eV), oxygen singly bonded to aliphatic carbon (532.4 eV) and oxygen singly bonded to aromatic carbon (533.3 eV). Detailed spectroscopic analysis by Ganguly *et al*. revealed that OH-moieties on basal plane are the most stable species.[211] Thus, from the C1s and O1s spectra it can be predicted that surface epoxides are dissociating to form carbonyl and phenol groups. Nonetheless, the presence of OH radicals in the plasma may also be a reason for this change. Confirmation of this theory would need further verification from NEXAFS studies.

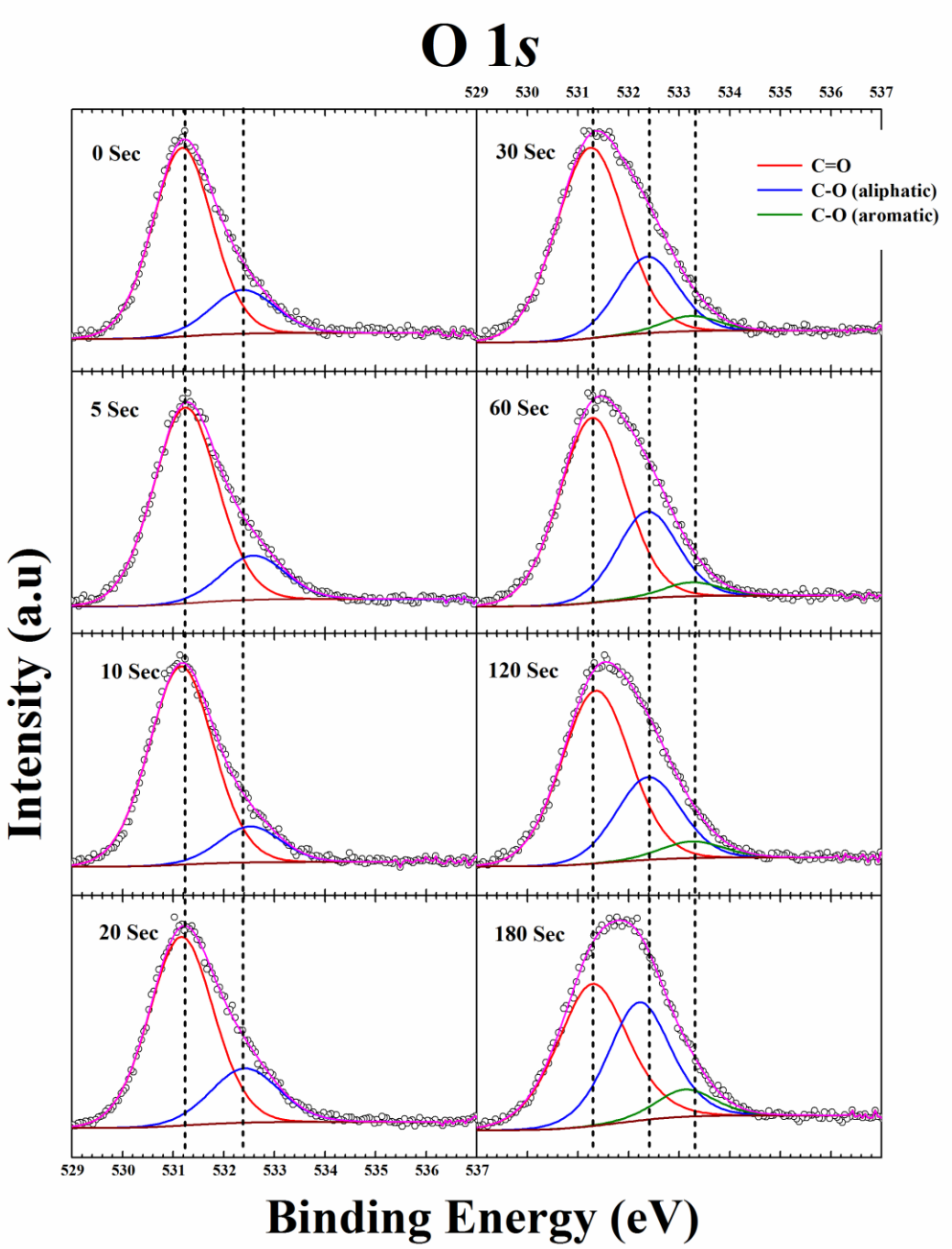

Figure 4.10 Fitted O1*s* spectra of GO (0 sec) and plasma functionalized GO for 5 to 180 seconds.

The Nitrogen spectra has been fitted with two components at 398.8 ± 0.1 eV and 401.1 ± 0.1 eV as shown in **Figure 4.11** . These corresponds to pyridinic and graphitic nitrogen configurations respectively.[217,218] All spectra are intensity normalized to reveal the changes in bonding environment of nitrogen with plasma functionalization. It is apparent from the figure that all functionalized samples have a prominent graphitic nitrogen signature. However, the spectral signature from pyridinic nitrogen increases till 10 sec mark and then decreases with longer plasma exposure. Since pyridinic nitrogen occupy the edge sites of graphene structure, it is easier to saturate the graphitic cluster with pyridinic nitrogen. While, with increased exposure to plasma, concentration of graphitic nitrogen at basal plane increases. Molecular dynamics (MD) simulations by XF Li *et al.* [205] revealed that to trap nitrogen in the graphitic lattice, point defects and vacancies are crucial (a crucial process/factor). It can be interpreted from the XPS results that during the initial stage of functionalization the excited nitrogen species in the plasma tend to attack the pre-existing defects and edge sites forming both graphitic and pyridine like configurations. However, with longer exposure the energetic nitrogen species in the plasma substitute carbon in the graphitic basal plane via defect formation and results in increased concentration of stable quaternary nitrogen states.

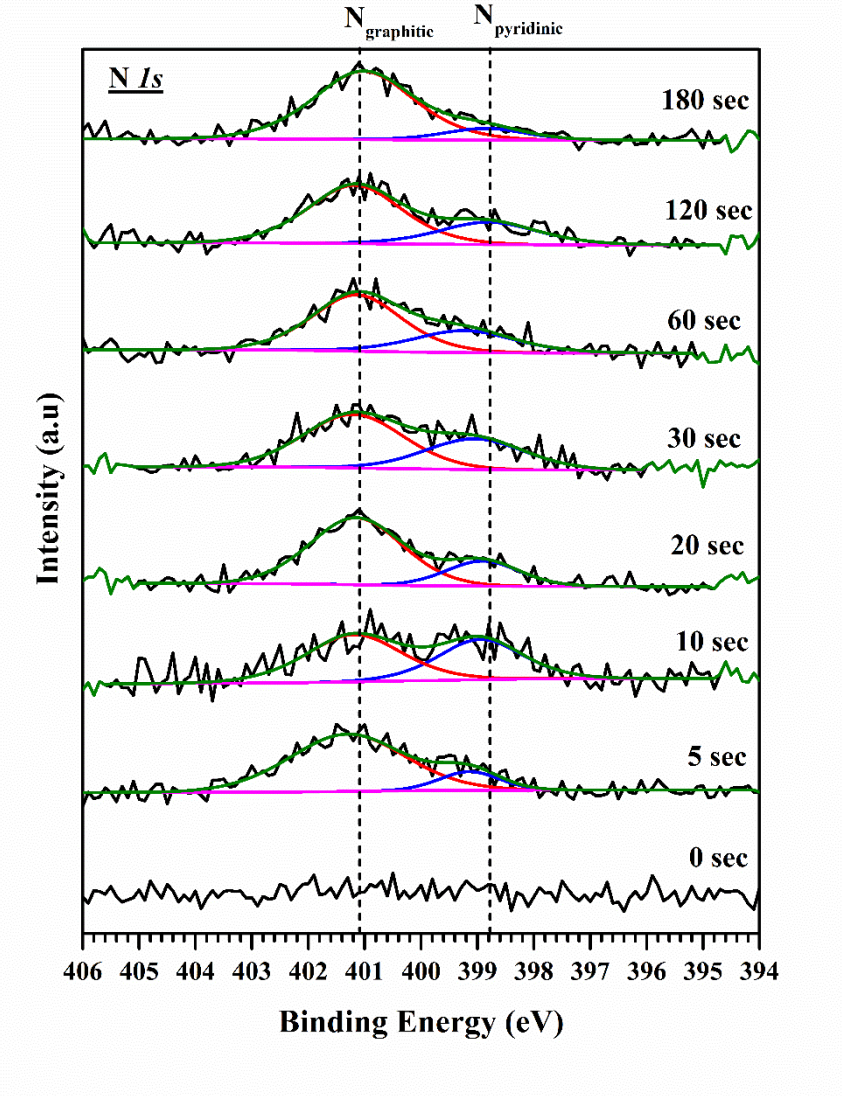

Figure 4.11 Fitted N1*s* spectra. Note, all spectra have been normalized to one unit in Intensity.

Valence Band spectra of GO and functionalized GO

Introduction of nitrogen into the graphitic lattice influences the delocalized π electron system of graphene. Nitrogen, having one electron more, will enhance the total density of states (DOS) below the Fermi level of graphene oxide. The bonding configuration of nitrogen play a crucial role in defining this increased DOS. N in the quaternary state (sp^2N) contributes two electrons to the π system of the carbon network. Similarly, pyridine N atoms

also contribute a lone pair to the π system. [219]. For graphitic nitrogen, of the five *p* electrons, three electrons are used to form σ bonds and the remaining two form bonding (π) and antibonding (π*) states .[220] However, for pyridinic nitrogen the two electrons contribute to the localized N lone pair state.[221]

Figure 4.12 presents the overlaid valence band spectra of GO and functionalized GO samples. The spectra were acquired with an incident photon energy of 230 eV. For GO, the density of states near Fermi level (0 to 4 eV) is dominated by the carbon 2p π states. The 2p σ contributions are at ~ 8 eV and these two states cross at around 6 eV binding energy. The feature at ~ 13 eV corresponds to the C 2p σ band and 2s-2p states hybridize at 10.6 eV. [222] The inclusion of electron rich nitrogen into the carbon network would result in the formation of donor levels near the conduction band edge and hence raising the Fermi level. After careful calibration of the energy levels, it is clear from the increased intensity that the π derived states are influenced by the increased concentration of N in the system (inset of **Figure 4.12)**. This also reflects to the substitution of C-C bonds by C-N bonds. Souto *et al.* have found that the top of the valence band for diamond like films undergoes profound changes upon nitrogen incorporation.[219] Similar observations were also made by Luo *et al.* for pyridinic N doped graphene. [221]

This increase in DOS with nitrogen doping, can be interpreted as the addition of three new bands (marked 1, 2 and 3 in **Figure 4.12**) resulting from the C-N bond formation. The band located at ~5 eV (marked as 1) arises form N lone pair state (a pair of electrons strongly localized on the nitrogen atom). The feature at ~7 eV is associated with electrons occupying the π orbitals of C-N bonds while the σ orbitals of C-N bonds are located between 9.5 to 11 eV.[219] As is seen in the figure, there is a consistent increase in the states 1, 2 and 3 till 120 sec, are increasing in intensity reflects to nitrogen substitution in the graphitic lattice. However, the state 2 shows a drop in the intensity after 120 sec mark. This can be due to the

decrease in C-C orbital overlap of resulting from increase in C-N bonds. Luo *et al*. reported similar results for pyridinic nitrogen doped graphene.[221] They found that nitrogen substituted in the carbon network would enhance C–N 2*p* electronic states while depressing the contribution from C=C 2*p* density of states. The DOS of states simulated by Souto *et al*.[219] also showed a similar trend, when N is progressively incorporated in the graphitic cluster. Thus from valence band spectra it is apparent that there is a strong electronic coupling between the GO and the incorporated nitrogen atoms.

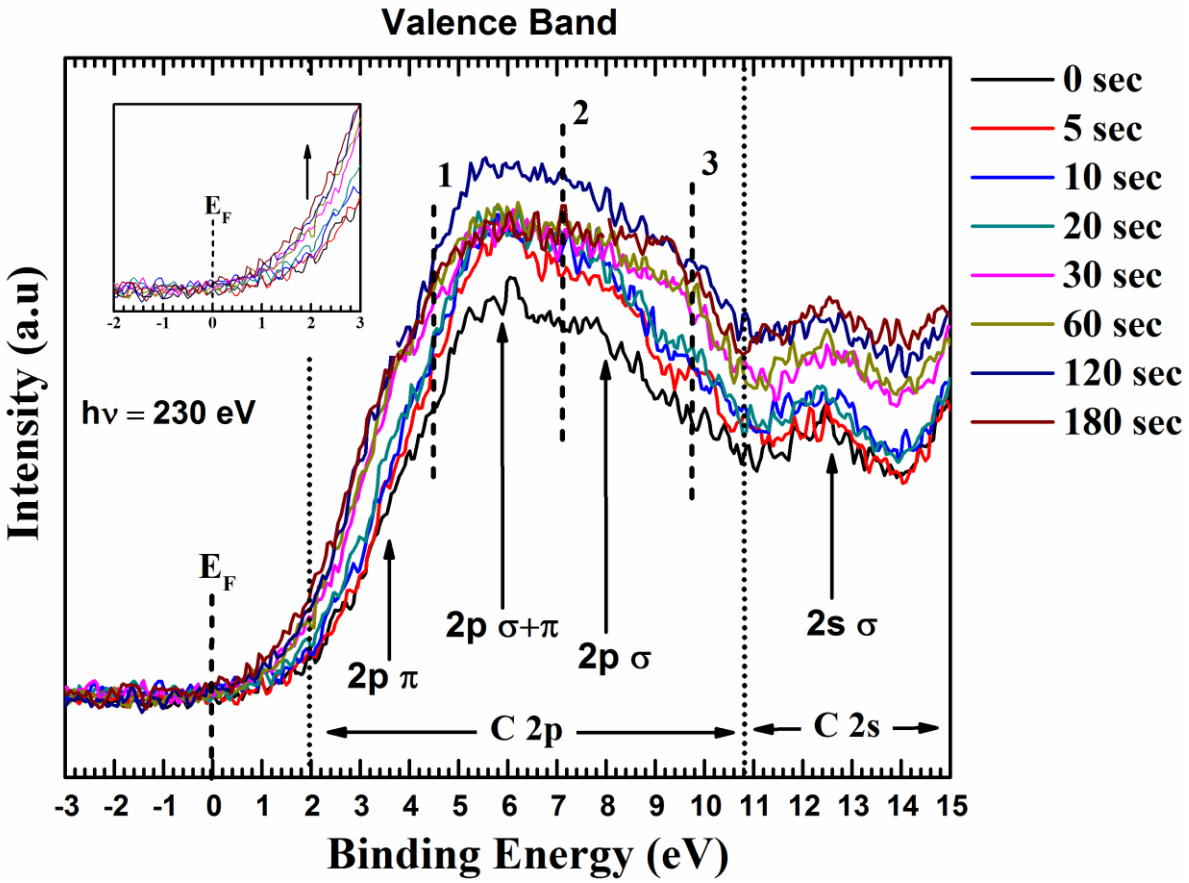

Figure 4.12 Valence band spectra of GO, functionalized GO.

4.6 X-ray Absorption spectroscopy

NEXAFS spectroscopy is a powerful tool to probe the electronic structure of GO upon functionalization using plasma jet. Here, low energy X-ray photons are used to excite core level electrons to unoccupied states above the Fermi level governed by dipole selections rules i.e. $\Delta l = \pm 1$. This dipole allowed transitions are highly sensitive to the local electronic structure, chemical configuration, oxidation state, molecular orientation and symmetry.[103] Also, NEXAFS can provide better insight into the molecular structure than XPS. In XPS the ground state electrons are strongly perturbed by the created core hole, while in NEXAFS the screening effect is pronounced leading to negligible influence on the ground state electron cloud. In XPS the line shapes for core level features (C 1*s*, O 1*s*, N 1*s*) are significantly broader resulting from multiple final state transitions, whereas in NEXAFS limited number of final states are (dipole) allowed. Thus, the overlapped structures in XPS can be easily resolved in NEXAFS.

Figure 4.13 shows the C K edge NEXAFS spectra of the GO films, acquired at an incident angle of 54.7° (magic angle) of the X-ray beam. This technique has been used to negate the anisotropic orientation of π and σ states of graphitic structure. The core level transitions at 285.2 eV and 292.8 eV are representative of the π^* and σ^* resonances respectively from sp^2 bonded C=C structure**.** However, the absence of exciton feature at 291.65 eV is indicative of the absence of long range order, a fact typical for GO, due to the presence of abundant defects. According to Lee *et al.* [223] the lowest energy peak (285.2 eV) corresponds to the transition of core level C1s electrons to antibonding π states along the M-L points of the graphene Brillouin zone and the broad peak a 292.8 eV originates from transitions to the dispersionless σ states at the Γ point of graphene Brillouin zone as shown in **Figure 4.13 (b)**

For GO the higher energy transitions (~310 eV) are quite featureless in comparison to HOPG (refer to **Figure 1.9** of chapter 1) . The main reason being the larger interlayer distance for GO (~1 nm) in comparison to graphite (0.34 nm).[224] Smaller interlayer spacing increases scattering of the excited electron wave function by neighboring atoms (multiple-scattering theory). Although the transitions from various functional groups are present above and below the ionization potential (IP), resonances below the IP can be more precisely defined. This is mainly because of the π^* features being more prominent and intense with respect to the σ^* transitions which are broader in nature and tend to overlap. For example, the peak at 292.8 eV can have contributions from π* C−O and σ* C−O absorptions along with the continuum background. Thus, a detailed analysis of the π^* transitions should be definitive enough for the determination of surface chemical changes.

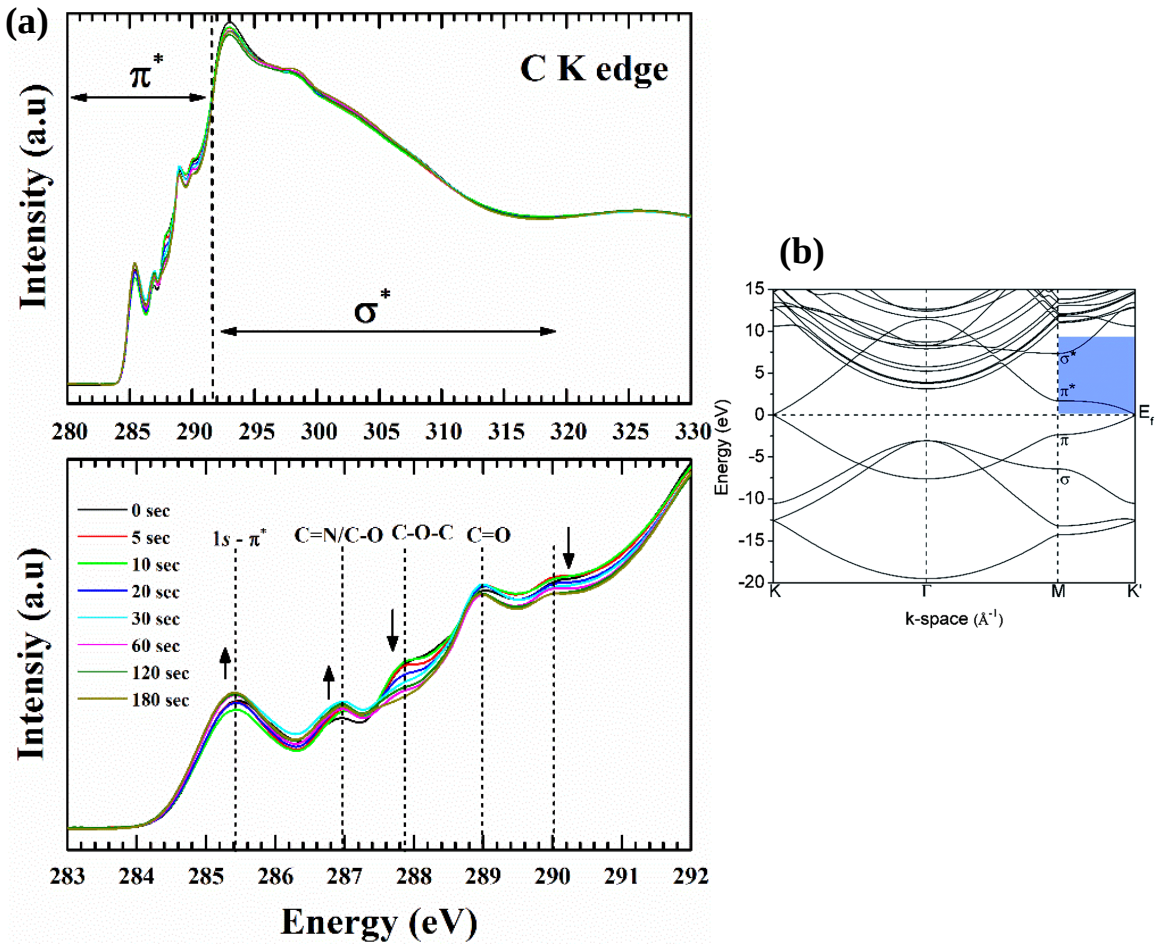

Figure 4.13 (a) C K-edge Nexafs spectra (b) ground state band structure of single-layer graphene where the highlighted blue region represents the unoccupied DOS probed in the C K-edge NEXAFS spectroscopy. Reproduced from Schultz *et. al.*[198] with permission from The Royal Society of Chemistry.

Region below the IP shown in **Figure 4.13 (a)** consists of spectral features at 289.8 eV, 288.8 eV, 287.7 eV, and 286.8 eV along with the C=C resonance at 285.2 eV. [225] The carbonyl core for the double bonded oxygen functionalities (C=O) can be associated with carboxyl or ketone environment. For carboxylic group the π* transitions are reported at 288.7 eV. However, this position will shift depending on the electronegativity of the carbonyl core. For ketone groups these transitions are found at lower photon energies**.**[225] The single bonded oxygen functionalities in the form of phenol (-OH) and epoxy groups (C−O−C) are known to shift the π* resonance of sp^2 structure to higher energy values. From the previous reported studies on graphene oxide, transition at 286.8 eV is due to the -OH moieties and 287.7 eV is due to epoxide moieties. [198] The resonances related to C-N bonding overlaps with oxygen moieties at 286.8 eV and 288.8 eV. Dennis *et al.* observed the π* resonances of C-N bonds at 286.8 eV and 288.6 eV in the C K-edge NEXAFS of imidazole.[226] Due to the low atomic concentration of nitrogen and the overlapped features it's hard to delimit the absolute contribution of C-O and C-N functionalities at the C K edge. From the figure it is apparent C-N/C-O transitions have increasing intensities along with a noticeable drop in the intensity of epoxide resonance. This is in-line with the known theories of GO reduction where C-O-C are reported to be less stable than C-OH functionalities. The peak at 288.8 eV can be associated with the C=O π* resonances in carboxyl groups (COOH). The reported values for C=O transitions in GO are between 288.5 to 289 eV whereas C=O in a ketone environment is found at lower energies. The feature around 290 eV can have contribution from several

unresolved components. Kuznetsova *et al.* [227] assigned this peak to σ* transitions of C-O by comparing acid treated carbon nanotubes with 9-phenanthrol and xanthene, while Gandhiraman *et al.* [225] associated this with Rydberg mixed OH-derived states from hydroxylated and ether-linked C-species (−O−C−OH). Seeing the trend of phenol (-OH, increasing) and epoxy groups (C−O−C, decreasing) it would be appropriate to justify this peak as epoxide derived σ* transitions of C-O.

From the carbon spectra, a presence of oxygen in different bonding environment is obvious. At the O K-edge (**Figure 4.14**) two distinctive features are discernible, one at ~531 eV and the other around 537 eV. The π* region has three main resonances at 530.4 eV, 531.4eV and 532.5 eV. Lower energy absorption peaks at 530.4 eV and 531.4 eV are π* resonances form carbonyl core of carboxylic groups (-COOH). [225] A feature around 533.5 eV is expected from the epoxy groups.[228,229] Due to the strong oxidation process, molecules of oxygen and water get trapped between the layers of graphene oxide. X-ray absorption studies of molecular oxygen revealed that the π* resonances for O-O is at 530.8 eV.[230,231] Due to prolonged plasma exposure, the defects created in the lattice might have resulted in the escape of intercalated oxygen, resulting in the intensity drop at ~531 eV. Since, XPS measurements and C K-edge NEXAFS spectra do not reflect to the decrease in concentration of C=O groups. On the other hand, the σ* region consists of rather broad and overlapped transitions. Features around 536 eV, 539 eV and 545 eV are primarily assigned to σ* states of O-H, C-O and C=O of carbonyl groups respectively. The noticeable broadening observed in the O1s XPS spectra points to the increase in surface bound hydroxyl groups and can be confirmed by comparing with O absorption spectra. The difference in spectral feature from hydroxyl-derived (O−H) σ* states validates this claim. Gradual de-epoxidation with plasma treatment is also evident for this results, as the π* and σ* transitions (regions 3 and 5) representative of C-O-C show decreased contribution in the spectra. The σ* transitions of

C-O-C are relatively broader than other functionalities and have been reported to exist between 539 to 543 eV and the region beyond that is related to carbonyl group (C=O) bonded to an aromatic ring.

After analyzing the carbon and oxygen spectra, both XPS and NEXAFS , we can find that GO undergoes sufficient surface chemical modifications upon plasma functionalization. But the dissociation of the epoxy groups with an increase in hydroxyl content needs an explanation. Similar phenomenon was observed by Stankovich *et al*. for hydrazine reduced GO.[85] They proposed a mechanism in which hydrazine ring-opens epoxides to form hydrazino alcohols and eventually dissociates via the formation of an aminoaziridine moiety. In this case the ring opening might be due to the nucleophilic attack of the excited nitrogen species in the plasma. As the carbon in an epoxide ring is a strong electrophile and would result in ring opening with the formation of new C-OH and C-N bonds as shown in **Figure 4.15.** Ring opening is also favoured due to the release of stresses in the structure.

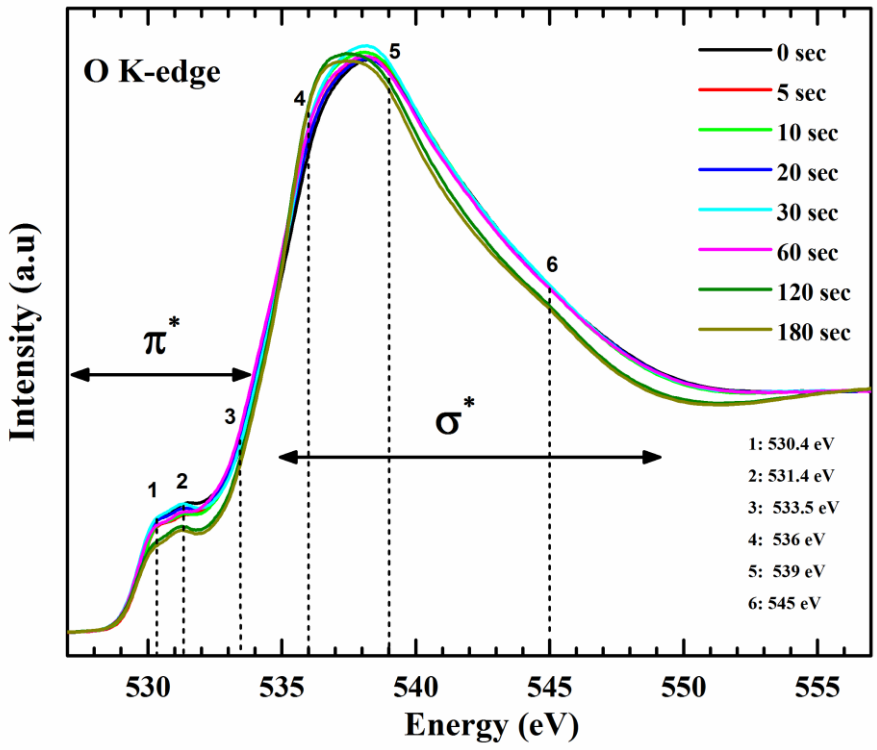

Figure 4.14 O K-edge NEXAFS spectra of GO and functionalized GO.

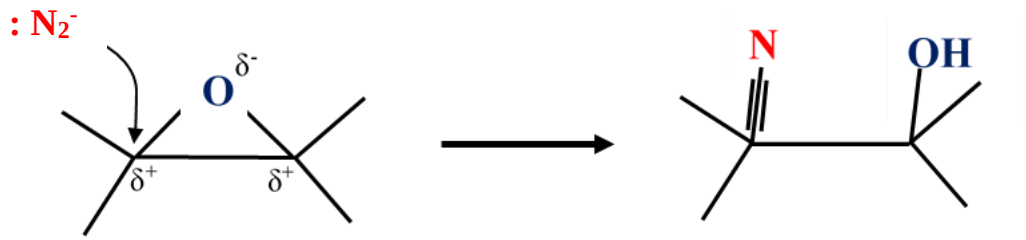

Figure 4.15 Epoxide Ring opening via nucleophilic attack.

Depending on the coordination (*sp*^{2} *or sp*^{3}) between carbon and nitrogen in the graphitic lattice, electron density of the nitrogen atom will change and should reflect in the absorption spectra. In spite of some minor variations, resonance features of the principal nitrogen configurations are always distinguishable.[232] This clear inference could not be drawn from the XPS spectra. Early studies on carbon nitride (CN_x) film produced by nitrogen ion implantation in graphite showed three sharp π* and one broad σ* resonances. These π* resonances were found to originate from pyridine like structure, cyanic structure and graphite like structure.[233] However the energy assignments is highly ambiguous. Schiros *et al.* [234] assigned the graphitic nitrogen at ~401 eV while Gao *et al.*[235] and Schultz *et al.*[198] assigned the same at 400 eV and 403.4 eV respectively. Schiros *et al.* validated their carbon and nitrogen K-edge spectra using cluster-based density functional theory (DFT) calculations. Recent studies by Kiuchi *et al.* [236] on nitrogen species incorporated into graphite using low energy nitrogen ion sputtering are in good agreement with the findings of Schiros *et al.* In any case, the vast range of energy values cited for the graphitic nitrogen species makes the absolute alignment quite debatable.

Nitrogen K-edge spectra for the plasma functionalized GO is presented in **Figure 4.16**. Note, due to low concentration of nitrogen all the peaks were area normalized after subtracting a linear background. The spectra are dominated by two features at 401.2 eV and

406 eV. Despite the sharp feature at 401 .2 eV there are other resonance features present in the edge region as well. The π* region can be assigned with four different resonance features: (N1) pyridinic N, (N2) cyanide or amide N, (N3) graphitic N sites, (N4) pyrrolic N. In addition, peak at 406 eV corresponds to the lowest energy σ* states. This large and broad resonance is attributed to transitions from N 1s core levels to σ* C–N states having contributions from broad range of C-N bonds (graphitic, pyrrole, pyridine). Due low nitrogen concentration, distortion of the graphitic lattice is suppressed in our case. Hence, distortion induced features is not expected to appear in the spectra. From **Figure 4.16** (region below the IP) it is evident that the concentration of graphitic nitrogen increases monotonically with increased plasma treatment. This finding is in line with the XPS measurements, where increased concentration of graphitic nitrogen has been noticed. The contribution from pyrrolic N (component around 402 eV) is seemingly decreasing along with apparent sharpening of the graphitic feature. For graphene sputtered with nitrogen ions, a continuous increase in pyridinic nitrogen has been related to greater amount of defects along with loss of carbon from the structure.[237] The contribution from the pyridinic groups occupying the edge sites is hard to discern from this spectrum. Since, pyridine nitrogen in the graphitic lattice are the most unstable, they readily convert to pyrrolic and graphitic N groups [204] Considering the nitrogen NEXAFS spectra, it is worth mentioning that the activated nitrogen atoms in plasma possess enough energy to substitute carbon atoms at graphitic sites.

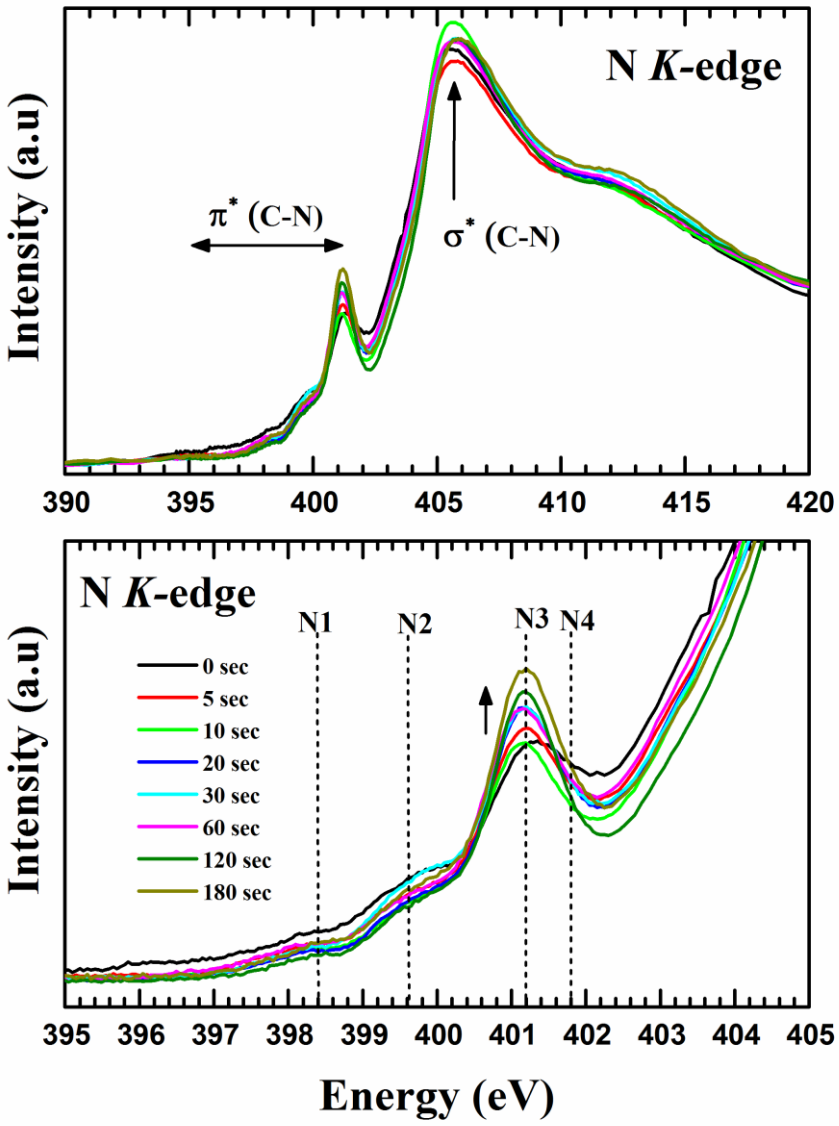

Figure 4.16 Nitrogen K-edge NEXAFS spectra of GO and functionalized GO

4.7 Topography and surface potential measurements of plasma functionalized GO.

Kelvin probe microscopy is a two-step process. In the first step, the afm tip scans over the surface to take the standard topographical image and in the second step the biased tip rises to a desired height (30 nm in this case) to take the surface potential measurements over the same area. **Figure 4.17** presents the topography image of GO and the functionalised GO films over an area of 100 μm^2. All the topography images are typical for GO thin films with abundant wrinkles on the surface.[238] However no substantial changes in topography could be observed from the images. The average roughness value of all the samples were calculated to be 3±0.5 nm. Thus, the low power plasma used in this case does not induce noticeable physical damage (sputtering) to the GO surface, effecting only the surface electronic and chemical properties.

Introduction of nitrogen into the graphitic lattice distorts the π electron cloud, inducing shift of its Fermi level and hence changes its work function. Scanning Kelvin probe force microscopy (SKPFM) can lead to a better understanding of the changes in the electronic properties of GO at different stages of the plasma functionalization process. In SKPFM the conducting tip with an applied bias scanning over a surface is highly sensitive to any changes in local surface potential. **Figure 4.18 (a)** shows the surface potential map of pristine GO and **Figure 4.18 (b)** is the surface potential distribution over the same area. The histogram plot of the surface potential showed a Gaussian distribution profile. Mean value of this distribution can be considered as the average surface potential difference between the tip and GO film. Considering the work function of the tip to be 4.55 eV the work function of the GO film is calculated to 4.967 eV. Which matches well with the reported values. [68] This process was adopted to calculate the average SP for all the functionalised GO films. In SKPFM it's not a good approximation to quantify the measured

work function values exactly with that of the sample, however the variations in surface potential are of absolute nature.

The effect of nitrogen configuration on the electronic structure of graphene have been reported by Schiros *et. al.* [234] and is shown schematically in **Figure 4.19 (b)**. Nitrogen atom has five valence electrons. In nitrogen doped graphene, nitrogen bonds to the carbon structure via three σ bonds and one π bond. For graphitic nitrogen part of outer electrons is transferred to the surrounding carbon atoms, making the graphitic structure more electron rich (n-doping). However, for pyridine nitrogen the electron lone pair is located on the nitrogen atom at the edge site. Thus, the electron density over the neighbouring carbon atoms is reduce resulting in p doping.[239]

From **Figure 4.19 (a)** it is apparent that, at the initial stages (till 10 seconds) the work function of GO increases and with increasing nitrogen concentration the WF drops below the initial value for as-synthesised GO. This variation in SP have strong resemblance with the N1s XPS spectra (**Figure 4.11**). Here the relative concentration of pyridine nitrogen is maximum at 10 secs and then gradually decreases with longer plasma exposure. The p doping effect caused by pyridine nitrogen increases the work function of GO. But with the increase in the in-plane graphitic nitrogen the GO energy bands will be more electron rich resulting in n-type doping effect and decrease in WF values.

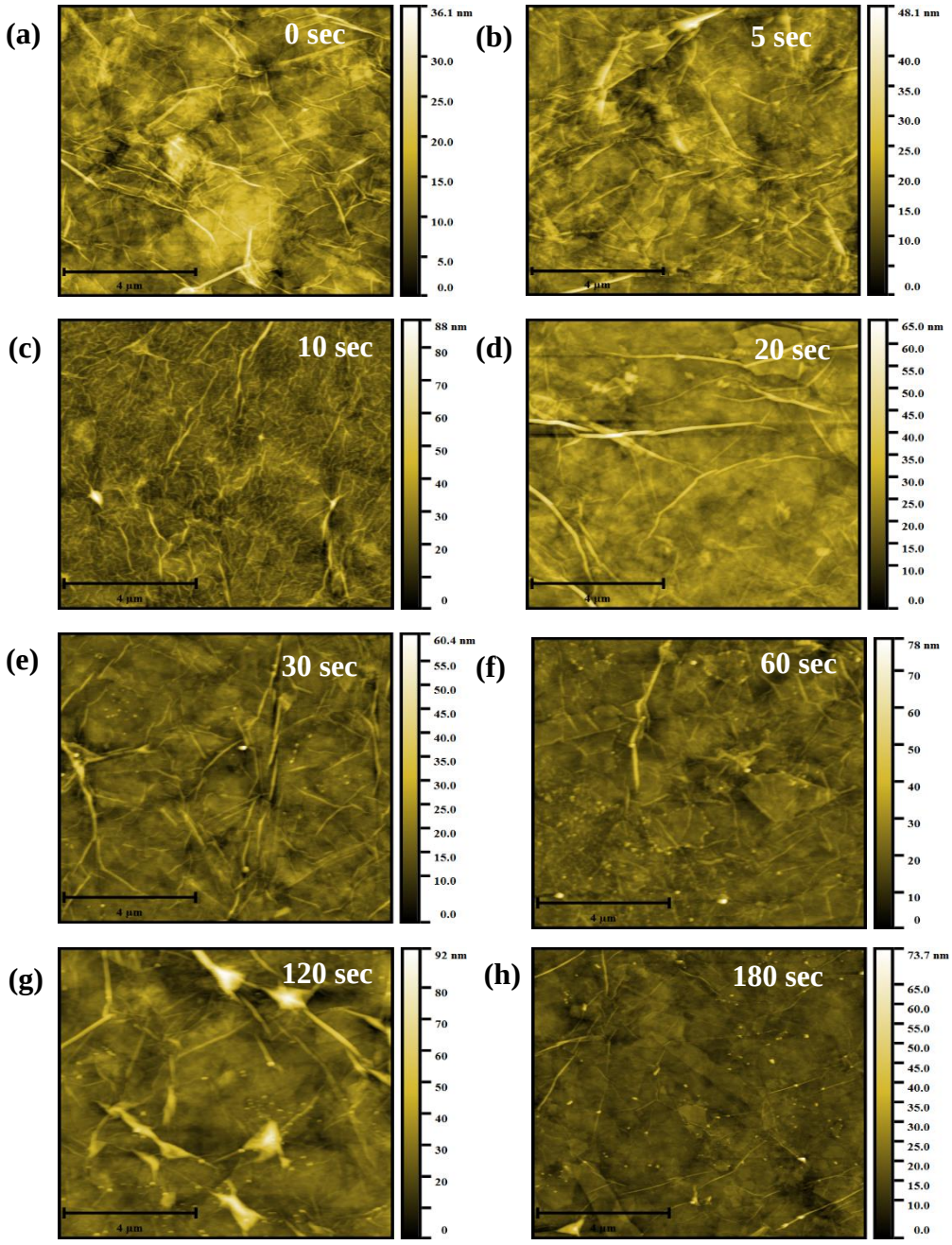

Figure 4.17 Tapping mode AFM height images of (a) drop-cast GO film, (b) to (h) plasma functionalized GO for varying time intervals.

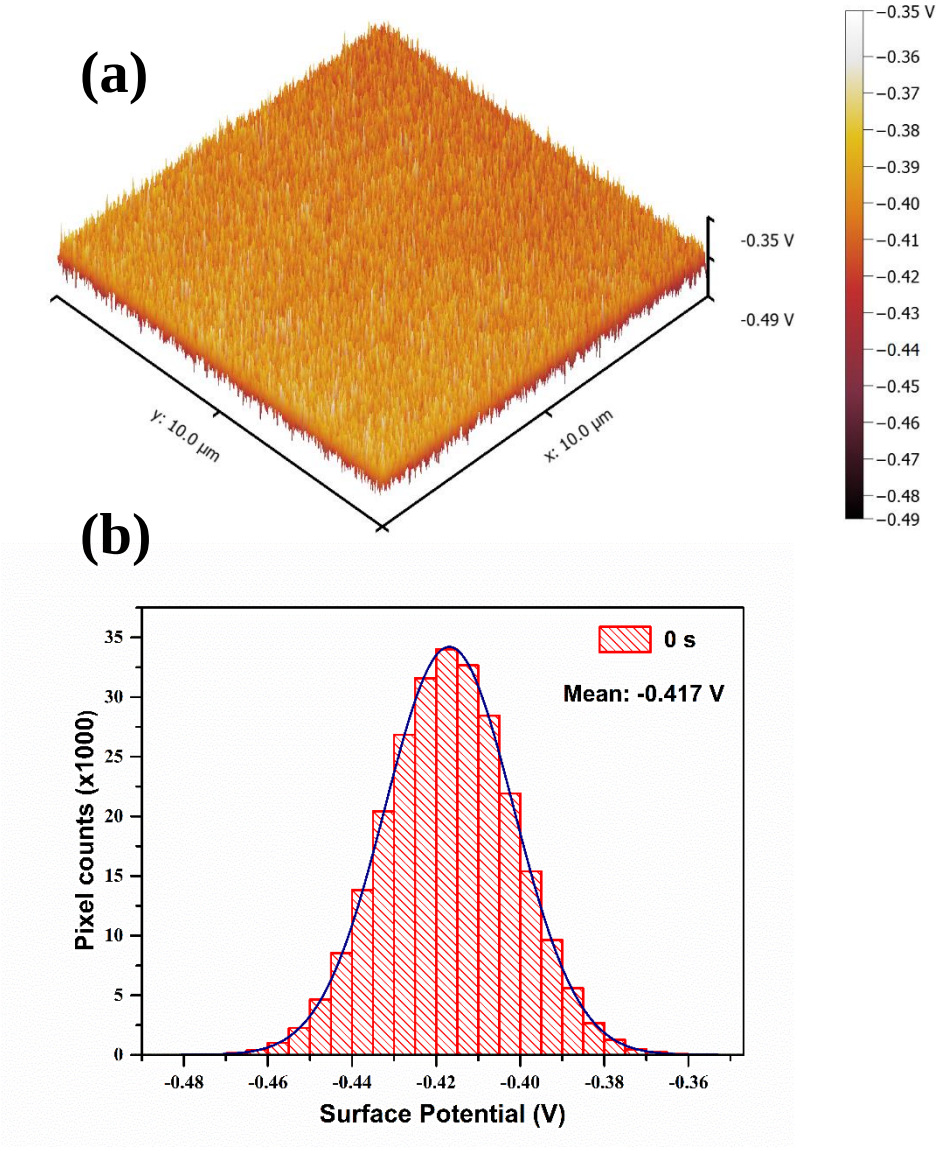

Figure 4.18 (a) SP map (b) Histogram plot of SP distribution of the refence GO sample.

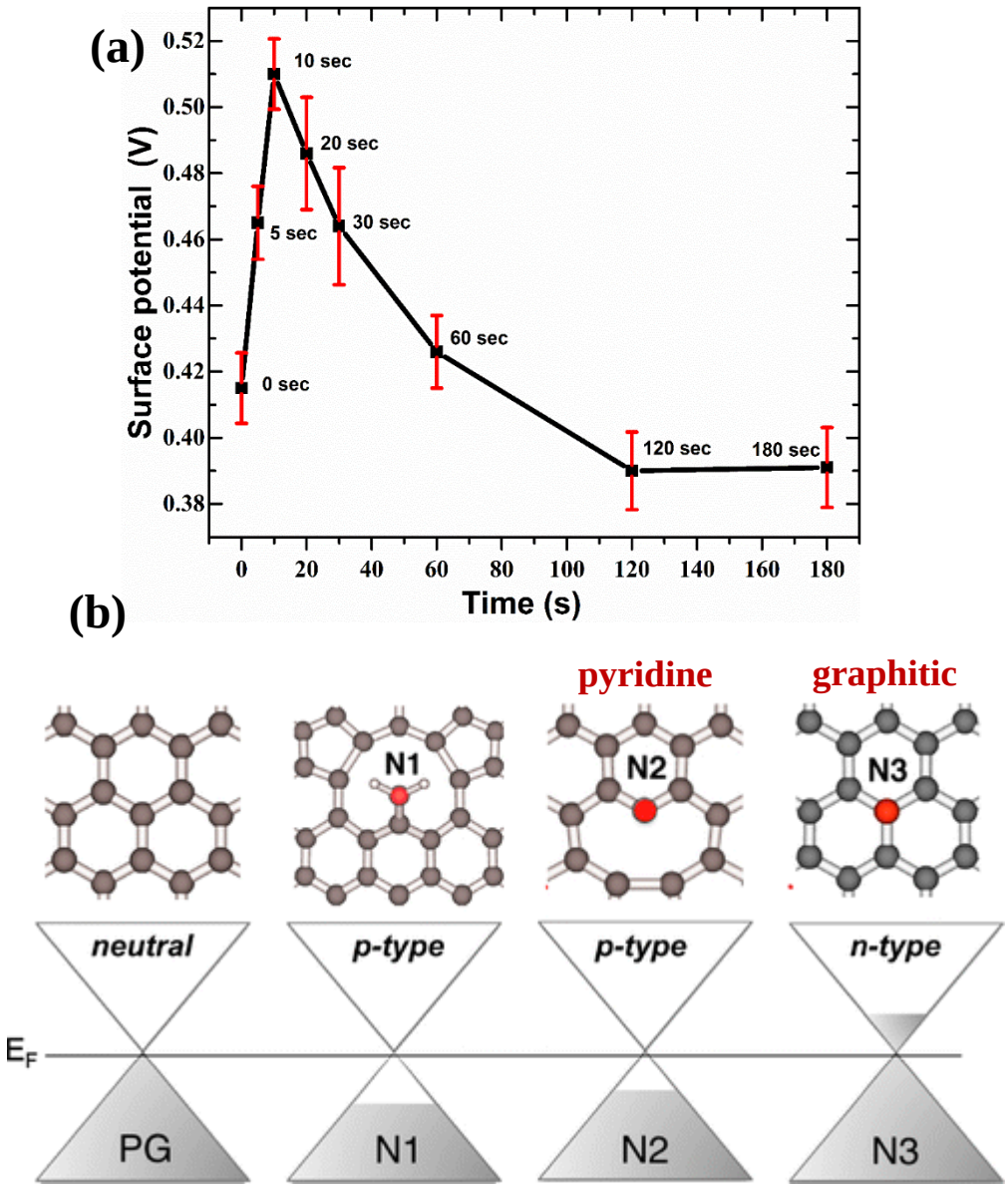

Figure 4.19 (a) Variation in surface potential of GO with duration of APPJ treatment, (b) Changes in electronic property of graphene with different nitrogen configuration as proposed by Schiros *et. al.*[234]

4.8 Conclusion

The properties of GO can be enhanced by various chemical and physical methods, but they lack the promise in precision. With major advantages being clean, reliable and ideal for industrial processes, APPJ is shown to be a promising candidate for surface functionalization GO. In this study, a low power (4 watt) plasma jet has been used to induce finite changes in surface chemistry and electronic properties of graphene oxide. Detailed X-ray spectroscopic studies revealed that the active species in plasma can react with graphene oxide changing its surface chemistry. The nitrogen ions can substitute carbon from the graphitic structure to form in-plane C-N bonds as revealed by the core level X-ray studies. Addition of nitrogen in the graphitic lattice introduces electronic density of states raising the Fermi level of GO. Finally, Kelvin probe studies showed that the bonding configuration can influence the work function of GO. Pyridine nitrogen transforms GO to p type while graphitic nitrogen increases the electron density of GO and transforming it to n type. Pointing to the fact, that a low power APPJ can effectively tune the work function of GO.

Chapter 5. Simultaneous reduction and deposition of highly acidic Graphene Oxide.

This chapter continues from the work presented in chapter 3. Here the plasma jet operated with He and H_2 gas mixture is used to deposit highly acidic graphene oxide solution on silicon substrates. The reducing environment of the plasma is found to be highly efficient in recovering the electronic structure of the oxidative exfoliated graphene oxide. Both XPS and NEXAFS studies show that graphene oxide can be reduced in-situ while carrying out the deposition. The recovery of the sp^2 carbon structure with plasma treatment is reflected both in the Raman and NEXAFS measurements. Furthermore, EFM measurements confirm the reduction process improves the conductivity of the GO films at the nanoscopic level. Hence plasma jet printing could be particularly useful for designing and fabricating solution processed graphene devices for a multitude of applications.

5.1 Introduction

Recently, there has been an increased interest in the fabrication of flexible electronics for diverse applications. This include flexible sensors, batteries, solar cells, supercapacitors, displays and many more. Printing nanostructured materials form colloidal solution (ink) on varied substrates has been the mainstay for the development of these technologies. Graphene oxide (GO) suspension has attracted significant interest in this field since graphene best known for its electronic properties, is hard to disperse in solutions.[33] Being dispersible in solvents, provides GO an added advantage for spin coating, drop-casting and spraying in the required substrates. Liquid phase exfoliation of GO from oxidation of graphite using processes proposed by Brodie, Staudenmaier, Hofmann and Hummers are most widely used for high yield synthesis of graphene oxide suspensions. [240] All these methods use concentrated sulfuric acid along with (a) concentrated nitric acid and $KClO_3$ (Hofmann method), (b) fuming nitric acid and $KClO_3$ (Staudenmaier method) and (c) $NaNO_3$ and $KMnO_4$ (Hummers method). [240] Studies by Poh *et al.* [241] revealed that GO prepared by these

techniques possess different properties. According to them Hummers method yields GO having better qualities in terms of higher heterogeneous electron transfer rate and enhanced electrochemical response. Though this technique results in high yield production, the strong oxidation involved results in the introduction of defects into the graphitic lattice. For GO the sp^2 network of the honeycomb structure is strongly disrupted by the oxygen moieties. Per Lerf–Klinowski model, the basal plane of GO is decorated with epoxide and hydroxyl groups, whereas carbonyl or carboxylic acid groups are located at the edge sites. Moreover, these induced defects adversely affect the electrical properties of GO. Subsequent deoxygenation is required to recover the electrical conductivity. The other issue with using strong acid is after completion of reaction the products need to be dispersed in de-ionized water for several cycles to neutralize the pH and to make it suitable for the desired application, printing in this case. Sonication based exfoliation and shear exfoliation of graphite has also been implemented to produce graphene inks. Paton *et al.* [242] reported the synthesis of unoxidized defect-free graphene using shear exfoliation. However, these processes requires special solvents whose surface energy should be well matched to that of graphene. Additionally, these solvents have high boiling point. In some cases, to keep the graphene ink stable, polymer stabilizers like ethyl cellulose are added to the mix, which needs to be decomposed to achieve optimal electrical performance.[243]

Several approaches have been reported so far to create patterned structures using graphene oxide ink such as micro-molding in capillary (MIMIC) method [244] , gravure printing [245] , screen printing [246] and ink jet printing.[247–250] Among the aforementioned techniques the first two suffer from limited scalability while screen printing has the lowest resolution of them all. Hence inkjet technology is the most accepted for fabrication of devices. Present Ink jet printing technologies, widely used to print graphene based electronic devices, suffer from various post processing steps and are substrate dependent as well. The major issue with GO based inks are, they need to be reduced after being printed. Which is

done either by high temperature (1000 ºC) annealing [251] or by reducing agents like hydrazine vapour [252]. Other techniques include UV reduction[253] and annealing in Ar/H_2 atmosphere [254]. For inkjet printing, tailoring the ink plays a key role for a successful printing process. Properties like viscosity, surface tension, density, of the ink are most important and need to be designed according to the substrate.[255]

While it is clear from the above factors that all the printing technologies have a strong relation with the ink in use, graphene inks require sophisticated pre-and post-processing steps. Thus, there is a strong drive to develop a robust technique that is independent of the ink in use and have the ability to perform additional processing steps in-situ. In this section, it will be demonstrated how a nonconventional APPJ operation with He and H_2 gas mixture can simultaneously reduce and deposit GO from a highly acidic precursor. The printing setup used in this section is described in detail in the **Chapter 3**. The deposited films were further treated with plasma to enhance their properties. To prove the effectiveness of the process the films (aerosolized, printed, printed and treated) were then characterized using Raman spectroscopy, X-ray based spectroscopy and Electrostatic force microscopy.

5.2 Experimental Details

The theme of this experiment is described schematically in **Figure 1.6.** Hummers method results in highly acidic suspension of GO. This suspension was then centrifuged at 8000 rpm for 15 mins and the supernatant was extracted to remove the unreacted graphite flakes. Note, no excess water was added to this suspension to increase the pH. This suspension with pH <2 was then used as ink for the plasma jet printer described in **Chapter 3.** Here, the plasma jet was operated with a gas mixture of He (1600 sccm) and H_2 (100 sccm). This GO suspension was drop cast as well as aerosolized onto a Si substrate for reference. Two more sets of samples were synthesized, first is the plasma deposited and

second is the plasma deposited with post treatment (extended print). The surface chemical and electronic properties of these films were then studied using photoelectron and NEXAFS spectroscopy. Raman spectroscopy has been used to realize any changes in the graphitic structure of GO. EFM was also used to depict the evolution of conductivity with plasma printing and treatment of these GO films. All the results thus obtained are explained sequentially in the sections to follow.

5.3 Raman Spectroscopy of Plasma deposited graphene oxide film

For graphene, there are two atoms per unit cell. Hence, graphene has six normal modes of vibrations at the Brillouin zone centre. These vibrational modes are represented as:[256]

$$\Gamma_{vib,2D} = A_{2u} + B_{2g} + E_{1u} + E_{2g} \qquad 5.1$$

Here A_{2u} and E_{1u} represent the in-plane translations of the carbon atoms while B_{2g} E_{2g} represent the optical phonon modes. In B_{2g} optical mode the carbon atoms move perpendicular to the graphene planes. E_{2g} mode is degenerate representing in-plane optical vibration. Only the E_{2g} modes are Raman active whereas the B_{2g} phonon is neither Raman nor infrared active.[256]

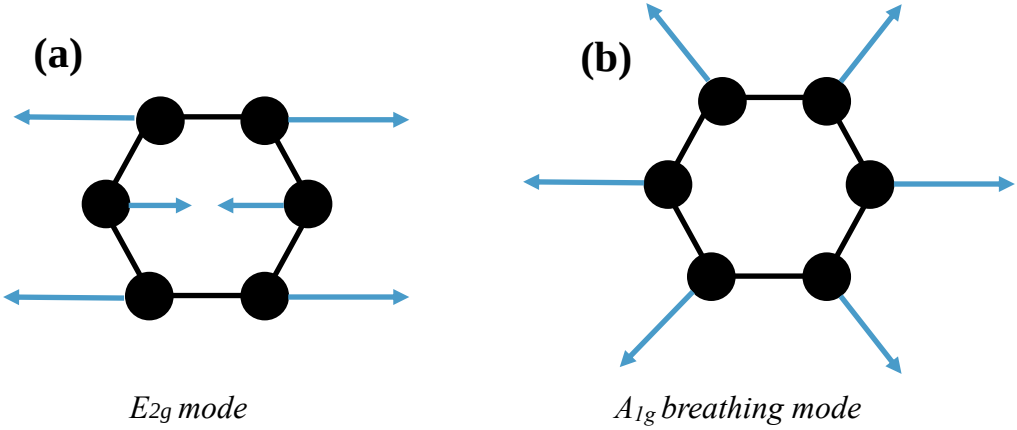

Figure 5.1 Vibration modes associated with the G and the D peak of graphene. Motion of carbon atom related to (a) G peak (b) D peak.[257]

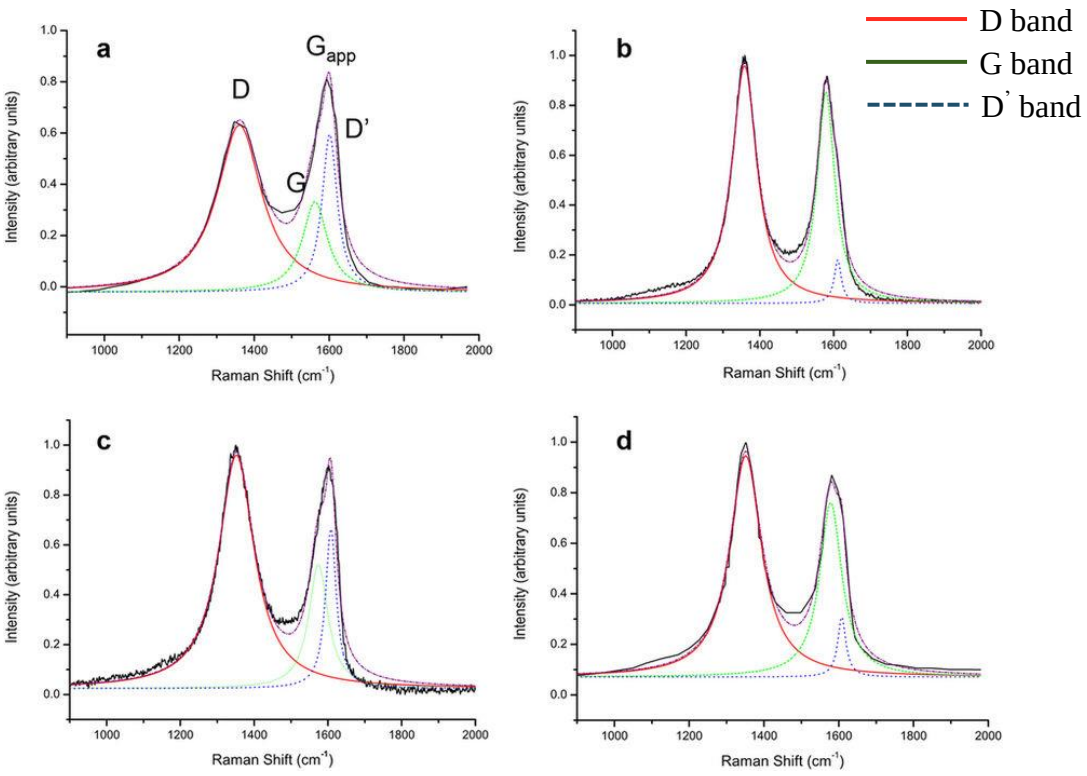

Figure 5.2 Example of two-peak fits applied to the G peak of GO and rGO. (a,b) GO before and after thermal reduction at 1,000 °C respectively and (c,d) GO before and after reduction with hydrazine, respectively. Reproduced from King *et al.* [258]

Figure 5.3 presents Raman spectra of the different graphene samples. The spectra consist of two peaks D band and G band, typical of GO. G band originates from the in-plane vibrations of E_{2g} phonons at the Brillouin zone centre while the D peak stems from the breathing modes of sp^2 rings having A_{1g} symmetry and requires a defect for its activation as shown in **Figure 5.1**.[259] For all the GO samples the disorder induced D band is located approximately at 1350 cm^{-1}.[260] For pristine graphite this D band is absent, while a prominent G peak features at 1581 cm^{-1}. For GO both the G band and D band shows appreciable broadening, resulting in an overlapped feature. **Figure 5.2** present the Raman spectra of GO and thermally reduced GO as reported by King *et al.* [258]. The broad G peak contains contribution from G and D' peak. Both the D and D' bands remains inactive for a defect-free infinite graphene sheet and become Raman active with the presence of defects. The vibrations at the defect sites provide enough energy for the intervalley (D) and intravalley (D') transitions to satisfy momentum conservation in the Raman scattering process.[261]

In this study, the as-synthesized sample was characterized by a corresponding G peak at 1600 cm^{-1} (**Figure 5.3 (a)**). Interestingly this peak showed a significant red shift of about 20 cm^{-1} after the printing process. With post-treatment, the peak position was further red shifted by ~5 cm^{-1}. For these measurements, to minimize any effect of heating the laser power was kept at ~ 0.5 mW. According to the reported values at this power the heat dissipated should cause a maximum shift of 2 cm^{-1} in the G band position.[262] The only viable reason for this red shift can be linked to the recovery of hexagonal network within the graphitic framework, mentioned as graphitic "self-healing" by Kudin *et al*.[260] On the other hand, ratio between the D and G bands intensity is often used as a measure of defect levels in graphitic systems and is also linked to the average size of graphitic domains. To estimate these values,

all the three spectra were normalized with respect the G band. Respective intensity ratios are presented in **Figure 5.3 (b)**. Its apparent that the ratio increased after printing and post treatment, from 0.96 to 0.98 and then to 1.04. Both the shift and increased I_D/I_G ratio is consistent with the formation of new graphitic domains during printing and plasma treatment, but are smaller in size with respect to synthesized GO. This finding can be correlated with those of Stankovich *et al*.[85] where reduced GO showed increase in I_D/I_G ratio. However, the effect of D' peak cannot be neglected as well. As it tends to overlap with G peak for highly defective graphitic system.[258]

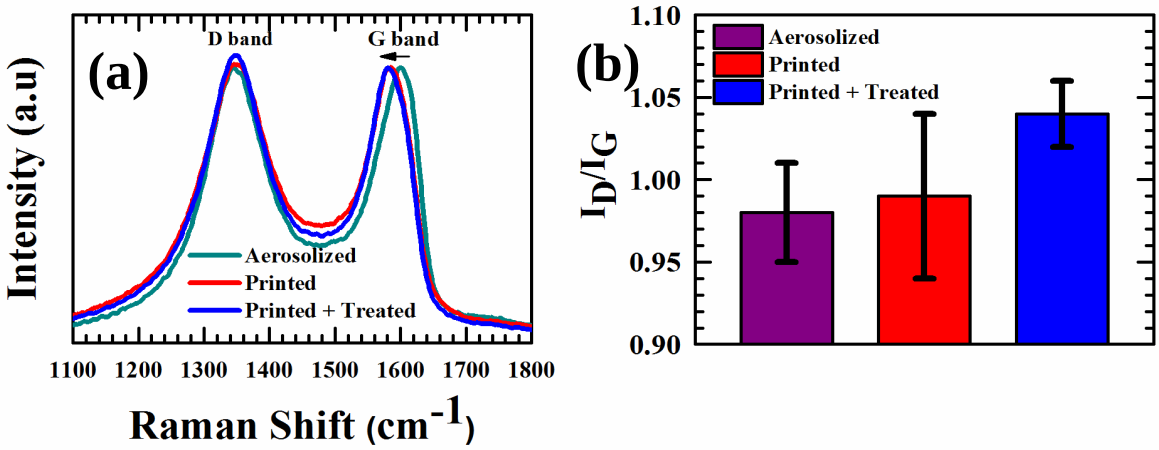

Figure 5.3 (a) Raman spectra of different GO films normalized to the G band. (b) variation in I_D/I_G values from Raman spectra.

5.4 X-ray Photoelectron Spectroscopy (XPS)

X-Ray photoelectron spectroscopy (XPS) was employed to analyse the changes in surface chemical properties of GO with the printing process. XPS is a widely used spectroscopic technique to qualitatively determine the changes in local coordination environment. The C1*s* spectra for drop cast GO is shown in **Figure 5.4 (a)** and represents the XPS spectrum of as-synthesized GO. In XPS, binding energies are strongly dependent on the chemical environment of the carbon atom. Due to stronger electronegativity, C=O in COOH occurs at higher B.E (~ 289 eV), whereas ketone and aldehydes are found at lower energies. [87] Thus, strong presence of carboxyl (O-C=O) moieties can be discerned from this spectrum, owing to the strong acidic suspension (pH<2) of GO. The peak around 292 eV (trace X) is not obvious for GO and might be attributed to the presence of reaction intermediates, in the form of carbonates or dicarboxylic acid functionalities. This feature may also arise due to strong ionic bond between K^+ and carboxylic acid functionalities, leading to a shift toward higher binding energy. Interestingly, the spectral signature for drop cast and aerosolized sample are quite different. Aerosolized GO shows an increased concentration of single bonded oxygen moieties (phenol, epoxides) around ~287 eV with respect to the drop cast GO. [87] This may be due to the air induced agitation promoting chemical reactivity during the aerosol formation. The presence of potassium ion is also evident in these two cases, and is mainly due to use of $KMnO_4$ during the synthesis. The K^+ ions are weakly bound at the graphene oxide surface as their probability of intercalation within the graphite interlayers is less. Dimiev and Tour [196] reported that during graphene oxide formation, molecules of sulphuric acid and the oxidising agent (Mn_2O_7) diffuse into the interlayer spacing of graphite and are stable unless large amounts of water have been added. Comparing **Figure 5.4 (b)**, **(c)** and **(d)** it is evident that potassium is absent after printing process. It has been reported that, at temperatures greater than 650 K potassium on the carbon surface can migrate into the carbon matrix. When the temperature is increased to

1123 K, potassium was found to evaporate form the carbon surface.[263] These results can be related to the findings in this section. Since the temperature of the plasma in the active region is significantly high, migration or sublimation of potassium can be a possibility.

For the printed GO film the concentration of carbonyl (C=O) functionalities are reduced considerably with respect to aerosolised and dropcast GO. With an extended exposure to the plasma after deposition the concentration of single bonded oxygen moieties are reduced as-well. **Table 5.1** presents the fitting parameters of the individual components in the carbon spectra, as shown in **Figure 5.4**. Full width at half maxima (FWHM) of both the oxygen functionalities (C-O, C=O) have decreased by ~0.5 eV with plasma treatment. Alongside this, the C-C peak at 284.5 eV had a FWHM of 2.4 eV for both aerosolized and printed GO but decreased to 2 eV after plasma treatment. According to Ganesan *et al.* [264] defects (sp^3 carbon) in the sp^2 structure broadens the C-C line shape. Hence, the decrease in FWHM of C-C can be correlated to the increase in sp^2 domains of the graphitic lattice. The presence of excited states of hydrogen and helium in the plasma would be the primary cause for this. When the aerosolized GO interacts with the plasma it is exposed to ions (He^+ and H^+), hydrogen radicals and neutral molecules (H_2 and He). Except for He, all of these will accelerate the deoxygenation of GO. Studies by Lee *et al.* [90] and Li *et al.* [91] provided insight into the efficient reduction of GO films using Ar+H_2 plasma. But both these studies showed plasma reduced graphene possesses enhanced properties either in electrochemical performance or as a transparent conductor. It's evident from the XPS results that all the steps involved in the printing process influence the chemistry of GO. To the best of our knowledge none of the available printing technologies can do this.

From the XPS spectra it can be interpreted that during deposition, the carboxylic acid undergoes reduction to form C-O groups. Post treating the deposited film further reduces the C-O moieties and consequently recovering the sp^2 structure of the graphitic lattice.

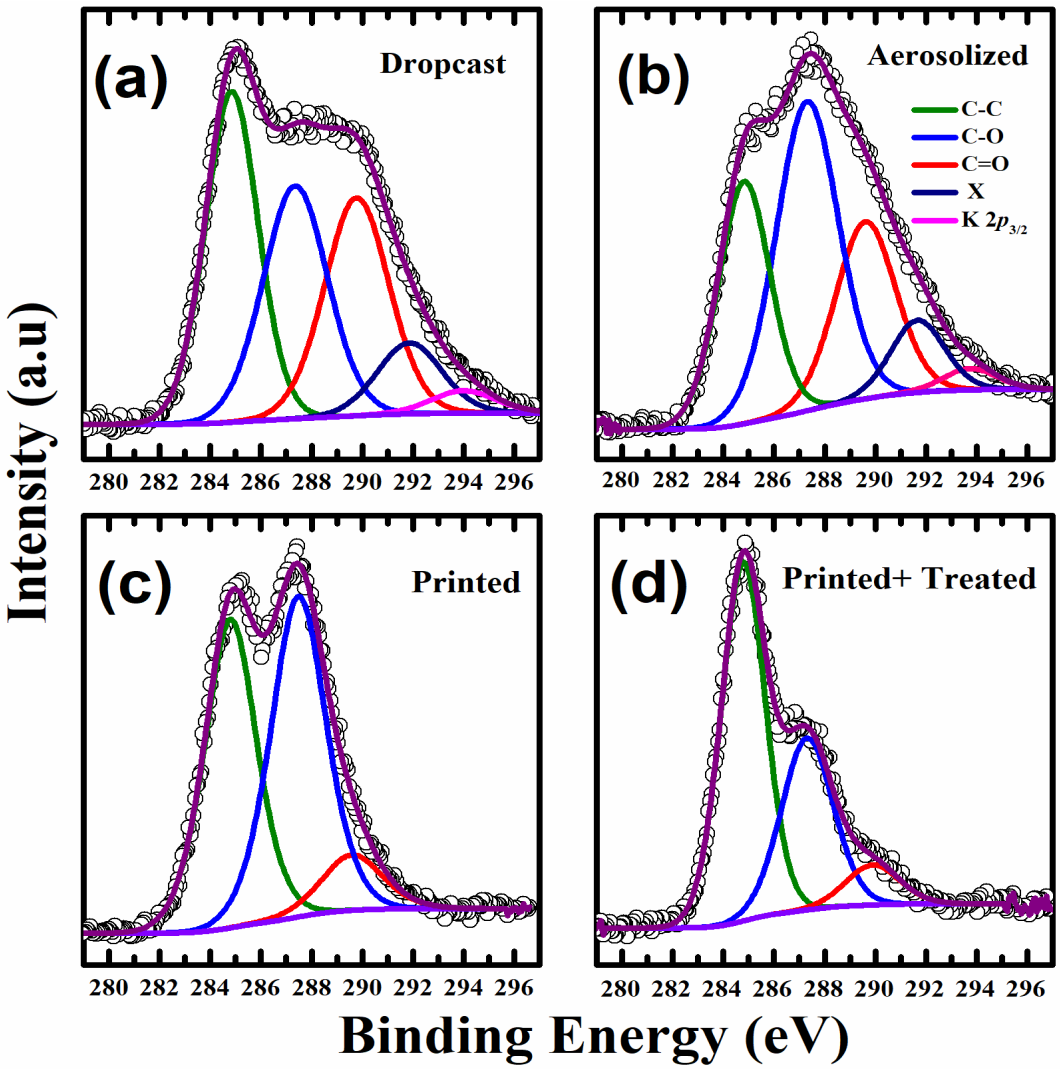

Figure 5.4 C1*s* XPS spectra of (a) dropcast (b) aerosolized (c) plasma printed/deposited (d) printed sample after post treatment.

GO sample	component	% concentration	FWHM
Drop cast	C-C	33.20	2.45
	C-O	28.60	3
	C=O	26.80	3
	X	8.70	3
	K $2p_{3/2}$	2.70	3
Aerosolized	C-C	26.40	2.40
	C-O	40.40	2.90
	C=O	22.60	2.80
	X	8.20	2.5
	K $2p_{3/2}$	2.4	2.5
Printed	C-C	43.20	2.40
	C-O	47.70	2.60
	C=O	9.10	2.80
	X	0	0
	K $2p_{3/2}$	0	0
Printed & treated	C-C	58.90	2.0
	C-O	33.10	2.4
	C=O	8	2.5
	X	0	0
	K $2p_{3/2}$	0	0

Table 5.1 Components used to fit carbon 1s spectra of GO and other plasma functionalized GO samples as shown in Figure 5.4.

5.5 X-ray Absorption spectroscopy

Near-edge X-ray absorption fine structure (NEXAFS) spectroscopy measurements were also carried out to underpin the XPS measurements. NEXAFS is a highly sensitive to the local electronic structure as well as chemical composition and coordination environment. Additionally, in (NEXAFS) limited number of final states are (dipole) allowed. Thus, the overlapped structures in XPS can be easily resolved in NEXAFS. [103] Carbon K-edge spectra presented in **Figure 5.5** were acquired at 54.7º (magic angle) incidence of the X-ray beam to eliminate effects of any preferential orientation. The low energy peak at 285.5 eV and the intense peak around 293 eV correspond to the 1s→ π* and 1s→ σ* transitions of sp^2 derived carbon structure.[225] The absence of a core-exciton peak around 291.65 eV reflects to the highly defective sp^2 structure of the graphene, as evinced form the Raman spectra.[225] The relative intensities of these two resonances i.e. I_{π^*}/I_{σ^*} can be used a measure of the restoration of π-conjugated network upon plasma induced reduction of GO.[223] For defect free graphene, the I_{π^*}/I_{σ^*} ratio has been calculated to be 1.30 and the ratio of integrated peak areas to be 1.49.[265] For the GO samples under study I_{π^*}/I_{σ^*} has almost doubled after the printing and post treatment as shown in the inset of **Figure 5.5**. Thus, indicating to the restoration of the π-conjugated sp^2 frame work of the graphitic lattice resulting from the removal of oxygen functionalities. These findings are perfectly in line with those of Raman measurements where the recovery of sp^2 framework is also reflected.

In the spectra, the region between the π* and σ* resonances is occupied by three distinct features, discernible at ~286.9 eV, ~289 eV and ~290 eV for all the three samples. The aerosolized GO show a strong resonance feature at 289 and 290 eV (marked b and c) corresponding to C1s to π* transitions of C=O symmetry in carboxylic acid (−COOH) and carbonyl (C=O) moieties, respectively.[223] The peak at 286.9 eV (marked a) results from the core level transitions to π* symmetry of carbon singly bonded to oxygen in phenol (C-OH)

configuration.[266] Going from aerosolized to printed plus treated GO, the spectral signature of C=O moieties decrease considerably, while the phenol groups increase in concentration. This can be attributed to the reducing environment of the plasma. The presence of highly reactive hydrogen species results in reduction of carboxylic acid functionalities to phenol groups.

For the aerosolized graphene oxide sample two additional distinctive features at 297.6 eV and 300.2 eV are visible. These features arise from $2p_{3/2}$ and $2p_{1/2}$ states at the potassium *L*-edge respectively. [225] However, these K *L*-edge peaks are shifted by 3 eV with respect to the reported values for potassium *L* edges at 294.6 eV and 297.3 eV. [266] This shift to higher energy value is due to the formation of strongly ionic bonds of potassium probably with carboxylate groups (K^+ - $RCOO^-$) during the strong oxidation of Graphite. Similar shift at the potassium *L*-edge have been reported by Lee *et al.* for KOH/hydrazine-reduced graphene oxide.[266] This result confirms the formation of ion pairs (K^+ - MnO_4^-) during the oxidative exfoliation of graphite using $KMnO_4$. However, these potassium features are absent for the plasma printed GO. This can be due to the high temperature associate with the DBD plasma jet, used for the printing process. Another reason might be the reaction with H^+ ions in the plasma with the potassium salt of carboxylate acid forming molecular acid as in equation 5.2 which eventually gets reduced to phenol groups. Further studies need to be carried out to understand the process involved.

$$\mathbf{RCOOK + H^+ + OH^- \leftrightarrow RCOOH + K^+ + OH^-} \qquad \mathbf{5.2}$$

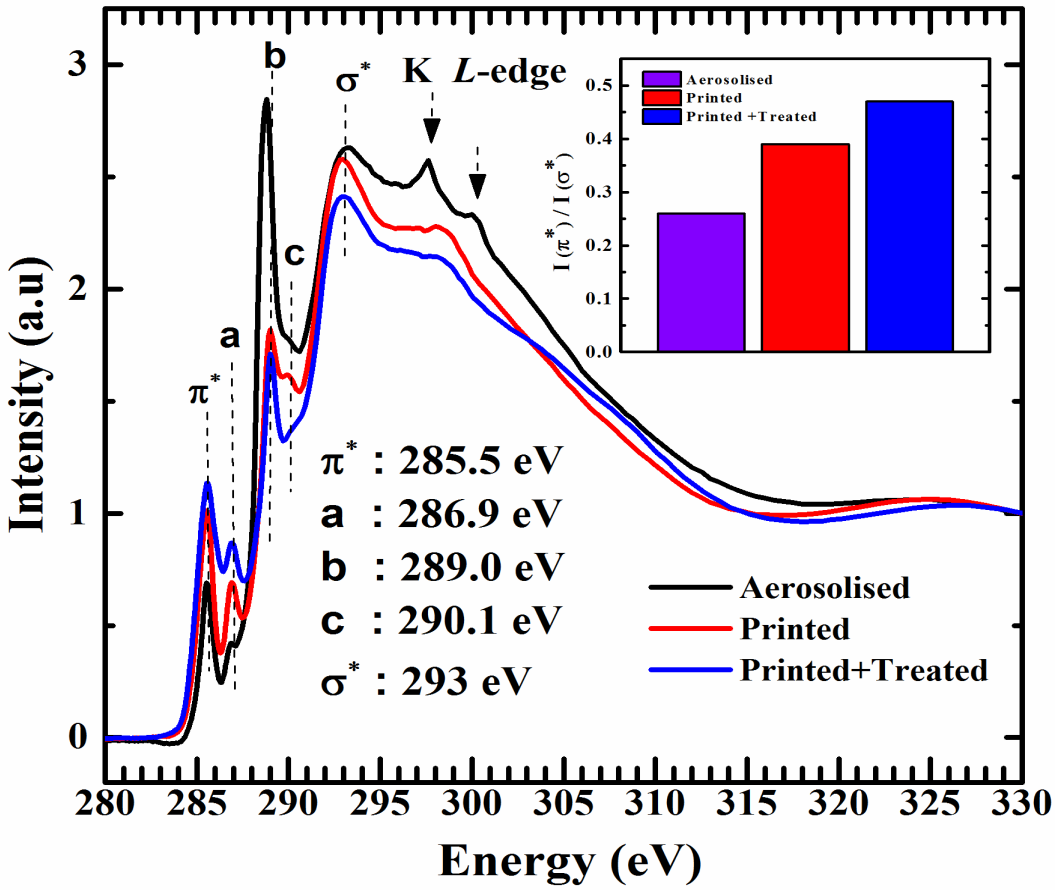

Figure 5.5 Carbon K edge NEXAFS spectra of as-synthesised GO and plasma functionalised GO films

5.6 Electrostatic force microscopy (EFM)

Electrical transport measurements are often used to measure the changes in conductivity of graphene oxide films. The conductivity values thus obtained result from the entire film and cannot provide direct information about the local changes. [267] Hence, by studying the local conducting properties a complete picture of the plasma induced reduction of GO can be obtained. EFM has evolved as a fast and non-invasive technique to determine the change in conductivity of graphene oxide upon reduction. Gomez-Navarro *et al.*[268] showed that EFM can be used as an in-situ, fast and contactless technique to evaluate the

conductivity of chemically derived graphene layers. Similarly, Jeong *et al.* [267] also reported that EFM can be used with high spatial resolutions to study the evolution of conductance in GO as it is reduced. Kulkarni *et al.* [94] studied the reduction of individual graphene oxide sheets using EFM. They were able to directly monitor the surface charge distribution of individual graphene oxide flakes during chemical reduction using EFM. On the other hand, Yalcin *et al.* [238] carried out EFM measurements to observe the propagation of charge carriers along the conducting pathways in reduced graphene oxide (rGO).

The removal of oxygen functionalities will have a definite effect on the electronic properties of the GO films. Tu *et al.* [269] reported that with progressive thermal reduction of GO, it can be transformed between *p* type and *n* type states. EFM is typically a two-step process. (Refer to section 2.5.3 of chapter 2 for detail) In the first step, the standard topography of the sample is recorded as in Atomic force microscopy (AFM). In the second step the AFM tip is with an applied dc bias (V_t) is lifted to a desired height above the sample to negate the influence of Vander Waals force on the electrical measurements. During this process only changes in the electrostatic force between the tip and the sample surface influence the phase and amplitude signals of the oscillating tip. The schematics of the EFM measurements presented in this section is shown in **Figure 5.6**. During EFM, the biased tip scanning over the substrate is subjected to a capacitive force. This force induces phase shifts in the tip oscillations. The dependence of phase shift on the electrostatic force between the tip and substrate can be represented as follows:

$$\Delta \boldsymbol{\Phi} = \frac{\boldsymbol{Q}}{\boldsymbol{2k}} \frac{\boldsymbol{d^2C}}{\boldsymbol{dz^2}} (\boldsymbol{V_t} - \boldsymbol{\phi}) \qquad \textbf{5.3}$$

In the above equation, $\Delta\Phi$ represents the phase shift, *Q* and *k* are the quality factor and the spring constant of the cantilever respectively, *C* is the capacitance of the system, V_t is the tip bias and ϕ is the surface potential. Thus by measuring the phase shift of the cantilever it will be possible to differentiate between conductive and insulating GO films.

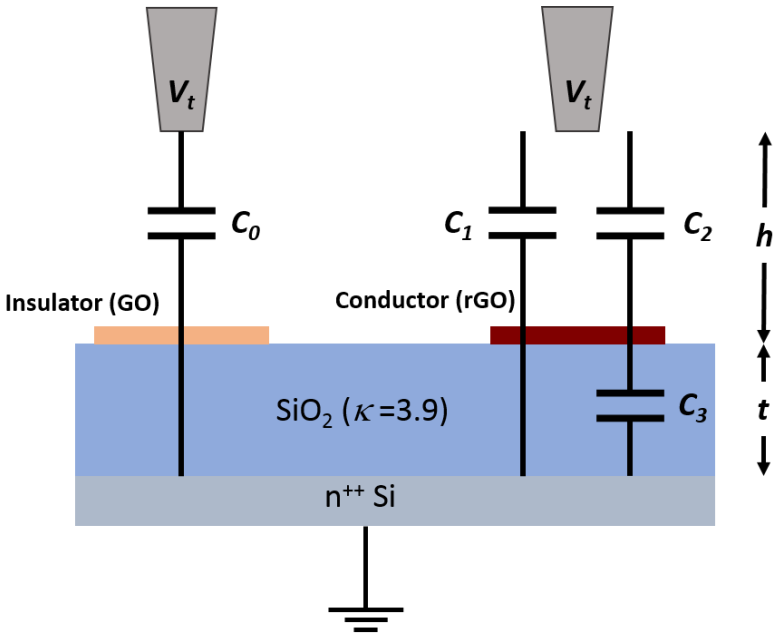

Figure 5.6 Schematics of the EFM setup used to study the changes in conductivity of GO after plasma treatment.[267] Tip and the grounded back lane acts as a capacitor. C_0 is the capacitance when the tip is over insulating GO. After GO being reduced the total capacitance (C_1) becomes series connection of two capacitors, C_2 (tip to rGO) and C_3 (rGO to back contact).

In this experiment EFM was used to map the sample surface with respect to the phase shift of the cantilever ($\Delta\Phi$), a lag between the drive frequency and the cantilever oscillation.[270] If the bias on the tip is kept constant along with the distance between tip and sample, then the measured variation in electrostatic force corresponds to the changes in surface potential distribution. For GO, due to the presence of lone pair of electrons on the oxygen atoms, oxygen functionalities such as hydroxyl, epoxy and carboxyl are known to decrease the surface potential. Thus, for a positively biased tip, $V_t - \phi$ (phase-lag) will be more for highly oxygenated GO and should progressively decrease with deoxygenation.

Figure 5.7 (a), (b), (c) presents the potential map of the three samples i.e. aerosolised GO, printed GO, printed and treated GO respectively. These maps show a clear contrast between the different GO samples. From **Figure 5.7** (d), representing the average value of phase shift over the measured area it is clear that the phase shift has considerably dropped with plasma treatment (~0.5 to 0.1 degrees). Also, the increased contrast between the EFM map of these samples it is apparent that there is increase of conductivity of the films.[267] However, due to non-uniformity of the surface there exists regions of residual oxide moieties which can be seen in phase maps of treated sample.

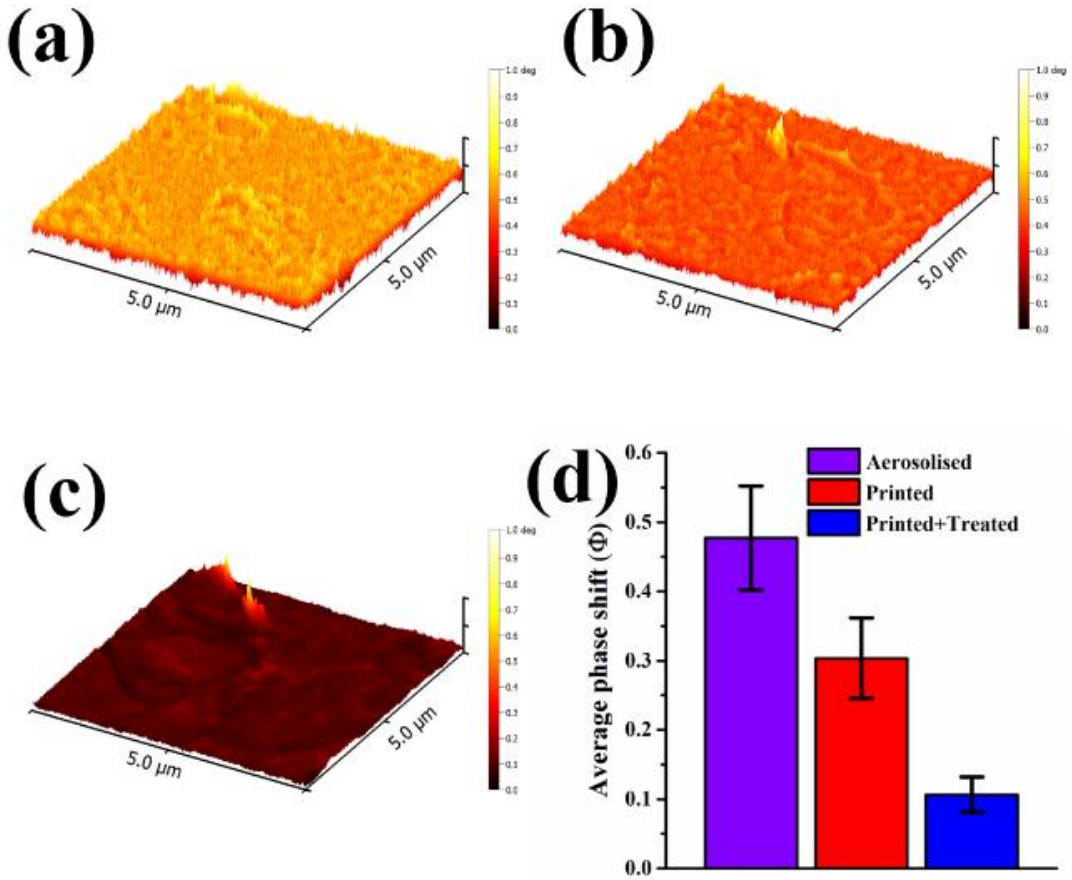

Figure 5.7 EFM phase map of (a) aerosolized GO (b) Printed /deposited GO (c) Post-treated GO, (d) average phase shifts for these three samples.

5.7 Conclusion

The major finding presented in this chapter is that a plasma jet can *in-situ* reduce highly acidic GO without the need of external post processes. No other printing technique have achieved this to date. XPS results presented in this chapter, confirms that the reaction intermediates during synthesis of GO can be eliminated using reducing gases in the plasma. Both XPS and NEXAFS results confirm that during deposition, carboxylic acid functionalities are reduced to phenol groups and with extended exposure to the plasma jet the oxygen content at the surface is reduced further yielding reduced graphene oxide films. Importantly, this reduction process aids in the recovery of sp^2 structure of the graphitic lattice. The I_{π^*}/I_{σ^*} ratio calculated form the carbon *K*-edge spectra is almost doubled with plasma treatment (~0.25 to~0.5) and are in accordance with the 25 cm^{-1} red shift of the G band in the Raman spectra. Both these findings are fingerprint of the recovery of sp^2 structure. Finally, EFM phase maps showed a distinguishable increase in contrast with plasma treatment. The decrease in phase shift confirms the increase in conductivity of the GO films at the nano-scopic level. Further studies need to be carried out to confirm this observation, along with fabrication of a prototype device exclusively using plasma jet.

Chapter 6. Atmospheric pressure plasma in air sterilization

Development of low temperature and portable technologies for disinfection and sterilization have gained attention for various industrial and medical applications. With the growing application of polymer based accessories in medical fields, plasma based sterilization becomes a topic of interest. Non-thermal plasmas are being explored as a potential technology for this purpose. Atmospheric pressure plasma technology has gained increased interest in the recent past for several environmental applications. This technology can potentially be used to deactivate airborne microbes as well as surface bound microbes and biofilms.

In this work, the efficacy of an atmospheric pressure dielectric barrier discharge (DBD) in air for inactivating airborne pathogens Staphylococcus epidermidis and Aspergillus niger is explored. Scanning Electron Microscopy (SEM) was used to understand the changes in morphology and cell structure of the pathogens. SEM micrographs showed that after exposure to the plasma the cellular structure of both microorganisms was severely distorted. NEXAFS studies also revealed that the chemistry at the surface of microbes changed upon interaction with excited species in the DBD. These changes were found to be responsible for the effective deactivation of the microbes. The Novel aspect of this enquiry is that it addresses airborne pathogens.

6.1 Introduction

Surface disinfection and sterilization using various non-thermal plasma sources is a well-established technique. [99] Low temperature plasmas have been found to be most suitable for surface sterilization of polymeric accessories which are either sensitive or susceptible to high temperature processes. Atmospheric pressure plasmas have already been investigated as an alternative approach for sterilization of surfaces, medical devices and surgical tools. [271–273] The efficiency of various atmospheric pressure plasma based tools in sterilization can vary according to the method of plasma generation, gas mixtures in the plasma, flow rates of input gases , gas temperature and treatment area. [274,275] Liu *et al.* [276] studied surface bacterial sterilization by an atmospheric non-thermal plasma jet. The deactivation

mechanism was mainly attributed to the active species in the plasma, as the temperature was characterized to be below 35 °C.[276] Similarly, literature is also available on the sterilization effect of atmospheric pressure helium/argon/oxygen plasmas on surface bound bacteria. [98,277,278] Weltmann *et al.* [279] showed that a radio frequency (RF) driven atmospheric pressure plasma jet with argon as the gas source can be used for antimicrobial treatment on catheters. As catheters are prone to pathogenic attacks. According to them the microbicidal effects of plasma are mainly due to the UV and VUV radiation as well as the reactive oxygen species.[279] Several groups have also studied the effect of atmospheric pressure plasmas that use helium or argon gas as a primary plasma source, on surface bound *S. epidermidis*. [280] All the above mentioned setups possess a drawback in the form of the need for an external gas supply, which reduces the portability of the equipment and also increases the running cost. One way to overcome this disadvantage is to use ambient air as the primary gas source. The reactive species in an air plasma should be comprised of reactive oxygen, reactive nitrogen, ozone, hydroxyl and nitrogen oxides. Studies by Klämpfl *et al.* showed that non thermal atmospheric air plasma can be used to sterilize spores and microorganisms. [281]

Most of the recent plasma technologies are for surface sterilization and there does not appear to be any work done to establish atmospheric plasmas for inactivation of airborne pathogens. DBD for airborne microbial inactivation is an entirely new approach .The use of atmospheric pressure plasmas for environmental applications in ambient air by eliminating the need for any use of additonal gas supply. Here DBD based atmospheric pressure plasma has been employed to develop a prototype device that can run continuously without any manual interference for deactivating air borne microbes in principle for days on end.

The focus of this study is to establish the ability of the DBD to deactivate airborne pathogens like *S. epidermidis* and *A. niger* and to study its morphological and chemical changes upon treatment. *S. epidermidis* nebulized in air was exposed to the DBD and the

bacterial sample collected from air was examined for detailed analysis. *Staphylococcus epidermidis* is a Gram-positive bacterium that colonizes the human epithelium. *S. epidermidis* emerges as an opportunistic pathogen and a common cause for nosocomial infections leading to chronic diseases.[282,283] These microorganisms are known to form biofilms on medical implants and catheters. [284–286] *S. epidermidis,* a coagulase-negative *Staphylococcus* is a leading cause of infection in immune compromised, long-term hospitalized and critically ill patients. [287,288]

Airborne fungal spores can cause allergies as well as serious hospital-acquired infections. *A. niger* is one of the most common groups of fungi, and causes problems for the food and medicine industry, this makes it a suitable candidate for study. *A. niger* is also known to affect human respiratory system causing Aspergillosis. And can be potentially life threatening for people with weak immune system. Reported deactivations processes include UV- light treatment [289], high pressure heat shock [290] , photocatalytic inactivation[291] . Raballand *et al.* used low pressure oxygen plasma along with Ar^+ bombardment for the inactivation of *A. niger*. [292] These processes independently didn't have any noticeable impact on the fungal spores. Another technique includes chitosan, a polysaccharide known for its anti-fungal activity. Chitosan is reported to cause molecular disorganization and structural alterations of the cytoplasm and structural membrane of the Fungus. [293,294] Plascencia-Jatomea *et al*., carried out the effect of chitosan and temperature on *A. niger* and also reported morphological anomalies of the spore upon treatment with chitosan .[295] But none of these reported processes involved decontamination of fungal spores suspended in air. Hence, the present study is focused on the systematic effect of air based DBD (with no additional gas supply) on airborne bacteria and fungus.

This study provides a detailed morphological and spectroscopic analysis of the impact of DBD on aerosolized *S. epidermidis* and *A. niger*. DBD for airborne microbial deactivation

is a radically new approach in exploring the use of atmospheric pressure plasmas by eliminating any process gas requirement and developing a process that can run continuously without any interference.

6.2 Experimental details

Test pathogens

The pathogens used in this study were purchased from ATCC (*Staphylococcus epidermidis* ATCC 14990, *Aspergillus niger* ATCC 15475 and phosphate buffered saline ATCC SCRR-2201), Becton Dickinson (nutrient broth BD 213000, nutrient agar BD 234000 and potato dextrose agar 213400), Sigma – Aldrich (ethyl alcohol 459844, glutaraldehyde G5882, hexamethyldisilazane 440191) and Ted Pella Inc. (osmium tetraoxide 18466).

Culture conditions:

Cultures of *Staphylococcus epidermidis* were grown in a nutrient broth at 37 °C, spun at 200 rpm until the cultures reached a mid-log phase. Log phase is referred in **Figure 6.1**. During this phase, the bacteria multiply exponentially to attain a stationary phase. After incubation, 100 µl of the bacterial suspension was used for plating on nutrient agar after suitable dilutions. After 16 hours of incubation, the colony forming units were counted. Aliquots of the mid-log phase cultures were then centrifuged at 1000 rpm for 10 minutes. The supernatant was discarded and the cells were re-suspended in distilled water.

Aspergillus niger was inoculated in sterile distilled water and incubated overnight at room temperature for propagation. *A. niger* spores were harvested aseptically in potato dextrose agar and incubated for 5 days at 24 °C. Individual spores were then isolated to conduct DBD studies.

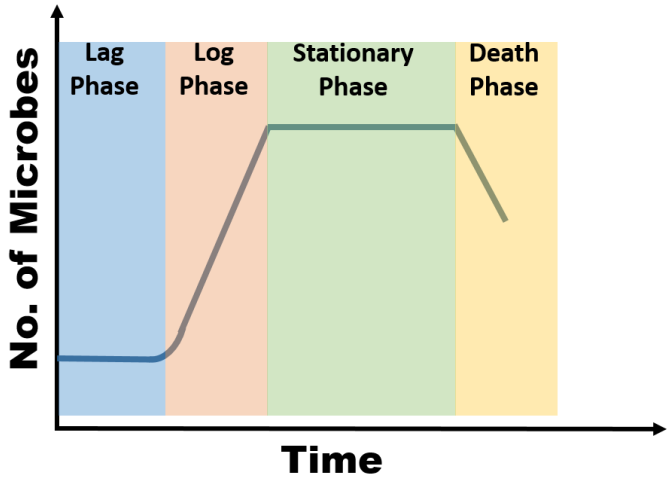

Figure 6.1 Bacteria growth curve showing different phases of bacterial life cycle. Microbes considered for this study were in log phase which is deemed as the most active phase of the bacterial life cycle.

6.3 Experimental setup

A compressor nebulizer was used to aerosolize bacterial cultures and spores into the DBD system for sterilization testing. The DBD system used for this purpose consisted of two coaxial cylindrical coils made from stainless steel (AISI:304) wires of 0.2 mm diameter. The coils were separated by a borosilicate glass tube, that acted as the dielectric barrier. The Dimensions of the glass tube being length = 80 mm, internal diameter = 22.5 mm, and outer diameter = 28 mm. The spores and microorganisms were nebulized using OMROM

Compressor nebulizer model NE-C29-E and the entire setup was kept inside a Bio-Safety Cabinet (Nuaire, Class II, Type A2, Model NU-425-400), shown in **Figure 6.3**. A high alternating voltage (4 kV) was applied between the electrodes to create the surface plasma discharge. The DBD system was equipped with a fan to draw the aerosolized output from the nebulizer. All the DBD system vents except the top one was sealed to prevent any undesired micro- organism from getting into the system.

The samples containing *S. epidermidis* and distilled water of quantity 1 ml was transferred to the compressor nebulizer. The aerosolized bacterial suspension was then passed through the discharge via the top input and any viable particles after DBD treatment were collected at the output on sterile silicon wafers. Concomitantly, the fungal suspension containing *A. niger* spores and distilled water of quantity 1 ml was transferred to the compressor nebulizer and recirculated through the DBD system. Any viable spores were collected at the output of the system on previously sterilized silicon wafers.

Statement:

The plasma system shown in **Figure 6.2** already existed at NASA. My contribution included helping in replicating the experimental setup reported previously by Dr. Gandhiraman [296], and analysis of the plasma treated pathogens to understand the efficacy of atmospheric pressure dielectric barrier discharge for inactivating airborne pathogens.

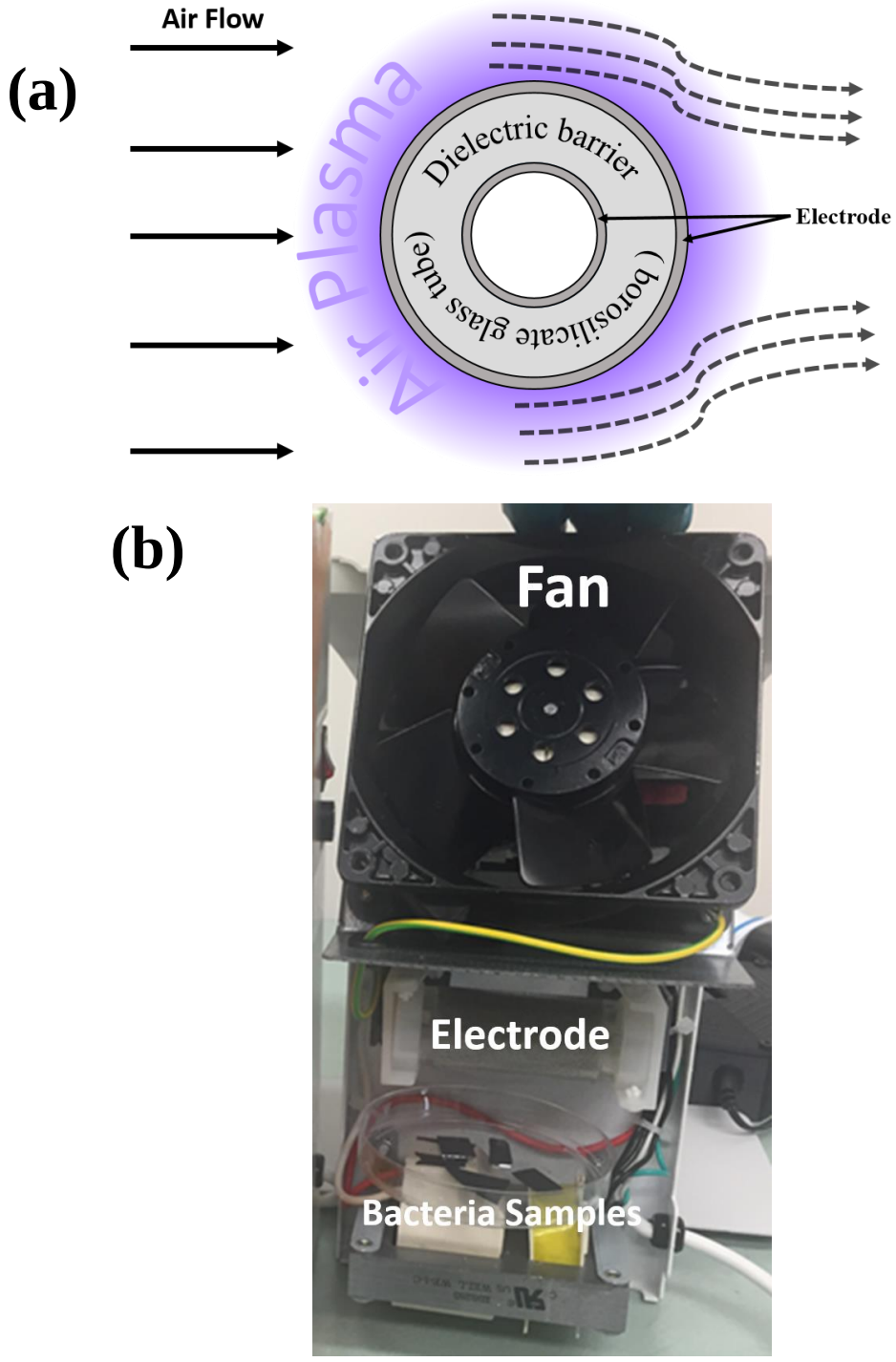

Figure 6.2 (a) Schematic of the plasma sterilization process (b) Prototype device for air sterilization. [N.B. refer to Attributions]

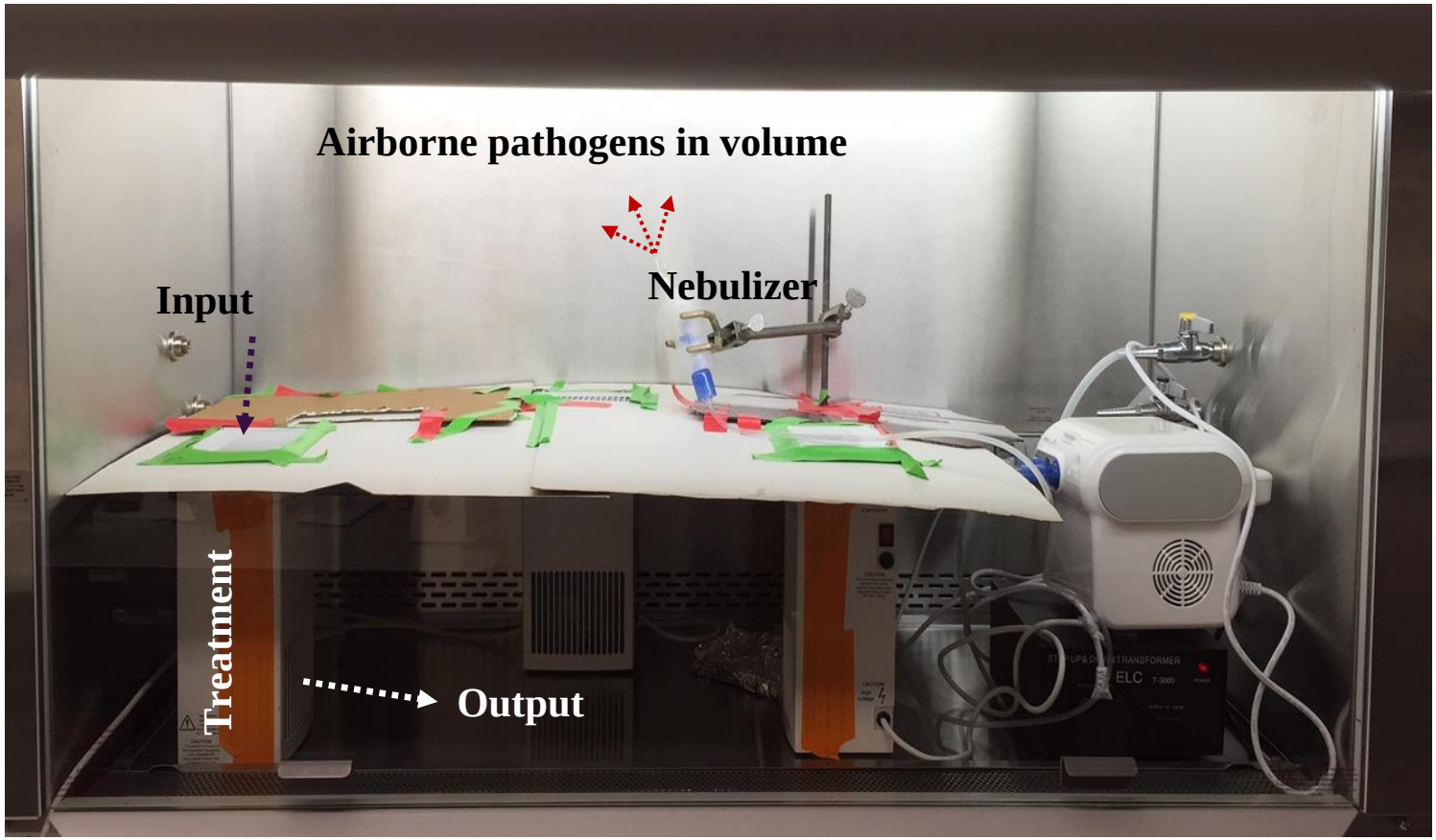

Figure 6.3 Setup to simulate the airborne microbial decontamination in a biosafety cabinet. Pathogens are made airborne by the compressor nebulizer . Three treatment units are setup to disinfect the air inside the biosafety cabinet. [N.B. refer to Attributions]

6.4 Sample preparation for characterization.

To image the bacterial cells using scanning electron microscopy (SEM), bacterial cells were fixed on to silicon wafer using the following process. The protocol included fixing in a solution of 2.5% Glutaraldehyde in Phosphate Buffered Saline (PBS) for 2 hours. To improve the contrast during SEM imaging the samples were post fixed in a 2% Osmium Tetroxide in PBS for 1.5 hours. The samples were then dehydrated in graded concentrations of ethanol (60 to 100 %) for 50 mins (10 mins each) and finally chemically dried with Hexamethyldisilazane for 5 minutes. To prevent the fixed samples from reacting with water and humidity, they were placed in a vacuum desiccator overnight.

The fixation of fungal spores was carried out in a similar way. Here, aerosolized spores were first deposited in previously sterilized 1cm×1cm bare silicon wafers. The spores were then fixed in a 2.5% Glutaraldehyde solution in phosphate buffered saline during 2 hours. After the first fixation procedure, the samples were rinsed with phosphate buffered saline and then, a 1% Osmium tetroxide solution in phosphate buffered saline was used as a second fixative process for 1 hour and 30 minutes. The samples were then dehydrated in gradually increasing concentrations of ethyl alcohol ranging from 60% to 100% for 50 minutes and exposed to hexamethyldisilazane for 5 minutes.

SEM imaging was performed using S4800 scanning electron microscope (Hitachi, Pleasanton, CA). Single side polished silicon wafers were used as substrates. To avoid the charging effect all the samples were coated with a 10-nm layer of gold. X-ray absorption spectroscopy was also used to understand the changes in surface chemistry of bacteria. Near edge X-ray absorption fine spectroscopy (NEXAFS) measurements were carried out at beamline 8–2 (bending magnet endstation, spherical grating monochromator) of Stanford Synchrotron Radiation Lightsource (SSRL). [147] The incoming flux was monitored using a

gold grid placed in the beam path upstream of the chamber. To carry out the measurements, the samples were mounted on an aluminium stick and placed in UHV chamber ($<1 \times 10^{-8}$ Torr). The chamber equipped with a PHI 15–255 G double pass cylindrical mirror analyser which was mounted perpendicular to the incoming beam axis in the horizontal plane. All the measurements were carried out at the incident magic angle of ~55° (magic angle), and the spectrometer detected electrons emitted along the e-vector of the incoming radiation. NEXAFS spectra were normalized 20–30 eV above the ionization potential after dividing by the incoming flux measured at the gold grid. XAS data was analysed using Igor Pro software. For this XAS measurements bacterial samples collected on silicon wafer were freeze-dried using Labconco's Free Zone 4.5 Litre Freeze Dry System.

6.5 Results and discussions

6.5.1 Scanning electron microscopy

Staphylococcus epidermidis samples were drop-cast on silicon wafer, fixed using standard protocols and imaged under SEM. **Figure 6.4 (a)** reveal the size, shape and morphology of the bacteria. From the SEM images it is very evident that the *S. epidermidis* bacteria has dimensions of less than 1µm and the microorganism's size varied from 500 nm to 1µm in diameter. As a control test, *S. epidermidis* was aerosolized and passed through the DBD system with both the fan and DBD turned off. When compared with bacterial samples drop-cast on silicon, it is observed that the bacteria retained its shape, size and morphology as shown in **Figure 6.4(b)**. As already mentioned, this setup consists of two separate units, one for the fan that pulls the air towards the discharge and another for the electrodes that create the discharge. When the actual inactivation process takes place, both the fan and the DBD should be turned on simultaneously. With the fan turned on, the airborne microbes will be effectively pulled towards the discharge. To realize the effect of fan, another experiment

was performed with DBD turned off and fan turned on. Herein also the SEM images showed no visible changes in the morphology of the bacteria **Figure 6.4(c)**. Thus, it is evident that the fan unit along with the aerosolizing process doesn't affect the morphology of the bacteria. To achieve the actual deactivation, the microorganisms were passed through the system with both DBD and fan turned on. **Figure 6.5 (d), (e), (f)** Shows that *S. epidermidis* has lost its spherical shape and the cell structure is damaged severely resulting in complete distortion of the cell morphology. Its apparent from the SEM images that the bacteria undergo severe structural damage, resulting in breakage of cell structure. Its noteworthy to say that not all microbes undergo structural damage to the same extent.

To demonstrate the potency of this system spores of *A. niger* were fed to the DBD system similar to *S. epidermidis.* It was found that the results were as promising as *S. epidermidis.* The fungal spores which are hard to annihilate were completely deformed after passing through the plasma discharge. **Figure 6.6** (a), (b), (c) shows the SEM images of spore of *A. niger* before being passed through the plasma discharge. It is evident from these images that the spores were spherical in shape and were clumped, probably indicating polarity. [295] **Figure 6.6** (b) shows the fungus with conidiophore present at an imaging resolution of 2 micrometres. It is evident from **Figure 6.6** (c) that the spores were echinulate. A similar observation was made by Plascencia-Jatomea *et al.*, in their work on chitosan based anti-fungal activity and attributed the echinulate spore formation to chitosan affected swelling.[295]

After passing through the discharge the round shaped fungal spores were found to be completely disfigured as shown in **Figure 6.6 (d), (e), (f)**. The morphological anomalies were evident in these DBD treated fungus. High resolution images (**Figure 6.6 (e), (f)**) of DBD treated fungus when compared with that of untreated fungus in **Figure 6.6 (b)** and **(c)**, it is evident that the cell envelope integrity is broken upon DBD treatment. Reduction in size

and severe distortion of the DBD treated spores indicate possible structural damage of the cell envelope, and leakage of cellular contents resulting in breakage of spores.

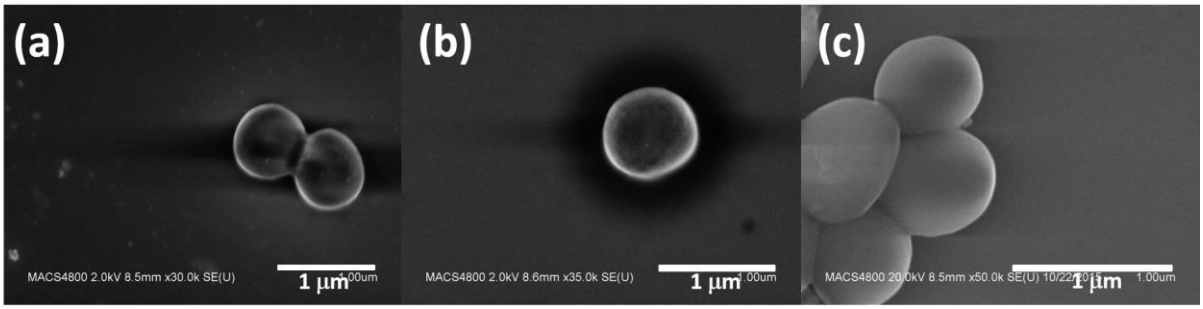

Figure 6.4 SEM images of (a) drop cast Staphylococcus *epidermidis* on silicon wafer , (b) aerosolized and collected in a silicon wafer with both DBD and Fan OFF ,(c) aerosolized and collected in a silicon wafer with just Fan ON. [N.B. refer to Attributions]

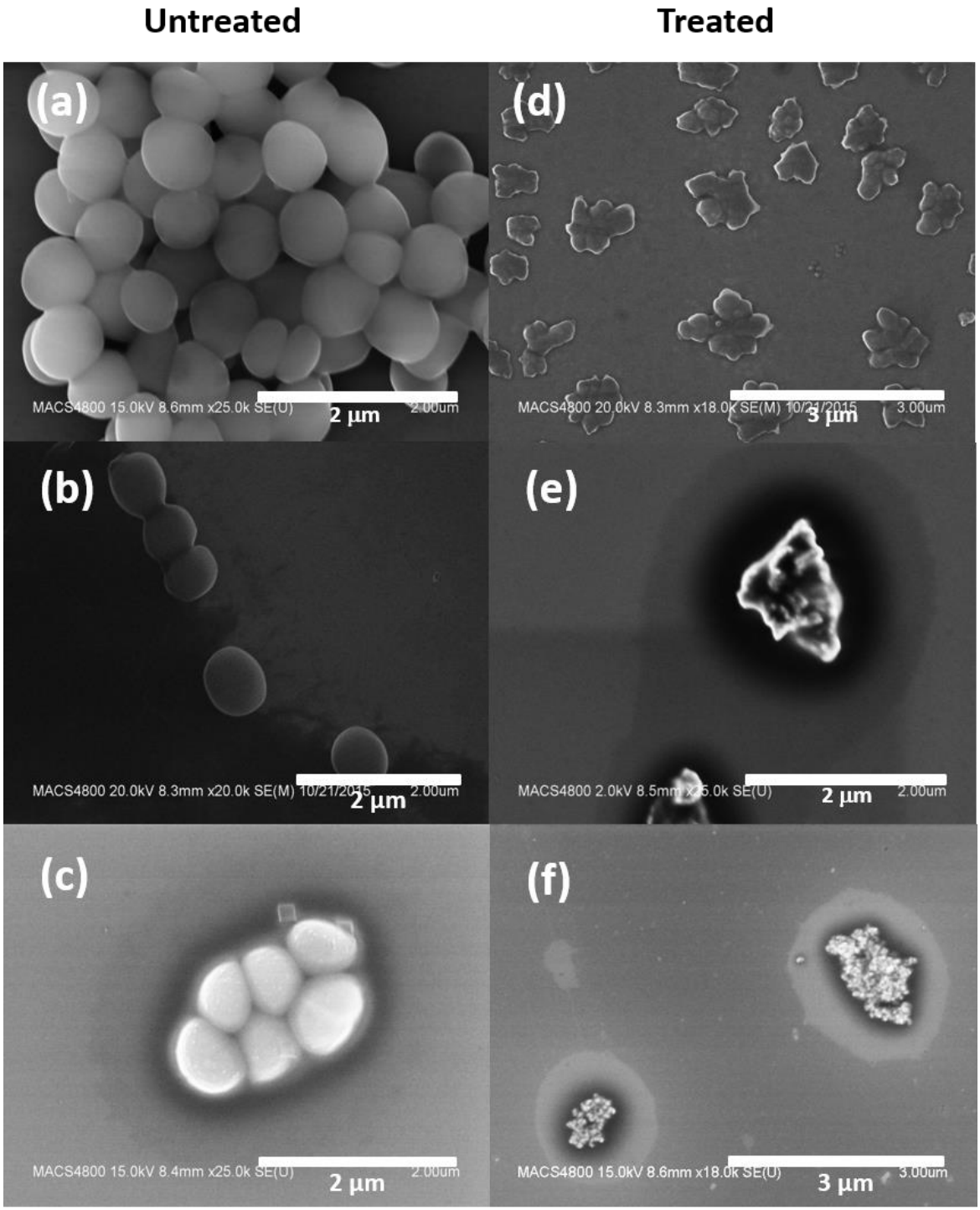

Figure 6.5 SEM images showing the morphological changes in *S. epidermidis* after passing through the discharge. [N.B. refer to Attributions]

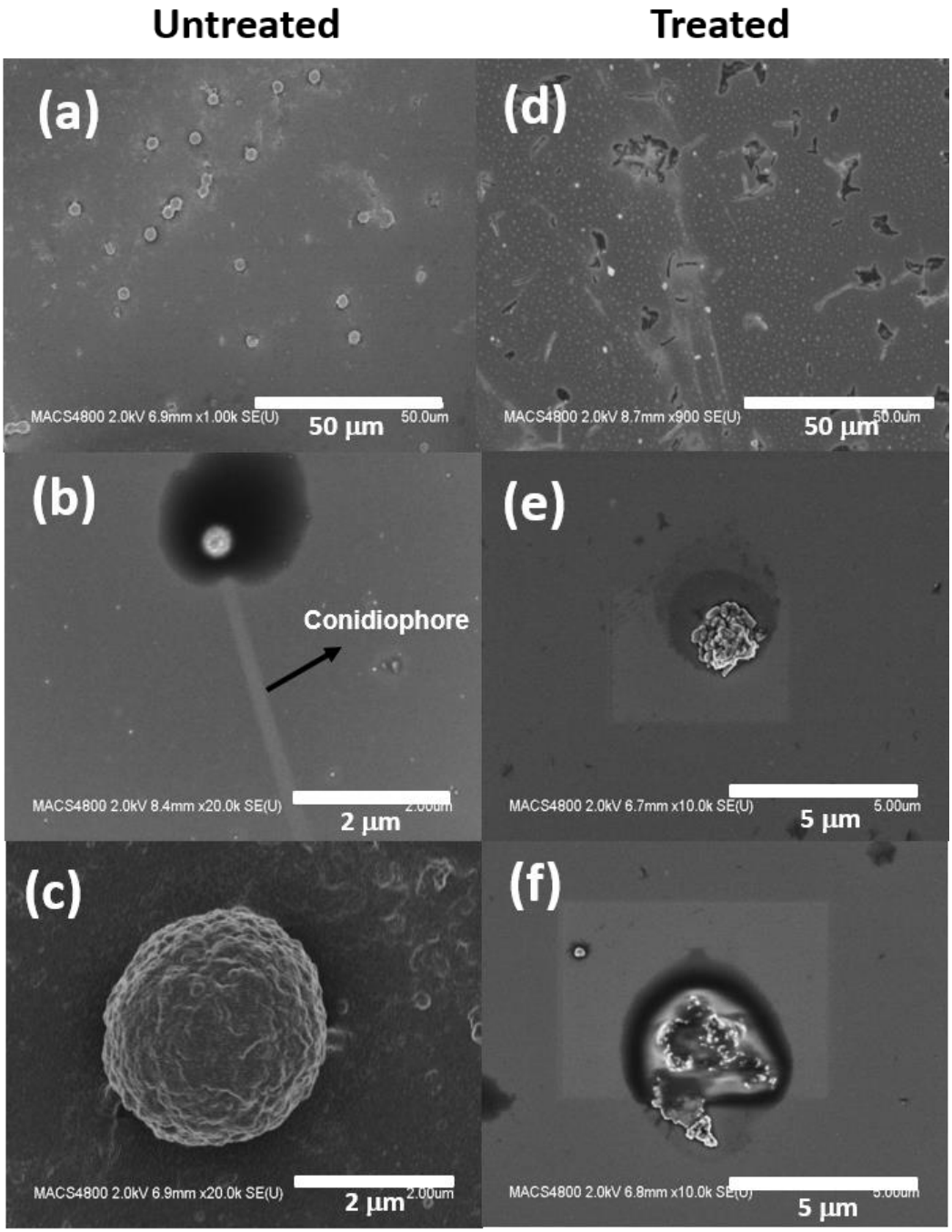

Figure 6.6 SEM images showing the morphological changes in *A. niger* after passing through the discharge. [N.B. refer to Attributions]

6.5.2 X- ray absorption spectroscopy

In addition to the structural distortions of the bacteria it is important to know whether plasma is able to induce changes in the chemical environment of the bacteria. As the functional groups and the bonding structure are the building blocks of a bigger chemical structure associated with the microorganism. NEXAFS being highly sensitive to the local chemical assembly, is an important tool to probe the minute chemical changes occurring in the framework of the bacteria.

For NEXAFS four different set of samples were prepared. Where sample (a) bacterial suspension dropcast on silicon wafers, sample (b) bacterial solution aerosolized and collected on silicon wafers, sample (c) bacteria collected after treatment where both fan and plasma is on (DonFon), sample (d) bacteria collected after treatment where only plasma is on (DonFoff). **Figure 6.7** shows the carbon K-edge NEXAFS spectra of these four different bacterial samples. Similarly, oxygen K-edge and nitrogen K-edge of same set of samples is presented in **Figure 6.8** and **Figure 6.9** respectively. For each sample spectra were collected at five different areas on the substrate. It is hard to negate the contribution of carbon and oxygen contaminants from the substrate and from ambient exposure. Thus, the precise determination of spectral contribution from the bacteria will not be a good approximation. But the difference in the spectral signature of untreated and DBD treated bacteria should be a strong enough evidence for the claim.

It is evident from these plots that with the exposure to plasma the chemical functionalities at the surface of bacteria can be changed. The uniformity of plasma functionalization also depends on the extent of exposure. When the fan is on, the duration of interaction of the bacteria with plasma is non-uniform with respect to the fan off condition. In the fan off state the bacteria have an extended interaction with the plasma, resulting in consistent spectral signature throughout the substrate. Apparent from the oxygen and carbon

spectra (DonFon & DonFof). There is a marked dissimilarity between the spectral signature at different places on the substrate when both the plasma and the fan were on. Evident from the π* transitions below the continuum, showing contribution form dissimilar chemical functionalities.

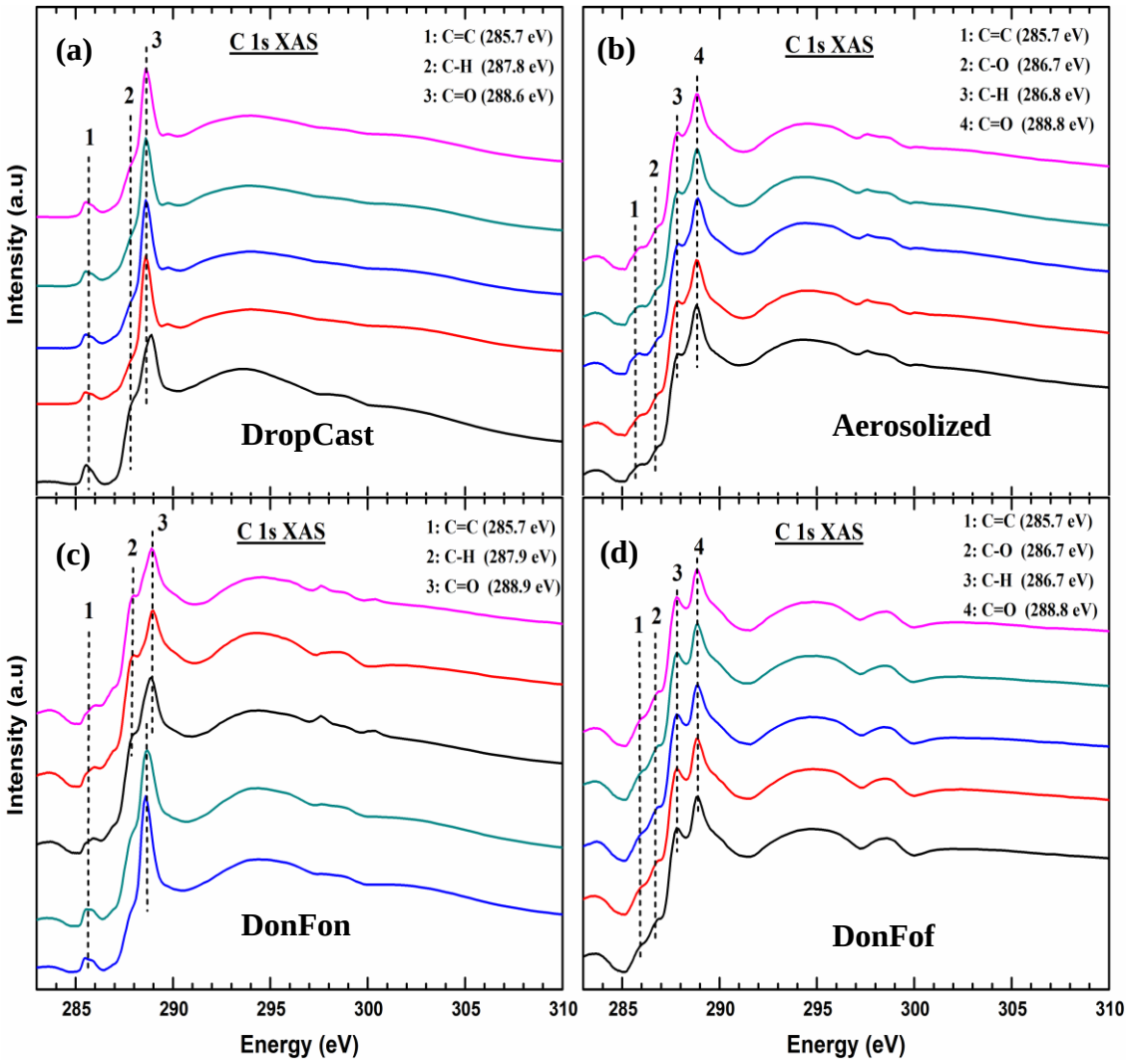

Figure 6.7 C K edge XAS spectra of bacteria (a) dropcast on silicon (b) aerosolized on silicon (c) Treated with plasma and fan being on (DonFon) (d) Treated with plasma with fan off (DonFof). Individual colours in the spectra represent averaged spectral signature from individual substrate. Five colours are representative of five differrent substrates. [N.B. refer to Attributions]

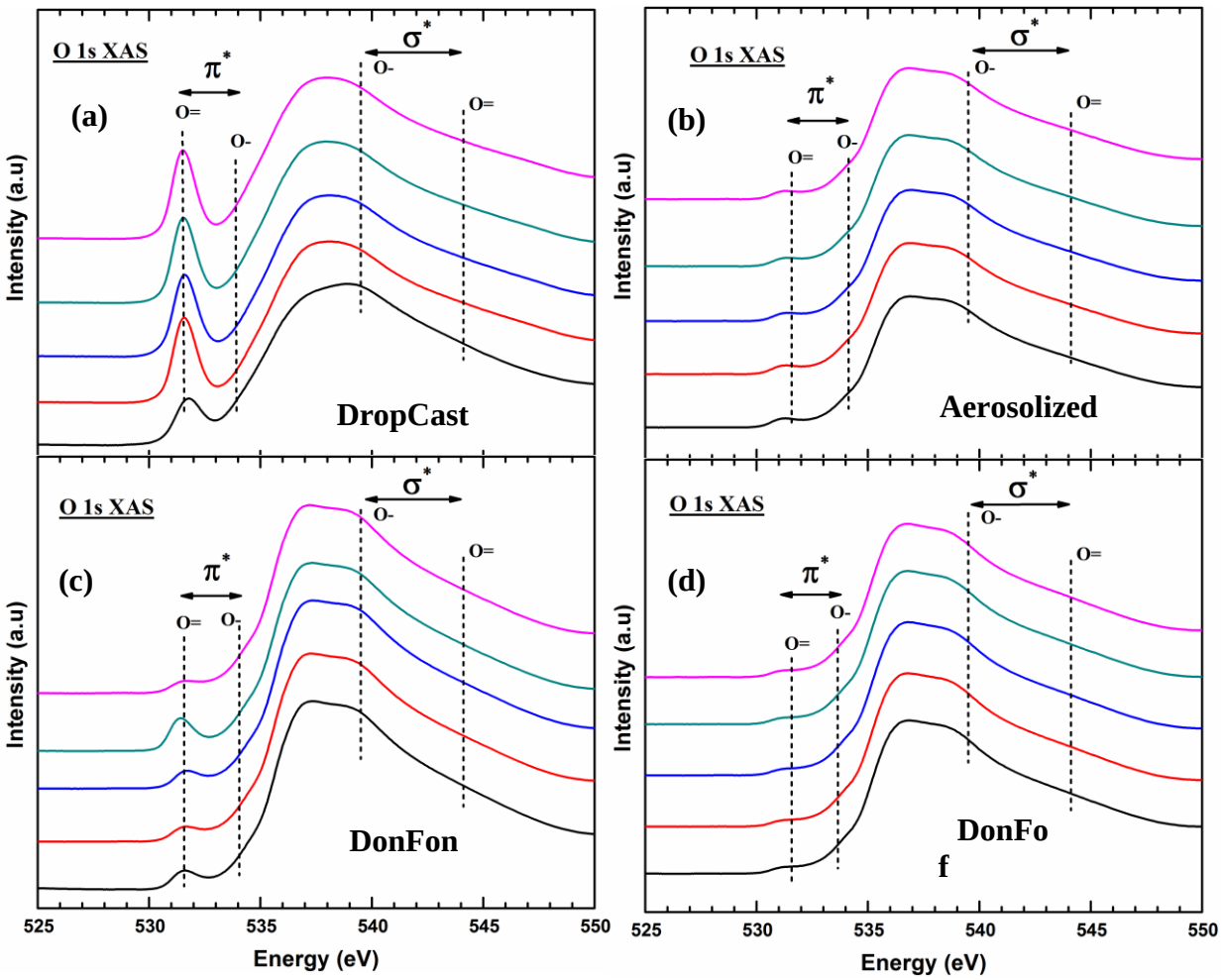

Figure 6.8 O K edge XAS spectra of bacteria (a) dropcast on silicon (b) aerosolized on silicon (c) Treated with plasma and fan being on (DonFon) (d) Treated with plasma with fan off (DonFof). Individual colours in the spectra represent averaged spectral signature from individual substrate. Five colours are representative of five differrent substrates. [N.B. refer to Attributions]

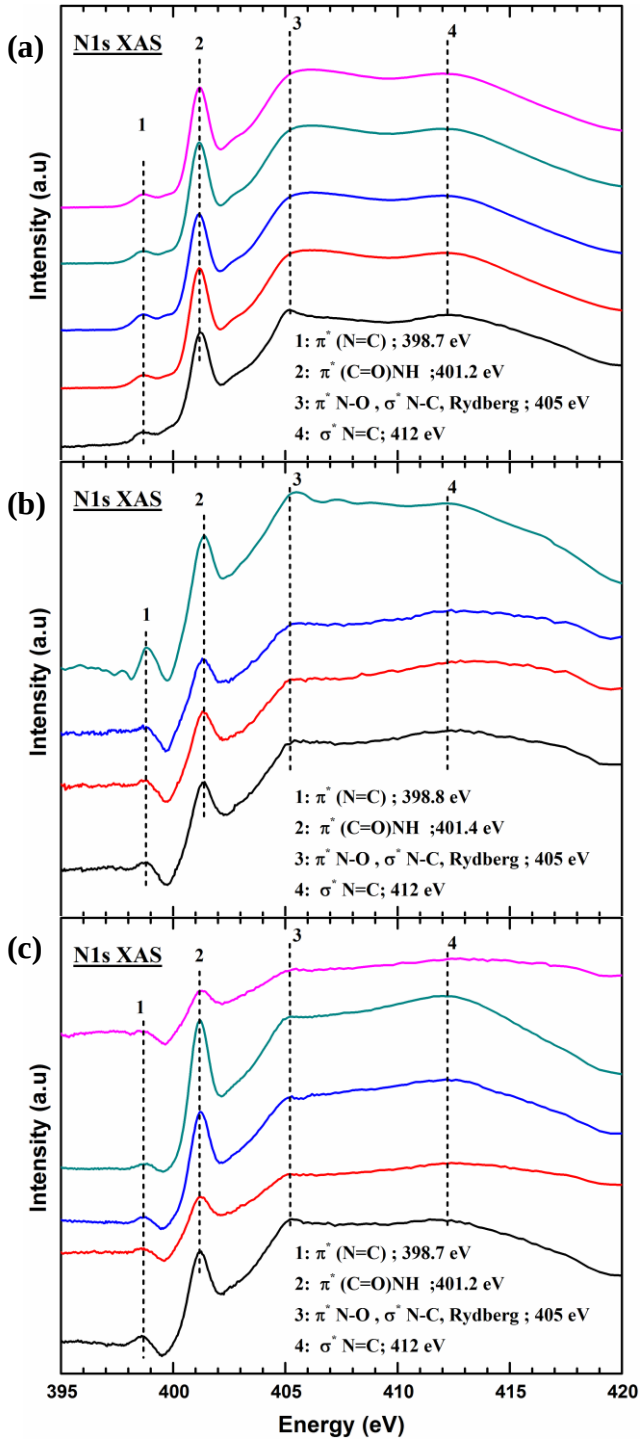

Figure 6.9 N K-edge XAS spectra of bacteria (a) dropcast on silicon (b) aerosolized on silicon (c) Treated with both plasma and fan being on (DonFon) . Individual colours in the spectra represent averaged spectral signature from individual substrate. Five colours are representative of five differrent substrates. [N.B. refer to Attributions]

NEXAFS spectra from each functionalized state at the carbon K edge, nitrogen K edge, and oxygen K edge (absorption edges) are shown in **Figure 6.10** , **Figure 6.11** and **Figure 6.12**. respectively. Changes in the surface chemistry between the treated and untreated states can be perceived from these spectra. To elucidate the changes in surface chemistry after exposure to plasma, average spectral signature form three different substrates (DonFon) are compared with the control sample (Aerosolized).

In the carbon spectra (**Figure 6.10**) the peak at 285.6 eV of all the samples correspond to π* C=C transitions. The intensity drop around 285 eV may be due to the effect of normalization of the spectra as it matches with carbon dip (284.7 eV) from the beamline optics, which arises due to the presence of amorphous carbon in the beam path. If the sample is thin, then the influence of carbon dip becomes substantial with respect to the signal from the sample. All the spectra were area normalized. The shoulder at 286.7 eV, relatively prominent for treated sample and corresponds to the contribution from π* (C−OH) and π* (C−O−C) transitions. The control sample shows negligible presence of aliphatic carbon (C−H) species, peak at 287.9 eV. Whereas after plasma treatment there is significant presence of aliphatic carbon at the surface. Thus, the increase in intensity at 287.9 eV can be related to the breaking of C=C bonds to form C−OH, aliphatic C−H & C−O−C species at the surface. The intense peak at 288.5 eV for the untreated bacteria arise from the π* (C=O) transitions and can be from either −COOH or $-CONH_2$ moieties. Studies by Gordon *et. al*. on inner shell excitation spectroscopy of the peptide bonds and proteins revealed that the π* (C=O) transitions occurs between 288.2 and 288.6 eV. For the treated samples a shift of 0.4 eV is observed for π* (C=O) transitions relative to the control sample. This red shift can be attributed to the increase in electronegativity of the carbonyl core induced by neighbouring atoms as reported by Urquhart and Ade. [297] Edwards and Myneni also reported the same in their NEXAFS studies of bacterial hydroxamate sidephores in aqueous solutions. [298] The peak at 289.4 eV for the control sample could be due to various functional groups. As C–H

and O-alkyl C groups in polysaccharides/carboxylic acids or CNH all have σ* transitions at this energy value. [299,300] The broad peak in the region of 292- 295 eV for all the samples comprises of multiple σ* transitions, e.g C–N in amino acids (291 eV) [301] and C–O in alcohols and carboxylic acids (292.5 eV). [302,303] A small peak at 297.5 eV likely due to σ*C−OH transitions is visible for the DBD treated state but not consistent throughout the substrate. The broad peak around 304 eV for untreated bacteria corresponds to σ*C=C transitions. It's evident from the C1s spectra that there is a definite disruption of C=C bonds in the chemical structure of the bacteria.

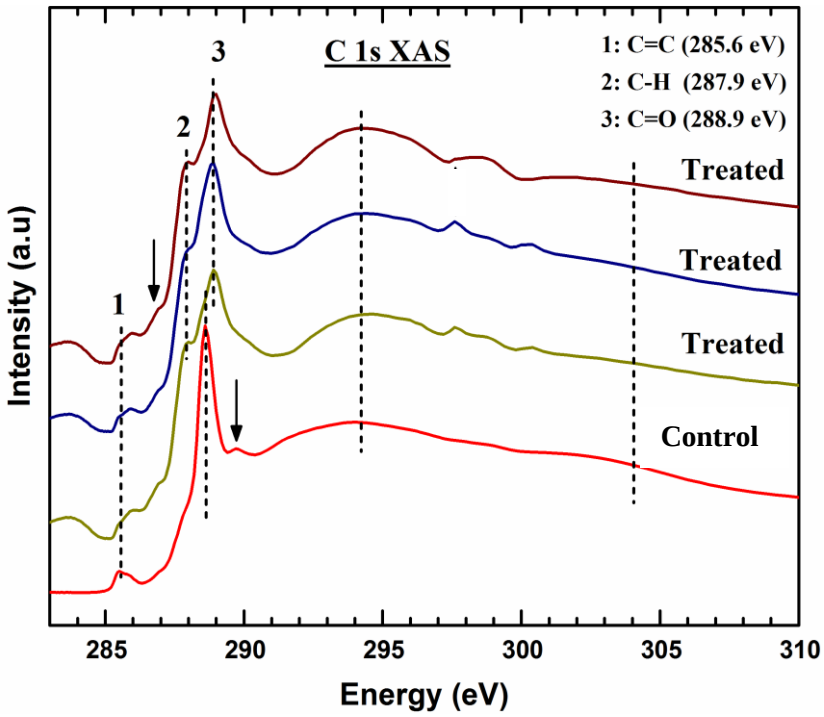

Figure 6.10 Comparison between the C K-edge NEXAFS spectra of DBD treated and control samples. Each treated spectrum corresponds to the average contribution from individual substrates. [N.B. refer to Attributions]

The O K-edge spectra for control sample exhibit an intense peak at 531.6 eV corresponding to π* transitions of oxygen double bond moieties, which has considerably decreased after DBD treatment (**Figure 6.11)**. According to Gordon *et al*. this peak can be attributed to O1s to π* transitions of C=O groups of COOH and $CONH_2$ functionalities. In turn the absorption due to O- groups (single bond) has increased (~534 eV) . Both C1s and O1s spectra indicate to the decreased concentration of C=O groups with respect to the control sample. The untreated sample shows a broad peak around 536 to 540 eV. Which can be due to contributions from multiple transitions comprising of Rydberg transitions, σ*O–H and σ*C–O transitions. [299,302,304]. After DBD treatment this broad peak can be clearly resolved into two peaks centered around 537 eV and 539 eV. According to previous report by Mangado *et al.* this peaks can be designated to σ*O–H and σ*C–O transitions respectively. [296]

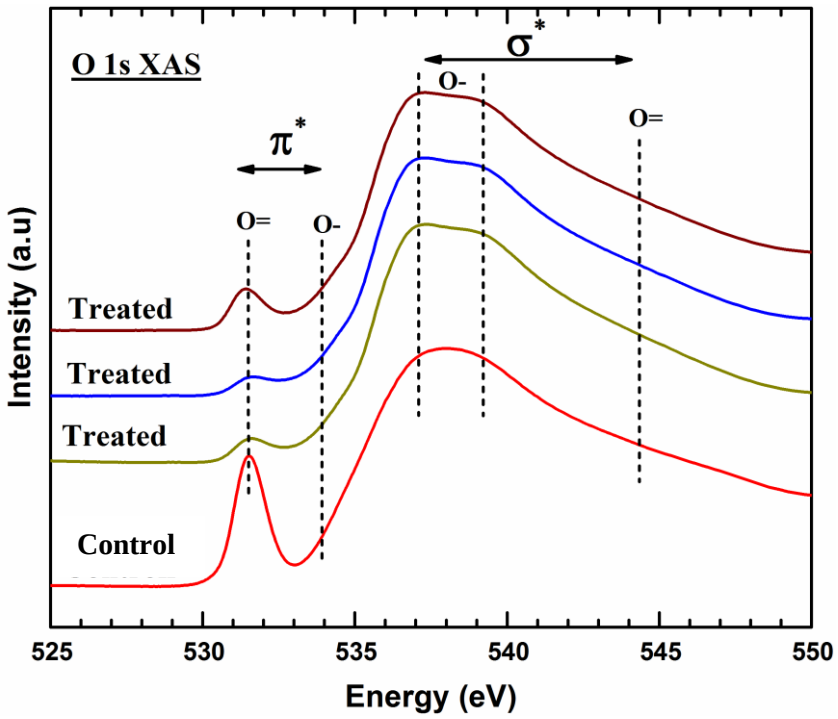

Figure 6.11 Comparison between the O K-edge NEXAFS spectra of three different DBD treated samples and a control sample. [N.B. refer to Attributions]

Figure 6.12 depicts variations in N K edge after DBD treatment. Special care was taken to plot the nitrogen spectra. Individual spectra were aligned to the nitrogen dip and then energy calibrated with respect to the second order Ni2*p* at 426.35 eV. The resonance features from nitrogen were particularly less intense for the DBD treated samples. Suffering from the low coverage of bacterial samples on the silicon wafer. To gain a better insight into the spectral features, all spectra were area normalized. A low intensity peak at 398.7 eV corresponds to N1s to π* transitions of N=C configuration. The intense peak around 401.5 eV can be related to the π* electronic transitions of amide group {(C=O) NH}. The decrease in intensity of this peak is consistent with the C1s and O1s spectra. Where a reduced concentration of C=O functional groups have also been observed. The peak around 405 eV is noticeably sharper after DBD treatment. For the untreated sample this broad peak can be arising from multiple transitions including σ^*_{N-C} and Rydberg transitions. [299,305] The sharpening of this peak after DBD treatment is likely due to the increased concentration of nitro groups (O-N=O) at the surface of the bacteria. The broad peak around 412 eV can be designated to the σ* (N=C) transitions in accordance to the reported value of Shard *et al.*[306] Another peak can be observed around 417 eV which is absent for untreated bacteria and is possibly due to σ* (N=O) transitions. Similar to the carbon and oxygen edge feature nitrogen functionality has also changed with respect to the pristine chemical architecture of the bacteria.

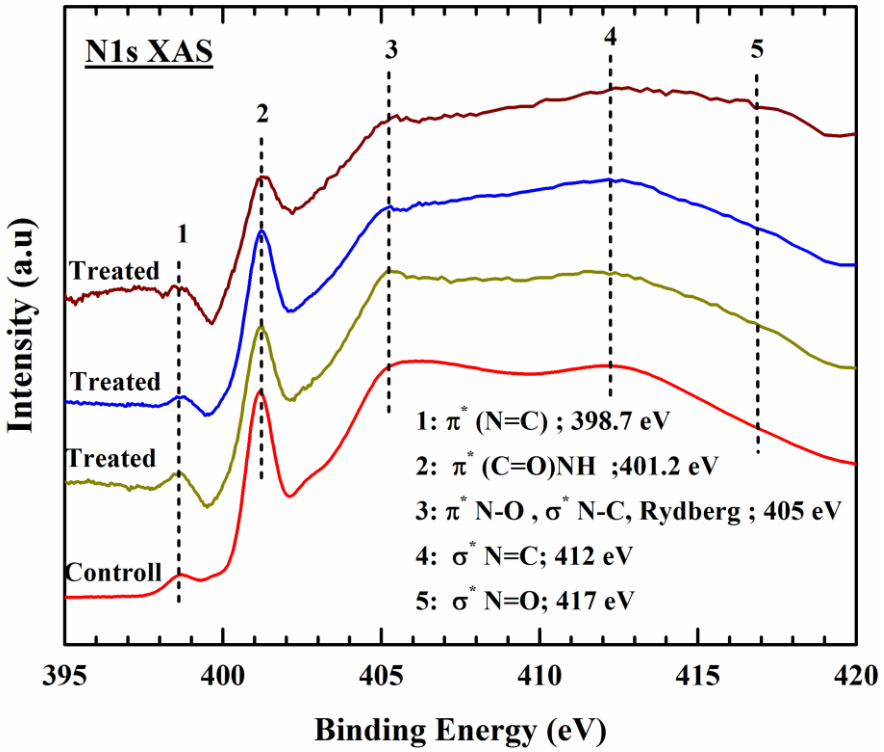

Figure 6.12 Comparison between the N K-edge Nexafs spectra of DBD treated and control samples. [N.B. refer to Attributions]

Although it is hard to deny the contribution of contaminants from the substrate and the limited spectral contrast that is observable for our low bacteria coverage on the silicon, the exposure to the plasma modifies not only the morphology but also the chemical functionalities at the surface of the bacteria. The carbon, nitrogen and oxygen bonding environments at the surface of the microbes clearly changed upon treatment with DBD. Atmospheric pressure plasmas sustained in ambient air contains short lived and highly reactive nitrogen and oxygen species like ozone, hydrogen peroxide, hydroxyl radical, and various NOx species. These active species can directly or indirectly affect the structure and function of proteins, lipids, and nucleic acids (DNA damage).[102] This is evident from increased signal intensity of single bonded oxygen bonds including OH and CO in O K edge

XAS. Also, a sharp rise in 405eV peak, in the nitrogen spectra, corresponding to a π* transition of a nitro group is a clear evidence of oxidation of the cell surface. Both the reactive nitrogen and oxygen species have been reported to cause irreversible cytoplasmic membrane damage and damage of the cell integrity eventually causing bacterial death.[307] NEXAFS for the *S. epidermidis* revealed that the deactivation resulted from damage to the chemical backbone at the surface. The changes in molecular environment of C–O, C–N, and C–C bonds are evident from the NEXAFS spectra. We attribute these changes to hydrogen bonding as can be seen from C K edge peak at 287.8 eV and the gradual disappearance of O π* from O K edge. Much work needs to be done in order to completely understand the mechanism behind these novel systems.

6.6 Conclusion

In this work, the efficacy of the atmospheric pressure dielectric barrier discharge (DBD) technology for inactivating airborne microbes was explored. A systematic study was carried out to understand the effect of DBD on the morphology of *S. epidermidis* and *A. niger*. The aerosolized bacterial samples were collected from air in the vicinity of DBD and was analysed for surface chemical changes and morphological changes upon DBD treatment. The scanning electron microscopic imaging of the *S. epidermidis* show that the bacteria undergo physical distortion to varying degrees resulting in loss of cellular materials. SEM images shows that S. *epidermidis* retains its shape, size and morphology when aerosolized and collected on a silicon wafer. Topographical changes in the structure of the bacteria were observed only after treatment with atmospheric pressure DBD. From the SEM images, it is concluded that the DBD causes severe damage to the cell structure possibly resulting in destruction of cellular components and eventually to cell death. A similar effect was also found on the fungal spores. This indicates the versatility of the equipment toward a range of microorganisms. NEXAFS studies also reveal that after DBD treatment the core

carbon and nitrogen chemistry of the microorganisms has changed. These changes are reflected by the core level shift of C=O species and increased intensity of O- species in the carbon and oxygen spectra respectively. These changes occurring to the surface chemistry of the bacteria may also lead to its deactivation.

Note that the deactivation of bacteria in these experiments was in airborne phase, without any settling onto surfaces and remote from any source of moisture or other substances. Further study with relevant microbes could prove this technology to be a possible alternative approach to air hygiene.

Chapter 7. Summary and Future work

This chapter provides and overview of what has been achieved in this thesis and where the prospect lies for the presented work.

7.1 Thesis summary

The work presented in this thesis focusses on the application of atmospheric pressure plasma for three distinct fields of applications namely printing, functionalization and sterilization. Chapter 1 summarizes the current plasma technologies used in these fields and presents the motivation to develop atmospheric pressure plasma as an alternative to current techniques. The following inferences can be made from the experimental results presented in this thesis.

1) Chapter 3 introduces a novel printing technology using an atmospheric pressure plasma jet (APPJ). Traditional printing technologies such as inkjet/aerosol/screen printing techniques do not alter the physical and chemical properties of the ink. Thus, additional process steps are often required to achieve desired properties. Conductive inks of copper are best suited for printed electronics and have emerged as an alternative to silver. However, copper readily becomes oxidized in the ink stock. An APPJ operated with a suitable gas mixture has the ability to reverse the undesired effect of oxidation. NEXAFS spectra at the copper L-edge provided the necessary evidence that with APPJ printing, the electronic properties of printed copper can be tuned *in-situ*. Both the total electron yield and the florescence yield spectra of the printed copper film showed the same trend. Thus, copper in the bulk and at the surface are in the same chemical state. I-V measurements showed that for an oxide ink after being plasma printed, conductance can be increased by several orders of magnitude. Additionally, the high temperature associated with the plasma also aided grain

growth as evident from the Raman spectroscopy results. Not only the electronic properties, but also the ability to control morphology of the printed films was also evident form the SEM images. By varying the gas mixture in the plasma, films with closed or porous surface can be reproduced. A printing resolution of 200 micrometers has been achieved at this stage with the possibility of achieving higher resolution with further optimization of the system.

2) Graphene Oxide has emerged as a promising alternative to graphene for solution based applications and device fabrications. To realize optimum performance of the fabricated device, GO either needs to be reduced or doped with substitutional impurities. In Chapter 4, a detailed X-ray spectroscopic analysis was presented for GO films doped with nitrogen. The doping was carried out using a low power (4W) rf plasma jet. Such a low power operation has not been reported so far. The reactive nitrogen species in the plasma was found to induce finite changes in the surface chemistry and electronic properties of GO films. Nitrogen introduced by the atmospheric pressure plasma is predominantly in a graphitic configuration with a varying concentration of pyridinic nitrogen. Both XPS and NEXAFS spectra showed that GO underwent gradual de-epoxidation with plasma exposure. During the initial stages of plasma exposure, nitrogen attached to the pre-existing defects. While, with exposure for longer duration, nitrogen substituted for carbon from the graphite structure forming a quaternary nitrogen configuration. The presence of one excess electron in nitrogen significantly distorts the valence band density of states of GO. In addition to these findings, Kelvin probe studies revealed that the bonding configuration can influence the work function of GO. With plasma functionalization, the work function of GO could be varied by 120 mV. This variation has been linked to the nitrogen bonding configuration with the graphitic lattice. With the increase in relative concentration of pyridinic nitrogen the electronic states of GO became electron deficient, inducing a p-type doping effect. However, the gradual increase in graphitic nitrogen increased the electron density of GO leading to an

n-type doping effect. These findings are extremely useful in fabricating heterojunction devices like perovskite solar cell, where GO is used as a charge transport layer.

3) GO is inherently an insulator. It is essential to reduce GO to improve its conductivity. However, reduced GO is harder to disperse in solvents. Conventional methods of GO reduction include chemical and thermal treatments. GO produced via Hummer's method requires multiple steps to neutralize the pH as shown in **Figure 1.5**. Chapter 6 introduces an APPJ based technique to deposit GO from a highly acidic suspension and simultaneously reducing it. This technique, overcomes the multiple intermediate steps required to increase the conductivity of GO. The plasma printer described in Chapter 3 has been used for this purpose. Plasma operated with He and H_2 gas mixture was used to successfully reduce highly acidic GO suspension (pH<2) during deposition. X-ray spectroscopic studies (XPS and NEXAFS) confirmed that the reaction intermediates and the concentration of oxygen functionalities bonded to GO can be reduced significantly after plasma processing. Moreover, the reduced GO films showed enhanced conductivity at the nanoscopic level, as revealed by the electrostatic force microscopy studies. Hence, this technique can be used for depositing conducting patterns of GO for transparent conductor applications.

4) The fourth contribution to this thesis is the study of the efficacy of atmospheric pressure air plasma for the deactivation of airborne microbes (*Staphylococcus epidermidis and Aspergillus Niger)*. Here, aerosolized microbes were exposed to an air plasma and then collected on silicon wafers. The changes in surface chemistry and morphology of microbes were then analyzed using scanning electron microscopy and NEXAFS spectroscopy. Exposure to the plasma was found to modify not only the morphology but also the chemical functionalities at the surface of the bacteria. The chemistry between carbon, oxygen and nitrogen underwent changes, emanating from the interaction with reactive species in plasma. These active species such as ozone, hydrogen peroxide, hydroxyl radical and NOx adversly

affect the structure and functioning of proteins, lipids and nucleic acids (DNA damage). Both the reactive nitrogen and oxygen species cause irreversible damage to the cytoplasmic membrane and disfigure the cell structure, eventually causing bacterial death. From SEM images, these effects are evident in the form of loss in cell integrity. NEXAFS studies at the carbon, oxygen and nitrogen K-edges for the *Staphylococcus epidermidis* revealed that the plasma resulted in damage to the chemical backbone at the microbial surface. The molecular environment of C-O, C-N, and C-C bonds underwent changes that are evident from the NEXAFS spectra. These chemical and morphological changes occurring to the surface of the bacteria lead to eventual deactivation. The findings in this chapter establish atmospheric pressure air plasma as a successful approach to air hygiene.

7.2 Future work

The results presented in this thesis provide evidence that atmospheric pressure plasmas possess enormous potential. The research initiated in this thesis has raised multiple questions that require further investigation to attain definitive interpretations. I would recommend the following activities to extend my research.

APPJ printing

Application of APPJ as a printing technology is a completely new approach and much progress needs to be made in order to compete commercially with the traditional printing techniques. The next step to develop this technology is to address the following issues:

1) **Resolution**: The printing resolution achieved in this work is ~200 micrometres. This value is one order of magnitude greater than that achieved by ink jet printing technology. Hence much progress is needed to be made to achieve a resolution

of < 50 micrometres. However, there are multiple factors that needs to be optimised to achieve this value such as dimension of the nozzle, material of the nozzle, gas flow rates etc.

2) **In-situ measurements**: Findings from NEXAFS spectroscopy provides the necessary evidence of *in-situ* reduction. However, further evidence is required to test this hypothesis. The interaction of active species in plasma with the nanomaterials in the active region (between electrodes) and in the after-glow (beyond electrodes) needs to be investigated. Hard X-rays can be used to probe the nanomaterials both during flight and on the substrate

3) **Influence of plasma temperature**: High temperature of the plasma is crucial in achieving the desired morphology of the deposited film. The temperature of the substrate was found to reach 200 degrees during the printing process. But the precise determination of the plasma temperature could not be carried out during this experiment. Hence to understand the physical properties of plasma and its influence on the deposited film is quite important.

Functionalisation of GO

4) **Magnetic properties of Nitrogen doped GO**: Recent studies have revealed that nitrogen doping triggers ferromagnetism in graphene. Graphitic nitrogen was found to be responsible for influencing the ferromagnetic ground state of Graphene. However, no work has been done to investigate the magnetic properties of nitrogen doped GO. Evidence of any magnetic behaviour in GO would be a breakthrough for GO based spintronics and optoelectronics devices.

7.3 Outlook

7.3.1 Nanomaterial synthesis using APPJ for targeted applications

Nano-dimensional materials are of enormous interest to the scientific community, as their applications are far reaching. Nanostructures of transition metal oxides (TMOs) are of industrial interest due to their wide ranging electronic, chemical and mechanical properties. Properties of TMOs stem from the nature of their valence electrons (*d*-orbital). [308,309] The bonding configuration between the metal and oxygen atoms in TMOs can be ionic, covalent or metallic. Engineered nanostructures of TMOs are crucial for energy conversion and energy storage applications.[310] Atmospheric pressure plasma can be used to synthesize nanostructures (nanoparticles/nanowires) of TMOs following the vapor–liquid–solid growth mechanism. Atmospheric pressure plasma is advantageous over conventional techniques (chemical, thermal and low-pressure plasma), as it is an eco-friendly and low-cost process. Clearly, these will have an impact in reducing the material processing cost and rendering it suitable for industrial implementation. TMOs like TiO_2, CuO, ZnO, Fe_2O_3, MoO_3 etc. known to be photo active i.e. absorb light and generate electron-hole pairs. This property has been used for photocatalytic hydrogen generation as well as to disinfect water. Thus, large scale production of TMOs can be used to address the global challenges of clean water and clean energy.

7.3.2 Fabrication of flexible electronic devices using APPJ

Miniaturization of electronic products and the advancement of the Internet of things (IoT), means that the need to power these devises has grown drastically. Wearable technology is of importance to safety, security, defence and military applications. UK based Juniper Research, projects the number of wearable devices will reach 130 million in 2018 with a market value of $19 billion. Wearable devices are expected to help wireless carriers

drive over $71 billion in additional service revenue by the end of 2020. Integration of wearable technology into military clothing is one of the main policies of the UK Department of Defence. Nanomaterials with dimensions of 1D, 2D or 3D structures possesses exciting opportunities for these wearable technologies.

For future applications, atmospheric pressure plasma jet based deposition will be developed as a novel technique for high throughput fabrication of flexible electronics. This technology would be primarily targeted towards smart clothes and wearables for military and defence applications. Advanced nanostructured materials will be coated onto fabrics in layers from liquid based precursors to yield a complete battery structure. Individual layers will be rigorously tested to achieve the optimum electronic and mechanical properties. This technology will be a game changer in wearable technology for military applications, health care diagnostics, real time intelligence and collection of 'Big Data'.

7.4 List of publications

Publications associated with this thesis:

1. **Dey, A**., Chroneos, A., Braithwaite, N. S. J., Gandhiraman, R. P. & Krishnamurthy, S. Plasma engineering of graphene. *Appl. Phys. Rev.* **3,** 21301 (2016).

2. Romero-Mangado, J., **Dey, A**., *et al.* Efficacy of atmospheric pressure dielectric barrier discharge for inactivating airborne pathogens. *J. Vac. Sci. Technol. A Vacuum, Surfaces, Film.* **35,** 41101 (2017).

3. **Dey, A.** *et al.* Plasma jet based in situ reduction of copper oxide in direct write printing. *J. Vac. Sci. Technol. B* **37**, 031203 (2019).

4. **Dey, A**. *et al*. Engineering work function of graphene oxide from p to n type using a low power atmospheric pressure plasma jet. *Phys. Chem. Chem. Phys.* (2020) doi:10.1039/C9CP06174F.

5. **Dey, A**. *et al.* Plasma Jet Printing and in situ Reduction of Highly Acidic Graphene Oxide. *ACS Nano* **12**, 5473–5481 (2018).

Other publications:

I. Duffy, E; He, X.; Nesterenko, E. P.; Brabazon, D. ; **Dey, A**.; Krishnamurthy, S.; Nesterenko, P. N.; Paull, B.;Thermally controlled growth of carbon onions within porous graphitic carbon-detonation nanodiamond monolithic composites. *RSC Adv.* **5**, 22906–22915 (2015).

II. Singh, A. P., Kodan, N., **Dey, A**., Krishnamurthy, S. & Mehta, B. R. Improvement in the structural, optical, electronic and photoelectrochemical properties of hydrogen treated bismuth vanadate thin films. *Int. J. Hydrogen Energy* **40,** 4311–4319 (2015).

III. Singh, A. P., Kodan, N., Mehta, B. R., **Dey, A**. & Krishnamurthy, S. In-situ plasma hydrogenated TiO_2 thin films for enhanced photoelectrochemical properties. *Mater. Res. Bull.* **76**, 284–291 (2016).

IV. Mehta, M. *et al.* Hydrogen treated anatase TiO_2 : a new experimental approach and further insights from theory. *J. Mater. Chem. A* **4,** 2670–2681 (2016).

V. Coto, M. *et al.* Tuning the properties of a black TiO_2-Ag visible light photocatalyst produced by rapid one-pot chemical reduction. *Mater. Today Chem.* **4,** 142–149 (2017).

Bibliography

1. Board on Physics and Astronomy, Plasma Science Committee, Panel on Plasma Processing of Materials, National Research Council, Division on Engineering and Physical Sciences, Commission on Physical Sciences, Mathematics, and A. *Plasma Processing of Materials: Scientific Opportunities and Technological Challenges*. (National Academies Press, 1991). doi:10.17226/1875.

2. Wolf, R. A. *Atmospheric Pressure Plasma for surface modification*. (John Wiley & Sons, Inc., 2013). doi:10.1002/9781118547519.

3. Laimer, J. & Störi, H. Recent Advances in the Research on Non-Equilibrium Atmospheric Pressure Plasma Jets. *Plasma Process. Polym.* **4**, 266–274 (2007).

4. Laroussi, M., Tendero, C., Lu, X., Alla, S. & Hynes, W. L. Inactivation of Bacteria by the Plasma Pencil. *Plasma Process. Polym.* **3**, 470–473 (2006).

5. Noh, J. H., Baik, H. K., Noh, I., Park, J.-C. & Lee, I.-S. Surface modification of polytetrafluoroethylene using atmospheric pressure plasma jet for medical application. *Surf. Coatings Technol.* **201**, 5097–5101 (2007).

6. Penkov, O. V., Khadem, M., Lim, W.-S. & Kim, D.-E. A review of recent applications of atmospheric pressure plasma jets for materials processing. *J. Coatings Technol. Res.* **12**, 225–235 (2015).

7. Marinov, D. & Braithwaite, N. S. J. Power coupling and electrical characterization of a radio-frequency micro atmospheric pressure plasma jet. *Plasma Sources Sci. Technol.* **23**, 062005 (2014).

8. Lieberman, M. & Lichtenberg, A. *Discharges and Materials Processing Principles of Plasma Discharges and Materials*. (Wiley-Interscience, 2005). doi:10.1007/s13398-014-0173-7.2.

9. Boulos, M. I. Thermal Plasma Processing. *IEEE Trans. Plasma Sci.* **19**, 1078–1089 (1991).

10. Liu, L., Liu, W., Cao, N. & Cai, C. Study on The Performance of PECVD Silicon Nitride Thin Films. *Def. Technol.* **9**, 121–126 (2013).

11. Roth, J. R. *Industrial Plasma Engineering, Vol. 2: Applications to Nonthermal Plasma Processing*. vol. 2 (Institute of Physics Pub, 2001).

12. Mariotti, D. *et al.* Low-Temperature Atmospheric Pressure Plasma Processes for ‘Green’ Third Generation Photovoltaics. *Plasma Processes and Polymers* vol. 13 70–90 (2016).

13. Korada, V. A., R, V. K. R., Ps, K. & Singh, S. P. Copper Conductive Inks: Synthesis and its Utilization in Flexible Electronics. *RSC Adv.* **5**, 63985–64030 (2015).

14. Magdassi, S., Grouchko, M. & Kamyshny, A. Copper nanoparticles for printed electronics: Routes towards achieving oxidation stability. *Materials (Basel).* **3**,

4626–4638 (2010).

15. Zenou, M., Ermak, O., Saar, A. & Kotler, Z. Laser sintering of copper nanoparticles. *J. Phys. D. Appl. Phys.* **47**, 025501 (2014).

16. Zhang, T. *et al.* A laser printing based approach for printed electronics. *Appl. Phys. Lett.* **108**, (2016).

17. Farraj, Y., Smooha, A., Kamyshny, A. & Magdassi, S. Plasma-Induced Decomposition of Copper Complex Ink for the Formation of Highly Conductive Copper Tracks on Heat-Sensitive Substrates. *ACS Appl. Mater. Interfaces* **9**, 8766–8773 (2017).

18. Penache, C. *et al.* Plasma printing: Patterned surface functionalisation and coating at atmospheric pressure. *IEE Proc. Nanobiotechnology* **151**, 139–144 (2004).

19. Thomas, M. *et al.* Plasma printing and related techniques - Patterning of surfaces using microplasmas at atmospheric pressure. *Plasma Process. Polym.* **9**, 1086–1103 (2012).

20. Magdassi, S., Grouchko, M. & Kamyshny, A. Copper nanoparticles for printed electronics: Routes towards achieving oxidation stability. *Materials (Basel).* **3**, 4626–4638 (2010).

21. Thostenson, E. T., Ren, Z. & Chou, T.-W. Advances in the science and technology of carbon nanotubes and their composites: a review. *Compos. Sci. Technol.* **61**, 1899–1912 (2001).

22. Zhao, Q., Gan, Z. & Zhuang, Q. Electrochemical Sensors Based on Carbon Nanotubes. *Electroanalysis* **14**, 1609–1613 (2002).

23. Baughman, R. H., Zakhidov, A. A. & de Heer, W. A. Carbon nanotubes--the route toward applications. *Science* **297**, 787–92 (2002).

24. Coleman, J. N., Khan, U. & Gun'ko, Y. K. Mechanical Reinforcement of Polymers Using Carbon Nanotubes. *Adv. Mater.* **18**, 689–706 (2006).

25. Novoselov, K. S. *et al.* Electric field effect in atomically thin carbon films. *Science* **306**, 666–9 (2004).

26. Balandin, A. A. *et al.* Superior thermal conductivity of single-layer graphene. *Nano Lett.* **8**, 902–7 (2008).

27. Mayorov, A. S. *et al.* Micrometer-scale ballistic transport in encapsulated graphene at room temperature. *Nano Lett.* **11**, 2396–9 (2011).

28. Morozov, S. *et al.* Giant Intrinsic Carrier Mobilities in Graphene and Its Bilayer. *Phys. Rev. Lett.* **100**, 016602 (2008).

29. Stoller, M. D., Park, S., Zhu, Y., An, J. & Ruoff, R. S. Graphene-based ultracapacitors. *Nano Lett.* **8**, 3498–502 (2008).

30. Nair, R. R. *et al.* Fine structure constant defines visual transparency of graphene. *Science* **320**, 1308 (2008).

31. Moser, J., Barreiro, A. & Bachtold, A. Current-induced cleaning of graphene. *Appl. Phys. Lett.* **91**, 163513 (2007).

32. Hummers, W. S. & Offeman, R. E. Preparation of Graphitic Oxide. *J. Am. Chem. Soc.* **80**, 1339–1339 (1958).

33. Eda, G., Fanchini, G. & Chhowalla, M. Large-area ultrathin films of reduced graphene oxide as a transparent and flexible electronic material. *Nat. Nanotechnol.* **3**, 270–274 (2008).

34. Brodie, B. C. On the Atomic Weight of Graphite. *Philos. Trans. R. Soc. London* **149**, 249–259 (1859).

35. Li, D., Müller, M. B., Gilje, S., Kaner, R. B. & Wallace, G. G. Processable aqueous dispersions of graphene nanosheets. *Nat. Nanotechnol.* **3**, 101–5 (2008).

36. Chen, D., Feng, H. & Li, J. Graphene oxide: preparation, functionalization, and electrochemical applications. *Chem. Rev.* **112**, 6027–53 (2012).

37. Loh, K. P., Bao, Q., Eda, G. & Chhowalla, M. Graphene oxide as a chemically tunable platform for optical applications. *Nat. Chem.* **2**, 1015–24 (2010).

38. Zhou, M., Zhai, Y. & Dong, S. Electrochemical sensing and biosensing platform based on chemically reduced graphene oxide. *Anal. Chem.* **81**, 5603–13 (2009).

39. Compton, O. C. & Nguyen, S. T. Graphene oxide, highly reduced graphene oxide, and graphene: versatile building blocks for carbon-based materials. *Small* **6**, 711–23 (2010).

40. Abe, H., Yoneda, M. & Fujiwara, N. Developments of Plasma Etching Technology for Fabricating Semiconductor Devices. *Jpn. J. Appl. Phys.* **47**, 1435–1455 (2008).

41. Meyyappan, M. Plasma nanotechnology: past, present and future. *J. Phys. D. Appl. Phys.* **44**, 174002 (2011).

42. Meyyappan, M. A review of plasma enhanced chemical vapour deposition of carbon nanotubes. *J. Phys. D. Appl. Phys.* **42**, 213001 (2009).

43. Neyts, E. C. PECVD growth of carbon nanotubes: From experiment to simulation. *J. Vac. Sci. Technol. B Microelectron. Nanom. Struct.* **30**, 030803 (2012).

44. Wang, Q., Wang, X., Chai, Z. & Hu, W. Low-temperature plasma synthesis of carbon nanotubes and graphene based materials and their fuel cell applications. *Chem. Soc. Rev.* **42**, 8821–34 (2013).

45. Bo, Z. *et al.* Plasma-enhanced chemical vapor deposition synthesis of vertically oriented graphene nanosheets. *Nanoscale* **5**, 5180–204 (2013).

46. Kato, T. *et al.* Room-temperature edge functionalization and doping of graphene by mild plasma. *Small* **7**, 574–577 (2011).

47. Baraket, M. *et al.* Aminated graphene for DNA attachment produced via plasma functionalization. *Appl. Phys. Lett.* **100**, 233123 (2012).

48. Zeng, J. J. & Lin, Y. J. Tuning the work function of graphene by nitrogen plasma treatment with different radio-frequency powers. *Appl. Phys. Lett.* **104**, 1–6 (2014).

49. Imran Jafri, R., Rajalakshmi, N. & Ramaprabhu, S. Nitrogen doped graphene nanoplatelets as catalyst support for oxygen reduction reaction in proton exchange membrane fuel cell. *J. Mater. Chem.* **20**, 7114 (2010).

50. Parambhath, V. B., Nagar, R. & Ramaprabhu, S. Effect of nitrogen doping on hydrogen storage capacity of palladium decorated graphene. *Langmuir* **28**, 7826–7833 (2012).

51. Wang, Y., Shao, Y., Matson, D. W., Li, J. & Lin, Y. Nitrogen-doped graphene and its application in electrochemical biosensing. *ACS Nano* **4**, 1790–1798 (2010).

52. Jeong, H. M. *et al.* Nitrogen-doped graphene for high-performance ultracapacitors and the importance of nitrogen-doped sites at basal planes. *Nano Lett.* **11**, 2472–2477 (2011).

53. Yang, W. *et al.* Nitrogen plasma modified CVD grown graphene as counter electrodes for bifacial dye-sensitized solar cells. *Electrochim. Acta* **173**, 715–720 (2015).

54. Lee, B.-J., Cho, S.-C. & Jeong, G.-H. Atmospheric pressure plasma treatment on graphene grown by chemical vapor deposition. *Curr. Appl. Phys.* **15**, 563–568 (2015).

55. Nourbakhsh, A. *et al.* Bandgap opening in oxygen plasma-treated graphene. *Nanotechnology* **21**, 435203 (2010).

56. Xie, X. *et al.* An asymmetrically surface-modified graphene film electrochemical actuator. *ACS Nano* **4**, 6050–6054 (2010).

57. Peltekis, N. *et al.* The effect of downstream plasma treatments on graphene surfaces. *Carbon N. Y.* **50**, 395–403 (2012).

58. Xiao, N. *et al.* Enhanced thermopower of graphene films with oxygen plasma treatment. *ACS Nano* **5**, 2749–2755 (2011).

59. Kim, J. H. *et al.* Large-Scale Plasma Patterning of Transparent Graphene Electrode on Flexible Substrates. *Langmuir* **31**, 2914–2921 (2015).

60. Mao, H., Wang, R., Zhong, J., Zhong, S. & Chen, W. Mildly O2 plasma treated CVD graphene as a promising platform for molecular sensing. *Carbon N. Y.* **76**, 212–219 (2014).

61. Wojtaszek, M., Tombros, N., Caretta, A., Van Loosdrecht, P. H. M. & Van Wees, B. J. A road to hydrogenating graphene by a reactive ion etching plasma. *J. Appl. Phys.* **110**, 1–7 (2011).

62. Xie, L., Jiao, L. & Dai, H. Selective etching of graphene edges by hydrogen plasma. *J. Am. Chem. Soc.* **132**, 14751–14753 (2010).

63. Russo, C. J. & Passmore, L. a. Controlling protein adsorption on graphene for cryo-EM using low-energy hydrogen plasmas. *Nat. Methods* **11**, 649–52 (2014).

64. Liu, J., Zeng, B., Wu, Z., Zhu, J. & Liu, X. Improved field emission property of graphene paper by plasma treatment. *Appl. Phys. Lett.* **97**, 033109 (2010).

65. Thiyagarajan, K., Saravanakumar, B. & Kim, S.-J. Gate-Tunable Photoresponse of Defective Graphene: from Ultraviolet to Visible. *ACS Appl. Mater. Interfaces* **7**, 2171–2177 (2015).

66. Dey, A., Chroneos, A., Braithwaite, N. S. J., Gandhiraman, R. P. & Krishnamurthy, S. Plasma engineering of graphene. *Appl. Phys. Rev.* **3**, 021301 (2016).

67. Xu, Y. & Liu, J. Graphene as Transparent Electrodes: Fabrication and New Emerging Applications. *Small* vol. 12 1400–1419 (2016).

68. Stratakis, E., Savva, K., Konios, D., Petridis, C. & Kymakis, E. Improving the efficiency of organic photovoltaics by tuning the work function of graphene oxide hole transporting layers. *Nanoscale* **6**, 6925–31 (2014).

69. Kumar, P. V, Bernardi, M. & Grossman, J. C. The impact of functionalization on the stability, work function, and photoluminescence of reduced graphene oxide. *ACS Nano* **7**, 1638–45 (2013).

70. Misra, A., Kalita, H. & Kottantharayil, A. Work function modulation and thermal stability of reduced graphene oxide gate electrodes in MOS devices. *ACS Appl. Mater. Interfaces* **6**, 786–794 (2014).

71. Cervantes-Sodi, F., Csányi, G., Piscanec, S. & Ferrari, a. C. Edge-functionalized and substitutionally doped graphene nanoribbons: Electronic and spin properties. *Phys. Rev. B - Condens. Matter Mater. Phys.* **77**, 1–13 (2008).

72. Tsetseris, L., Wang, B. & Pantelides, S. T. Substitutional doping of graphene: The role of carbon divacancies. *Phys. Rev. B* **89**, 035411 (2014).

73. Martins, T. B., Miwa, R. H., da Silva, A. J. R. & Fazzio, A. Electronic and Transport Properties of Boron-Doped Graphene Nanoribbons. *Phys. Rev. Lett.* **98**, 196803 (2007).

74. Calandra, M. & Mauri, F. Electronic structure of heavily doped graphene: The role of foreign atom states. *Phys. Rev. B* **76**, 161406 (2007).

75. Wei, D. *et al.* Synthesis of n-doped graphene by chemical vapor deposition and its electrical properties. *Nano Lett.* **9**, 1752–1758 (2009).

76. Wang, H., Maiyalagan, T. & Wang, X. Review on recent progress in nitrogen-doped graphene: synthesis, characterization, and its potential applications. *Acs Catal.* **2**, 781–794 (2012).

77. Guo, B. *et al.* Controllable N-doping of graphene. *Nano Lett.* **10**, 4975–80 (2010).

78. Lv, R. *et al.* Nitrogen-doped graphene: beyond single substitution and enhanced molecular sensing. *Sci. Rep.* **2**, 586 (2012).

79. Reddy, A. L. M. *et al.* Synthesis of nitrogen-doped graphene films for lithium battery application. *ACS Nano* **4**, 6337–42 (2010).

80. Wu, Z.-S., Ren, W., Xu, L., Li, F. & Cheng, H.-M. Doped graphene sheets as anode materials with superhigh rate and large capacity for lithium ion batteries. *ACS Nano* **5**, 5463–71 (2011).

81. Qu, L., Liu, Y., Baek, J.-B. & Dai, L. Nitrogen-doped graphene as efficient metal-free electrocatalyst for oxygen reduction in fuel cells. *ACS Nano* **4**, 1321–6 (2010).

82. Liu, H.-W. *et al.* Rapid atmospheric pressure plasma jet processed reduced graphene oxide counter electrodes for dye-sensitized solar cells. *ACS Appl. Mater. Interfaces* **6**, 15105–12 (2014).

83. Kuok, F.-H. *et al.* Atmospheric pressure plasma jet processed reduced graphene oxides for supercapacitor application. *J. Alloys Compd.* **692**, 558–562 (2017).

84. Huang, W. & Ptasinska, S. Functionalization of graphene by atmospheric pressure plasma jet in air or H2O2 environments. *Appl. Surf. Sci.* **367**, 160–166 (2016).

85. Stankovich, S. *et al.* Synthesis of graphene-based nanosheets via chemical reduction of exfoliated graphite oxide. *Carbon N. Y.* **45**, 1558–1565 (2007).

86. Wei, Z. *et al.* Nanoscale Tunable Reduction of Graphene Oxide for Graphene Electronics. *Science (80-.).* **328**, 1373–1376 (2010).

87. Zhan, D. *et al.* Electronic structure of graphite oxide and thermally reduced graphite oxide. *Carbon N. Y.* **49**, 1362–1366 (2011).

88. Jung, I. *et al.* Reduction Kinetics of Graphene Oxide Determined by Electrical Transport Measurements and Temperature Programmed Desorption. *J. Phys. Chem. C* **113**, 18480–18486 (2009).

89. Senthilnathan, J., Liu, Y.-F., Rao, K. S. & Yoshimura, M. Submerged liquid plasma for the synchronized reduction and functionalization of graphene oxide. *Sci. Rep.* **4**, 4395 (2014).

90. Lee, S. W., Mattevi, C., Chhowalla, M. & Sankaran, R. M. Plasma-assisted reduction of graphene oxide at low temperature and atmospheric pressure for flexible conductor applications. *J. Phys. Chem. Lett.* **3**, 772–777 (2012).

91. Li, J., Chen, C., Wei, J., Li, J. & Wang, X. Enhanced Electrochemical Performance of Reduced Graphene Oxides by H 2 /Ar Plasma Treatment. *J. Phys. Chem. C* **118**, 28440–28447 (2014).

92. Singh, G. *et al.* Study of simultaneous reduction and nitrogen doping of graphene oxide Langmuir-Blodgett monolayer sheets by ammonia plasma treatment. *Nanotechnology* **24**, 355704 (2013).

93. Kumar, N. A. *et al.* Plasma-assisted simultaneous reduction and nitrogen doping of graphene oxide nanosheets. *J. Mater. Chem. A* **1**, 4431 (2013).

94. Kulkarni, D. D. *et al.* Chemical reduction of individual graphene oxide sheets as revealed by electrostatic force microscopy. *J. Am. Chem. Soc.* **136**, 6546–9 (2014).

95. Moisan, M. *et al.* Low-temperature sterilization using gas plasmas: A review of the experiments and an analysis of the inactivation mechanisms. *Int. J. Pharm.* **226**, 1–

21 (2001).

96. Moisan, M., Levif, P., Séguin, J. & Barbeau, J. Sterilization/disinfection using reduced-pressure plasmas: some differences between direct exposure of bacterial spores to a discharge and their exposure to a flowing afterglow. *J. Phys. D. Appl. Phys.* **47**, 285404 (2014).

97. Lerouge, S., Wertheimer, M. R. & Yahia, L. Plasma sterilization: A review of parameters, mechanisms, and limitations. *Plasmas Polym.* **6**, 175–188 (2001).

98. Laroussi, M. Low temperature plasma-based sterilization: Overview and state-of-the-art. *Plasma Processes and Polymers* vol. 2 391–400 (2005).

99. Moreau, M., Orange, N. & Feuilloley, M. G. J. Non-thermal plasma technologies: New tools for bio-decontamination. *Biotechnol. Adv.* **26**, 610–617 (2008).

100. Fridman, A., Chirokov, A. & Gutsol, A. Non-thermal atmospheric pressure discharges. *J. Phys. D. Appl. Phys.* **38**, R1 (2005).

101. Cullen, P. J. *et al.* Inducing a Dielectric Barrier Discharge Plasma Within a Package. *IEEE Trans. Plasma Sci.* **42**, 2368–2369 (2014).

102. Privat-Maldonado, A., O'Connell, D., Welch, E., Vann, R. & van der Woude, M. W. Spatial Dependence of DNA Damage in Bacteria due to Low-Temperature Plasma Application as Assessed at the Single Cell Level. *Sci. Rep.* **6**, 35646 (2016).

103. Hahner, G. Near edge X-ray absorption fine structure spectroscopy as a tool to probe electronic and structural properties of thin organic films and liquids. *Chem. Soc. Rev.* **35**, 1244–1255 (2006).

104. Szabó, D. & Schlabach, S. Microwave Plasma Synthesis of Materials—From Physics and Chemistry to Nanoparticles: A Materials Scientist's Viewpoint. *Inorganics* **2**, 468–507 (2014).

105. Reece Roth, J. *Industrial Plasma Engineering Volume 1: Principles*. *Industrial Plasma Engineering* vol. 1 (Institute of Physics Pub, 1995).

106. Hossain, M. M. *Plasma Technology for Deposition and Surface Modification*. (Logos Verlag, 2008).

107. Attwood, D. Soft X-rays and Extreme Ultraviolet Radiation. *Soft X-Rays Extrem. Ultrav. Radiat. Princ. Appl.* 504 (1999) doi:10.1017/CBO9781139164429.

108. Samson, J. A. & Ederer, D. L. *Vacuum Ultraviolet Spectroscopy*. ([Academic Press], 1998).

109. Reinert, F. & Hüfner, S. Photoemission spectroscopy - From early days to recent applications. *New Journal of Physics* vol. 7 97–97 (2005).

110. Celotta, R. J., Unguris, J., Kelley, M. H. & Pierce, D. T. *Characterization of Materials*. *John Wiley and Sons* (John Wiley and Sons, 2002). doi:10.1002/0471266965.

111. Briggs, D. (David) & Seah, M. P. *Practical surface analysis*. (J. Wiley, 1996).

112. Seah, M. P. & Dench, W. A. Quantitative electron spectroscopy of surfaces: A standard data base for electron inelastic mean free paths in solids. *Surf. Interface Anal.* **1**, 2–11 (1979).

113. Baker, A. D. (Arthur D. . & Brundle, C. R. *Electron spectroscopy : theory, techniques and applications. Vol. 3*. (Academic Press, 1979).

114. Pauly, N., Tougaard, S. & Yubero, F. Determination of the Cu 2p primary excitation spectra for Cu, Cu 2O and CuO. *Surf. Sci.* **620**, 17–22 (2014).

115. Brucker, C. F. Electron spectroscopy: Theory, techniques and applications, vol. 4. C. R. Brundle and A. D. Baker (Editors). Academic Press London, 1982. *Surf. Interface Anal.* **4**, i–ii (1982).

116. Ament, L. J. P., van Veenendaal, M., Devereaux, T. P., Hill, J. P. & van den Brink, J. Resonant inelastic x-ray scattering studies of elementary excitations. *Rev. Mod. Phys.* **83**, 705–767 (2011).

117. Stöhr, J. *NEXAFS Spectroscopy*. vol. 25 XV, 404 (Springer-Verlag Berlin Heidelberg, 1992).

118. Struve, W. & Mills, I. *Fundamentals of Molecular Spectroscopy*. *Vibrational Spectroscopy* vol. 1 (McGraw-Hill, 1990).

119. Jorio, A. *et al. Raman Spectroscopy in Graphene Related Systems*. *Raman Spectroscopy in Graphene Related Systems* (Wiley-VCH, 2011). doi:10.1002/9783527632695.

120. Binnig, G., Quate, C. F. & Gerber, C. Atomic force microscope. *Phys. Rev. Lett.* **56**, 930–933 (1986).

121. Binnig, G. & Rohrer, H. Scanning tunneling microscopy from birth to adolescence. *Rev. Mod. Phys.* **59**, 615–625 (1987).

122. Bonnell, D. A. *Scanning probe microscopy and spectroscopy : theory, techniques, and applications*. (Wiley-VCH, 2001).

123. Leng, Y. *Materials Characterisation: Introduction to Microscopic and Spectroscopic Methods*. *Materials Characterization* (2008).

124. Nonnenmacher, M., O'Boyle, M. P. & Wickramasinghe, H. K. Kelvin probe force microscopy. *Appl. Phys. Lett.* **58**, 2921–2923 (1991).

125. Girard, P. Electrostatic force microscopy: principles and some applications to semiconductors. *Nanotechnology* **12**, 485–490 (2001).

126. Roberts, F. S., Kuhl, K. P. & Nilsson, A. High selectivity for ethylene from carbon dioxide reduction over copper nanocube electrocatalysts. *Angew. Chemie - Int. Ed.* **54**, 5179–5182 (2015).

127. Ko, S. H. *et al.* All-inkjet-printed flexible electronics fabrication on a polymer substrate by low-temperature high-resolution selective laser sintering of metal nanoparticles. *Nanotechnology* **18**, 345202 (2007).

128. Rathmell, A. R., Bergin, S. M., Hua, Y. L., Li, Z. Y. & Wiley, B. J. The growth mechanism of copper nanowires and their properties in flexible, transparent conducting films. *Adv. Mater.* **22**, 3558–3563 (2010).

129. Gawande, M. B. *et al.* Cu and Cu-Based Nanoparticles: Synthesis and Applications in Catalysis. *Chem. Rev.* **116**, 3722–3811 (2016).

130. Li, C. W., Ciston, J. & Kanan, M. W. Electroreduction of carbon monoxide to liquid fuel on oxide-derived nanocrystalline copper. *Nature* **508**, 504–7 (2014).

131. Shchukin, D. G. & Caruso, R. A. Template synthesis and photocatalytic properties of porous metal oxide spheres formed by nanoparticle infiltration. *Chem. Mater.* **16**, 2287–2292 (2004).

132. Khan, S., Lorenzelli, L. & Dahiya, R. S. Technologies for printing sensors and electronics over large flexible substrates: A review. *IEEE Sens. J.* **15**, 3164–3185 (2015).

133. Goth, C., Putzo, S. & Franke, J. Aerosol Jet printing on rapid prototyping materials for fine pitch electronic applications. in *2011 IEEE 61st Electronic Components and Technology Conference (ECTC)* 1211–1216 (IEEE, 2011). doi:10.1109/ECTC.2011.5898664.

134. Jang, S. *et al.* Sintering of inkjet printed copper nanoparticles for flexible electronics. *Scr. Mater.* **62**, 258–261 (2010).

135. Woo, K., Kim, D., Kim, J. S., Lim, S. & Moon, J. Ink-jet printing of Cu-Ag-based highly conductive tracks on a transparent substrate. *Langmuir* **25**, 429–433 (2009).

136. Campos-Cuerva, C. *et al.* Screen-printed nanoparticles as anti-counterfeiting tags. *Nanotechnology* **27**, 095702 (2016).

137. Kim, Y. *et al.* Use of copper ink for fabricating conductive electrodes and RFID antenna tags by screen printing. *Curr. Appl. Phys.* **12**, 473–478 (2012).

138. Vander Voort, G. F. & Committee, A. S. M. I. H. *ASM Handbook*. (2004).

139. Donnelly, T. & Lunney, J. G. Confined laser ablation for single-shot nanoparticle deposition of silver. *Appl. Surf. Sci.* **282**, 133–137 (2013).

140. K., D., Jeandin, M., Irissou, E., Legoux, J.-G. & Knapp, W. Laser-Assisted Cold Spray (LACS). in *Nd YAG Laser* (InTech, 2012). doi:10.5772/36104.

141. Dharmadasa, R., Jha, M., Amos, D. a & Druffel, T. Room temperature synthesis of a copper ink for the intense pulsed light sintering of conductive copper films. *ACS Appl. Mater. Interfaces* **5**, 13227–34 (2013).

142. Draper, G. L., Dharmadasa, R., Staats, M. E., Lavery, B. W. & Druffel, T. Fabrication of Elemental Copper by Intense Pulsed Light Processing of a Copper Nitrate Hydroxide Ink. *ACS Appl. Mater. Interfaces* **7**, 16478–85 (2015).

143. Gandhiraman, R. P. *et al.* Plasma jet printing for flexible substrates. *Appl. Phys. Lett.* **108**, 123103 (2016).

144. Gandhiraman, R. P. *et al.* Plasma jet printing of electronic materials on flexible and nonconformal objects. *ACS Appl. Mater. Interfaces* **6**, 20860–20867 (2014).

145. Yeshchenko, O. A., Dmitruk, I. M., Alexeenko, A. A. & Dmytruk, A. M. Size-dependent melting of spherical copper nanoparticles embedded in a silica matrix. *Phys. Rev. B - Condens. Matter Mater. Phys.* **75**, 1–16 (2007).

146. Ahmed, A., Elvati, P. & Violi, A. Size-and phase-dependent structure of copper(ii) oxide nanoparticles. *RSC Adv.* **5**, 35033–35041 (2015).

147. Tirsell, K. G. & Karpenko, V. P. A general purpose sub-keV X-ray facility at the Stanford Synchrotron Radiation Laboratory. *Nucl. Inst. Methods Phys. Res. A* **291**, 511–517 (1990).

148. Wang, H. *et al.* Nickel L-edge soft X-ray spectroscopy of nickel-iron hydrogenases and model compounds - Evidence for high-spin nickel(II) in the active enzyme. *J. Am. Chem. Soc.* **122**, 10544–10552 (2000).

149. Wang, H. *et al.* Integrated X-ray L Absorption Spectra. Counting Holes in Ni Complexes. *J. Phys. Chem. B* **102**, 8343–8346 (1998).

150. Moravej, M. *et al.* Physics of high-pressure helium and argon radio-frequency plasmas. *J. Appl. Phys.* **96**, 7011–7017 (2004).

151. Wang, Q. *et al.* Experimental and theoretical study of the effect of gas flow on gas temperature in an atmospheric pressure microplasma. *J. Phys. D. Appl. Phys.* **40**, 4202–4211 (2007).

152. Jonkers, J., Sande, M. Van De, Sola, A., Gamero, A. & Mullen, J. Van Der. On the differences between ionizing helium and argon plasmas at atmospheric pressure. *Plasma Sources Sci. Technol.* **12**, 30–38 (2002).

153. Shao, X.-J., Jiang, N., Zhang, G.-J. & Cao, Z. Comparative study on the atmospheric pressure plasma jets of helium and argon. *Appl. Phys. Lett.* **101**, 253509 (2012).

154. Yunker, P. J., Still, T., Lohr, M. A. & Yodh, A. G. Suppression of the coffee-ring effect by shape-dependent capillary interactions. *Nature* **476**, 308–311 (2011).

155. Khelifa, F., Ershov, S., Habibi, Y., Snyders, R. & Dubois, P. Free-Radical-Induced Grafting from Plasma Polymer Surfaces. *Chemical Reviews* vol. 116 3975–4005 (2016).

156. Wang, R., Shen, Y., Zhang, C., Yan, P. & Shao, T. Comparison between helium and argon plasma jets on improving the hydrophilic property of PMMA surface. *Appl. Surf. Sci.* **367**, 401–406 (2016).

157. Yamamura, S., Shiota, H., Murakami, K. & Nakajima, H. Evaluation of porosity in porous copper fabricated by unidirectional solidification under pressurized hydrogen. *Mater. Sci. Eng. A* **318**, 137–143 (2001).

158. George, S. J., Lowery, M. D., Solomon, E. I. & Cramer, S. P. Copper L-edge spectral studies: a direct experimental probe of the ground-state covalency in the blue copper site in plastocyanin. *J. Am. Chem. Soc.* **115**, 2968–2969 (1993).

159. Kau, L., Spira-Solomon, D. J., Penner-Hahn, J. E., Hodgson, K. O. & Solomon, E. I. X-ray absorption edge determination of the oxidation state and coordination number of copper. Application to the type 3 site in Rhus vernicifera laccase and its reaction. *J. Am. Chem. Soc.* **109**, 6433–6442 (1987).

160. Shimizu, K., Maeshima, H., Yoshida, H., Satsuma, A. & Hattori, T. Ligand field effect on the chemical shift in XANES spectra of Cu(II) compounds. *Phys. Chem. Chem. Phys.* **3**, 862–866 (2001).

161. Yang, J. *et al.* Soft X-ray induced photoreduction of organic Cu(II) compounds probed by X-ray absorption near-edge (XANES) spectroscopy. *Anal. Chem.* **83**, 7856–7862 (2011).

162. Grioni, M. *et al.* Studies of copper valence states with Cu L3 x-ray absorption spectroscopy. *Phys. Rev. B* **39**, 1541–1545 (1989).

163. Grioni, M., Van Acker, J. F., Czyayk, M. T. & Fuggle, J. C. Unoccupied electronic structure and core-hole effects in the x-ray-absorption spectra of Cu2O. *Phys. Rev. B* **45**, 3309–3318 (1992).

164. Henzler, K. *et al.* Investigation of reactions between trace gases and functional CuO nanospheres and octahedrons using NEXAFS-TXM imaging. *Sci. Rep.* **5**, 17729 (2016).

165. Sharma, A. *et al.* XANES, EXAFS and photocatalytic investigations on copper oxide nanoparticles and nanocomposites. *RSC Adv.* **5**, 21762–21771 (2015).

166. Pearce, C. I., Pattrick, R. A. D., Vaughan, D. J., Henderson, C. M. B. & van der Laan, G. Copper oxidation state in chalcopyrite: Mixed Cu d9 and d10 characteristics. *Geochim. Cosmochim. Acta* **70**, 4635–4642 (2006).

167. DeGroot, F. M. E., Grioni, M., Fuggle, J. C., Ghijsen, J. & Sawatzky, G. A. Oxygen 1s XAS edges of TM oxides.pdf. *Physical Review B* vol. 40 5715–5723 (1989).

168. Filipič, G. & Cvelbar, U. Copper oxide nanowires: a review of growth. *Nanotechnology* **23**, 194001 (2012).

169. Gao, D. *et al.* Room temperature ferromagnetism in CuO/Cu2O microspheres: Towards interface effect. *Appl. Phys. Lett.* **104**, 022406 (2014).

170. Asbrink S & Waskowska A. CuO: X-ray single-crystal structure determination at 196 K and room temperature. *J. Phys. Condens. Matter* **3**, 8173 (1991).

171. Wyckoff, R. W. G. *Crystal structures*. vol. 1 (Interscience Publishers, 1963).

172. Debbichi, L., Marco de Lucas, M. C., Pierson, J. F. & Krüger, P. Vibrational Properties of CuO and Cu_4O_3 from First-Principles Calculations, and Raman and Infrared Spectroscopy. *J. Phys. Chem. C* **116**, 10232–10237 (2012).

173. Reimann, K. & Syassen, K. Raman scattering and photoluminescence in Cu 2 O under hydrostatic pressure. *Phys. Rev. B* **39**, 11113–11119 (1989).

174. Sander, T. *et al.* Correlation of intrinsic point defects and the Raman modes of cuprous oxide. *Phys. Rev. B* **90**, 045203 (2014).

175. Yu, W. L. *et al.* Diversity of electronic transitions and photoluminescence properties of p-type cuprous oxide films:A temperature-dependent spectral transmittance study. *J. Appl. Phys.* **045701**, 045701 (2015).

176. Levitskii, V. S. *et al.* Raman spectroscopy of copper oxide films deposited by reactive magnetron sputtering. *Tech. Phys. Lett.* **41**, 1094–1096 (2015).

177. Meyer, B. K. *et al.* Binary copper oxide semiconductors: From materials towards devices. *Phys. status solidi* **249**, 1487–1509 (2012).

178. Xu, J. F. *et al.* Preparation and Characterization of CuO Nanocrystals. *J. Solid State Chem.* **147**, 516–519 (1999).

179. Liu, Y. *et al.* Efficient enhancement of hydrogen production by Ag/Cu2O/ZnO tandem triple-junction photoelectrochemical cell. *Appl. Phys. Lett.* **106**, 123901 (2015).

180. Piscanec, S. *et al.* Raman spectroscopy of silicon nanowires. *Phys. Rev. B* **68**, 2–5 (2003).

181. Reichardt, W., Gompf, F., Aïn, M. & Wanklyn, B. M. Lattice dynamics of cupric oxide. *Zeitschrift für Phys. B Condens. Matter* **81**, 19–24 (1990).

182. Reuter, S., Niemi, K., Schulz-von der Gathen, V. & Döbele, H. F. Generation of atomic oxygen in the effluent of an atmospheric pressure plasma jet. *Plasma Sources Sci. Technol.* **18**, 015006 (2008).

183. Hwang, H.-J., Oh, K.-H. & Kim, H.-S. All-photonic drying and sintering process via flash white light combined with deep-UV and near-infrared irradiation for highly conductive copper nano-ink. *Sci. Rep.* **6**, 19696 (2016).

184. Eda, G. & Chhowalla, M. Chemically derived graphene oxide: towards large-area thin-film electronics and optoelectronics. *Adv. Mater.* **22**, 2392–415 (2010).

185. Mishra, M., Joshi, R. K., Ojha, S., Kanjilal, D. & Mohanty, T. Role of oxygen in the work function modification at various stages of chemically synthesized graphene. *J. Phys. Chem. C* **117**, 19746–19750 (2013).

186. Wu, Z. *et al.* Efficient planar heterojunction perovskite solar cells employing graphene oxide as hole conductor. *Nanoscale* **6**, 10505–10 (2014).

187. Jiao, K., Wang, X., Wang, Y. & Chen, Y. Graphene oxide as an effective interfacial layer for enhanced graphene/silicon solar cell performance. *J. Mater. Chem. C* **2**, 7715 (2014).

188. Garg, R., Dutta, N. & Choudhury, N. Work Function Engineering of Graphene. *Nanomaterials* **4**, 267–300 (2014).

189. Sygellou, L., Paterakis, G., Galiotis, C. & Tasis, D. Work Function Tuning of Reduced Graphene Oxide Thin Films. *J. Phys. Chem. C* **120**, 281–290 (2015).

190. Benayad, A. *et al.* Controlling work function of reduced graphite oxide with Au-ion concentration. *Chem. Phys. Lett.* **475**, 91–95 (2009).

191. Li, J., Qi, X., Hao, G., Ren, L. & Zhong, J. In-situ investigation of graphene oxide under UV irradiation: Evolution of work function. *AIP Adv.* **5**, 067154 (2015).

192. Lin, C.-Y. *et al.* Synchrotron Radiation Soft X-ray Induced Reduction in Graphene Oxide Characterized by Time-Resolved Photoelectron Spectroscopy. *J. Phys. Chem. C* **119**, 12910–12915 (2015).

193. Kang, B., Lim, S., Lee, W. H., Jo, S. B. & Cho, K. Work-function-tuned reduced graphene oxide via direct surface functionalization as source/drain electrodes in bottom-contact organic transistors. *Adv. Mater.* **25**, 5856–5862 (2013).

194. Laimer, J. & Störi, H. Recent advances in the research on non-equilibrium atmospheric pressure plasma jets. *Plasma Process. Polym.* **4**, 266–274 (2007).

195. Fu, M., Jiao, Q., Zhao, Y. & Li, H. Vapor diffusion synthesis of CoFe 2 O 4 hollow sphere/graphene composites as absorbing materials. *J. Mater. Chem. A* **2**, 735–744 (2014).

196. Dimiev, A. M. & Tour, J. M. Mechanism of Graphene Oxide Formation. *ACS Nano* **8**, 3060–3068 (2014).

197. Dreyer, D. R., Park, S., Bielawski, C. W. & Ruoff, R. S. The chemistry of graphene oxide. *Chem. Soc. Rev.* **39**, 228–240 (2010).

198. Schultz, B. J. *et al.* X-ray absorption spectroscopy studies of electronic structure recovery and nitrogen local structure upon thermal reduction of graphene oxide in an ammonia environment. *RSC Adv.* **4**, 634–644 (2014).

199. Shirley, D. A. High-resolution x-ray photoemission spectrum of the valence bands of gold. *Phys. Rev. B* **5**, 4709–4714 (1972).

200. Marinov, D. & Braithwaite, N. S. J. Power coupling and electrical characterization of a radio-frequency micro atmospheric pressure plasma jet. *Plasma Sources Sci. Technol.* **23**, 062005 (2014).

201. Clay, K. J., Speakman, S. P., Amaratunga, G. A. J. & Silva, S. R. P. Characterization of a-C:H:N deposition from CH4/N2 rf plasmas using optical emission spectroscopy. *J. Appl. Phys.* **79**, 7227–7233 (1996).

202. Singh, M. K., Ogino, A. & Nagatsu, M. Inactivation factors of spore-forming bacteria using low-pressure microwave plasmas in an N $_2$ and O $_2$ gas mixture. *New J. Phys.* **11**, 115027 (2009).

203. Arkhipenko, V., Kirillov, A., Simonchik, L. & Zgirouski, S. Influence of nitrogen impurities on an electron-excited helium atoms concentration in the self-sustained normal dc glow discharge at atmospheric pressure. *12th Int. Congr. Plasma Phys.* 1–10 (2004).

204. Lai, L. *et al.* Exploration of the active center structure of nitrogen-doped graphene-based catalysts for oxygen reduction reaction. *Energy Environ. Sci.* **5**, 7936 (2012).

205. Li, X.-F. *et al.* Unraveling the formation mechanism of graphitic nitrogen-doping in thermally treated graphene with ammonia. *Sci. Rep.* **6**, 23495 (2016).

206. Zhao, Y., Nakamura, R., Kamiya, K., Nakanishi, S. & Hashimoto, K. Nitrogen-doped carbon nanomaterials as non-metal electrocatalysts for water oxidation. *Nat. Commun.* **4**, 1–7 (2013).

207. Li, X.-F., Lian, K.-Y., Qiu, Q. & Luo, Y. Half-filled energy bands induced negative differential resistance in nitrogen-doped graphene. *Nanoscale* **7**, 4156–4162 (2015).

208. Hu, T. *et al.* Rapid synthesis of nitrogen-doped graphene for a lithium ion battery anode with excellent rate performance and super-long cyclic stability. *Phys. Chem. Chem. Phys.* **16**, 1060–6 (2014).

209. NIST X-ray Photoelectron Spectroscopy (XPS) Database Main Search Menu. https://srdata.nist.gov/xps/main_search_menu.aspx.

210. Rani, J. R. *et al.* Epoxy to carbonyl group conversion in graphene oxide thin films: Effect on structural and luminescent characteristics. *J. Phys. Chem. C* **116**, 19010–19017 (2012).

211. Ganguly, A., Sharma, S., Papakonstantinou, P. & Hamilton, J. Probing the Thermal Deoxygenation of Graphene Oxide Using High-Resolution In Situ X-ray-Based Spectroscopies. *J. Phys. Chem. C* **115**, 17009–17019 (2011).

212. Lerf, A., He, H., Forster, M. & Klinowski, J. Structure of Graphite Oxide Revisited ‖. *J. Phys. Chem. B* **102**, 4477–4482 (1998).

213. Doniach, S. & Sunjic, M. Many-electron singularity in X-ray photoemission and X-ray line spectra from metals. *J. Phys. C Solid State Phys.* **3**, 285–291 (1970).

214. Li, X. *et al.* Simultaneous nitrogen doping and reduction of graphene oxide. *J. Am. Chem. Soc.* **131**, 15939–44 (2009).

215. Bagri, a, Grantab, R., Medhekar, N. V & Shenoy, V. B. Stability and formation mechanisms of carbonyl-and hydroxyl-decorated holes in graphene oxide. *J. Phys. Chem. C* **114**, 12053–12061 (2010).

216. Bagri, A. *et al.* Structural evolution during the reduction of chemically derived graphene oxide. *Nat. Chem.* **2**, 581–587 (2010).

217. Moon, J. *et al.* One-step synthesis of N-doped graphene quantum sheets from monolayer graphene by nitrogen plasma. *Adv. Mater.* **26**, 3501–3505 (2014).

218. Usachov, D. *et al.* Nitrogen-doped graphene: Efficient growth, structure, and electronic properties. *Nano Lett.* **11**, 5401–5407 (2011).

219. Souto, S., Pickholz, M., dos Santos, M. & Alvarez, F. Electronic structure of nitrogen-carbon alloys (a-CNx) determined by photoelectron spectroscopy. *Phys. Rev. B* **57**, 2536–2540 (1998).

220. Li, Y., Zhou, Z., Shen, P. & Chen, Z. Spin gapless semiconductor-metal-half-metal properties in nitrogen-doped zigzag graphene nanoribbons. *ACS Nano* **3**, 1952–1958 (2009).

221. Luo, Z. *et al.* Pyridinic N doped graphene: synthesis, electronic structure, and electrocatalytic property. *J. Mater. Chem.* **21**, 8038 (2011).

222. Luo, Z. *et al.* Modulating the electronic structures of graphene by controllable hydrogenation. *Appl. Phys. Lett.* **97**, 2010–2012 (2010).

223. Lee, V. *et al.* Soft X-ray Absorption Spectroscopy Studies of the Electronic Structure Recovery of Graphene Oxide upon Chemical Defunctionalization. *J. Phys. Chem. C* **116**, 20591–20599 (2012).

224. Pacilé, D. *et al.* Electronic properties and atomic structure of graphene oxide membranes. *Carbon N. Y.* **49**, 966–972 (2011).

225. Gandhiraman, R. P. *et al.* X-ray Absorption Study of Graphene Oxide and Transition Metal Oxide Nanocomposites. *J. Phys. Chem. C* **118**, 18706–18712 (2014).

226. Dennis, R. V. *et al.* Near-edge x-ray absorption fine structure spectroscopy study of nitrogen incorporation in chemically reduced graphene oxide. *J. Vac. Sci. Technol. B Microelectron. Nanom. Struct.* **31**, 041204 (2013).

227. Kuznetsova, A. *et al.* Oxygen-containing functional groups on single-wall carbon nanotubes: NEXAFS and vibrational spectroscopic studies. *J. Am. Chem. Soc.* **123**, 10699–10704 (2001).

228. Jeong, H.-K. K. *et al.* X-ray absorption spectroscopy of graphite oxide. *EPL (Europhysics Lett.* **82**, 67004 (2008).

229. Zhang, L. *et al.* Electronic structure and chemical bonding of a graphene oxide-sulfur nanocomposite for use in superior performance lithium-sulfur cells. *Phys. Chem. Chem. Phys.* **14**, 13670–5 (2012).

230. Chen, J., Lin, C. L., Qiu, S. L., Strongin, M. & denBoer, M. L. Auger and x-ray absorption studies of solid molecular oxygen. *J. Vac. Sci. Technol. A Vacuum, Surfaces, Film.* **8**, 2591–2594 (1990).

231. Matsui, F., Yeom, H. W., Amemiya, K., Tono, K. & Ohta, T. Reinterpretation of the molecular O2 chemisorbate in the initial oxidation of the Si(111)7 x 7 surface. *Phys. Rev. Lett.* **85**, 630–633 (2000).

232. Hellgren, N. *et al.* Nitrogen bonding structure in carbon nitride thin films studied by soft x-ray spectroscopy. *Appl. Phys. Lett.* **79**, 4348–4350 (2001).

233. Shimoyama, I., Wu, G., Sekiguchi, T. & Baba, Y. Evidence for the existence of nitrogen-substituted graphite structure by polarization dependence of near-edge x-ray-absorption fine structure. *Phys. Rev. B - Condens. Matter Mater. Phys.* **62**, 6053–6056 (2000).

234. Schiros, T. *et al.* Connecting dopant bond type with electronic structure in n-doped graphene. *Nano Lett.* **12**, 4025–4031 (2012).

235. Gao, Y. *et al.* Nitrogen-doped sp2-hybridized carbon as a superior catalyst for selective oxidation. *Angew. Chem. Int. Ed. Engl.* **52**, 2109–13 (2013).

236. Kiuchi, H. *et al.* Characterization of nitrogen species incorporated into graphite using low energy nitrogen ion sputtering. *Phys. Chem. Chem. Phys.* **18**, 458–465 (2016).

237. Zhao, W. *et al.* Production of Nitrogen-Doped Graphene by Low-Energy Nitrogen Implantation. *J. Phys. Chem. C* **116**, 5062–5066 (2012).

238. Yalcin, S. E. *et al.* Direct Imaging of Charge Transport in Progressively Reduced Graphene Oxide Using Electrostatic Force Microscopy. *AC nano* **9**, 2981–8 (2015).

239. Akada, K., Terasawa, T., Imamura, G., Obata, S. & Saiki, K. Control of work function of graphene by plasma assisted nitrogen doping. *Appl. Phys. Lett.* **104**, 131602 (2014).

240. Singh, R. K., Kumar, R. & Singh, D. P. Graphene oxide: strategies for synthesis, reduction and frontier applications. *RSC Adv.* **6**, 64993–65011 (2016).

241. Poh, H. L. *et al.* Graphenes prepared by Staudenmaier, Hofmann and Hummers methods with consequent thermal exfoliation exhibit very different electrochemical properties. *Nanoscale* **4**, 3515 (2012).

242. Paton, K. R. *et al.* Scalable production of large quantities of defect-free few-layer graphene by shear exfoliation in liquids. *Nat. Mater.* **13**, 624–630 (2014).

243. Secor, E. B., Ahn, B. Y., Gao, T. Z., Lewis, J. A. & Hersam, M. C. Rapid and Versatile Photonic Annealing of Graphene Inks for Flexible Printed Electronics. *Adv. Mater.* **27**, 6683–6688 (2015).

244. He, Q. *et al.* Micropatterns of Reduced Graphene Oxide Films : Fabrication and Sensing Applications. *ACS Nano* **4**, 3201–3208 (2010).

245. Secor, E. B. *et al.* Gravure printing of graphene for large-area flexible electronics. *Adv. Mater.* **26**, 4533–4538 (2014).

246. Arapov, K. *et al.* Conductive Screen Printing Inks by Gelation of Graphene Dispersions. *Adv. Funct. Mater.* 586–593 (2015) doi:10.1002/adfm.201504030.

247. Majee, S., Song, M., Zhang, S.-L. L. & Zhang, Z.-B. Bin. Scalable inkjet printing of shear-exfoliated graphene transparent conductive films. *Carbon N. Y.* **102**, 51–57 (2016).

248. Dodoo-Arhin, D. *et al.* Inkjet-printed graphene electrodes for dye-sensitized solar cells. *Carbon N. Y.* **105**, (2016).

249. Porro, S. & Ricciardi, C. Memristive behaviour in inkjet printed graphene oxide thin layers. *RSC Adv.* **5**, 68565–68570 (2015).

250. Lawes, S., Riese, A., Sun, Q., Cheng, N. & Sun, X. Printing nanostructured carbon for energy storage and conversion applications. *Carbon N. Y.* **92**, 150–176 (2015).

251. Wang, S. *et al.* High mobility, printable, and solution-processed graphene electronics. *Nano Lett.* **10**, 92–98 (2010).

252. Shin, K. Y., Hong, J. Y. & Jang, J. Micropatterning of graphene sheets by inkjet printing and its wideband dipole-antenna application. *Adv. Mater.* **23**, 2113–2118 (2011).

253. Kim, H. *et al.* Sheet Size-Induced Evaporation Behaviors of Inkjet-Printed

Graphene Oxide for Printed Electronics. *ACS Appl. Mater. Interfaces* **8**, 3193–9 (2016).

254. Huang, L., Huang, Y., Liang, J., Wan, X. & Chen, Y. Graphene-based conducting inks for direct inkjet printing of flexible conductive patterns and their applications in electric circuits and chemical sensors. *Nano Res.* **4**, 675–684 (2011).

255. Torrisi, F. *et al.* Inkjet-printed graphene electronics. *ACS Nano* **6**, 2992–3006 (2012).

256. Reich, S. & Thomsen, C. Raman spectroscopy of graphite. *Philos. Trans. R. Soc. A Math. Phys. Eng. Sci.* **362**, 2271–2288 (2004).

257. Ferrari, A. C. & Robertson, J. Interpretation of Raman spectra of disordered and amorphous carbon. *Phys. Rev. B* **61**, 14095–14107 (2000).

258. King, A. A. K. *et al.* A New Raman Metric for the Characterisation of Graphene oxide and its Derivatives. *Sci. Rep.* **6**, 19491 (2016).

259. Ferrari, A. C. Raman spectroscopy of graphene and graphite: Disorder, electron-phonon coupling, doping and nonadiabatic effects. *Solid State Commun.* **143**, 47–57 (2007).

260. Kudin, K. N. *et al.* Raman spectra of graphite oxide and functionalized graphene sheets. *Nano Lett.* **8**, 36–41 (2008).

261. Beams, R., Gustavo Cançado, L. & Novotny, L. Raman characterization of defects and dopants in graphene. *J. Phys. Condens. Matter* **27**, 083002 (2015).

262. Hulman, M., Haluška, M., Scalia, G., Obergfell, D. & Roth, S. Effects of charge impurities and laser energy on Raman spectra of graphene. *Nano Lett.* **8**, 3594–3597 (2008).

263. Matsukata, M., Fujikawa, T., Kikuchi, E. & Morita, Y. Interaction between potassium carbonate and carbon substrate at subgasification temperatures. Migration of potassium into the carbon matrix. *Energy & Fuels* **2**, 750–756 (1988).

264. Ganesan, K. *et al.* A comparative study on defect estimation using XPS and Raman spectroscopy in few layer nanographitic structures. *Phys. Chem. Chem. Phys.* **18**, 22160–22167 (2016).

265. Schultz, B. J. *et al.* Imaging local electronic corrugations and doped regions in graphene. *Nat. Commun.* **2**, 372 (2011).

266. Lee, V. *et al.* Large-Area Chemically Modified Graphene Films: Electrophoretic Deposition and Characterization by Soft X-ray Absorption Spectroscopy. *Chem. Mater.* **21**, 3905–3916 (2009).

267. Jeong, H., Lee, K. M., Ahn, Y. H., Lee, S. & Park, J.-Y. Non-Contact Local Conductance Mapping of Individual Graphene Oxide Sheets during the Reduction Process. *J. Phys. Chem. Lett.* **6**, 2629–2635 (2015).

268. Gómez-Navarro, C., Guzmán-Vázquez, F. J., Gómez-Herrero, J., Saenz, J. J. & Sacha, G. M. Fast and non-invasive conductivity determination by the dielectric

response of reduced graphene oxide: an electrostatic force microscopy study. *Nanoscale* **4**, 7231–6 (2012).

269. Tu, N. D. K., Choi, J., Park, C. R. & Kim, H. Remarkable Conversion between n- and p-Type Reduced Graphene Oxide on Varying the Thermal Annealing Temperature. *Chem. Mater.* **27**, 7362–7369 (2015).

270. Shi, Y., Dong, X., Chen, P., Wang, J. & Li, L.-J. Effective doping of single-layer graphene from underlying <math display="inline"> <mrow> <msub> <mrow> <mtext>SiO</mtext> </mrow> <mn>2</mn> </msub> </mrow> </math> substrates. *Phys. Rev. B* **79**, 115402 (2009).

271. Fridman, G. *et al.* Applied plasma medicine. *Plasma Processes and Polymers* vol. 5 503–533 (2008).

272. Morfill, G. E., Kong, M. G. & Zimmermann, J. L. Focus on plasma medicine. *New J. Phys.* **11**, 115011 (2009).

273. Lee, M. H. *et al.* Removal and sterilization of biofilms and planktonic bacteria by microwave-induced argon plasma at atmospheric pressure. *New J. Phys.* **11**, 115022 (2009).

274. Weltmann, K. D. *et al.* Atmospheric-pressure plasma sources: Prospective tools for plasma medicine. *Pure Appl. Chem.* **82**, 1223–1237 (2010).

275. Kong, M. G. *et al.* Plasma medicine: an introductory review. *New J. Phys.* **11**, 115012 (2009).

276. Liu, X., Hong, F., Guo, Y., Zhang, J. & Shi, J. Sterilization of Staphylococcus Aureus by an Atmospheric Non-Thermal Plasma Jet. *Plasma Sci. Technol.* **15**, 439–442 (2013).

277. Daeschlein, G. *et al.* Antibacterial activity of an atmospheric pressure plasma jet against relevant wound pathogens in vitro on a simulated wound environment. *Plasma Process. Polym.* **7**, 224–230 (2010).

278. Laroussi, M. Low-Temperature Plasmas for Medicine? *IEEE Trans. Plasma Sci.* **37**, 714–725 (2009).

279. Weltmann, K.-D. *et al.* Antimicrobial treatment of heat sensitive products by miniaturized atmospheric pressure plasma jets (APPJs). *J. Phys. D. Appl. Phys.* **41**, 194008 (2008).

280. Matthes, R. *et al.* Antimicrobial efficacy of an atmospheric pressure plasma jet against biofilms of Pseudomonas aeruginosa and Staphylococcus epidermidis. *Plasma Process. Polym.* **10**, 161–166 (2013).

281. Klämpfl, T. G. *et al.* Cold atmospheric air plasma sterilization against spores and other microorganisms of clinical interest. *Appl. Environ. Microbiol.* **78**, 5077–82 (2012).

282. Cheung, G. Y. C. *et al.* Staphylococcus epidermidis strategies to avoid killing by human neutrophils. *PLoS Pathog.* **6**, e1001133 (2010).

283. Otto, M. Staphylococcus epidermidis--the ‘accidental’ pathogen. *Nat. Rev. Microbiol.* **7**, 555–67 (2009).

284. Otto, M. Staphylococcal biofilms. *Curr. Top. Microbiol. Immunol.* **322**, 207–28 (2008).

285. Costerton, J. W., Stewart, P. S. & Greenberg, E. P. Bacterial biofilms: a common cause of persistent infections. *Science* **284**, 1318–22 (1999).

286. Vuong, C. & Otto, M. Staphylococcus epidermidis infections. *Microbes Infect.* **4**, 481–9 (2002).

287. Domingo, P. & Fontanet, A. Management of complications associated with totally implantable ports in patients with AIDS. *AIDS Patient Care STDS* **15**, 7–13 (2001).

288. Ziebuhr, W. Staphylococcus aureus and Staphylococcus epidermidis: emerging pathogens in nosocomial infections. *Contrib. Microbiol.* **8**, 102–7 (2001).

289. Jun, S., Irudayaraj, J., Demirci, A. & Geiser, D. Pulsed UV-light treatment of corn meal for inactivation of Aspergillus niger spores. *Int. J. Food Sci. Technol.* **38**, 883–888 (2003).

290. Tribst, A. A. L., Franchi, M. A., Cristianini, M. & De Massaguer, P. R. Inactivation of *Aspergillus niger* in Mango Nectar by High-Pressure Homogenization Combined with Heat Shock. *J. Food Sci.* **74**, M509–M514 (2009).

291. Mitoraj, D. *et al.* Visible light inactivation of bacteria and fungi by modified titanium dioxide. *Photochem. Photobiol. Sci.* **6**, 642–648 (2007).

292. Raballand, V. *et al.* Inactivation of Bacillus atrophaeus and of Aspergillus niger using beams of argon ions, of oxygen molecules and of oxygen atoms. *J. Phys. D. Appl. Phys.* **41**, 115207 (2008).

293. Zhang, D. & Quantick, P. C. Antifungal effects of chitosan coating on fresh strawberries and raspberries during storage. *J. Hortic. Sci. Biotechnol.* **73**, 763–767 (1998).

294. Roller, S. & Covill, N. The antifungal properties of chitosan in laboratory media and apple juice. *Int. J. Food Microbiol.* **47**, 67–77 (1999).

295. Plascencia-Jatomea, M., Viniegra, G., Olayo, R., Castillo-Ortega, M. M. & Shirai, K. Effect of Chitosan and Temperature on Spore Germination of Aspergillus niger. in *Macromolecular Bioscience* vol. 3 582–586 (WILEY-VCH Verlag, 2003).

296. Romero-Mangado, J. *et al.* Morphological and chemical changes of aerosolized E. coli treated with a dielectric barrier discharge. *Biointerphases* **11**, 011009 (2016).

297. Urquhart, S. G. & Ade, H. Trends in the Carbonyl Core (C 1S, O 1S) → π* C=O Transition in the Near-Edge X-ray Absorption Fine Structure Spectra of Organic Molecules. *J. Phys. Chem. B* **106**, 8531–8538 (2002).

298. Edwards, D. C. & Myneni, S. C. B. Near edge X-ray absorption fine structure spectroscopy of bacterial hydroxamate siderophores in aqueous solutions. *J. Phys. Chem. A* **110**, 11809–18 (2006).

299. Gordon, M. L. *et al.* Inner-shell excitation spectroscopy of the peptide bond: Comparison of the C 1s, N 1s, and O 1s spectra of glycine, glycyl-glycine, and glycyl-glycyl-glycine. *J. Phys. Chem. A* **107**, 6144–6159 (2003).

300. Solomon, D., Lehmann, J., Kinyangi, J., Liang, B. & Schafer, T. Carbon K-Edge NEXAFS and FTIR-ATR Spectroscopic Investigation of Organic Carbon Speciation in Soils. *Soil Sci. Soc. Am. J.* **69**, 107–119 (2005).

301. Kaznacheyev, K. *et al.* Innershell absorption spectroscopy of amino acids. *J. Phys. Chem. A* **106**, 3153–3168 (2002).

302. Outka, D. A. *et al.* NEXAFS studies of complex alcohols and carboxylic acids on the Si(111)(7×7) surface. *Surf. Sci.* **185**, 53–74 (1987).

303. Sette, F., Stöhr, J. & Hitchcock, A. P. Determination of intramolecular bond lengths in gas phase molecules from K shell shape resonances. *J. Chem. Phys.* **81**, 4906 (1984).

304. Stewart-Ornstein, J. *et al.* Using intrinsic X-ray absorption spectral differences to identify and map peptides and proteins. *J. Phys. Chem. B* **111**, 7691–7699 (2007).

305. Vairavamurthy, A. & Wang, S. Organic nitrogen in geomacromolecules: Insights on speciation and transformation with K-edge XANES spectroscopy. *Environ. Sci. Technol.* **36**, 3050–3056 (2002).

306. Shard, A. G. *et al.* A NEXAFS Examination of Unsaturation in Plasma Polymers of Allylamine and Propylamine. *J. Phys. Chem. B* **108**, 12472–12480 (2004).

307. Han, L. *et al.* Mechanisms of Inactivation by High-Voltage Atmospheric Cold Plasma Differ for Escherichia coli and Staphylococcus aureus. *Appl. Environ. Microbiol.* **82**, 450–8 (2015).

308. Cheong, S.-W. The exciting world of orbitals. *Nat. Mater.* **6**, 927–928 (2007).

309. Rao, C. N. R. Transition Metal Oxides. *Annu. Rev. Phys. Chem.* **40**, 291–326 (1989).

310. Li, Q. & Qiang. Nanostructured transition metal oxides for energy storage and conversion. *ProQuest Diss. Theses; Thesis (M.S.)--The Univ. Texas - Pan Am. 2014.; Publ. Number AAT 1559964; ISBN 9781321010060; Source Masters Abstr. Int. Vol. 53-02.; 131 p.* (2014).